WRF Meteorological Modeling in Support of SIP Regional Air Quality Modeling for Base Year 2007

David Brown
Iowa Department of Natural Resources

03/06/2012

Contributors
Debra Baker, MDE
Tom Downs, ME DEP
Mike Ku, NYS DEC
Winston Hao, NYS DEC
Gopal Sistla, NYS DEC
Mike Kiss, VA DEQ
Nick Witcraft, NC DENR
Matthew Johnson, IA DNR
Da-Lin Zhang, UMD

Table of Contents

1. INTRODUCTION 4

1.1 Background 4
1.2 Objectives 5

2. MODEL SELECTION AND DESCRIPTION 6

2.1 Selection Background 6
2.2 Description 7
2.2.1 Model Features 7
2.2.2 Modeling System Components 9

3. TIME PERIOD 12

4. MODELING DOMAIN 14

4.1 Horizontal Grid 14
4.2 Vertical Levels 15

5. INPUT DATA ACQUISITION AND PROCESSING 18

5.1 Initial and Boundary Conditions 18
5.2 Static Terrestrial Data 19
5.3 Surface and 3D Analysis Nudging 21

6. SENSITIVITY TESTING 22

6.1 Methodology 22
6.2 Benchmark Simulation 24
6.3 Sensitivity Simulations 25
6.4 Episode Selection 28
6.5 Results 28

7. PRODUCTION CONFIGURATION AND EXECUTION 53

7.1 Final Configuration 53
7.1.1 Physics Parameterizations 53
7.1.2 Dynamics Options 55
7.2 Model Execution 56

8. PERFORMANCE EVALUATION 58

8.1 Methodology 58
8.2 Results 60
8.2.1 Course Domain (36 km) 60
8.2.2 Nested Domain (12 km) 85

9. CONCLUSIONS 110

10. REFERENCES 112

APPENDIX A: ANALYSIS OF 2008 CLIMATOLOGY 115

APPENDIX B: WRF NAMELISTS 127

APPENDIX C: OTC WRF CONFIGURATION 133

1. INTRODUCTION

1.1 Background

Recent and anticipated revisions to the National Ambient Air Quality Standards (NAAQS) for ozone and $PM_{2.5}$ have warranted a new round of continental scale numerical modeling exercises. The primary function of this modeling is to generate air quality datasets that can support development of State Implementation Plans (SIPs). The new datasets are designed to fulfill a one-atmosphere approach to air quality modeling for addressing multiple SIP obligations in a consistent framework. It is envisioned these datasets will be capable of supporting SIPs developed for the implementation, maintenance, and attainment of revised NAAQS, as well as regional haze and interstate transport planning activities. This document serves as the technical support document which describes the first component, the meteorological modeling, of the new air quality modeling projects. The purpose of this paper is to serve as the protocol for generating an annual meteorological dataset, as well as to document the statistical performance of the simulation over the state of Iowa and geographic regions associated with the Central States Air Resources Agency (CenSARA) and the Lake Michigan Air Directors Consortium (LADCo).

The United States Environmental Protection Agency (EPA) recommends that a modeling protocol be developed to reflect consensus among various organizations on the methods and procedures to be followed (40 CFR § 51, App. W, 10.2.1(a)). To meet this requirement, portions of the modeling protocol were prepared in collaboration with a specially formed "WRF Work Group." Its members included the State of Iowa, LADCo, the Southeastern States Air Resource Managers Inc. (SESARM), and the Mid-Atlantic/Northeast Visibility Union (MANE-VU) which includes the Ozone Transport Commission (OTC) and the University of Maryland (UMD). A map of the Regional Planning Organizations (RPO) is shown in Figure 1-1.

Figure 1-1. Map of Regional Planning Organizations for air quality activities across the U.S.

1.2 Objectives

The purpose of this technical support document is twofold. The first is to serve as the protocol which communicates the steps and decisions required to complete the meteorological modeling project, which include:

- Selection and description of the modeling system;
- Modeling episodes, extent and resolution of the three-dimensional grid;
- Selection of appropriate databases and modeling episodes;
- Establishing performance benchmarks, model configuration sensitivity simulations;
- Final model configuration and operational testing of the meteorological model;
- Performance evaluation methodology;
- Delivery of the meteorological model outputs for subsequent use in air quality modeling;
- Documentation of the meteorological modeling study findings.

This document benefits from EPA guidance on regulatory modeling, published scientific literature, and modeling experience of staff at various regulatory agencies involved in this process. Consensus within the WRF Work Group was reached on the mesoscale model, domain, vertical layers, and some of the physics parameterization options. Ultimately, regional differences warranted the use of slightly different parameterizations but all participants agreed that the meteorology fields prepared would be shared among all groups.

The SESARM organization established a contract (AER #S2009-09-01) with Atmospheric and Environmental Research, Inc to conduct a comprehensive model performance evaluation for the meteorological datasets developed by the WRF collaborative group. The second objective of this report is to document the methodology and results of the statistical performance evaluation of the meteorological dataset conducted by AER. The error statistics generated by this analysis put into a historical context the accuracy and reliability of the simulated meteorological fields. A strong understanding of these error quantities is important, because these uncertainties will be input into the photochemical transport model and comprise a component of the errors in predicted ambient pollution concentrations. This section of the document focuses upon model performance in Iowa, CenSARA, and LADCo. A detailed write-up of the performance evaluation for the southeastern states is included in the SESARM contract. While documenting model performance in Iowa and other adjacent areas of interest was beyond the scope of the contract, the raw statistics for these regions were generated and provided by AER.

The ultimate goal of this project is to create scientifically sound simulations of atmospheric dynamics observed over the Central and Eastern United States. The simulated fields can be used for air quality modeling by various groups in the Central and Eastern United States to determine the effectiveness of emission control strategies in attaining the ozone and $PM_{2.5}$ NAAQS, reviewing Regional Haze visibility goals and progress, and investigating intestate pollutant transport concerns. The WRF Work Group concurrently addressed these requirements using a single integrated, one-atmosphere air quality modeling platform because similar pollutants, emissions, and atmospheric processes control chemical formation and transport for fine particles, ozone, and regional haze.

2. MODEL SELECTION AND DESCRIPTION

2.1 Selection Background

The meteorological model is a critical component of air quality simulations. High quality meteorological inputs are necessary for accurate representations of transport and dispersion, cloud properties, radiative fluxes, temperature and humidity fields, boundary layer evolution, and surface fluxes of both meteorological quantities (heat, moisture, and momentum) and chemical species (dry deposition) (Gilliam et al., 2009).

Air quality agencies have traditionally utilized the Pennsylvania State University/National Center for Atmospheric Research Mesoscale Model (MM5) (Dudhia, 1993) to produce meteorological fields for photochemical modeling. Several annual simulations have been completed in the past decade to support SIP development for the ozone and $PM_{2.5}$ NAAQS and the Regional Haze Rule (McNally, 2003; Olerud and Sims, 2004; Johnson, 2007; Baker et al., 2007; McNally and Stella, 2009). During this time MM5 was considered a state-of-the-science model for developing meteorological datasets. The capability to employ Four Dimensional Data Assimilation (FDDA) techniques made MM5 ideal for retrospective air quality simulations. However, within the past few years, meteorological model development has shifted away from MM5 to its successor, the Weather Research and Forecasting (WRF) model. The development of WRF has been a collaborative partnership, principally among the National Center for Atmospheric Research (NCAR), National Oceanic and Atmospheric Administration (NOAA), National Centers for Environmental Prediction (NCEP), Forecast Systems Laboratory (FSL), Air Force Weather Agency (AFWA), the Naval Research Laboratory (NRL), University of Oklahoma, and the Federal Aviation Administration (FAA). WRF represents the current state of the science, and includes improvements to mass conservation, updated dynamics, and new physics parameterizations.

WRF was selected for use in upcoming SIP air quality modeling by a consensus of several RPOs because the model is:

- Generally considered the most technically advanced public-domain prognostic model available for operational use in preparing inputs to urban- and regional- scale photochemical air quality models.
- Suitable for a broad spectrum of applications across scales ranging from meters to thousands of kilometers.
- Flexible and efficient computationally, while offering the advances in physics, numerics, and data assimilation contributed by the research community.

In addition, EPA expects that air quality modelers will also shift from MM5 to WRF (http://www.epa.gov/scram001/metmodel.htm).

Several research studies have compared the performance of MM5 and WRF. After comparing ozone concentrations to observations Lin et al. (2009) found that WRF was better for generating meteorological input to the Models-3/Community Multiscale Air Quality model (CMAQ) than MM5. In particular, WRF was better at reproducing the magnitude and spatial variation of rainfall.

Appel et al. (2009) did a thorough performance comparison of WRF and MM5 meteorology fields by comparing CMAQ results for the Eastern United States using both types of input. They compared a winter month (January 2006) and summer month (August 2006) and examined both ozone and $PM_{2.5}$ concentrations produced by CMAQ. They found that WRF had similar performance for 2 m temperature as MM5, but WRF had a lower bias in winter during nighttime. For 2 m water vapor mixing ratio, WRF had a significant reduction in bias in summer during daytime. MM5 had a lower bias for 10 m wind speeds in the winter. Both WRF and MM5 over-predicted precipitation but WRF has a smaller over-prediction than MM5 for summer convective precipitation. WRF also had a lower bias and smaller error for wet deposition. WRF had a slightly higher bias for ozone and $PM_{2.5}$ in both seasons but better performance for nitrates and similar performance for total carbon. The differences between the models were due to different formulas for friction velocity, predicted cloud cover, vegetation fraction, leaf area index, and convective precipitation. Overall, this study concluded that the WRF model generally performs in a manner comparable to MM5 for the meteorological variables required by CMAQ.

Gilliam et al. (2009) found that WRF is comparable or better than MM5 in error statistics for 2-m temperature, 2-m water vapor mixing ratio, and 10-m wind as long as objective analysis (OBSGRID) and FDDA are used. They found that WRF temperature in the planetary boundary layer (PBL) had a median absolute error of 1.0 to 1.5 K or less. They also found that WRF wind speed profiles had a low error of less than 2.0 m s^{-1} and were able to accurately reproduce the nocturnal low level jets (NLLJ) and the convective mixed layer.

In de Meij et al. (2009), researchers compared WRF to MM5 as input for another chemical transport model (CHIMERE). The biggest differences were in PBL height: at noon in January, WRF PBL height was 2.8 times higher than MM5. WRF did a better job of simulating the hourly diurnal changes in relative humidity. For winter simulations, they found that rain was overestimated by WRF but underestimated by MM5. The hit rate scores for WRF were generally better in winter. For summer, WRF catches the precipitation events better than MM5. In the winter and summer, MM5 and WRF underestimated relative humidity, but MM5 had the larger root mean square error (RMSE) and smaller correlation values. While both models overestimated wind speed, WRF had lower RMSE in winter and similar performance in summer. Wind direction accuracy was comparable for both models: good in winter and poor in summer. Both underestimated temperatures, but WRF had lower errors in the winter and similar results in the summer. WRF outperformed MM5 for potential temperature gradient profiles from soundings.

Gilliam and Pleim (2010) concluded WRF performance is now at or above the level of MM5 [and] is thus recommended to drive future air quality applications.

2.2 Description

2.2.1 Model Features

The WRF version 3.1.1 mesoscale meteorological model is a fully compressible, non-hydrostatic model with an Eulerian mass dynamical core (Skamarock et al., 2008). Two dynamical cores are available: the Advanced Research WRF (ARW) core, developed and supported by NCAR, and the Non-hydrostatic Mesoscale Model (NMM) core, whose development is centered at NCEP's

Environmental Modeling Center (EMC) and support is provided by NCAR's Development Testbed Center (DTC). The ARW core is preferred by air quality modelers due to its flexibility in physics options and its FDDA capabilities. Hereinafter references to WRF will refer to the ARW core.

The ARW core contains several major features. The prognostic equations are fully compressible and non-hydrostatic and are written in flux form to conserve mass, momentum, entropy, and scalars. Second- to 6th-order advection options in the horizontal and vertical are available for spatial discretization. WRF performs time-split integration using a 2nd- or 3rd-order Runge-Kutta scheme with a smaller time step for acoustic and gravity wave modes. A variable time step capability, known as Adaptive Time Step, is available. This method optimizes the computational efficiency of the simulation, while maintaining numerical stability.

The ARW equations are formulated using a terrain-following, hydrostatic-pressure coordinate

$$\eta = \frac{p_h - p_{ht}}{\mu}, \mu = p_{hs} - p_{ht} \tag{1}$$

where p_h is the hydrostatic component of the pressure at the vertical model level, and p_{hs} and p_{ht} are the hydrostatic pressures at the surface and top boundaries, respectively. The top boundary of the model is a constant pressure surface. The grid structure follows the Arakawa C staggering, shown in Figure 2-1.

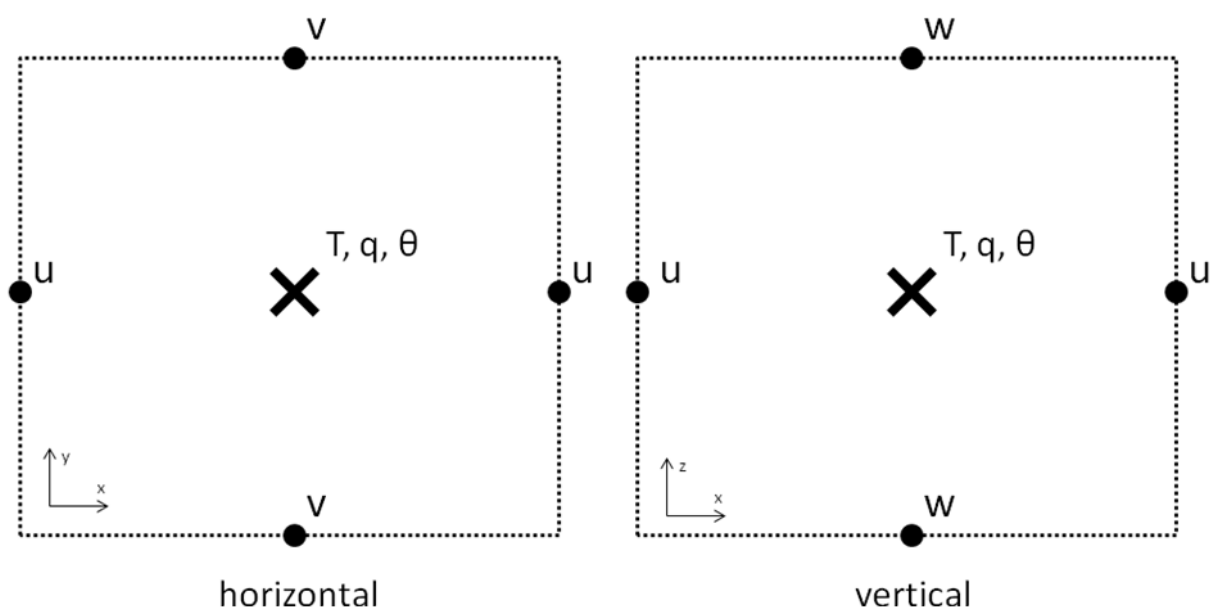

Figure 2-1. An example of the Arakawa C grid staggering used by WRF.

Multiple nested grids with multiple integer ratios are permitted. The interactions between nested grids and their parent grids may be one-way concurrent, one-way consecutive, or two-way.

WRF contains the option of FDDA to nudge modeled fields towards observed. Gridded analysis and observational nudging capabilities are available. This allows air quality modelers the ability to incorporate observations in retrospect in an attempt to reduce model error.

A full suite of physics options are available to represent sub-grid scale processes related to atmospheric radiation, surface and boundary layers, convection, and cloud and precipitation processes. For each of these sub-grid schemes, WRF offers three to nine different parameterizations from which a user may select. To make these choices, the modeler must consider not only the individual merits of each parameterization but also how it interacts with the other physics parameterization options. Figure 2-2 illustrates the interaction of the WRF physics modules.

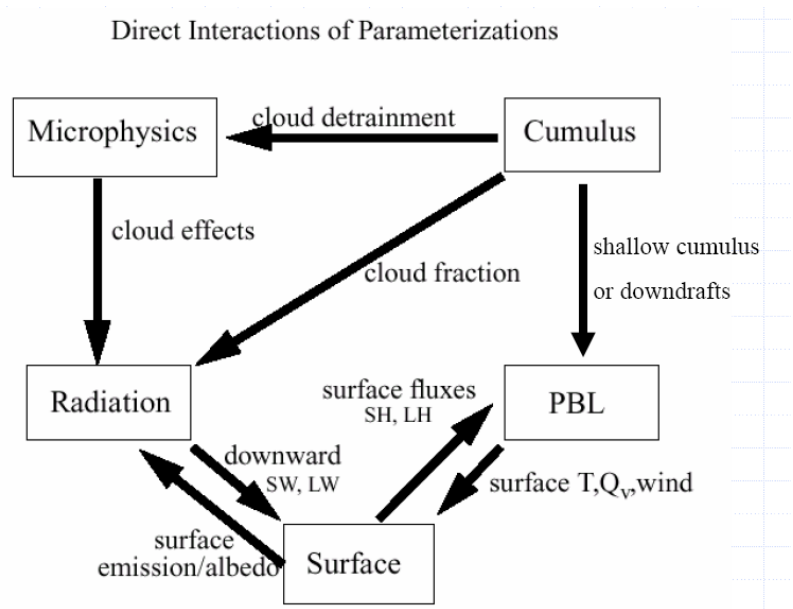

Figure 2-2. The direct interaction between the various parameterizations of sub-grid processes in WRF (source unknown).

2.2.2 Modeling System Components

The WRF modeling system consists of several processors to complete the various simulation tasks, from ingesting the input fields required to generate initial and boundary conditions, to generating the surface nudging fields, to running the dynamical core. The WRF components are illustrated in Figure 2-3. The modeling system is divided into two three main groups: the WRF Pre-processing System (WPS), the WRF model, and the post-processing and visualization tools.

WPS consists of three pre-processors: ungrib, geogrid, and metgrid. Ungrib reads gridded analysis files, extracts the necessary variables, and outputs them into an intermediate format. Geogrid operates independently from ungrib to define the modeling domain, extract terrestrial data, interpolate them to the model grid, and output the data to netCDF format. The metgrid program reads the output from geogrid and ungrib and combines the terrestrial and analysis data into a single netCDF file. The analysis data is interpolated to the horizontal domain, while the vertical structure of the original data is preserved for the time being. The program obsgrid may be considered a part of WPS; however it is obtained and compiled separately from the other

WPS pre-processors. The purpose of this routine is to read observational data in little_r format and the gridded output of metgrid (which is considered the first-guess field) and perform an objective analysis. Obsgrid then outputs a surface analysis to be used by the FDDA routine and a 3D analysis to be input by the WRF model.

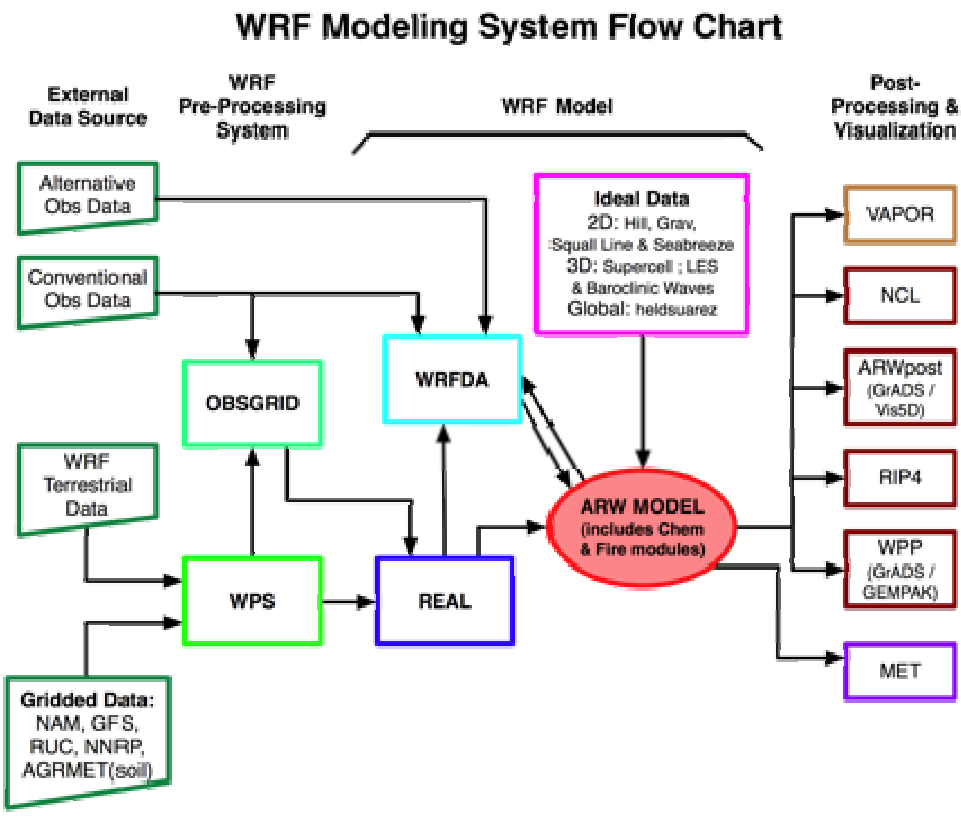

Figure 2-3. Illustration of the various components of the WRF modeling system (from WRF User's Guide).

The modeling component consists of two processors: real and the ARW core itself. Real is responsible to reading the analysis fields output by WPS and interpolating them to the model's vertical layers. Real generates the initial and boundary conditions required by the ARW core to integrate the model equations. Real also outputs the 3D gridded analysis nudging files used by the FDDA scheme.

Several packages are available to post-process and visualize the output of a WRF simulation. More detail on each package may be found in the WRF-ARW V3 Modeling System User's Guide (http://www.mmm.ucar.edu/wrf/users/docs/user_guide_V3.1/ARWUsersGuideV3.pdf). The Iowa DNR used the Read Interpolate Plot version 4 (RIP4) plotting software (Stoelinga, 2006). RIP4 invokes NCAR Graphics routines to visualize output from MM5, WRF, and potentially, any mesoscale model.

WRF version 3.1.1, released July 2009, is used for the meteorological modeling activities. The main update to the model in this release was the addition of objective analysis (OBSGRID) and

surface analysis nudging capabilities, an option preferred for generating meteorological data for input to air quality simulations.

3. TIME PERIOD

The selection of the time period for which the meteorology across the Central and Eastern U.S. would be simulated is an important decision for air quality modelers. The start date and length of the simulation should follow guidelines set forth by air quality regulatory needs. Regulatory exercises which commonly utilize meteorological modeling are attainment demonstrations and interstate transport assessments (e.g. for regional haze). Thus meteorological modeling time periods should accommodate ozone, $PM_{2.5}$, and visibility episodes. The EPA's "Guidance on the Use of Models and Other Analyses Demonstrating Attainment of Air Quality Goals for Ozone, $PM_{2.5}$, and Regional Haze" (http://www.epa.gov/scram001/guidance/guide/final-03-pm-rh-guidance.pdf) identifies four criteria which should be followed when selecting time periods to model:

1) Simulate a variety of meteorological conditions:

a) 8-Hour Ozone - Choose time periods which reflect a variety of meteorological conditions which frequently correspond with observed 8-hour daily maxima > 75 ppb at multiple monitoring sites.

b) 24-Hour $PM_{2.5}$ - Choose time periods which reflect a variety of meteorological conditions which frequently correspond with observed 24-hour averages > 35 $\mu g/m^3$ at violating monitoring sites.

c) Annual $PM_{2.5}$ - Choose time periods from each quarter which reflect the variety of meteorological conditions which represent average concentrations for that quarter and year.

d) Regional Haze - Choose time periods which reflect the variety of meteorological conditions which represent visibility impairment on the 20% best and 20% worst days in the Class I areas being modeled.

2) Model time periods in which observed concentrations are close to the appropriate baseline design value.

3) Model periods for which extensive air quality/meteorological databases exist.

4) Model a sufficient number of days so that the modeled attainment test applied at each monitor violating the NAAQS is based on multiple days.

Due to advancements in computing technology, simulating the meteorological conditions across an entire calendar year is feasible. A simulation length of one year satisfies the aforementioned criteria. The exact calendar year to model should be recent enough to reflect the most up to date development of emissions inventories. The most recent reporting year available for the National Emissions Inventory (NEI) is 2008, making this year a logical choice.

The simulated year of meteorology should also capture conditions conducive to both high ozone and $PM_{2.5}$ concentration episodes. The modeled year should be representative of recent

climatology and thus should not contain any climatological anomalies. An investigation into the climatological statistics of 2008 by the Iowa DNR found this year to be unrepresentative of climatology across the Central and Eastern U.S. In general this part of the country was extremely wet and cool, especially during the ozone season. These meteorological conditions noticeably impacted ozone and $PM_{2.5}$ concentrations. Air quality episodes were weaker and much less frequent compared to the previous year. A detailed summary of these findings are provided in Appendix A.

Following these guidelines, the Iowa DNR's first choice for a modeling time period was calendar year 2007. The members of the WRF Work Group were in agreement that 2007 was the optimal year to conduct air quality modeling. A consensus was reached among participants of the Southeastern Modeling, Analysis, and Planning (SEMAP) project, initiated by SESARM, that the modeled year be 2007 (Witcraft at al., 2010). LADCo also reached a consensus to select 2007 as the initial base year.

While it has been determined that 2007 will be the modeling base year, 2008 may also be modeled as a secondary simulation. There are several benefits to modeling 2008. As previously mentioned, it is a reporting year for the NEI. It is a year expected to be included in baseyear design value calculations for modeled attainment demonstrations for the latest revision to the ozone NAAQS. A secondary simulation may be used for weight-of-evidence analyses and to contribute to a more robust performance evaluation for the meteorological and photochemical models.

4. MODELING DOMAIN

The domain used by the Iowa DNR for meteorological modeling was determined during the collaborative process by the members of the WRF Work Group. It was designed to serve the needs of all parties involved, allowing for consistency among modeling centers. It is an expansion of the previous Iowa DNR meteorological modeling domain used in the 2002 annual simulation (Johnson, 2004).

4.1 Horizontal Grid

The computational domain for this simulation consists of a coarse and nested grid (Figure 4-1) with horizontal resolutions of 36 and 12km, respectively. The domains reside on a Lambert conic conformal projection with specifications used in previous modeling projects, with true latitudes of 33 and 45° N. The coarse grid is centered at 40° N and 97° W, and consists of an array of 165 staggered grid points (164 grid cells) in the west-east direction and 129 staggered grid points (128 grid cells) in the south-north direction. As indicated previously, the grid spacing is 36 km in both directions. This domain was initially designed to maximize the usage of the Eta model 212 analysis domain.

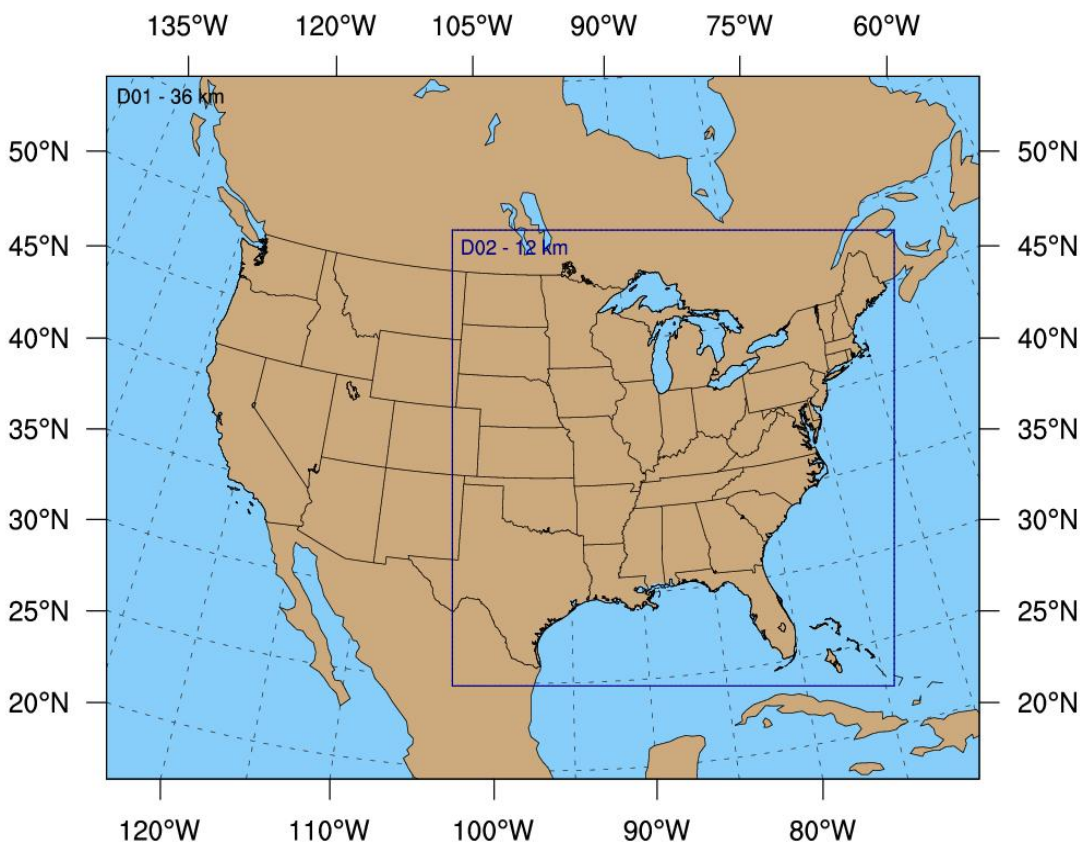

Figure 4-1. Coarse (36 km) and fine (12 km) grids utilized in the Iowa DNR 2007 WRF simulation.

A nested domain is implemented to resolve finer scale meteorological features. The nested domain is a 250 by 250 array of staggered grid points (249 by 249 grid cells) with a grid spacing of 12 km. This domain begins at grid coordinate (66, 18) of the course domain. The nested domain shares the northern, eastern, and southern boundaries of the EPA 12 km Eastern domain and western boundary of the Iowa/LADCO 12 km domain. A summary of the horizontal structure of the modeling domain is given in Table 4-1. The namelist settings used by WPS to create the model domain are provided in Appendix B.

Table 4-1. Grid parameters for the course and nested WRF domains.

Domains	**Outer (1)**	**Inner (2)**
Resolution (km)	36	12
Starting Location (i,j)	1,1	66,18
nx (E-W)	165	250
ny (N-S)	129	250
SW Coordinate (km)	-2952, -2304	-612, -1692
NE Coordinate (km)	2952, 2304	2376, 1296

4.2 Vertical Levels

The vertical grid structure consists of 35 full sigma levels (34 layers) beginning at the surface and extending to the model top (50 millibars). Figure 4-2 shows the thickness (in sigma coordinates) of each layer increases with height until the 26th model layer, then decreases until the top of the model. The purpose of this design is to provide increased resolution near layer interfaces. The planetary boundary layer near the surface is the location of many important atmospheric processes, and thus warrants increased resolution in the vertical. Near the top of the model the tropopause is another layer interface where increased resolution is desired. The second full sigma level was placed at approximately 20 meters so the midpoint of the first layer is located at 10 meters and corresponds to the standard National Weather Service (NWS) anemometer height. The top of the model is fixed at 50 millibars. Table 4-2 summarizes the vertical structure of the modeling domain.

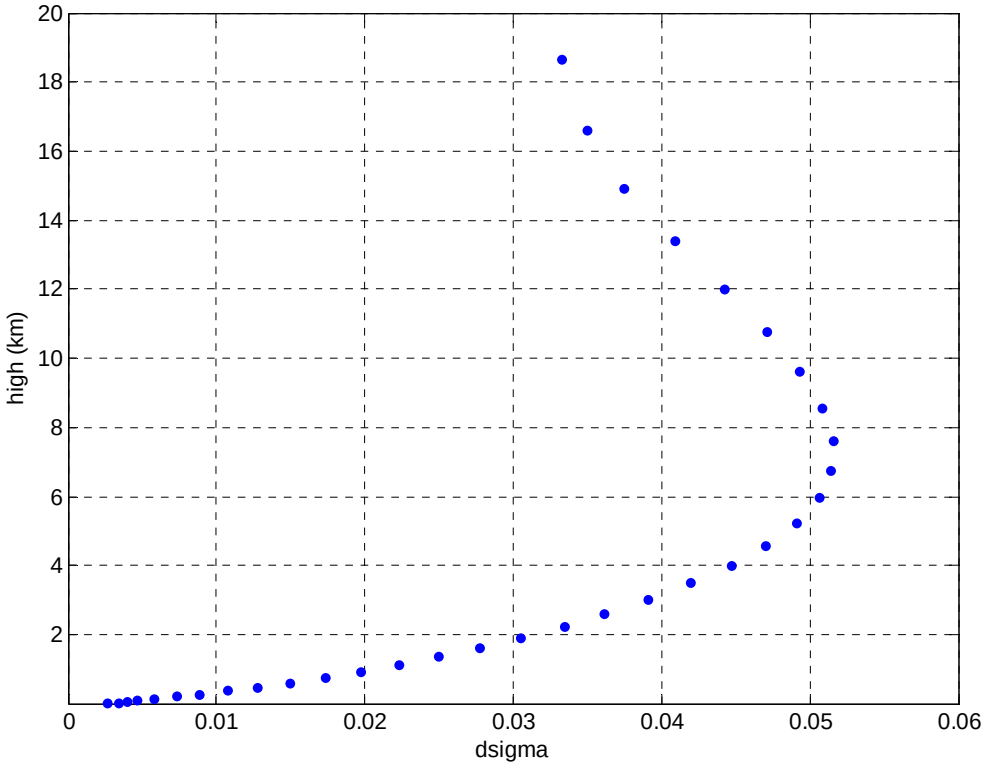

Figure 4-2. The vertical structure of the WRF modeling domain.

Table 4-2. Detailed statistics of the vertical structure of the WRF modeling domain.

Level	Sigma	Height (m)	Pressure (mb)	Depth (m)
35	0.0000	18663	50	2034
34	0.0332	16629	82	1715
33	0.0682	14914	115	1515
32	0.1056	13399	150	1375
31	0.1465	12024	189	1255
30	0.1907	10769	231	1145
29	0.2378	9624	276	1045
28	0.2871	8579	323	955
27	0.3379	7624	371	870
26	0.3895	6754	420	790
25	0.4409	5964	469	715
24	0.4915	5249	517	645
23	0.5406	4604	564	580
22	0.5876	4024	608	520
21	0.6323	3504	651	465
20	0.6742	3039	690	415
19	0.7133	2624	728	370
18	0.7494	2254	762	330
17	0.7828	1924	794	293
16	0.8133	1631	823	259
15	0.8410	1372	849	228
14	0.8659	1144	873	200
13	0.8882	944	894	174
12	0.9079	770	913	150
11	0.9252	620	929	128
10	0.9401	492	943	108
9	0.9528	384	955	90
8	0.9635	294	965	74
7	0.9723	220	974	60
6	0.9796	160	981	48
5	0.9854	112	986	38
4	0.9900	74	991	30
3	0.9940	44	994	24
2	0.9974	20	998	20
1	1.0000	0	1000	0

5. INPUT DATA ACQUISITION AND PROCESSING

The WRF model requires input of initial and boundary conditions, land-use and topography data, as well as conventional observations for objective analysis. As shown in Figure 2-3 gridded atmospheric fields, typically the output of another model or assimilation system, are processed by WPS. Static terrestrial fields are also read and processed by WPS. When objective analysis is required to generate surface and 3D nudging fields, conventional observations in little_r format are required by obsgrid.

5.1 Initial and Boundary Conditions

The initial and boundary conditions for the WRF model are obtained from the NCEP Eta modeling system (Black, 1994), which was replaced operationally by the WRF-NMM model beginning June 20, 2006. The modeling system contains the Eta Data Assimilation System (EDAS) which generates pre-forecast surface and 3D analyses at 3-hourly intervals. These fields are output on the NCEP 212 grid, a modeling grid on a Lambert conformal projection with 40 km resolution, shown by the solid black outline in Figure 5-1. These data were obtained from the Research Data Archive (RDA) which is maintained by the Computational and Information Systems Laboratory (CISL) at NCAR. NCAR is sponsored by the National Science Foundation (NSF). The original data are available from the RDA (http://dss.ucar.edu) in dataset number ds609.2. The analysis dataset has the following data assimilated:

- Rawinsonde pressure, temperature and wind;
- Pilot Balloon (PIBAL) winds;
- Dropwindsondes;
- Wind profiles;
- Surface land temperature and moisture;
- Oceanic surface data (ship and buoys);
- Aircraft winds;
- Satellite cloud-drift winds;
- Oceanic TOVS thickness retrievals; and
- GOES and SSM/I precipitable water retrievals.

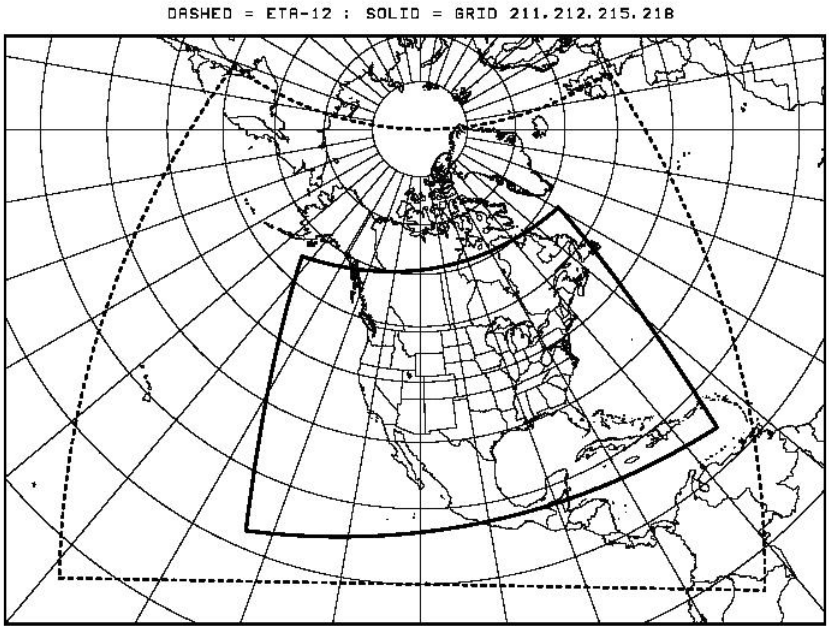

Figure 5-1. The output domain (solid black line) of the EDAS analysis fields used to generate the initial and boundary conditions for the 2007 WRF annual simulation.

5.2 Static Terrestrial Data

WRF requires static terrestrial fields to describe surface and soil characteristics which influence atmospheric processes. These data include albedo, terrain elevation, vegetation/land-use type, land/water mask, soil texture category, soil temperature, and vegetation greenness fraction and are provided with the WRF model code. Beginning with version 3.1, WRF includes a gravity wave drag parameterization option (Shin et al., 2009), and the input data for this scheme must be provided whether the option is enabled or not. There are 16 soil categories, shown in Table 5-1. The United States Geological Survey (USGS) 24 land use categories, shown in Table 5-2, were used. These data are archived on a latitude-longitude grid and are available at resolutions of 30 seconds, and two, five, and 10 minutes. Ten minute resolution was chosen for the coarse domain, while five minute resolution was chosen for the nested domain. The default interpolation options were selected for geogrid.

Table 5-1. Soil texture categories used to initialize the soil layers.

Code	Soil Category
1	Sand
2	Loamy sand
3	Sandy loam
4	Silt loam
5	Silt
6	Loam
7	Sandy clay loam
8	Silty clay loam
9	Clay loam
10	Sandy clay
11	Silty clay
12	Clay loam
13	Organic matter
14	Water
15	Bedrock
16	Other

Table 5-2. USGS land-use categories used to initialize the surface layer.

Code	Land Use Category
1	Urban
2	Dryland crop pasture
3	Irrigated crop pasture
4	Mixed crop pasture
5	Cropland and grassland
6	Cropland and woodland
7	Grassland
8	Shrubland
9	Shrubland and grassland
10	Savanna
11	Deciduous broadleaf
12	Deciduous needleleaf
13	Evergreen broadleaf
14	Evergreen needleleaf
15	Mixed forest
16	Water bodies
17	Herbaceous wetland
18	Wooded wetland
19	Barren or sparse vegetation
20	Herbaceous tundra
21	Wooded tundra
22	Mixed tundra
23	Bare ground tundra
24	Snow and ice

5.3 Surface and 3D Analysis Nudging

The FDDA scheme used in WRF for retrospective simulations requires gridded fields of analyzed atmospheric variables. These fields are generated by the program, obsgrid, which performs an objective analysis using a first-guess field and conventional observations. The first-guess field originates from the same input data provided for the initial and boundary conditions, as explained in Section 5.1. In fact, these fields are processed through obsgrid before initial and boundary conditions are generated. During this step, the surface and nudging fields are generated. It is important to note the input fields provided to obsgrid are not truly first-guess fields, which are typically short term model forecasts. Since these fields are output from EDAS, they have already been analyzed by incorporating observations using a 3D variational (3D-Var) technique. Therefore, the objective analysis performed by obsgrid is a second-pass, and is required in order to generate the surface and 3D nudging fields. The additional objective analysis has been shown to improve the initial analysis fields (Pleim and Gilliam, 2009).

The conventional observations used in the objective analysis are obtained from the Meteorological Assimilation Data Ingest System (MADIS) operated by the Earth System Research Laboratory (ESRL) Global Systems Division (GSD) of NOAA. The datasets from MADIS include observations from most North American networks. Land-based surface observations originate from standard METARs (ASOS, AWOS, non-automated stations), SAOs (Canadian stations), the UrbaNet mesonet, and the Integrated mesonet, comprised of observations from local, state, and federal agencies and private mesonets. Maritime reports are also available, including the Coastal Marine Automated Network (C-MAN), fixed and drifting buoys, and ship reports. Upper air observations include radiosondes, wind profilers, automated aircraft reports and airport profiles, and satellite derived wind fields. These observations are archived in netCDF format and must be converted to little_r format by an external utility in order to be ingested by obsgrid.

6. SENSITIVITY TESTING

One of the goals of the collaboration of the various State agencies was to establish a universal configuration of physics parameterizations and model options for WRF. This configuration would provide an optimal simulation of meteorological fields. The preferred configuration was determined by running WRF with a matrix of configuration options and performing a statistical analysis of the errors and biases of relevant meteorological fields from each simulation to determine which configuration lent the most desirable results. Due to the complexity of the WRF modeling system, it was not reasonable to test every possible configuration. Therefore only the most important configuration options were tested. Some settings were not tested, while the determination of others was assisted by previous studies. The responsibility of executing these simulations was split across the modeling centers involved in the project.

6.1 Methodology

Several meteorological variables important in the chemistry, transport, and fate of air pollution were evaluated. The primary fields for evaluation were 2 meter temperature, 2 meter water vapor mixing ratio, and 10 meter wind speed and direction. Like many other meteorological model evaluations, this study implements the operational evaluation component of the evaluation philosophy described by Tesche (1994). Hourly model meteorological variables were interpolated to observation locations and paired with their respective hourly observations. Statistical performance metrics, bias error and root mean square error (RMSE), were used to estimate the accuracy of the sensitivity simulations. The model-observed pairs are binned by geographic location and time for calculation of the statistics, which require a robust sample of data pairs in order to provide a meaningful quantity. The boundaries of these geographical regions are shown in Figure 6-1. Model-observed pairs are also grouped into hourly and daily time samples.

Bias error, hereinafter bias, is the degree of correspondence between the mean prediction and the mean observation. It is calculated using the following formula:

$$B = \frac{1}{IJ} \sum_{j=1}^{J} \sum_{i=1}^{I} \left(P_j^i - O_j^i \right) \tag{2}$$

where P and O are the prediction and observation, respectively, at observation location i within the geographic region of interest, and at time j, and I and J are the number of modeled-observed pairs in the geographical region and number of time periods, respectively. An unbiased set of model predictions will have a bias value of zero. Model predictions with a bias greater than zero indicate a general tendency for over-prediction of a variable, while conversely a bias less than zero implies a tendency for under-prediction.

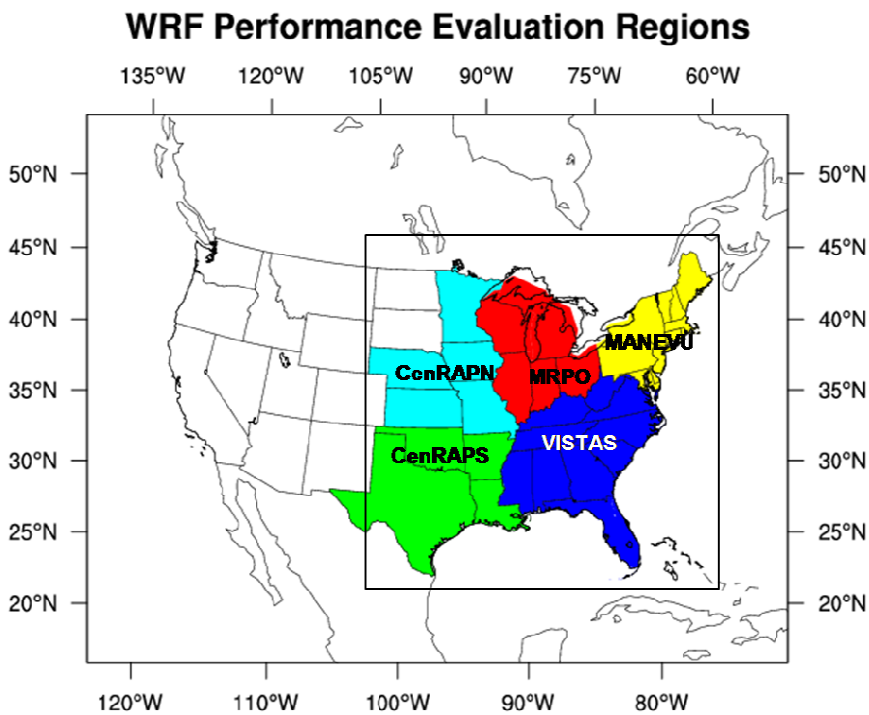

Figure 6-1. Geographical regions used to group the model-observed data pairs for evaluating the sensitivity simulations.

Root mean square error is a useful overall measure of model performance. It is defined as the square root of the mean of the squared differences between modeled and observed values, and is calculated as follows:

$$RMSE = \left[\frac{1}{IJ} \sum_{j=1}^{J} \sum_{i=1}^{I} \left(P_j^i - O_j^i \right)^2 \right]^{1/2} \tag{3}$$

where P and O are the same parameters described in Equation (2). The squaring of the differences produces only positive values. Values of RMSE range from zero, for a perfect model simulation to large positive values, as the accuracy of the simulation degrades. Since large errors are weighted heavily (due to squaring), large errors in a small sub-region may produce a large RMSE even though the majority of errors may be small and quite acceptable elsewhere. RMSE is calculated in tandem with bias because desirable bias values near zero may be the result of the cancellation of positive and negative differences between modeled and observed values.

The observational data used to evaluate the sensitivity simulations are the Techniques Data Laboratory U.S. and Canada surface hourly observations (Vincent et al., 2007). These data were obtained from the RDA at NCAR. The original data are available from the RDA (http://dss.ucar.edu) in dataset number ds472.0.

Cloud cover and precipitation are also important fields to evaluate in model performance studies; however the methods used are different than the surface fields. Due to the complexity and size of the 2D observational fields, standard error calculations are impractical for the sensitivity simulations. Subjective comparison of modeled cloud and precipitation versus observed fields at fixed time periods is necessarily sufficient for evaluating the performance of WRF in simulating these processes.

The logistics of the sensitivity analysis were developed by the WRF group, but the analysis tasks were split between subgroups and the results were not completely shared across the group. Therefore, documentation of these results is limited and incomplete. Decisions on the final configuration were made by the group as a whole based on the entire collection of results, but due to the lack of availability, documentation of the results in this report relies upon an independent sensitivity analysis conducted by the Iowa DNR. AER also provides documentation of the sensitivity analysis in AER (2011) as part of the contract with SESARM. It should be noted AER reached a consensus with the WRF group on the final configuration based on their analysis.

6.2 Benchmark Simulation

Since the modeling work load was to be divided among the members of the WRF Work Group, it was imperative to ensure the various computing platforms would generate binary identical results when running WRF with common inputs, physics parameterizations, and model settings. A five and a half day period in the summer of 2007 was selected and UMD prepared and distributed the inputs for use by each modeling center. Significant differences in results were discovered between modeling centers utilizing different compilers. In some cases, results were not identical even when the same compiler, with varied versions, was used. An example of the spatial variability in WRF output between the modeling centers' benchmark simulations is shown in Figure 6-2.

WRF developers were notified that the WRF simulations were inconsistent between modeling centers, however it was unclear if and when this issue would be resolved. Rather than wait for a resolution to the hardware/compiler issues, it was decided that a statically compiled version (prepared by UMD) would be used by all modeling centers.

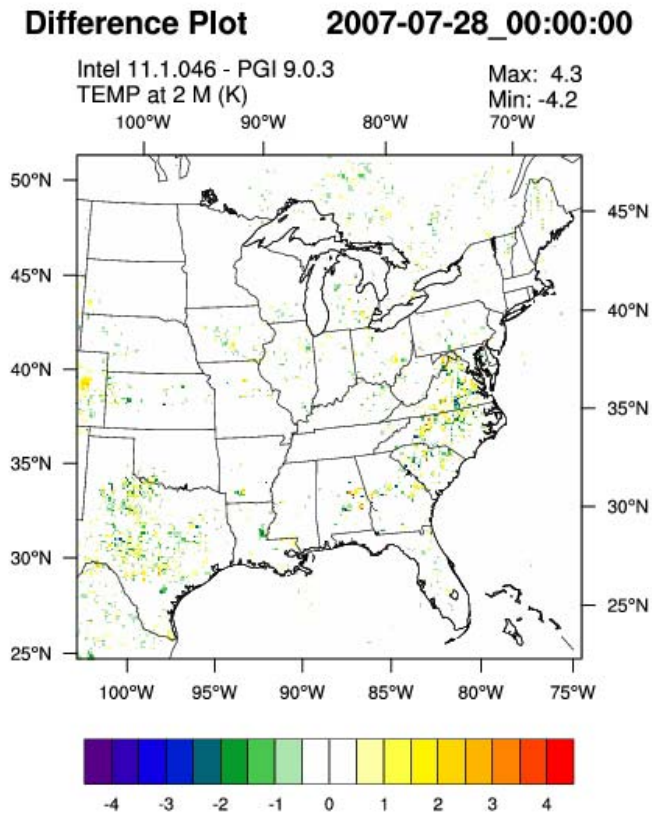

Figure 6-2. Spatial differences between two WRF benchmark simulations with identical configurations. One simulation was completed with a version of WRF compiled with PGI, while the other by WRF compiled with Intel.

6.3 Sensitivity Simulations

Eight sensitivity simulations, shown in Table 6-1, were chosen based on the variation of three planetary boundary layer schemes, three cloud microphysical schemes, two radiation schemes, and two soil temperature and moisture initialization schemes. The main focus of the sensitivity analysis was the effect of the various planetary boundary layer schemes on surface meteorological fields. This parameterization is important to air quality studies due to its strong influence on near-surface temperature and moisture, which affect atmospheric chemistry, and near-surface winds, which affect dispersion and transport. It also determines the boundary layer depth and diurnal profile, which affects vertical mixing and dispersion of pollutants away from the surface. Four PBL schemes were tested: the Asymmetric Convective Model version 2 (ACM2), the Mellor, Yamada, and Janjic scheme (MYJ), and the Yonsei University scheme.

Modeled cloud fields strongly affect ozone formation through attenuation of the ultra-violet radiation responsible for driving photolytic reactions. Three cloud microphysical schemes were chosen to test the sensitivity of cloud and precipitation fields to this parameterization: the WRF Single-Moment 5-class (WSM5) and 6-class (WSM6) schemes and the Morrison et al. scheme. The cumulus parameterization was held constant and not tested. Future sensitivity studies, especially those performed at resolutions less than 12 kilometers, may benefit from testing this parameterization.

Six of the sensitivity configurations are simply the matrix of combinations of the three PBL and the WSM5 and WSM6 schemes. One sensitivity configuration was chosen to mimic the WRF configuration used by EPA for their regional modeling activities. This sensitivity simulation uses the ACM2 PBL scheme with the Morrison et al. microphysics scheme and RRTMG radiation scheme. The Morrison et al. scheme is more complex and resource intensive than the WSM5 and WSM6 schemes. The RRTMG scheme is very similar to the RRTM scheme with the exception of the interaction with clouds and CO_2. Another configuration adds the soil temperature and moisture scheme, IPXWRF, used by EPA (Gilliam and Pleim, 2010). This scheme serves two functions. The first is to initialize the deep soil temperature based on an analysis of two-meter ambient air temperature. The second is to carry soil temperature and moisture fields from the end of one simulation to the start of the next. The default implementation is to initialize soil parameters from the input analysis fields used to create the initial and boundary conditions and reinitialize these fields at the start of every simulation.

The University of Maryland conducted an additional two sensitivity simulations to test their PBL scheme, the Blackadar scheme modified for use in WRF. This scheme was paired with the Pleim-Xiu land surface model in one configuration and the Noah land surface model in the other. Both schemes used the WSM6 cloud microphysics, Dudhia shortwave, and RRTM longwave schemes. These sensitivities are not evaluated in this document.

Table 6-1. The physics options for the sensitivity simulations conducted by the WRF Work Group.

	1	2	3	4	5	6	7	8
Planetary Boundary Layer	Asymmetric Convective Model 2	Asymmetric Convective Model 2	Asymmetric Convective Model 2	Asymmetric Convective Model 2	Mellor-Yamada-Janjic	Mellor-Yamada-Janjic	Yonsei University	Yonsei University
Surface Layer	Pleim-Xiu	Pleim-Xiu	Pleim-Xiu	Pleim-Xiu	Monin-Obukhov (Janjic Eta)	Monin-Obukhov (Janjic Eta)	Monin-Obukhov	Monin-Obukhov
Land Surface Model	Pleim-Xiu	Pleim-Xiu	Pleim-Xiu	Pleim-Xiu w/ IPXWRF	Noah	Noah	Noah	Noah
Microphysics	WRF Single Moment 5-class	WRF Single Moment 6-class	Morrison et al.	Morrison et al.	WRF Single Moment 5-class	WRF Single Moment 6-class	WRF Single Moment 5-class	WRF Single Moment 6-class
Radiation (Shortwave)	Dudhia	Dudhia	Rapid Radiative Transfer Model for GCMs	Rapid Radiative Transfer Model for GCMs	Dudhia	Dudhia	Dudhia	Dudhia
Radiation (Longwave)	Rapid Radiative Transfer Model	Rapid Radiative Transfer Model	Rapid Radiative Transfer Model for GCMs	Rapid Radiative Transfer Model for GCMs	Rapid Radiative Transfer Model	Rapid Radiative Transfer Model	Rapid Radiative Transfer Model	Rapid Radiative Transfer Model
Cumulus	Kain-Fritsch	Kain-Fritsch	Kain-Fritsch	Kain-Fritsch	Kain-Fritsch	Kain-Fritsch	Kain-Fritsch	Kain-Fritsch

6.4 Episode Selection

It was not feasible to conduct the sensitivity analysis across the entire calendar year to be modeled by the final production run. A consensus was reached by the WRF Work Group on the selection of two short time periods, described in Table 6-2. Both periods would be covered by four 5.5 day simulation blocks, with 12 hours of overlap to account for model spin-up time at the beginning of each simulation block. More information on this model execution strategy is discussed in Section 7.2. The timing of the episodes was chosen to capture meteorological conditions in the Eastern U.S. conducive to secondary particulate formation in the winter and ozone formation in the summer.

Table 6-2. Episode selection for the sensitivity simulations.

Episode	Start Date	End Date	Simulation Blocks
Summer	July 28, 2007	August 16, 2007	2007/07/27 12Z–2007/08/02 00Z 2007/08/01 12Z–2007/08/07 00Z 2007/08/06 12Z–2007/08/12 00Z 2007/08/11 12Z–2007/08/17 00Z
Winter	December 05, 2007	December 24, 2007	2007/12/04 12Z–2007/12/10 00Z 2007/12/09 12Z–2007/12/15 00Z 2007/12/14 12Z–2007/12/20 00Z 2007/12/19 12Z–2007/12/25 00Z

6.5 Results

Near-surface temperature, wind speed, and humidity fields generated by each sensitivity simulation were evaluated against each other by calculating bias and root mean square statistics for model-observational pairs in each of the geographic regions in Figure 6-1 for each day of the summer and winter episodes. Hourly statistics were also calculated for each region and were binned into daytime and nighttime distributions.

In theory, a superior configuration would stand out from the rest of the sensitivity simulations with significantly lower RMSE and bias. However, the results generally show the performance of all sensitivity simulations was very similar, with the exception of a few specific instances. Figure 6-3 through Figure 6-8 show the daily performance of modeled 10 meter wind speed, 2 meter temperature, and 2 meter mixing ratio during the summer episode within the CenRAPN region (labeled cenrapN in the figures), which includes the states of Minnesota, Iowa, Nebraska, Kansas, and Missouri. Note for the summer episode performance statistics for the seventh sensitivity are not available. Daily wind speed bias and RMSE distributions are very similar for all sensitivity simulations. The median bias and median RMSE are approximately -0.2 and 1.4 m/s, respectively. The distributions of daily temperature bias vary across sensitivity simulations. Sensitivities 1 and 2 have a median bias of about -0.3 K. Sensitivity 3 has a median bias of approximately -0.1 K. Sensitivity 4 has a significantly worse bias, with a median value of 0.7 K. Sensitivities 5-6 are nearly identical, with median biases of around -0.4 K. Sensitivity 8 has a median bias near 0 K, however, the range of bias values varies by about 2 K. The distributions of temperature RMSE are all similar, with median values ranging from 2.1 to 2.4 g/kg. Sensitivities 1-3 had the lowest median RMSE. Like temperature bias, the humidity bias distributions varied among sensitivities. Simulations 1, 2, 5, and 6 had median bias values near

zero. Sensitivity 4 was again poorest with a median bias of 1.2 g/kg. Sensitivity 8 had a median bias of approximately -1.1 g/kg. Median humidity RMSE values ranged from 2.0 to 2.3 g/kg.

Figure 6-9 through Figure 6-14 show the performance of modeled wind speed, temperature, and mixing ratio for the CenRAPS region (labeled cenrapS in the figures), which includes the states of Oklahoma, Arkansas, Texas, and Louisiana, during the summer episode. Daily wind speed bias and RMSE distributions are similar across sensitivity simulations. Median bias values range from -0.3 to -0.4 m/s. Median RMSE values range from 1.2 to 1.3 m/s. With the exception of sensitivities 4 and 8, daily temperature bias distributions are similar and centered near zero. However these distributions have a wide range from -0.9 to 0.6 K. Sensitivities 4 and 8 have median bias values near 0.4 K. Median temperature RMSE values range from 1.7 to 1.9 K. Sensitivities 4 and 8 have a larger range of RMSE values than the rest of the sensitivities. For humidity bias distributions, again all sensitivities except 4 and 8 were similar. Median bias values were approximately -0.5 g/kg. Sensitivity 4 had a median bias near zero, while sensitivity 8 had a median bias of approximately -2.2 g/kg. Sensitivity 4 had the lowest median RMSE, 1.9 g/kg. Sensitivities 1, 3, 4, 5, and 6 all had median RMSE of about 2.3 g/kg. Sensitivity 8 had the highest median RMSE, 2.8 g/kg.

Figure 6-15 through Figure 6-20 show the performance of modeled wind speed, temperature, and mixing ratio for the MRPO region (labeled mwrpo in the figures), which includes the states of Wisconsin, Illinois, Indiana, Ohio, and Michigan. Sensitivities 1-4, and 8 have similar wind speed bias distributions, with median values near -0.2 m/s. Sensitivities 5 and 6 had slightly improved median bias values (-1.0 m/s), however these sensitivities had a larger range of bias values (-0.3 to 0.3 m/s). Daily wind speed RMSE distributions were similar for all sensitivities, with median values between 1.2 and 1.3 m/s. Sensitivities 1-3 had median temperature bias values near -0.5 K, with a large range in their distributions. Sensitivity 4 had a median bias value around 0.2 K. Sensitivities 5, 6, and 8 had median temperature bias values near -0.6 K. Sensitivities 5 and 6 had a much smaller range of values than the remainder of the sensitivities. Daily temperature RMSE median values ranged from 2.0 to 2.3 K, with sensitivities 1 and 2 having the lowest values and sensitivity 8 having the highest. For daily humidity bias, sensitivities 1 and 2 had the most ideal distributions, with median values near 0.0 g/kg. Sensitivity 3 had a slightly higher median bias value of about 0.3 g/kg. Sensitivities 5 and 6 have median bias values near 0.2 g/kg, with a much more narrow range of values compared to the other sensitivities. Sensitivity 4 had a large positive median bias values near 1.0 g/kg, while sensitivity 8 had a large negative bias value near -0.8 g/kg. Sensitivities 1, 2, 3, and 8 had median RMSE values between 1.7 and 1.9 g/kg. Sensitivities 4-6 had median RMSE values between 2.0 and 2.1 g/kg.

Figure 6-21 through Figure 6-26 show daily performance of near-surface wind speed, temperature, and mixing ratio during the winter episode for the CenRAPN region. Daily wind speed bias distributions are similar across all sensitivities. Sensitivities 1-6 had median bias values between -0.2 and -0.1 m/s, while sensitivities 7 and 8 had median values near zero. Median RMSE values were approximately 1.3 m/s for all sensitivities. Daily temperature bias distributions varied significantly across the sensitivity simulations. Sensitivities 1-4 had median biases near 1.0 K, while sensitivities 5 and 6 had median biases of approximately -1.0 K. Sensitivities 7 and 8 had median biases near zero. Daily temperature RMSE distributions were

all similar, with median values of about 2.8 K. Sensitivities 1-4 have daily humidity median biases of approximately 0.3 g/kg, while sensitivities 5-8 have values of about 0.1 g/kg. Daily humidity median RMSE varied from 0.35 to 0.55 g/kg, with sensitivity 2 having the lowest value.

Figure 6-27 through Figure 6-32 show daily performance during the winter period for the CenRAPS region. Daily wind speed bias distributions are similar across all sensitivities, with all median biases near -0.25 m/s. Daily wind speed RMSE median values ranged from 1.3 to 1.4 m/s. Sensitivities 1-4 had similar daily temperature bias distributions. Median biases ranged from 0.4 to 0.8 K. The range of bias values was very large for these sensitivities, with biases ranging from -1.8 to 3.0 K. Sensitivities 5-8 had daily temperature median biases of approximately -0.4 K, with much narrower distributions. Sensitivities 1-4 also have similar daily temperature RMSE distributions, with median values of approximately 2.8 K. Sensivities 5-8 had daily temperature RMSE median values of approximately 2.2 K. Distributions of daily humidity bias were generally similar. Sensitivities 1-6 had median values between 0.1 and 0.2 g/kg, while sensitivities 7 and 8 had median biases of approximately -0.1 g/kg. Median daily humidity RMSE values ranged from 1.0 to 1.1 g/kg.

Figure 6-33 through Figure 6-38 show daily performance during the winter period for the MRPO region. Daily wind speed bias distributions are similar for sensitivities 1-4. Median values for these sensitivities range from 0.1 to 0.2 m/s. The distributions for sensitivities 5 and 6 are slightly lower, with median values near zero. The distributions for sensitivities 7 and 8 contain mostly positive values, with median values of approximately 0.4 m/s. Daily wind speed RMSE distributions are similar for all sensitivities. Median values range from 1.3 to 1.4 m/s. Daily temperature bias distributions are similar for sensitivities 1-4, with median values ranging from 0.0 to 0.3 K. Sensitivities 1 and 2 have a large range of values (-2.0 to 2.0 K). Sensitivities 5-8 have similar distributions, with median values ranging from -1.0 to -0.7 K. Daily temperature RMSE distributions are similar for sensitivities 1-4. Median values for these sensitivities are approximately 2.1 K. Sensitivities 5 and 6 had median bias values of 2.6 K. Sensitivities 7 and 8 had median bias values of approximately 2.3 K. Daily humidity bias distributions are similar for sensitivities 1 and 2. Median values are near 0.3 g/kg. Median values for sensitivities 3 and 4 are also near 0.3 g/kg, however these distributions are skewed towards larger values, while the distributions for sensitivities 1 and 2 are skewed towards smaller values. Sensitivities 5-8 have median values near 0.1 g/kg. Sensitivities 7 and 8 have a smaller range of values than sensitivities 5 and 6. Daily humidity RMSE values are lowest for sensitivity 2, whose median value is just below 0.4 g/kg. All other sensitivities have similar narrow distributions with median values ranging from 0.4 to 0.6 g/kg.

The most notable observation when comparing the results of the sensitivity simulations is all configurations yield similar, reasonable results. No one configuration sticks out with superior performance. This is desirable because it suggests any configuration may be used to produce a reliable simulation. The results show changing the PBL parameterization has the largest impact on results, while changing the physics or radiation schemes usually results in negligible change in performance. During the summer episode the ACM2 PBL scheme performed slightly better than the other schemes for temperature and nearly identically for wind speed and humidity. However, when the IPXWRF soil scheme was implemented the expected improvement in

temperature and humidity performance was not realized. In fact, implementing IPXWRF resulted in a positive bias in temperature and humidity and larger errors. In a few instances, primarily with regard to humidity, the YSU scheme performed noticeably worse than the other PBL schemes. During the winter episode all configurations were again very similar, with the YSU PBL sensitivities just barely exhibiting the best performance. The ACM2 sensitivities exhibited a larger range of daily bias and RMSE values for temperature.

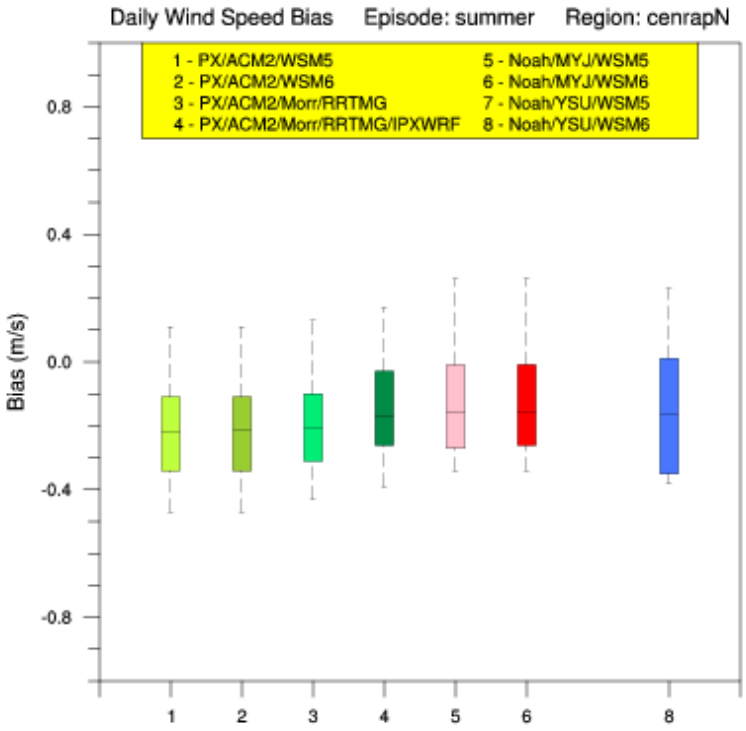

Figure 6-3. Daily wind speed bias distributions during the summer episode for the cenrapN region.

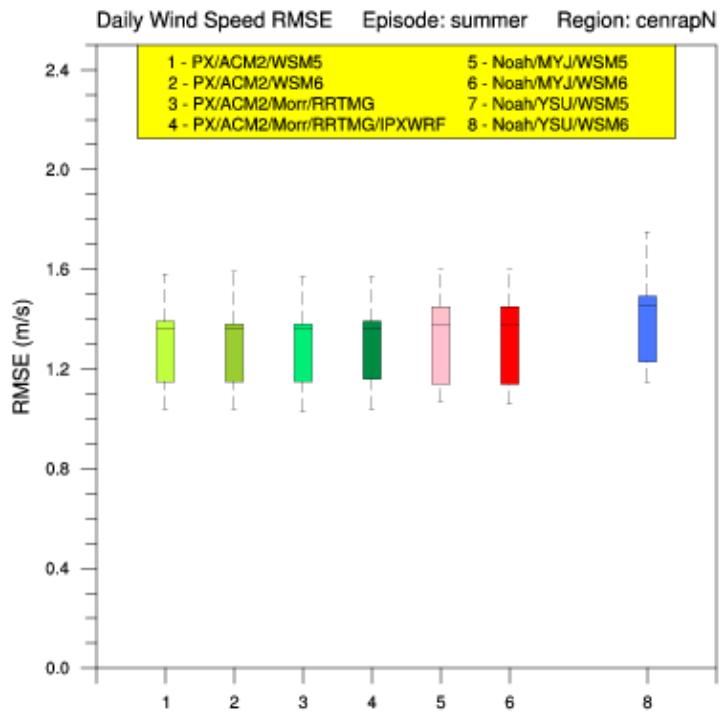

Figure 6-4. Daily wind speed RMSE distributions during the summer episode for the cenrapN region.

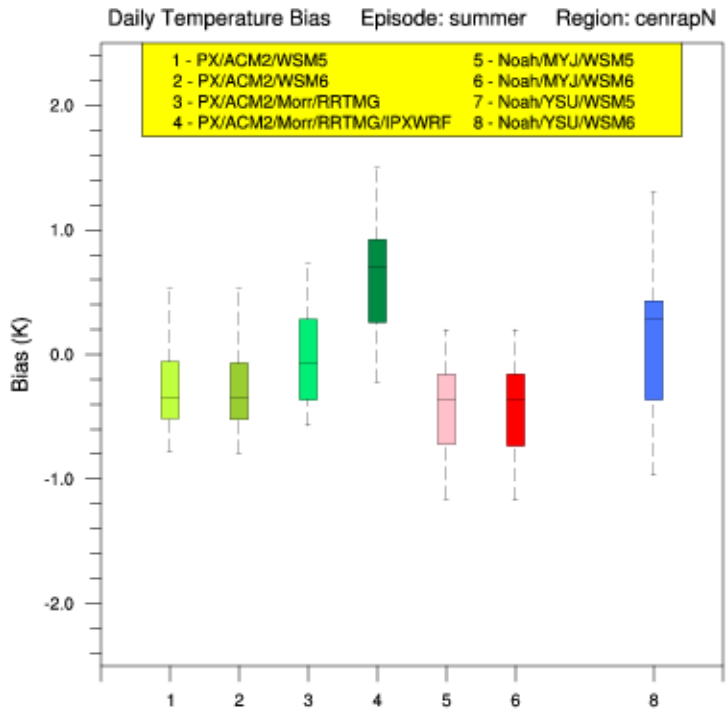

Figure 6-5. Daily temperature bias distributions during the summer episode for the cenrapN region.

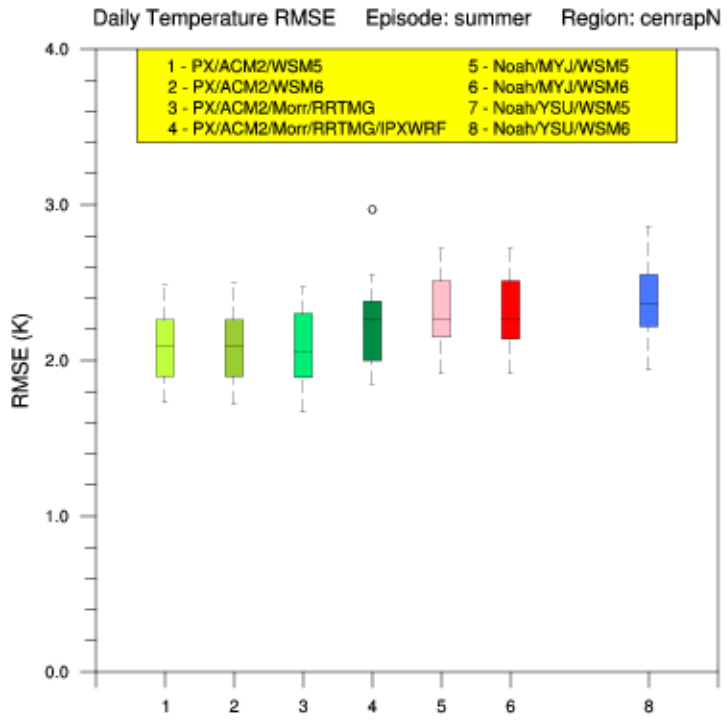

Figure 6-6. Daily temperature RMSE distributions during the summer episode for the cenrapN region.

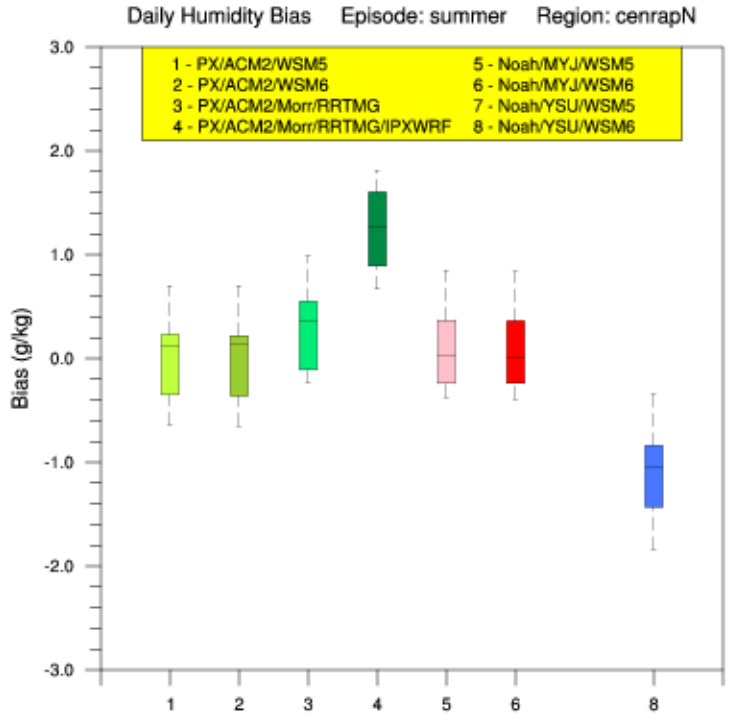

Figure 6-7. Daily humidity bias distributions during the summer episode for the cenrapN region.

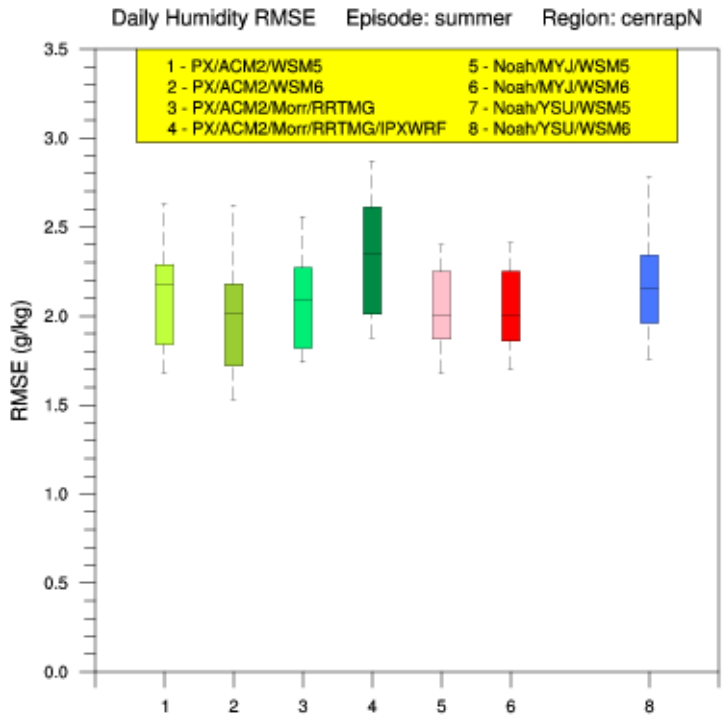

Figure 6-8. Daily humidity RMSE distributions during the summer episode for the cenrapN region.

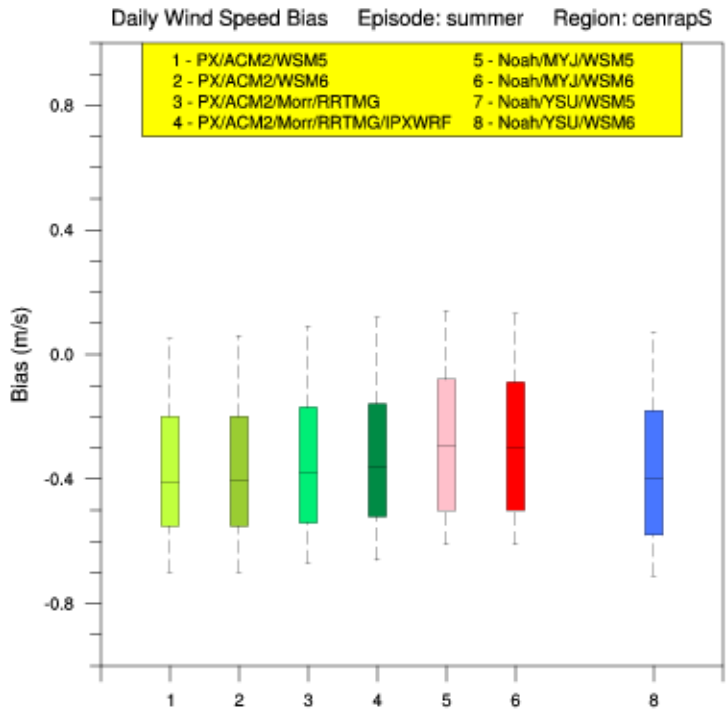

Figure 6-9. Daily wind speed bias distributions during the summer episode for the cenrapS region.

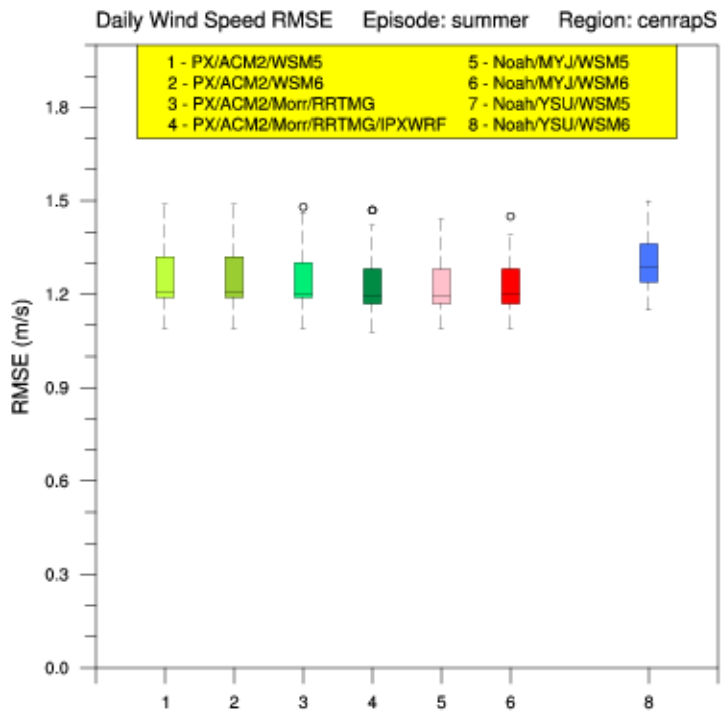

Figure 6-10. Daily wind speed RMSE distributions during the summer episode for the cenrapS region.

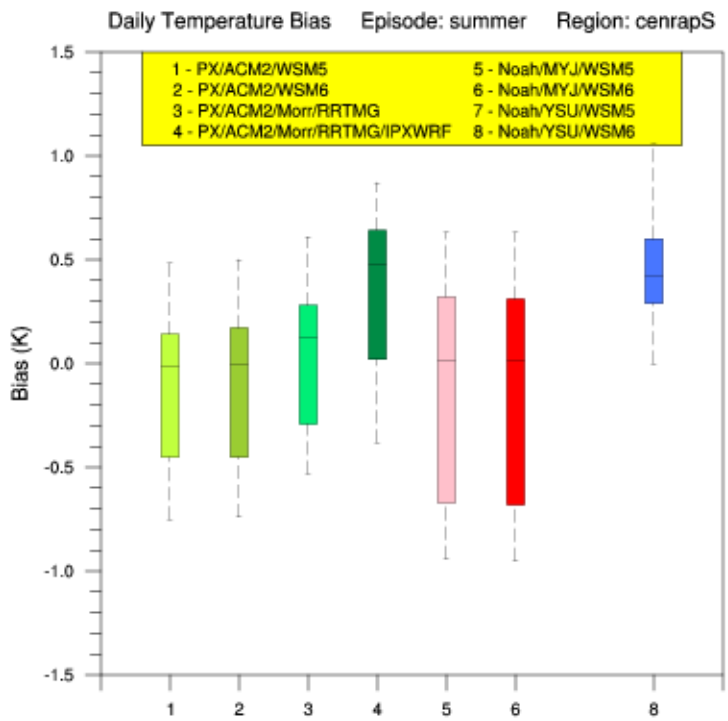

Figure 6-11. Daily temperature bias distributions during the summer episode for the cenrapS region.

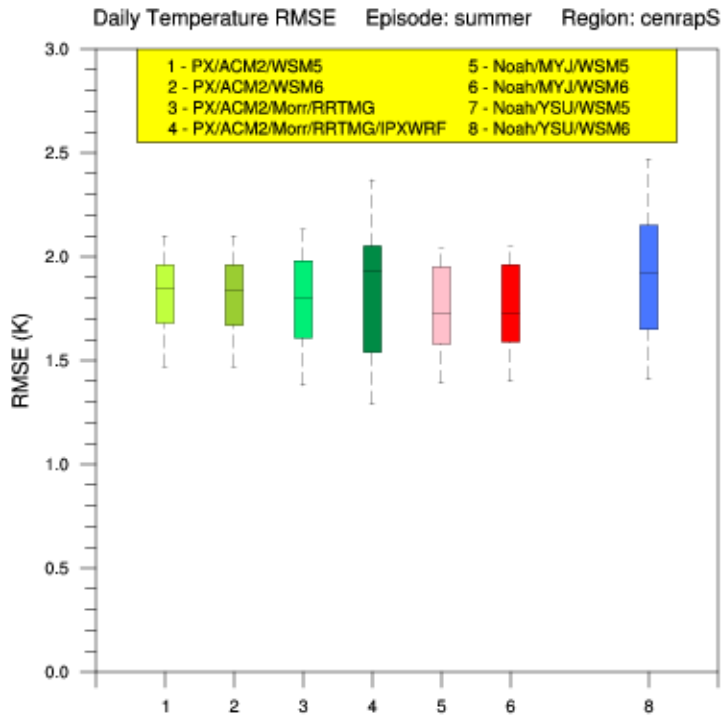

Figure 6-12. Daily temperature RMSE distributions during the summer episode for the cenrapS region.

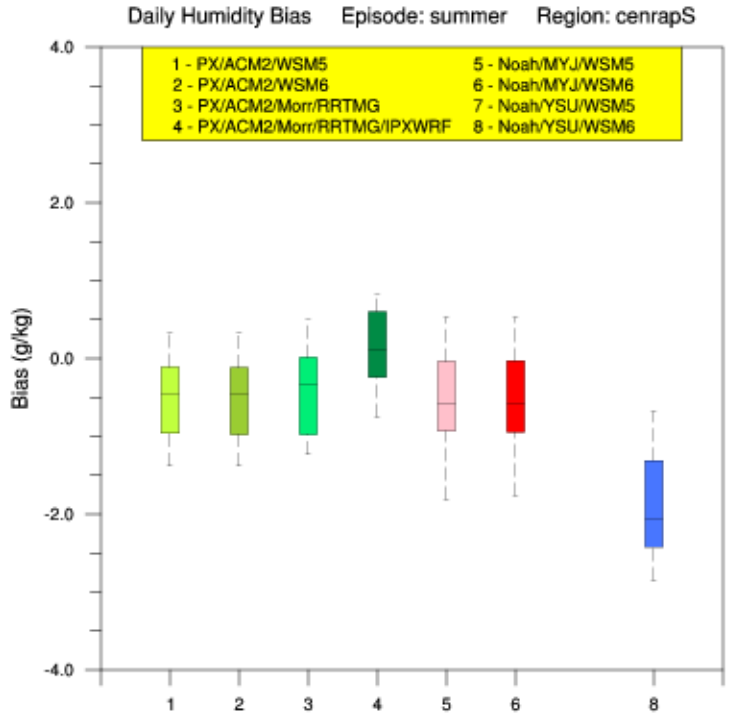

Figure 6-13. Daily humidity bias distributions during the summer episode for the cenrapS region.

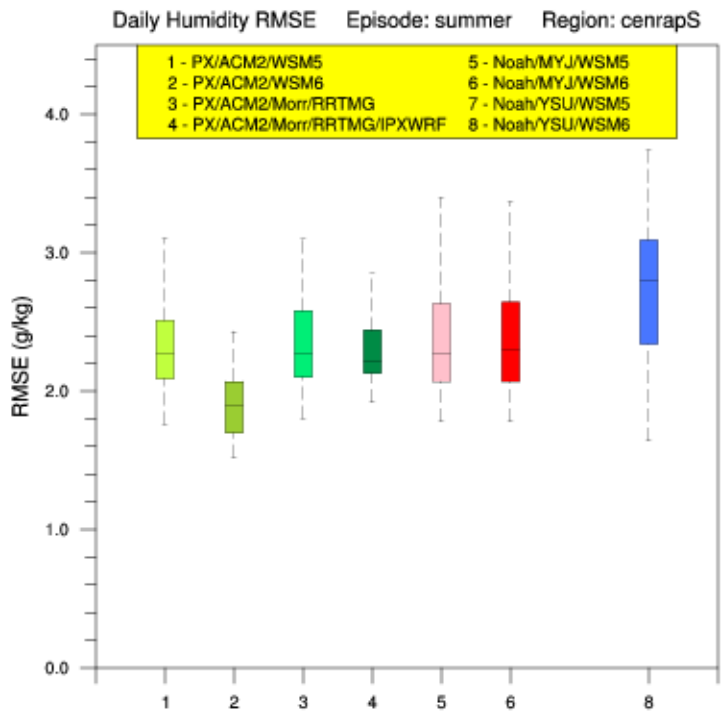

Figure 6-14. Daily humidity RMSE distributions during the summer episode for the cenrapS region.

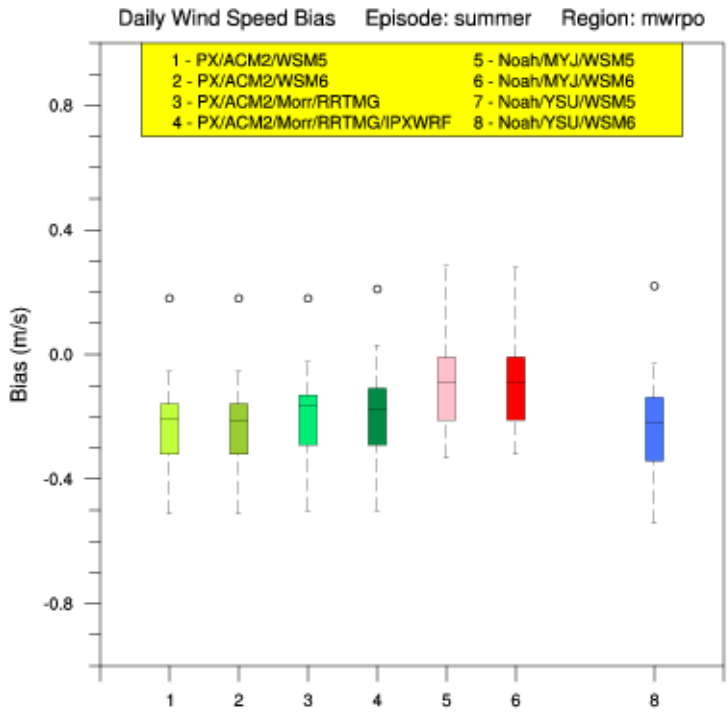

Figure 6-15. Daily wind speed bias distributions during the summer period for the mwrpo region.

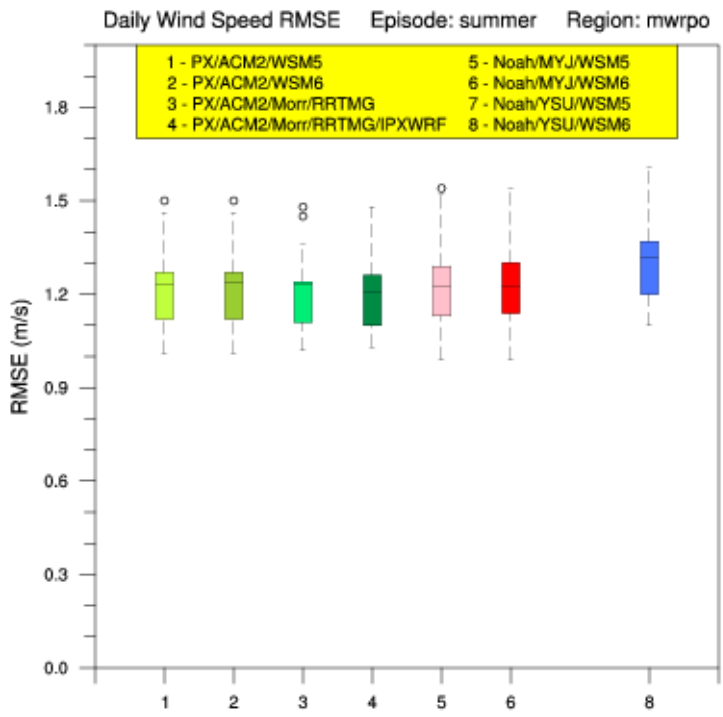

Figure 6-16. Daily wind speed RMSE distributions during the summer period for the mwrpo region.

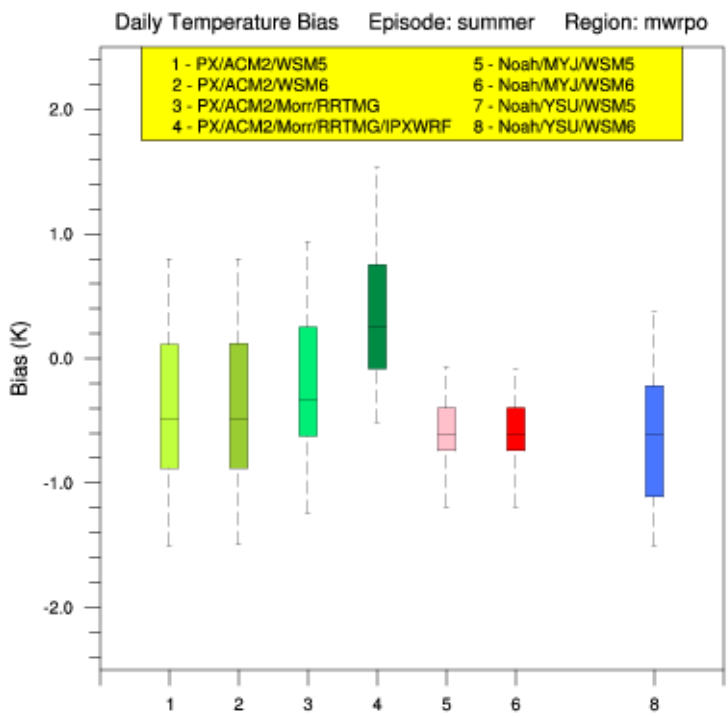

Figure 6-17. Daily temperature bias distributions during the summer period for the mwrpo region.

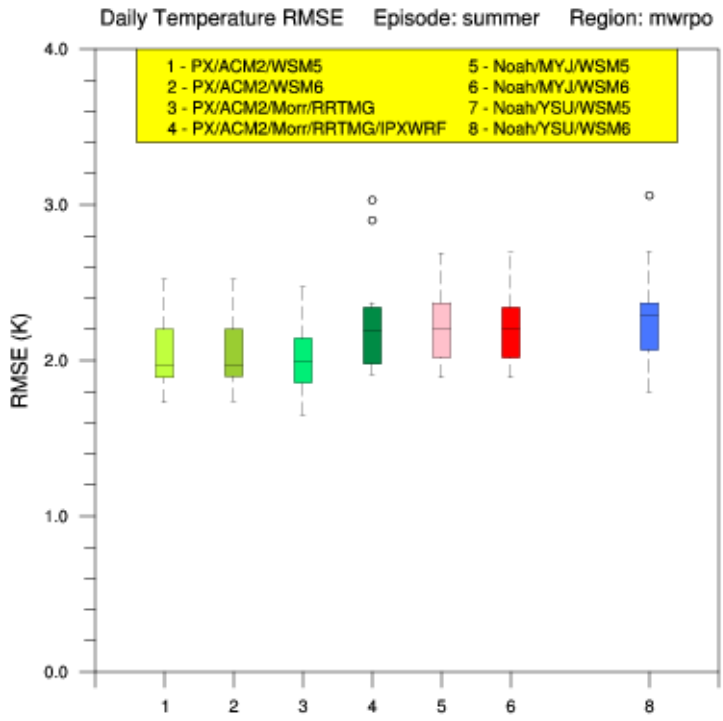

Figure 6-18. Daily temperature RMSE distributions during the summer period for the mwrpo region.

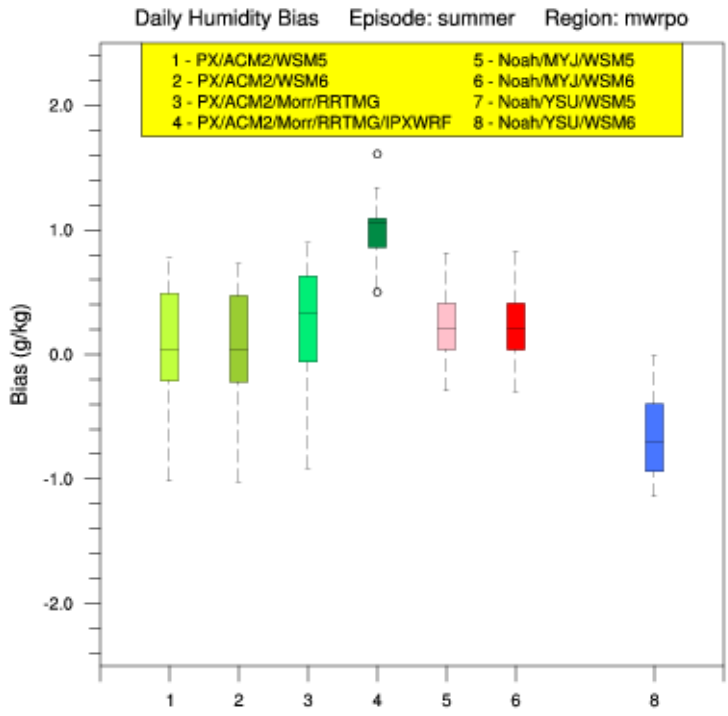

Figure 6-19. Daily humidity bias distributions during the summer period for the mwrpo region.

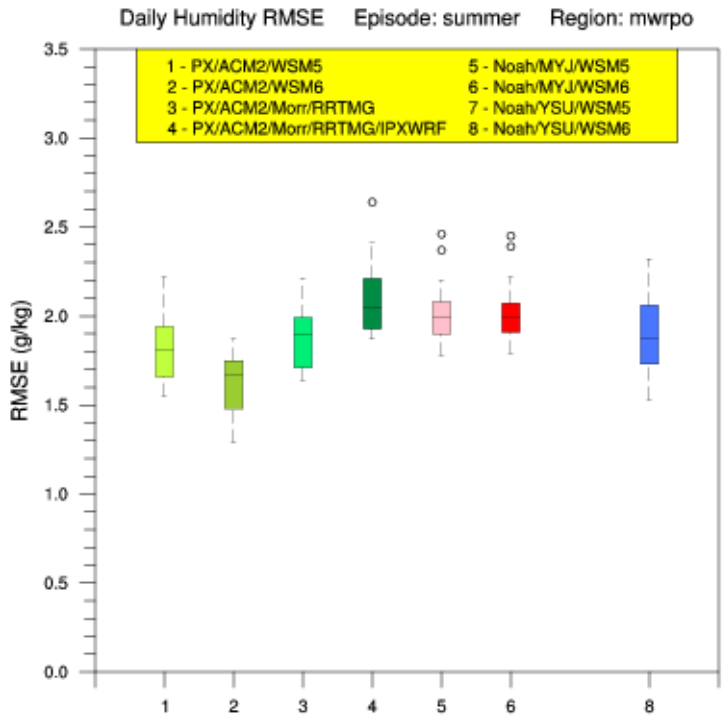

Figure 6-20. Daily humidity RMSE distributions during the summer period for the mwrpo region.

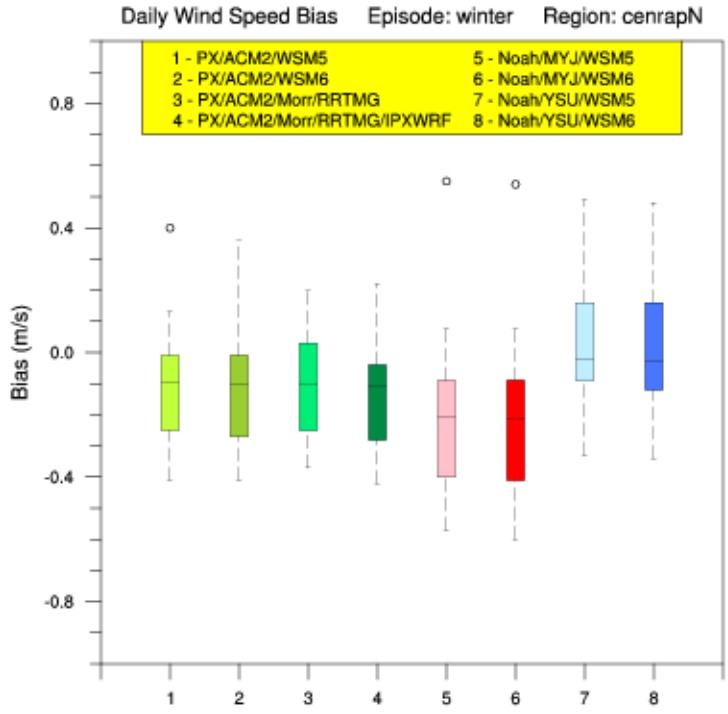

Figure 6-21. Daily wind speed bias distributions during the winter period for the cenrapN region.

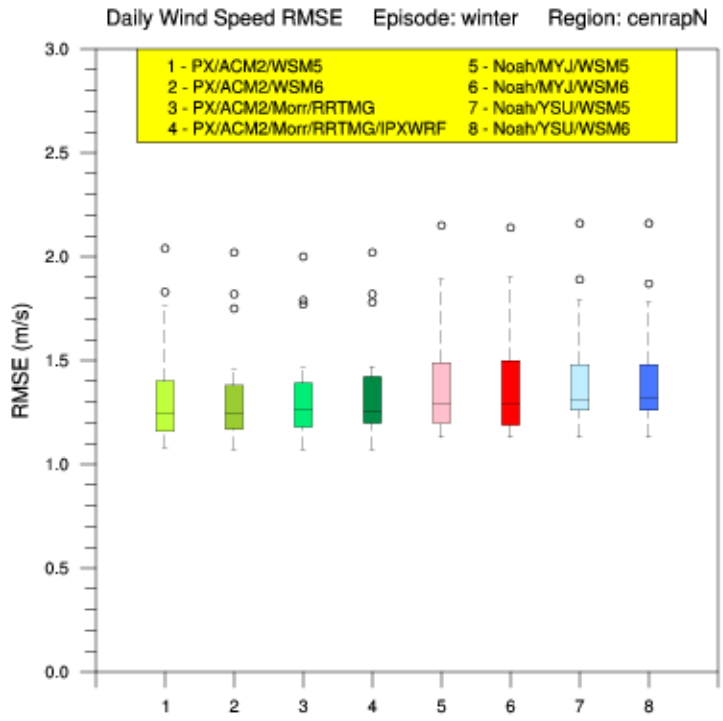

Figure 6-22. Daily wind speed RMSE distributions during the winter period for the cenrapN region.

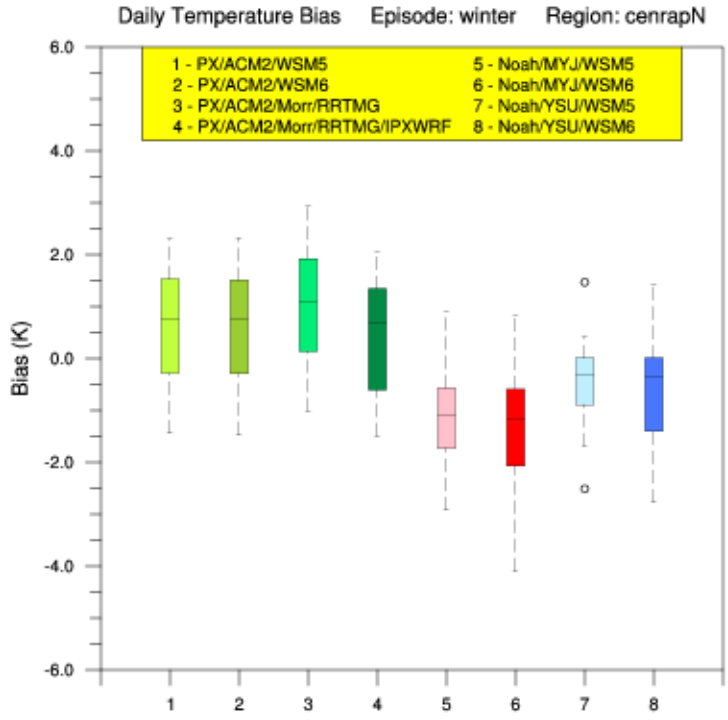

Figure 6-23. Daily temperature bias distributions during the winter period for the cenrapN region.

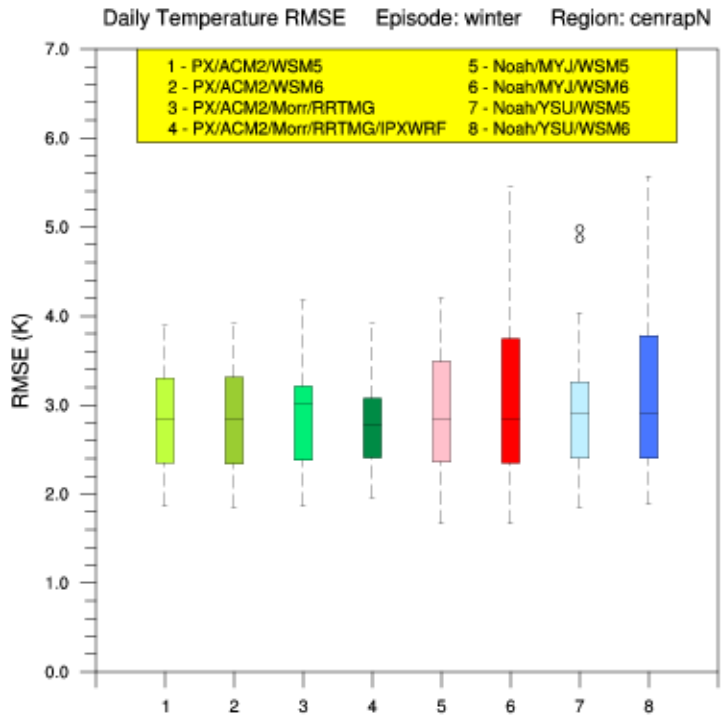

Figure 6-24. Daily temperature RMSE distributions during the winter period for the cenrapN region.

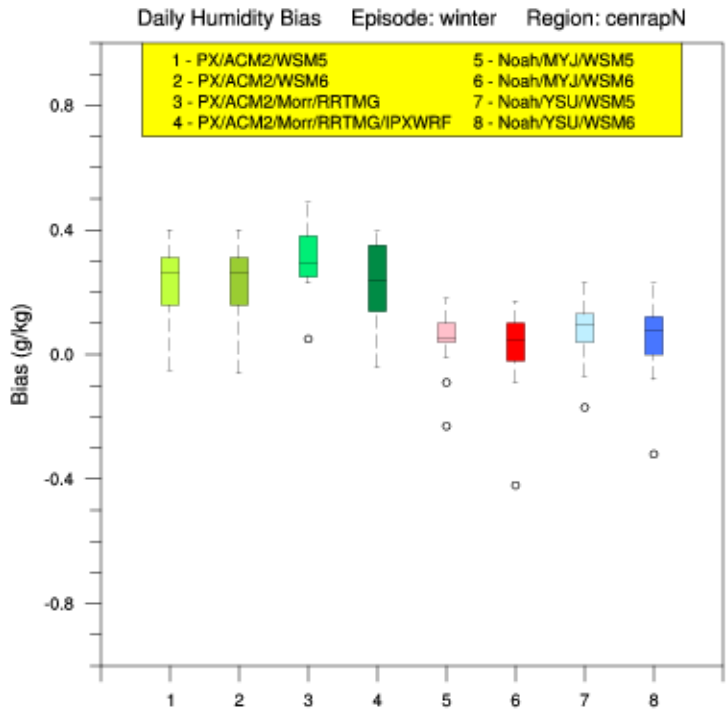

Figure 6-25. Daily humidity bias distributions during the winter period for the cenrapN region.

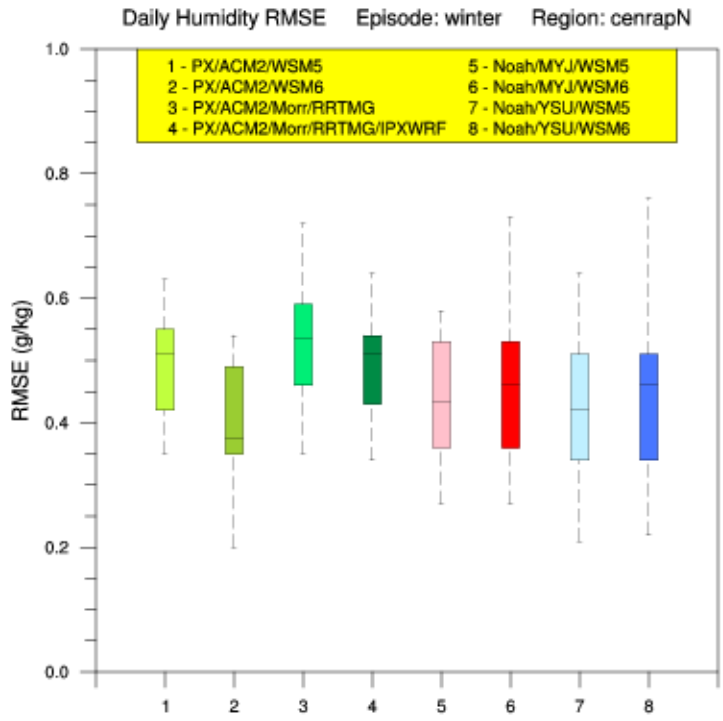

Figure 6-26. Daily humidity RMSE distributions during the winter period for the cenrapN region.

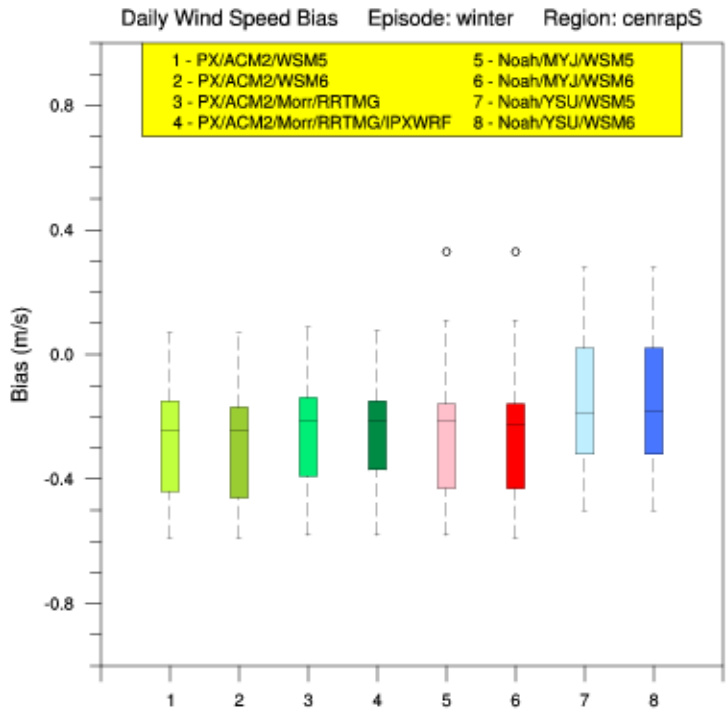

Figure 6-27. Daily wind speed bias distributions during the winter period for the cenrapS region.

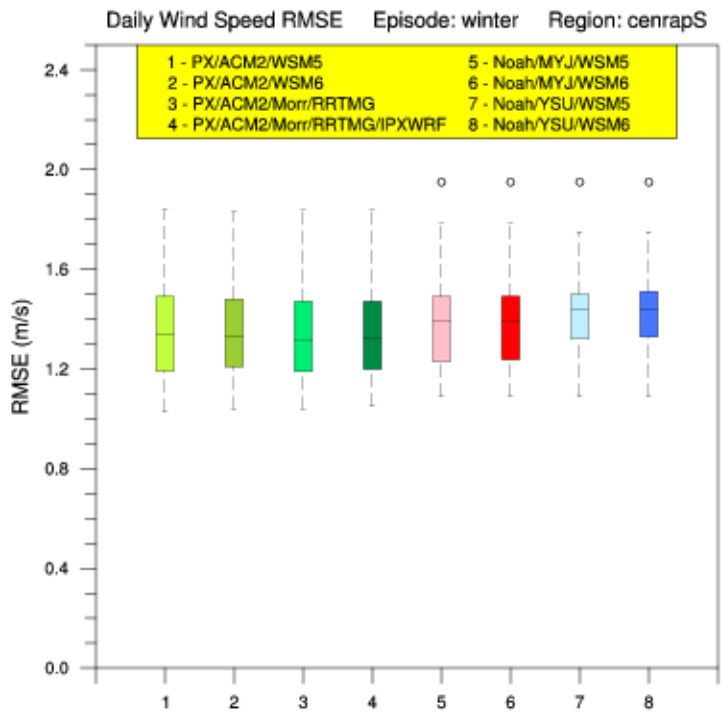

Figure 6-28. Daily wind speed RMSE distributions during the winter period for the cenrapS region.

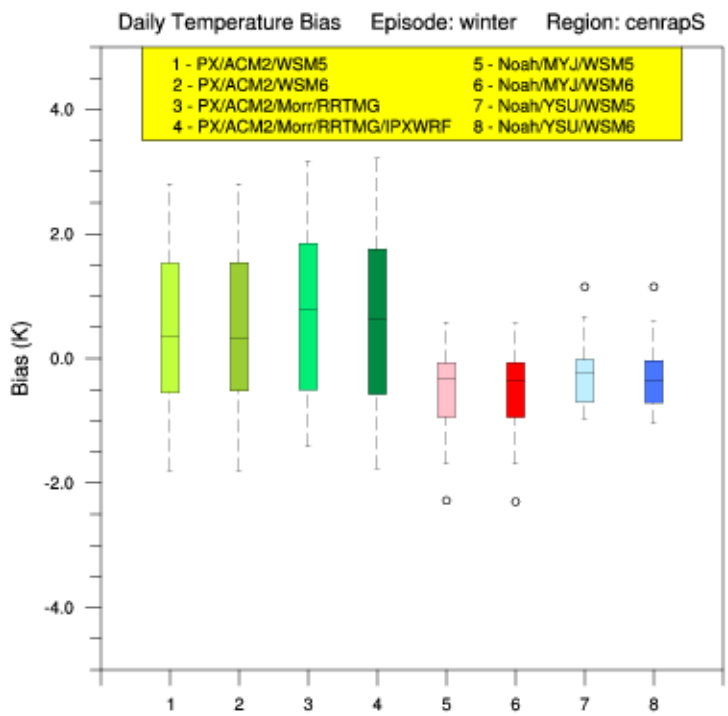

Figure 6-29. Daily temperature bias distributions during the winter period for the cenrapS region.

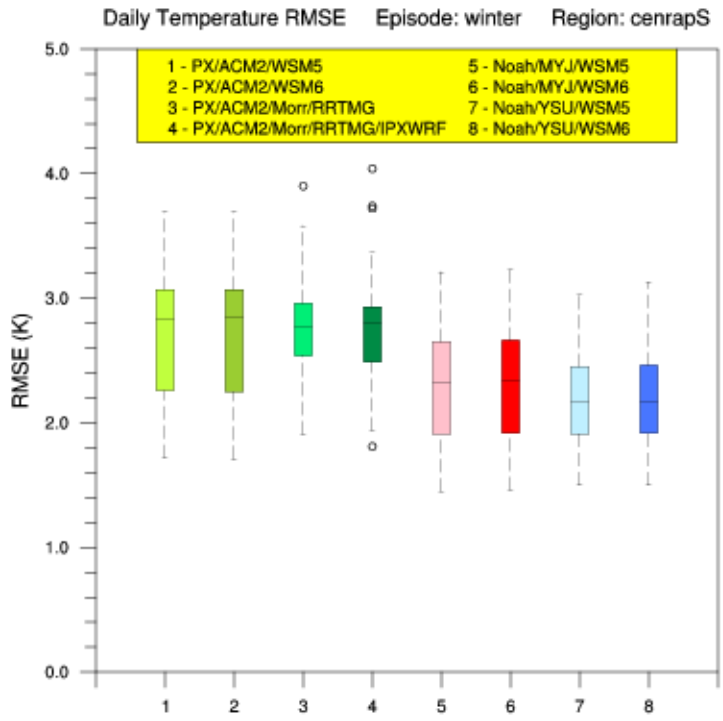

Figure 6-30. Daily temperature RMSE distributions during the winter period for the cenrapS region.

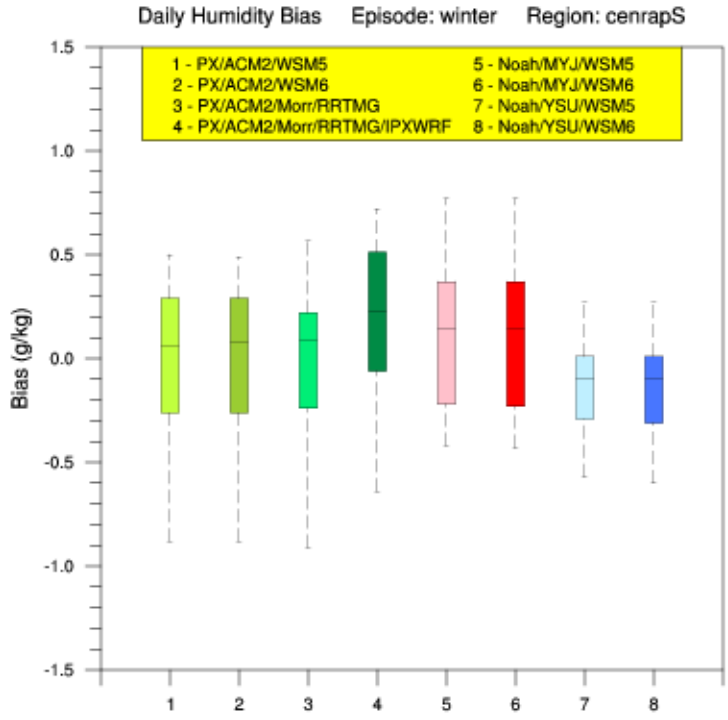

Figure 6-31. Daily humidity bias distributions during the winter period for the cenrapS region.

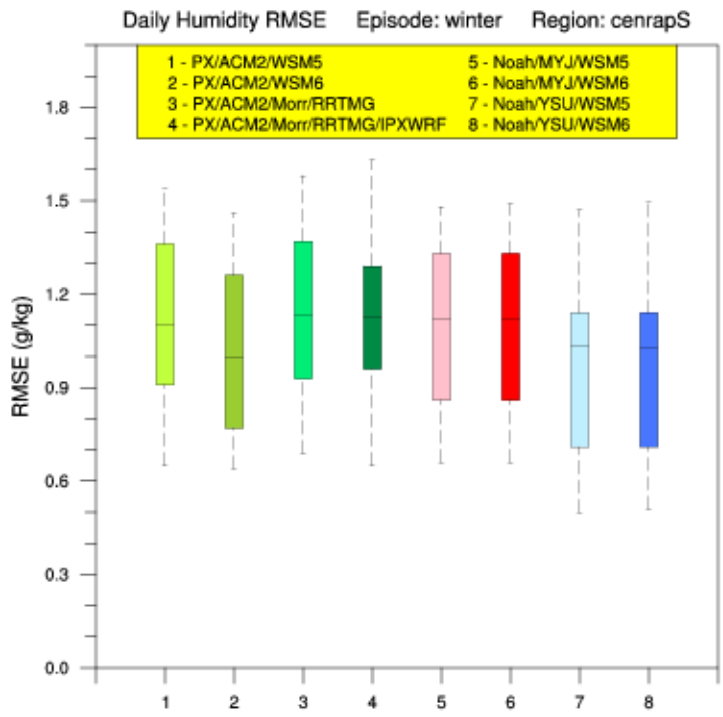

Figure 6-32. Daily humidity RMSE distributions during the winter period for the cenrapS region.

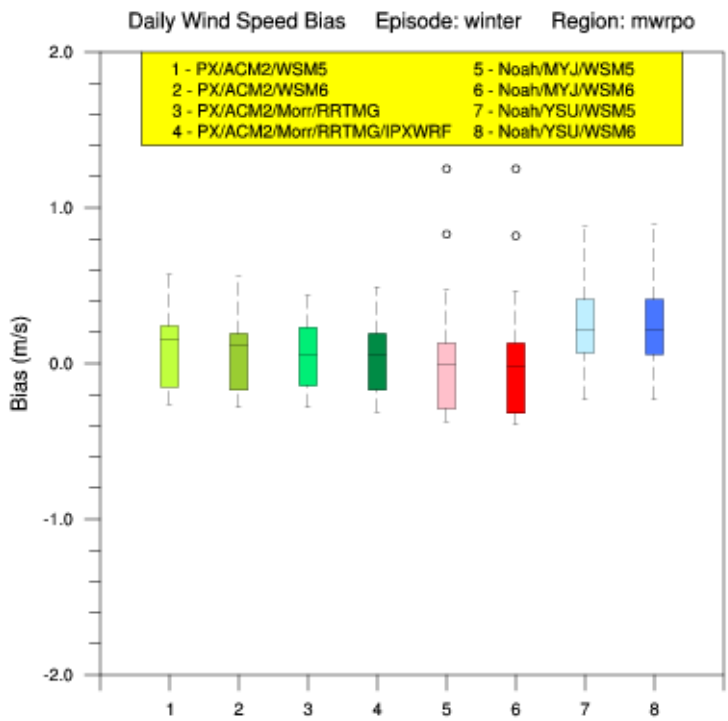

Figure 6-33. Daily wind speed bias distributions during the winter period for the mwrpo region.

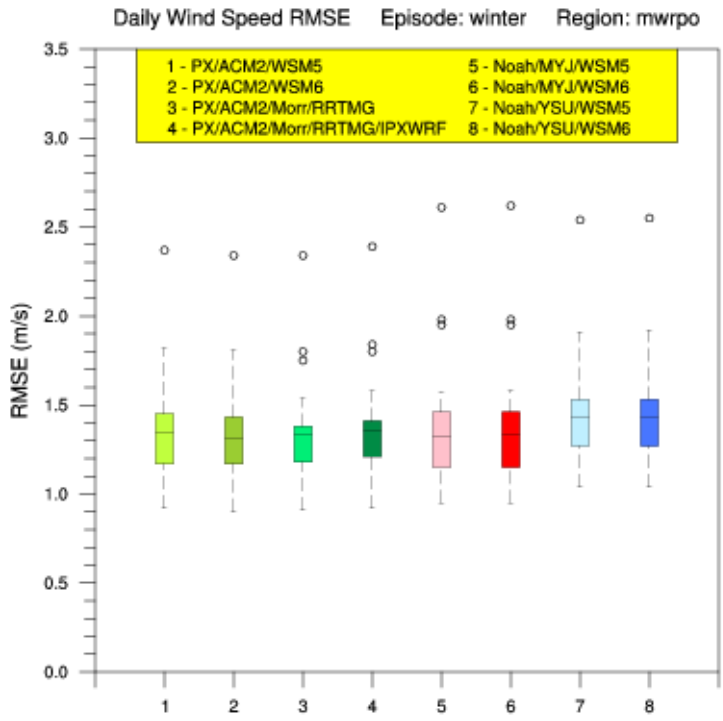

Figure 6-34. Daily wind speed RMSE distributions during the winter period for the mwrpo region.

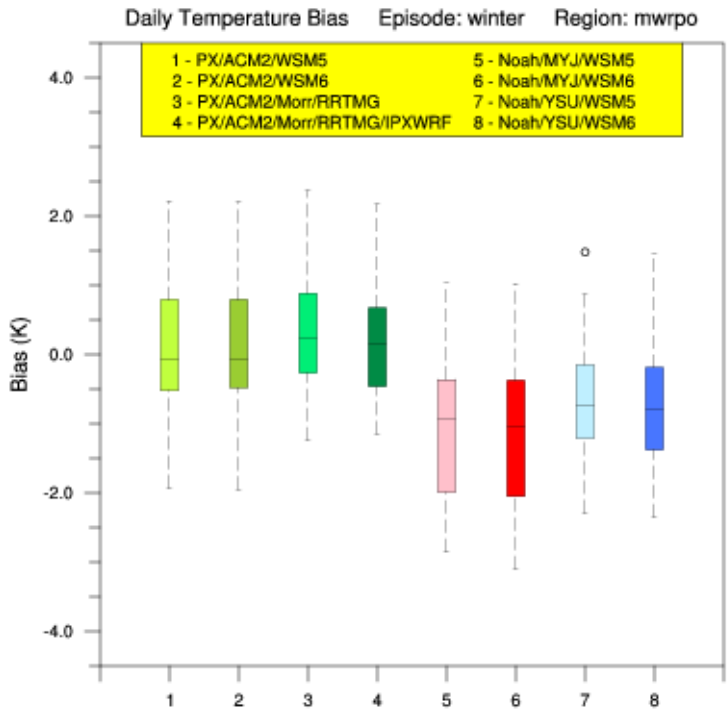

Figure 6-35. Daily temperature bias distributions during the winter period for the mwrpo region.

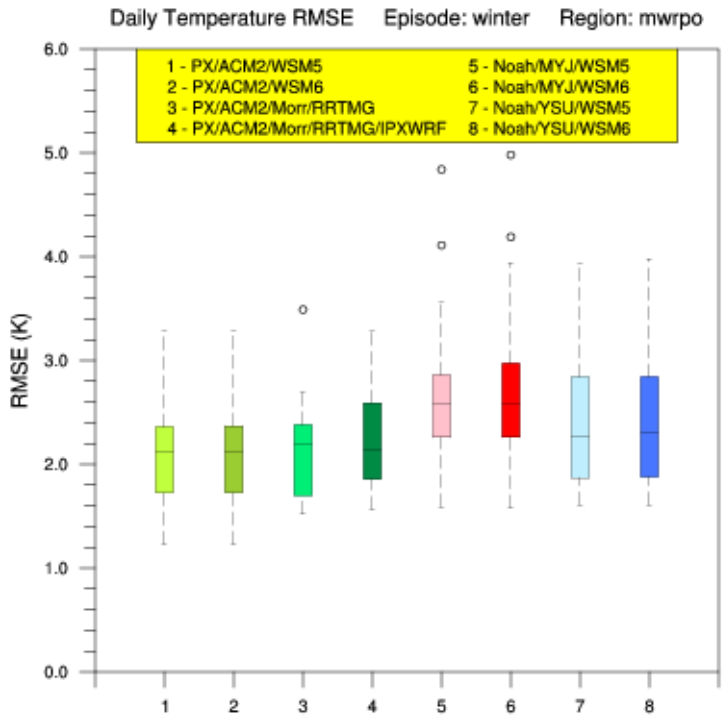

Figure 6-36. Daily temperature bias distributions during the winter period for the mwrpo region.

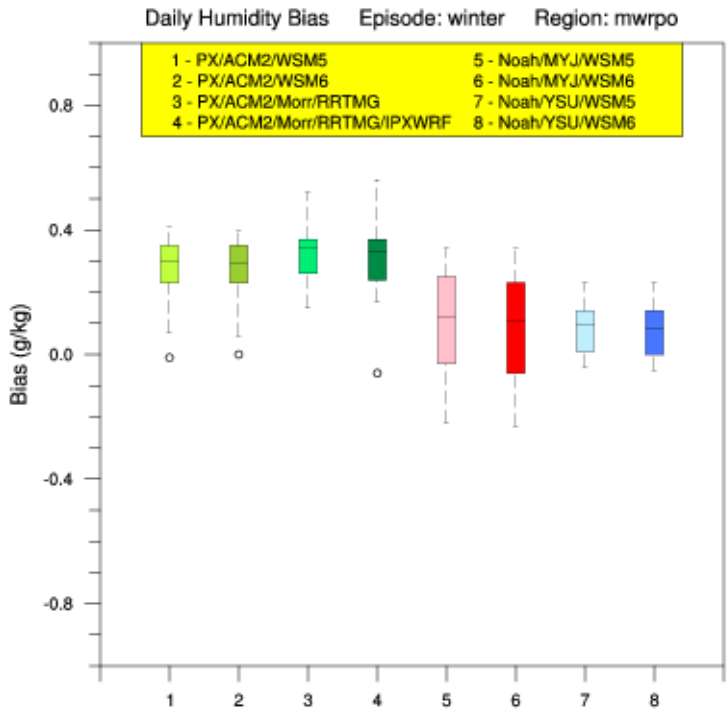

Figure 6-37. Daily humidity bias distributions during the winter period for the mwrpo region.

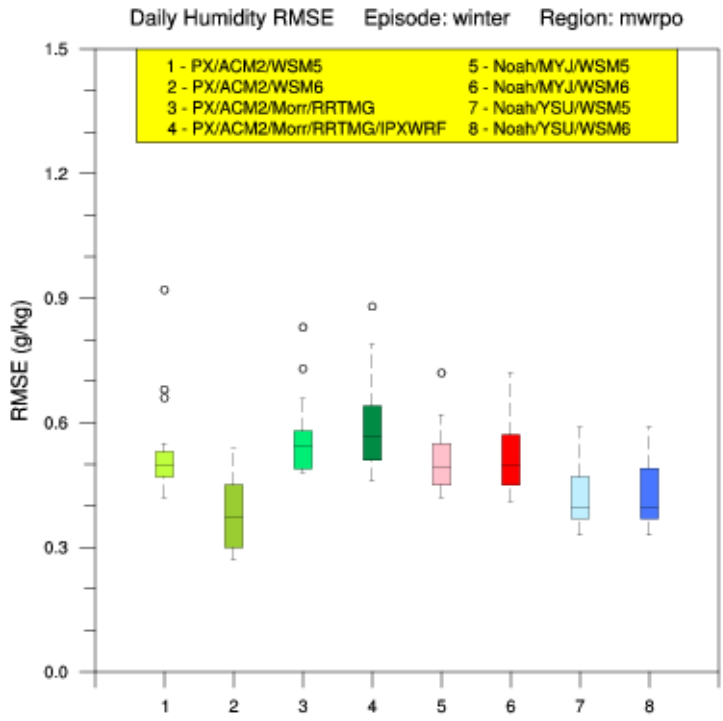

Figure 6-38. Daily humidity RMSE distributions during the winter period for the mwrpo region.

WRF model output was processed through MCIP to obtain suitable cloud parameters to compare to observations. Two-dimensional modeled cloud fraction estimated from cloud water mixing ratios was compared to gridded observed cloud fraction derived from satellite measurements of surface radiation (Pinker and Laszlo, 1992). Figure 6-39 shows a comparison of cloud fraction produced by sensitivity simulations of varying PBL schemes. These sensitivities generally capture the overall cloud patterns and extents. They each underestimate total cloud fraction across much of the northern portion of the domain, while overestimating cloud cover in Kansas and the Dakotas. Looking in greater detail in a given location can reveal differences among the sensitivities. For example the PX configuration underestimates cloud cover in Minnesota to a greater extent than other configurations. Overall however, the results of these three sensitivities show little variation for this particular hour, and additional hours were reviewed but not shown. No configuration produces cloud fields superior to another.

To evaluate the simulation of precipitation processes modeled fields were compared to the NCEP Stage IV precipitation analysis (Lin and Mitchell, 2005). This product is derived from rain gauge and radar estimated precipitation data analyzed to regional grids and later mosaicked onto a national 4 km grid. Accumulated precipitation was evaluated on a daily basis during the sensitivity periods. The valid time for each day is 12Z the day before to 12Z on the current day. Figure 6-40 shows an example plot of observed precipitation for August 5, 2007. Figure 6-41 shows modeled precipitation for the same period for four sensitivity runs with various PBL schemes. These figures are representative of the performance of precipitation on days during the sensitivity period containing significant precipitation. The sensitivity simulations contain similar precipitation patterns. All sensitivity simulations underestimate non-convective precipitation over the northern half of the domain, while slightly over-predicting convective precipitation over

the southeastern U.S. Although the choice of PBL scheme is shown to have some effect on on surface meteorological variables these figures shown they have much less impact on precipitation. Figure 6-42 and Figure 6-43 show precipitation accumulated across the summer and winter sensitivity periods for the PX/ACM2 variant sensitivities. In the summer, these sensitivity simulations reasonably captured spatial precipitation patterns with the exception of over-predicting convective rainfall in the Southeast. The fields for the three sensitivity simulations are nearly indistinguishable. These figures show precipitation fields are not sensitive to the choice of the microphysics scheme. This is expected during the summer period, as precipitation is dominated by the convective component. During the winter, the spatial patterns are again well represented by all sensitivities, however all under-predict the total accumulation. Again, the modeled fields are nearly identical.

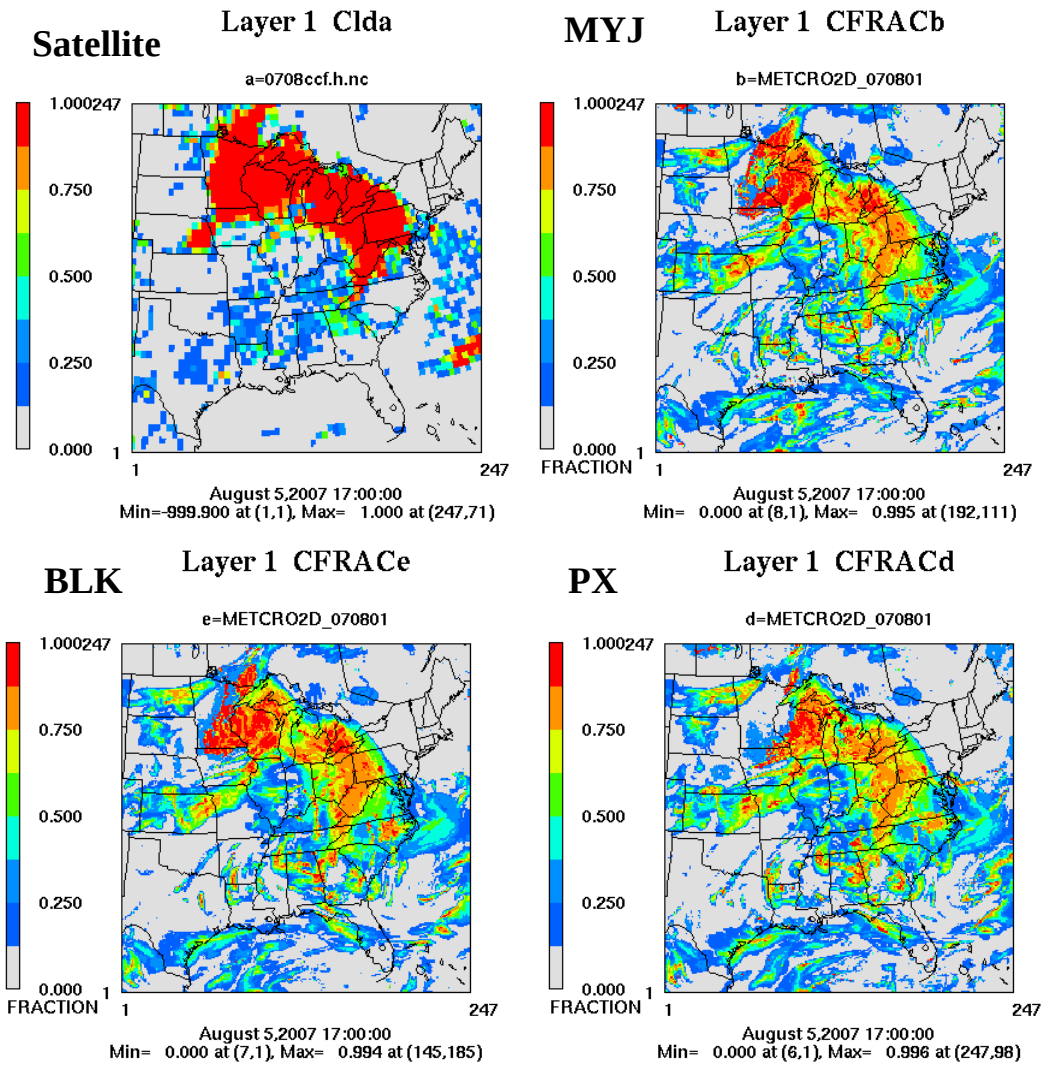

Figure 6-39. Comparison of observed (top-left) and modeled total cloud fraction on August 5, 2007 at 17Z.

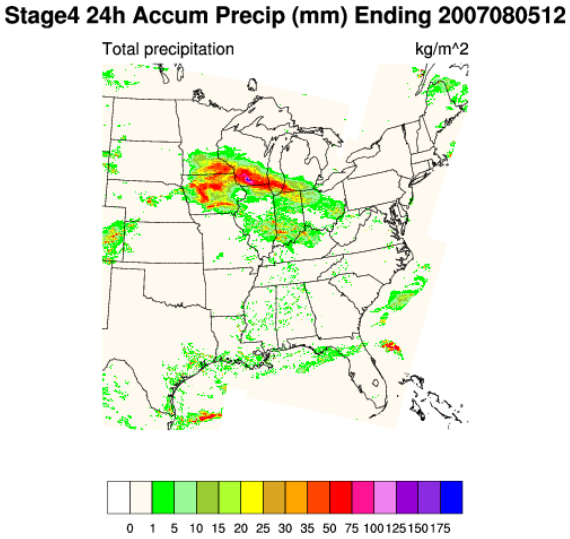

Figure 6-40. Daily accumulated precipitation from the NCEP Stage IV analysis valid for August 5, 2007.

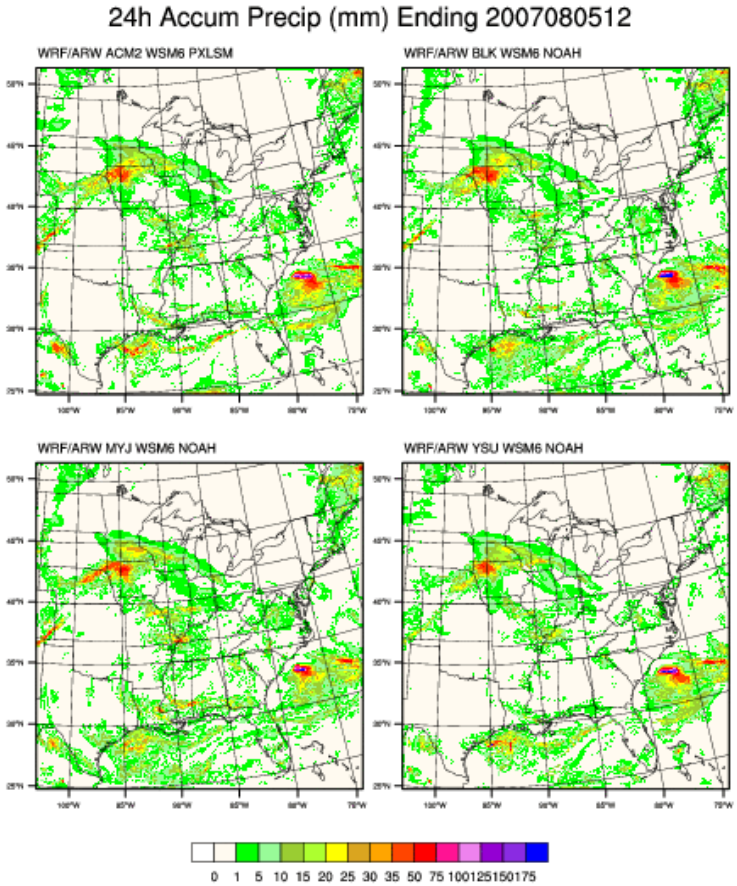

Figure 6-41. Daily accumulated precipitation from four sensitivity simulations with varying PBL schemes valid for August 5, 2007.

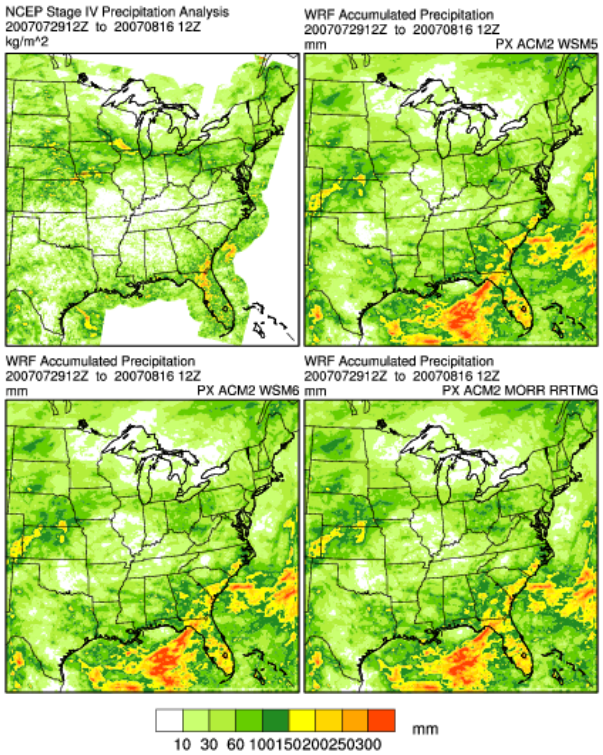

Figure 6-42. Observed (upper-left) and modeled (rest) precipitation accumulated across the summer sensitivity period, from July 29, 2007 12Z to August 16, 2007 12Z.

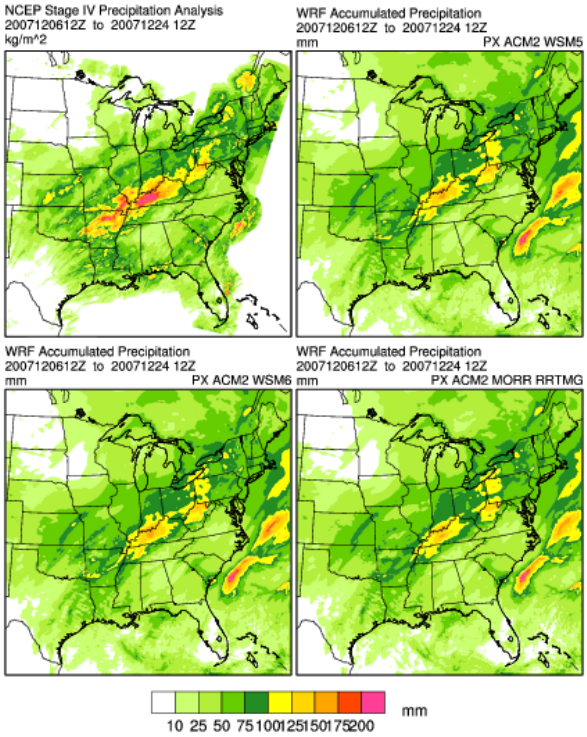

Figure 6-43. Observed (upper-left) and modeled (rest) precipitation accumulated across the winter sensitivity period, from December 6, 2007 12Z to December 24, 2007 12Z.

7. PRODUCTION CONFIGURATION AND EXECUTION

7.1 Final Configuration

The goal of the sensitivity analysis was to produce a configuration whose performance was superior to the others during the time periods simulated. However, the results show there was no configuration that consistently outperformed all others. Instead, there were several configurations which performed better at certain times, in certain geographical areas, and for certain meteorological variables. This is not discouraging as it means the WRF modeling system contains a robust suite of scientifically sound physics parameterizations.

The results showed the choice of PBL parameterization most strongly influenced the performance of each sensitivity configuration. The non-local schemes, Blackadar and ACM2, performed better than the local schemes, YSU and MYJ. The choice of land surface model also influenced the results, however the selection was dictated by compatibility with the PBL scheme. The choice of microphysics and radiation packages did not appear to influence the results of the sensitivity analysis. For these options the most sophisticated schemes were selected. These options increased run times significantly, however the states of Iowa and North Carolina had sufficient computing resources to handle the computational requirements.

Dynamics options were not tested as part of the sensitivity analysis. These options typically do not strongly influence model performance, but are instead selected for their desired numerical properties and to maintain numerical stability. These options were selected per the recommendations of EPA. Sixth-order diffusion was selected to resolve a specific numerical issue discovered after the first iteration of the annual simulation. This is discussed in more detail below.

7.1.1 Physics Parameterizations

The planetary boundary layer parameterization is responsible for representing vertical sub-grid fluxes of heat, momentum, and moisture in the whole atmospheric column, but primarily in a shallow layer near the Earth's surface. The WRF Group did not come to an agreement on the choice of PBL scheme. The representatives from OTC and the University of Maryland selected the Blackadar scheme, while SESARM and Iowa chose ACM2. This PBL scheme is used in modeling performed by EPA and it is preferred to maintain consistency in our model configuration. The Blackadar scheme is not officially supported by the WRF development team and this option is not included as an option in the official, public release of WRF. While this option is obtainable, in the public realm it is not readily available. Because of this disagreement the group diverged and two annual simulations were produced. The final configuration of the OTC simulation is available in Appendix C. The Asymmetric Convective Model, version 2 includes the nonlocal scheme of the original ACM combined with an eddy diffusion scheme (Pleim, 2007). Thus, the ACM2 is able to represent both the supergrid- and subgrid-scale components of turbulent transport in the convective boundary layer. The top of the PBL is diagnosed from the critical bulk Richardson number. The ACM2 performs equally well for both meteorological parameters and trace chemical concentrations.

The land-surface parameterization uses atmospheric information from other parameterizations along with internal information on the land's state variables and land-surface properties to provide heat and moisture fluxes over land and sea-ice points. These fluxes provide a lower boundary condition for the vertical transport calculated by the PBL scheme. The Pleim-Xiu (PX) land surface model (LSM) (Xiu and Pleim, 2001) was chosen as the land surface parameterization due to its compatibility with the ACM2 PBL scheme. It is a two layer force-restore soil temperature and moisture model. The two layers include a 1 cm surface layer and 1 m root zone layer. The PXLM features three pathways for moisture fluxes: evapotranspiration, soil evaporation, and evaporation from wet canopies. Evapotranspiration is controlled by bulk stomatal and aerodynamics resistance that is dependent on root zone soil moisture, photosynthetically active radiation, air temperature, and the relative humidity at the leaf surface (Xiu and Pleim, 2001). It requires snow cover data to be input from another numerical model or analysis.

The surface layer scheme calculates friction velocities and exchange coefficients required for the calculation of surface heat and moisture fluxes by the land-surface models and surface stress in the planetary boundary layer scheme. The Pleim-Xiu surface layer scheme (Pleim, 2006) was chosen as this scheme was developed as part of the PX LSM. This parameterization is a simple scheme for analytical estimation of the surface-layer similarity functions from state variables. It determines vertical eddy diffusivity based on boundary layer scaling similarity theory. This eddy diffusion component is critical for realistic gradients in the surface layer. It is different from other surface layer schemes in that it includes parameterizations of a viscous sub-layer in the form of a quasi-laminar boundary layer resistance. This accounts for differences in the diffusivity of heat, water vapor, and trace chemical species. For very stable surface layers, it uses a reduced slope to avoid decoupling from the surface (Pleim, 2006).

The microphysics scheme includes explicitly resolved water vapor, cloud, and precipitation processes and their associated heat and moisture tendencies. The Morrison Double-Moment parameterization (Morrison et al., 2009) was selected. This scheme generates both mixing ratios and number concentration of cloud ice, rain, snow, and graupel/hail and mixing ratios of cloud droplets and water vapor. The simulation of two moments allows for a more robust treatment of the particle size distribution.

The cumulus parameterization is responsible for the sub-grid effect of convective and/or shallow clouds. The schemes are designed to estimate vertical fluxes due to unresolved updrafts and downdrafts and compensating motion outside the clouds. The modified version of the Kain-Fritsch scheme was selected. This scheme is based on Kain and Fritsch (1990) and Kain and Fritsch (1993), with modifications made based on testing within the Eta model. The scheme uses a simple cloud model with moist updrafts and downdrafts and includes the effects of detrainment, entrainment, and relatively simple microphysics. The scheme includes a minimum entrainment rate imposed to suppress widespread convection in marginally unstable, yet relatively dry environments. The entrainment rate is allowed to vary as a function of low-level convergence. The convective available potential energy (CAPE) removal time scale is used for closure (Fritsch, 1993).

The radiation parameterization is responsible for simulating the interaction between shortwave and longwave radiation with atmospheric gases and particles and the Earth's surface. For shortwave radiation, these processes include absorption, reflection, and scattering in the atmosphere and at surfaces and heating at the surface due to downwelling radiation. For longwave radiation, processes include infrared and thermal radiation absorbed and emitted by gases and surfaces and heating due to radiative flux divergence and downwelling radiation at the surface. The Rapid Radiative Transfer Model for GCMs (RRTMG) (Iacono et al., 2008) was chosen to estimate both shortwave and longwave processes. It is a sophisticated radiative transfer model that utilizes a correlated-k approach to calculate fluxes and heating rates efficiently and accurately. More information on the key features of RRTMG along with the differences from the original RRTM is available at http://rtweb.aer.com/rrtm_frame.html.

7.1.2 Dynamics Options

The WRF model was run in non-hydrostatic mode. The simple diffusion option is used for horizontal diffusion. The horizontal eddy viscosity is calculated from the 2D deformation field. The vertical eddy viscosity is assumed to be estimated by the PBL scheme. An implicit gravity wave damping layer was selected to control reflection from the upper boundary. Vertical velocity damping is enabled to prevent the model from becoming unstable with locally large vertical velocities. After the first iteration of the annual simulation a severe numerical artifact was discovered in the results. A checkerboard pattern in the moisture, temperature, and precipitation fields was found. To resolve the issue, a 6th order diffusion scheme (Kneivel et al., 2007) was enabled. This scheme is an explicit, 6th order diffusion scheme that preserves the high effective resolution of WRF and uses a flux limiter to ensure monotonicity. The scheme is effective in removing the high frequency numerical noise that is worst when grid-relative wind speeds are low and stratification is nearly neutral or unstable (Kneivel et al., 2007). Monotonic advection was enabled for moisture and scalars. Figure 7-1 shows a sample precipitation field before and after the 6th order diffusion scheme is enabled.

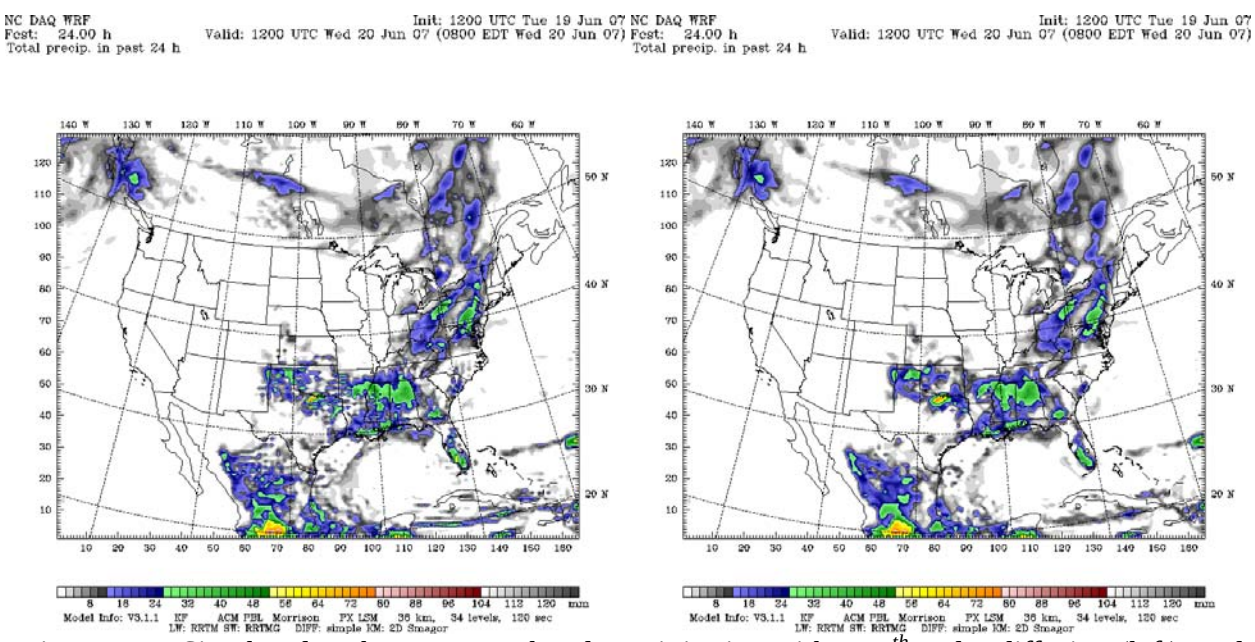

Figure 7-1. Simulated 24-hour accumulated precipitation without 6th order diffusion (left), and with 6th order diffusion enabled (right).

A model time step of 90 seconds was used in the sensitivity simulations. A larger time step was tested, prior to the production run, for computational stability in an attempt to decrease run times. Numerical stability was violated for time steps as low as 150 seconds. A time step of 120 seconds was selected as a compromise between model execution time and numerical stability. This time step applies to integration on the course (36 km) domain. For the nested (12 km) domain, the time step is divided by the grid ratio. The planetary boundary layer, surface layer, land-surface, and microphysics parameterizations are called every integration time step. The radiation scheme is called every 30 minutes on the course domain and every 15 minutes on the nest. The cumulus parameterization is called every 5 minutes on both domains.

The course and nested domains are run in a concurrent 1-way nesting mode. Both domains are simulated during the same WRF run. The course grid output provides lateral boundary conditions to the nested grid. The course grid integrates one time step, and then the nested grid integrates up to the same time. Feedback of the nested grid output to the course grid cells containing the nested domain is disabled. In this manner the exchange of information during the simulation is only in one direction.

Specified lateral boundary conditions are used for the course domain's boundary. The model dataset described in Chapter 5 provides the lateral boundary conditions. A relaxation zone five grid cells in width is used to nudge or relax the model towards the boundary values.

7.2 Model Execution

The purpose of the simulation is to provide meteorological inputs to a photochemical transport model for an entire calendar year. Therefore, WRF must be run for a period of one year plus at least 10 additional days prior to the start of the year to allow adequate spin-up time for the photochemical transport model. The simulation must continue beyond the end of the calendar year long enough to account for time zone differences between U.S. time zones and UTC when the photochemical transport model is run using local standard time.

In order to minimize the growth of errors as the forecast hour increases during the simulation, the WRF simulation is split into many short runs with the model being re-initialized for each new simulation. Each simulation is fundamentally independent of each other. Each simulation is integrated for 132 hours (5.5 days) with 12 hours of overlap between consecutive runs in order to account for spin-up time. The first 12 hours of each run are discarded. The runs are then stitched together to provide a continuous meteorological dataset to the photochemical transport model. Table 7-1 shows the initialization dates for the 77 runs that comprise the annual simulation.

The task of executing the WRF model runs was divided between the Iowa DNR and North Carolina DENR. The Iowa DNR's share of model runs were executed on a modeling platform consisting of two identical workstations each housing two quad-core Intel Xeon X5460 3.16 GHz processors. A mix of internal and external storage capacity of over 20 terabytes was continuously accessible to accommodate the WRF simulations while maintaining sufficient reserve capacity.

Table 7-1. Initialization dates for the 77 runs that make up the WRF 2007 annual simulation. All runs are initialized at 12Z.

12/16/06	03/06/07	05/25/07	08/13/07	11/01/07
12/21/06	03/11/07	05/30/07	08/18/07	11/06/07
12/26/06	03/16/07	06/04/07	08/23/07	11/11/07
12/31/06	03/21/07	06/09/07	08/28/07	11/16/07
01/05/07	03/26/07	06/14/07	09/02/07	11/21/07
01/10/07	03/31/07	06/19/07	09/07/07	11/26/07
01/15/07	04/05/07	06/24/07	09/12/07	12/01/07
01/20/07	04/10/07	06/29/07	09/17/07	12/06/07
01/25/07	04/15/07	07/04/07	09/22/07	12/11/07
01/30/07	04/20/07	07/09/07	09/27/07	12/16/07
02/04/07	04/25/07	07/14/07	10/02/07	12/21/07
02/09/07	04/30/07	07/19/07	10/07/07	12/26/07
02/14/07	05/05/07	07/24/07	10/12/07	12/31/07
02/19/07	05/10/07	07/29/07	10/17/07	
02/24/07	05/15/07	08/03/07	10/22/07	
03/01/07	05/20/07	08/08/07	10/27/07	

8. PERFORMANCE EVALUATION

AER conducted a comprehensive performance evaluation of the 2007 WRF simulation as part of contract #S2009-09-01. The purpose of this study was to determine the suitability of the WRF output for use in air quality simulations. The results of the study were used to determine if the WRF output fields fit our conceptual understanding of atmospheric processes, if the relevant meteorological fields matched closely to observations, and if meteorological fields will produce reasonable air quality simulation results. For more information on this study, refer to the AER final report. The AER document does not provide a summary of the evaluation conducted for the CenSARA and LADCo states. This chapter will provide the summary for these regions. All plots and tables were produced by AER and may be found at http://sesarm.aer.com.

8.1 Methodology

Version 2.0 of the Model Evaluation Tools (MET) software (http://www.dtcenter.org/met/users/) was used to calculate quantitative performance statistics for temperature, dewpoint temperature, specific humidity, relative humidity, wind speed, and wind direction. All fields are estimated at 2 m above ground, except wind speed and direction which are estimated at 10 m. The software uses the PrepBUFR observational dataset (http://dss.ucar.edu/datasets/ds337.0/) to evaluate the modeled output.

The statistics calculated are similar to those described in Section 6.1, and are shown in Table 8-1. Similar to the methodology related to the evaluation of the sensitivity runs, the gridded meteorological fields are interpolated to observation locations at every hour of the simulation. The modeled values are paired with the hourly observations collected at these locations. The statistics are calculated using the pairs that fall within the geographic regions described previously (see Figure 6-1) on a daily and monthly basis. Statistics are also calculated for individual observation locations. Hourly average modeled and observed values for each geographic region of interest are also calculated and plotted. In order to assess the performance of the simulation, the daily statistics are compared to a set of benchmark values (Emery et al., 2001). The purpose of these benchmarks is not to determine whether the simulation is either sufficient or unusable, but rather to put the errors in the context of the performance of past simulations. The benchmark values are shown in Table 8-2.

When evaluating modeled wind speeds the presence of observed calm wind speeds must be addressed. The NWS ASOS network historically used cup and vane anemometers to measure wind speed and direction. The instruments possess a minimum measurement threshold, due to the mechanical friction of the instrument, of 2 knots (NOAA, 1998). Due to truncation of the reported decimal places all wind speeds below 3 knots are reported as calm, or 0 knots. Therefore, light winds may be reported as zero. Meteorological models never produce a truly zero wind speed. Thus, this measurement artifact introduces an artificial positive bias in the wind speed evaluation. This bias becomes most pronounced in areas such as the southeastern U.S. at night and during the summer when the synoptic scale pattern over the region is dominated by high pressure and calm winds are routinely produced (Olerud and Sim, 2004). The simplest approaches to this issue are to exclude all model-observed pairs in which the observed winds are 0 knots or to include all wind speeds. The drawback to the first approach is it may

greatly reduce the sample size of model-observed pairs used in the calculation of the performance metrics when numerous calm winds are measured. There is also no way to distinguish between winds less than 3 knots that are reported as calm (0 knots) and winds that are actually near 0 knots. The drawback to the second approach, obviously, is the introduction of the artificial positive bias. Olerud and Sims (2004) approached this problem by setting all calm wind speeds equal to 1.5 knots, halfway between 0 knots and the measurement threshold.

It should be noted that from 2002 to 2010 the NWS ASOS anemometers were upgraded to sonic anemometers to eliminate the measurement issues related to instrument icing. These instruments possess measurement thresholds approaching 0 knots. At the beginning of 2007 approximately 35% of ASOS anemometers were upgraded, and by the end of the year the percentage increased to roughly 80%. It is unclear if the transition to sonic anemometers increased the number of reported wind speeds less than 3 knots that would otherwise have been reported as 0 knots in the PrepBUFR dataset.

Model-observed pairs containing a calm wind observation were included in the wind speed evaluation by AER. The Iowa DNR does not agree with this approach. Zero knot winds as reported in the PrepBUFR dataset are most likely measurement artifacts and not true measured values. Therefore, they should be treated as missing values and ignored. The results of the performance evaluation are assessed as is, but it should be noted that wind speed statistics contain an artificial, positive bias component.

Table 8-1. Performance metrics calculated to evaluate the WRF production run.

Metric	Equation
Bias	$B = \frac{1}{IJ}\sum_{j=1}^{J}\sum_{i=1}^{I}\left(P_j^i - O_j^i\right)$
Mean Absolute Error	$MAE = \frac{1}{IJ}\sum_{j=1}^{J}\sum_{i=1}^{I}\left\lvert P_j^i - O_j^i\right\rvert$
Root Mean Square Error	$RMSE = \sqrt{\frac{1}{IJ}\sum_{j=1}^{J}\sum_{i=1}^{I}\left(P_j^i - O_j^i\right)^2}$
Correlation Coefficient	$r = \frac{\sum_{i=1}^{n}\left(\left(O_i - \overline{O}\right)\left(P_i - \overline{P}\right)\right)}{\sqrt{\sum_{i=1}^{n}\left(O_i - \overline{O}\right)^2\sum_{i=1}^{n}\left(P_i - \overline{P}\right)^2}}$
Multiplicative Bias	$MB = \frac{\sum_{j=1}^{J}\sum_{i=1}^{I}P_j^i}{\sum_{j=1}^{J}\sum_{i=1}^{I}O_j^i}$

Table 8-2. Benchmark values for the performance metrics used to evaluate the WRF simulation.

Variable	Statistic	Benchmark
Wind Speed	Bias	≤ ± 0.5 m/s
	RMSE	≤ 2 m/s
Temperature	Bias	≤± 0.5 °C
	MAE	≤ 2 °C
Mixing Ratio	Bias	≤± 1 g/kg
	MAE	≤ 2 g/kg

8.2 Results

8.2.1 Course Domain (36 km)

Figure 8-1 shows annual plots of the monthly performance statistics for all variables for the course domain for the CENRAPN region. Temperature bias ranges from -0.5 to 1.0 °C, and values are near zero for most months out of the year. An over-prediction exists during the autumn and winter months. Mean absolute error ranges from 1.5 to 2.5 °C, and values are lowest during the summer months. Specific humidity is slightly over-predicted across the entire year, with the largest over-prediction occurring in the summer months. Bias values range from 0.0 to 0.5 g/kg. Mean absolute error ranges from 0.5 to 1.5 g/kg. Wind speed is slightly under-predicted across the entire year. The largest under-prediction occurs during the spring. Bias values range from -0.5 to 0.0 m/s. Root mean square error values are consistently near 2.0 m/s.

Figure 8-2 shows similar monthly plots for the CENRAPS region of the course domain. Temperature is unbiased during the late spring and summer, while slightly over-predicted during the autumn and winter. Bias values range from 0.0 to 1.0 °C. Mean absolute error values range from 1.5 to 2.5 °C, with the lowest errors occurring in the summer, and highest errors occurring in the winter. Specific humidity bias is generally near zero, with values ranging from -0.5 to 0.25 g/kg. Mean absolute error ranges from 1.0 to 2.0 g/kg. The highest errors occur in the late summer and early fall, while the lowest errors occur during the winter. Wind speed is generally under-predicted during the year, and is most under-predicted in the late winter and early spring. Bias values range from -0.5 to 0.0 m/s. Root mean square error is consistently near 2.0 m/s all year.

Figure 8-3 shows similar monthly plots for the MRPO region of the course domain. Temperature bias ranges from -0.5 to 0.5 °C. Under-prediction occurs during the spring, while over-prediction occurs during the fall and winter. Mean absolute error ranges from 1.5 to 2.5 °C, with the largest errors occurring during the spring. Specific humidity is generally over-predicted across the year; the greatest over-prediction occurs during the summer. Bias values range from 0.0 to 0.5 g/kg. Mean absolute error ranges from 0.5 to 1.5 g/kg, with the largest errors occurring in the summer. Wind speed is slightly under-predicted in the winter and spring, but generally unbiased in the summer and fall. Bias values range from -0.5 to 0.0 m/s. Root mean square error is consistently near 2.0 m/s, but is lowest during the summer.

Figure 8-4 shows an annual plot (Bakergram) of daily temperature bias for the course domain calculated for the CENRAPN region. Figure 8-5 shows a similar plot for daily temperature mean absolute error. Daily performance of temperature is highly variable in all seasons except

summer. Daily bias values are only within the benchmark values approximately half the days of the year. Values are occasionally as large as ±2.5 °C. Mean absolute error values are within the benchmark the majority of days in the year. Nearly all values are less than 3.0 °C.

Figure 8-6 shows an annual plot of daily wind speed bias for the course domain for the CENRAPN region. Figure 8-7 shows a similar plot for daily wind speed mean absolute error. Daily performance of wind speed is very consistent across the year. Bias values are within the benchmarks on a significant portion of days (around 80%). Most of the under-predictions greater than the benchmark are in the spring. Mean absolute error values are less than the benchmark on nearly all days. It should be noted, though, that for wind speed the benchmark applies to root mean square error, which is always greater than mean absolute error. Bakergrams of daily RMSE were not generated by AER. Bakergrams showing daily specific humidity performance were not generated, but based on the monthly statistics humidity statistics were most likely within the benchmarks for most, if not all, days. It should be noted the humidity benchmarks apply to mixing ratio, however mixing ratio and specific humidity are approximately equal.

Spatial bubble plots of monthly performance statistics calculated at individual observation locations shows the distribution of errors across the continental U.S. Figure 8-8 shows a bubble plot of temperature bias for June for the course domain model output. Figure 8-9 shows a similar bubble plot for temperature mean absolute error. In the summer temperature performance is best over the Midwest, Northern Plains, and gulf coast states and worst over California, the Rocky Mountains, surrounding the Great Lakes, and along the Atlantic coast. Figure 8-10 shows a bubble plot of temperature bias for December. Figure 8-11 shows a similar plot for temperature mean absolute error for December. In the winter temperature performance is best over the Midwest and worst across the entire extent of the Rockies.

Figure 8-12 shows a bubble plot of specific humidity bias for June. Figure 8-13 shows a similar plot for specific humidity mean absolute error. Humidity performance is consistently good across most of the continental U.S. A few areas of weaker performance exist over portions of the southeastern and extreme southwestern U.S. Figure 8-14 shows a bubble plot of specific humidity bias for December. Figure 8-15 shows a similar plot for specific humidity mean absolute error. Winter humidity performance appears best over the Midwest and Northern Plains and worst over the Southeast and California. However, in the colder regions of the U.S. the low specific humidity values during winter lead to small bias and error values. Performance in the southern half of the U.S. is typically within benchmark goals, and relative humidity errors in the winter months (e.g. see Figure 8-1) were acceptable.

Figure 8-16 shows a bubble plot of wind speed bias for June. Figure 8-17 shows a similar plot for wind speed mean absolute error. Wind speed performance is best over the Midwest and Southeast and worst over the Mountain West and along the Pacific coast. Figure 8-18 shows a bubble plot of wind speed bias for December. Figure 8-19 shows a similar plot for wind speed mean absolute error. Winter wind speed performance is best over the Midwest, Northern Plains, and Southeast and worst over southern California.

Timeseries plots of observed and modeled surface variables averaged across the evaluation geographic regions show the diurnal profile of model performance. Figure 8-20 through Figure 8-25 show timeseries of observed and modeled temperature, wind speed, and specific humidity averaged across the CENRAPN region. Two sample time periods are shown: May 11-15 and August 19-23. Modeled temperature reproduced the diurnal variations in temperature reasonably well. Daily minimums were frequently underpredicted slightly. Daily maximums were occasionally overpredicted and underpredicted. Modeled wind speed did not reproduce all the diurnal variation in the observations. Daily maximum wind speeds were frequently underpredicted. Daily minimum wind speeds were frequently overpredicted. However, the large drop in observed wind speeds at night was partly due to the inclusion of calm winds in the evaluation. The underprediction during the day nearly canceled the overprediction at night leading to daily bias values near zero. Removing observed calm winds from the evaluation would lead to daily wind speed bias values that are slightly negative. Specific humidity was generally slightly overpredicted and the diurnal variation was exaggerated due to significant overprediction of daytime maximums.

For periods of poor performance for a particular meteorological variable, reviewing the diurnal profile of model performance is very useful to discern the time of day the error occurs. Figure 8-26 and Figure 8-27 show timeseries of observed and modeled temperature averaged across the CENRAPN region from January 11-20. From January 12-17 daily temperature bias ranged from 0.6 to 3.0 K. The timeseries show modeled temperature was consistently too high across this period, though the diurnal variation was still adequately captured. This suggests the error originates from uncertainties in the representation of large scale flow. On January 18 and 19 when large negative bias was reported the timeseries shows a significant underprediction of nighttime minimum temperatures. Figure 8-28 shows a timeseries of observed and modeled temperature averaged across the CENRAPN region from October 8-12. During this time daily temperature bias values ranged from 1.0 to 2.7 K. The timeseries shows again that modeled temperature was consistently too high across the entire period.

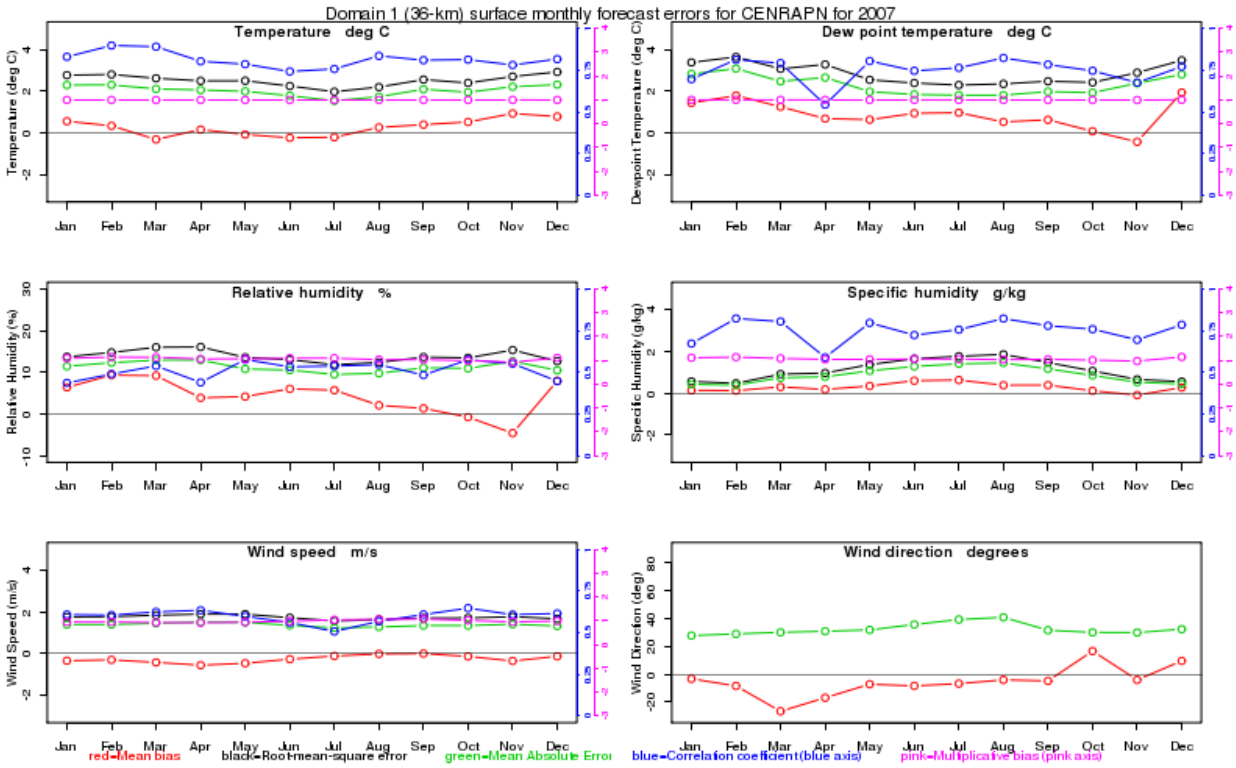

Figure 8-1. Monthly surface statistics for the course domain for the CENRAPN region.

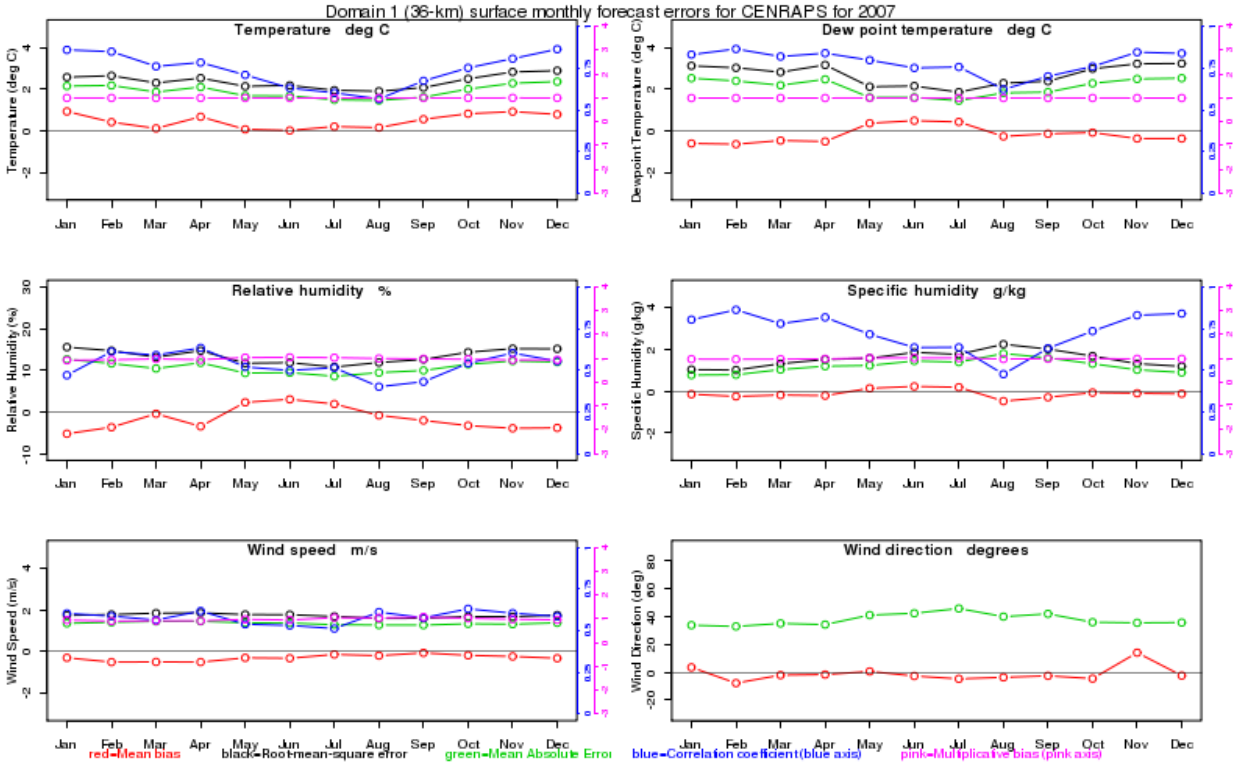

Figure 8-2. Monthly surface statistics for the course domain for the CENRAPS region.

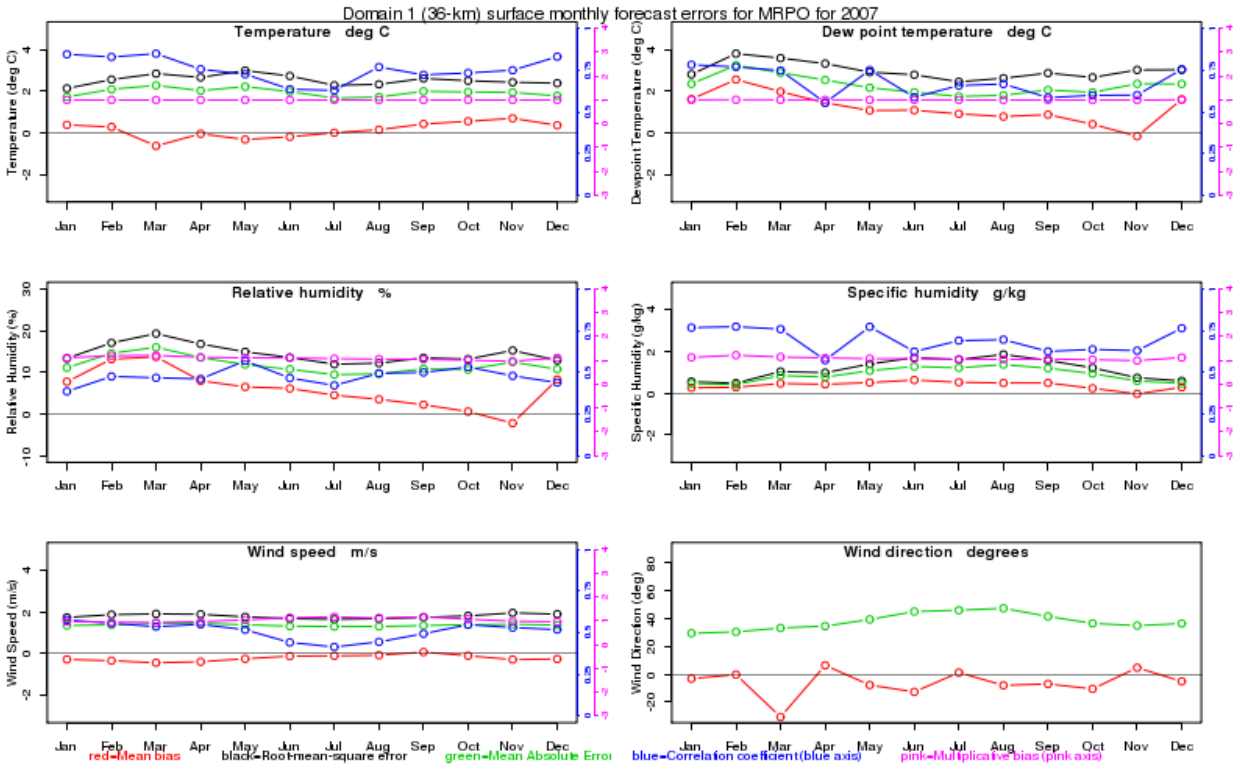

Figure 8-3. Monthly surface statistics for the course domain for the MRPO region.

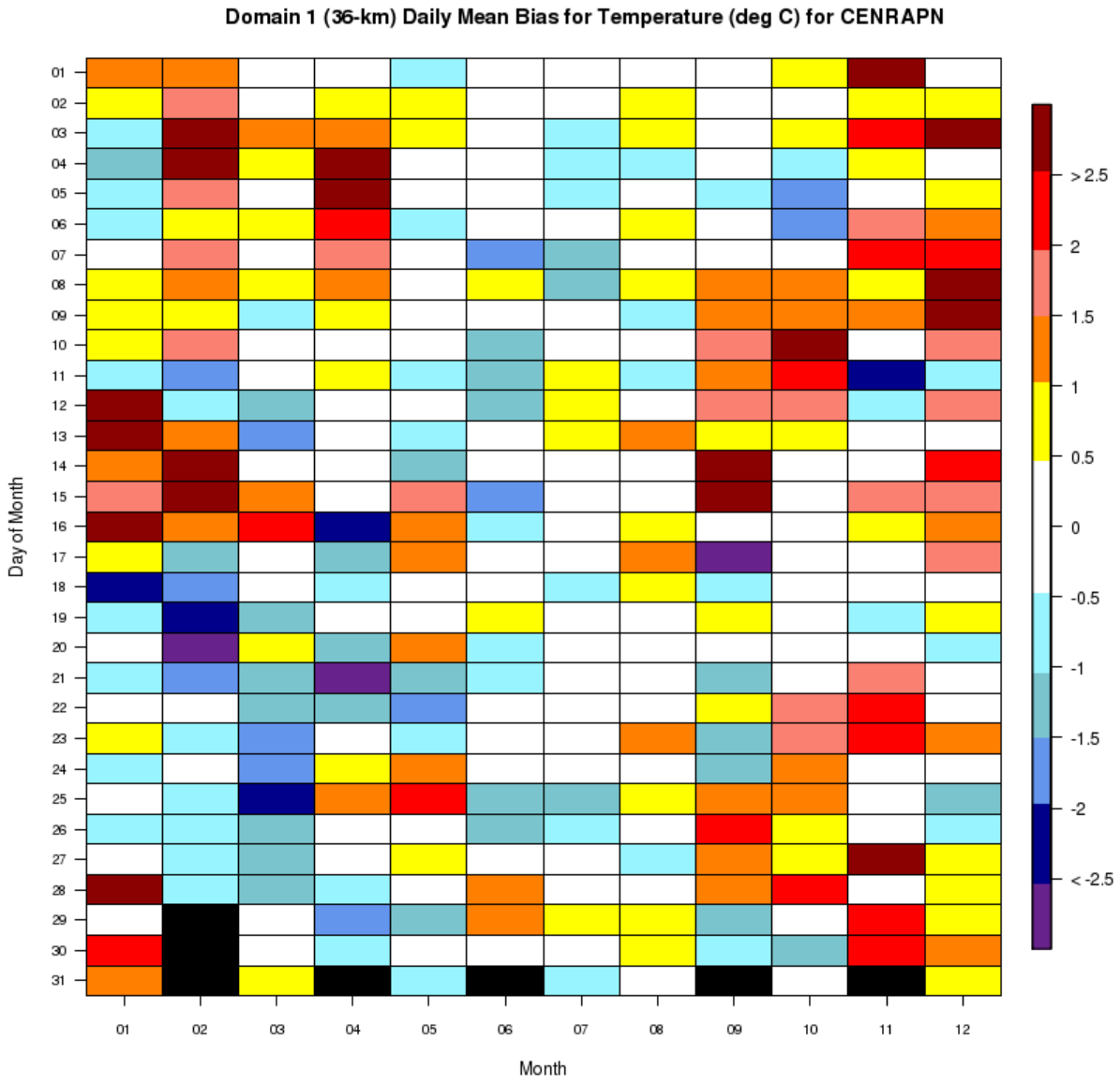

Figure 8-4. Bakergram showing daily temperature bias for the course domain for the CENRAPN region.

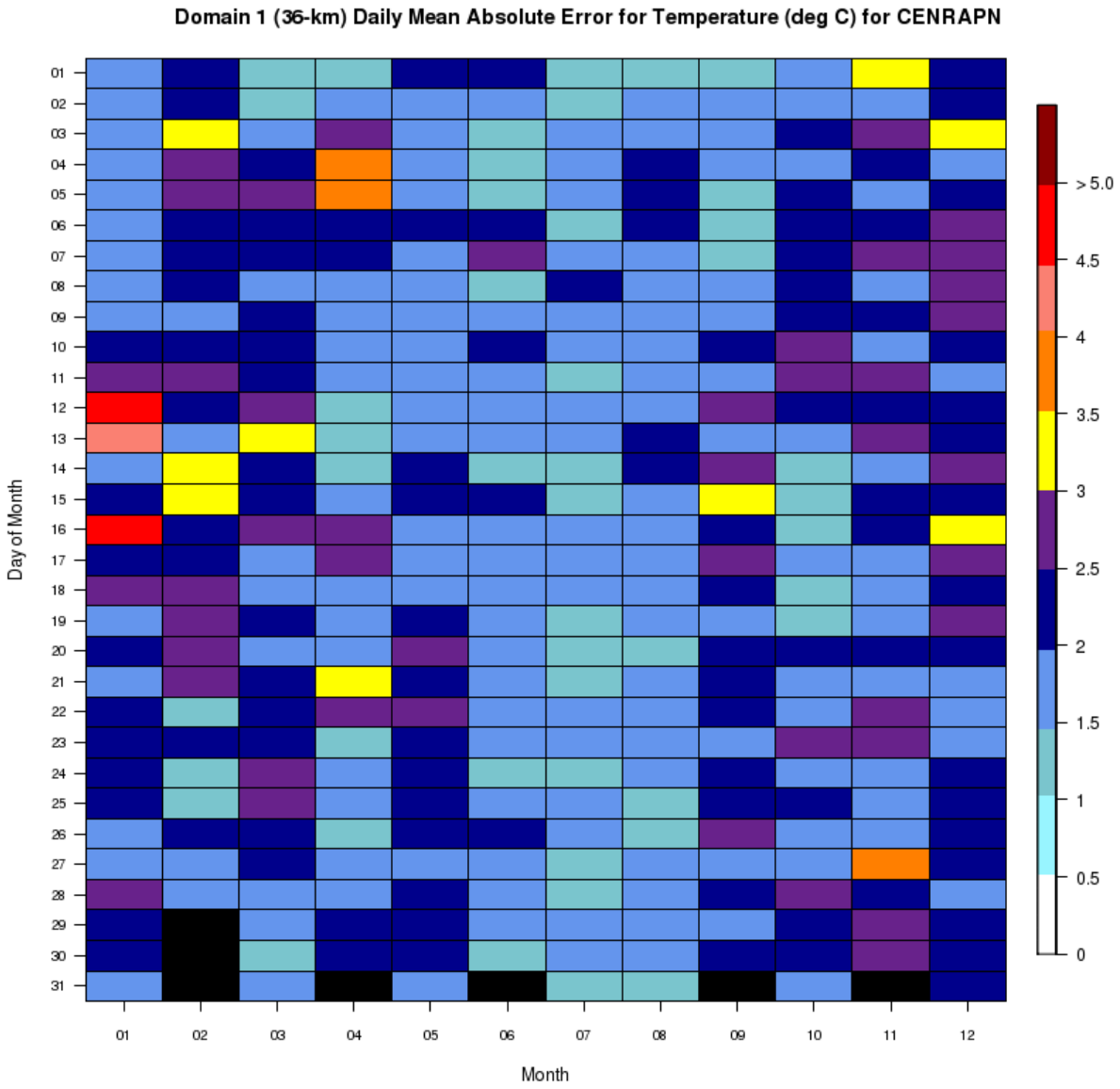

Figure 8-5. Bakergram showing daily temperature mean absolute error for the course domain for the CENRAPN region.

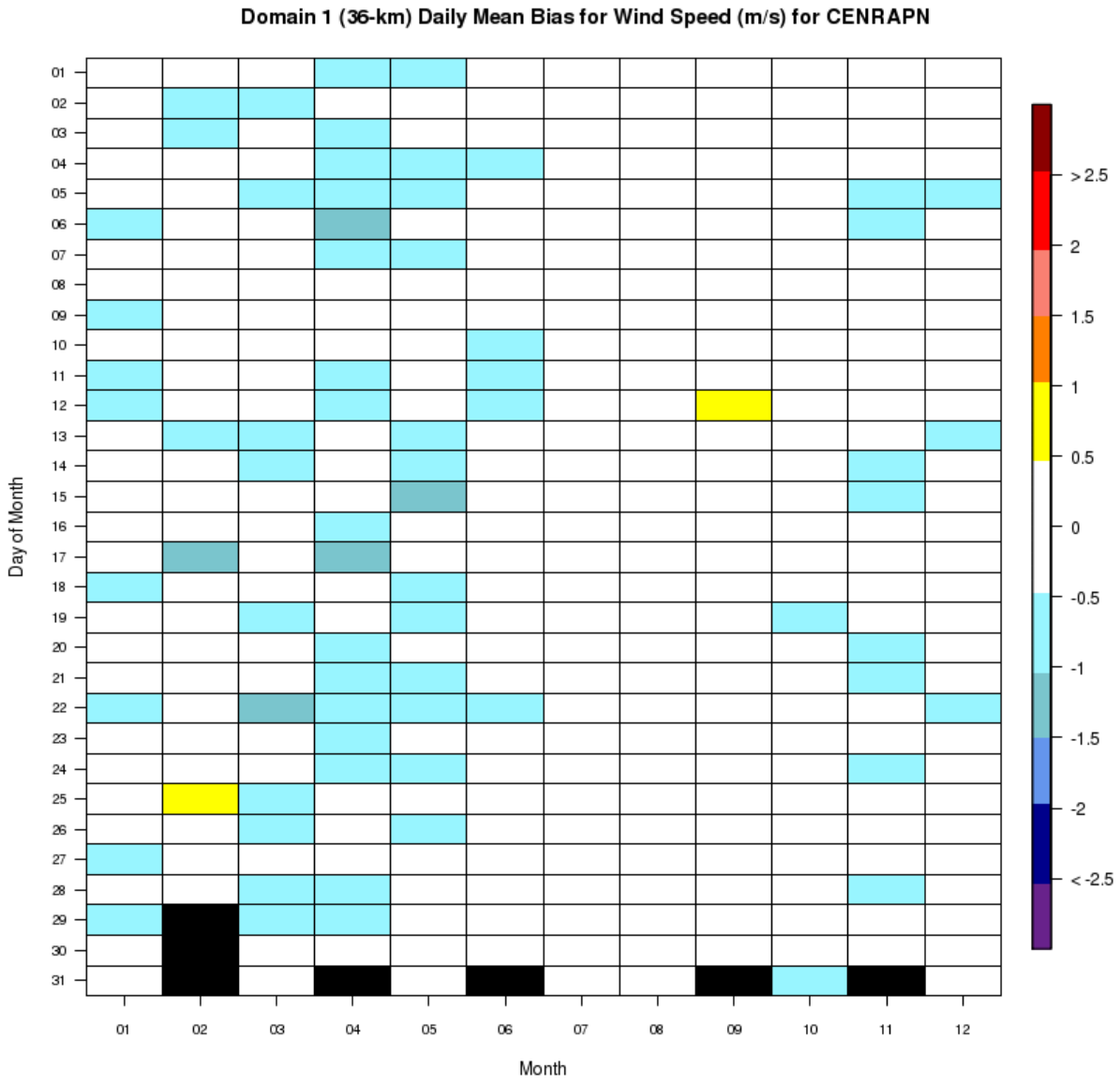

Figure 8-6. Bakergram showing daily wind speed bias for the course domain for the CENRAPN region.

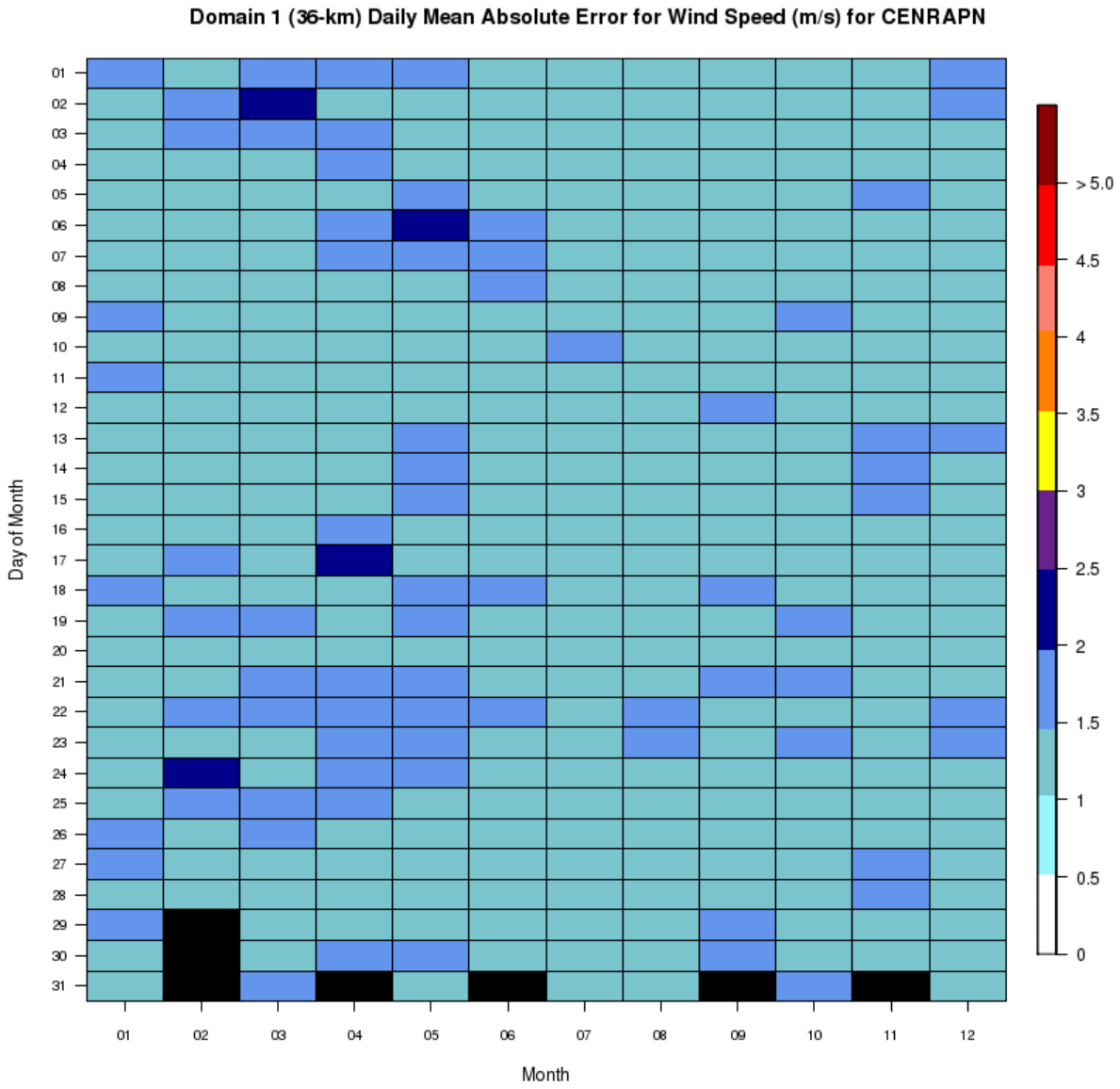

Figure 8-7. Bakergram showing daily wind speed mean absolute error for the course domain for the CENRAPN region.

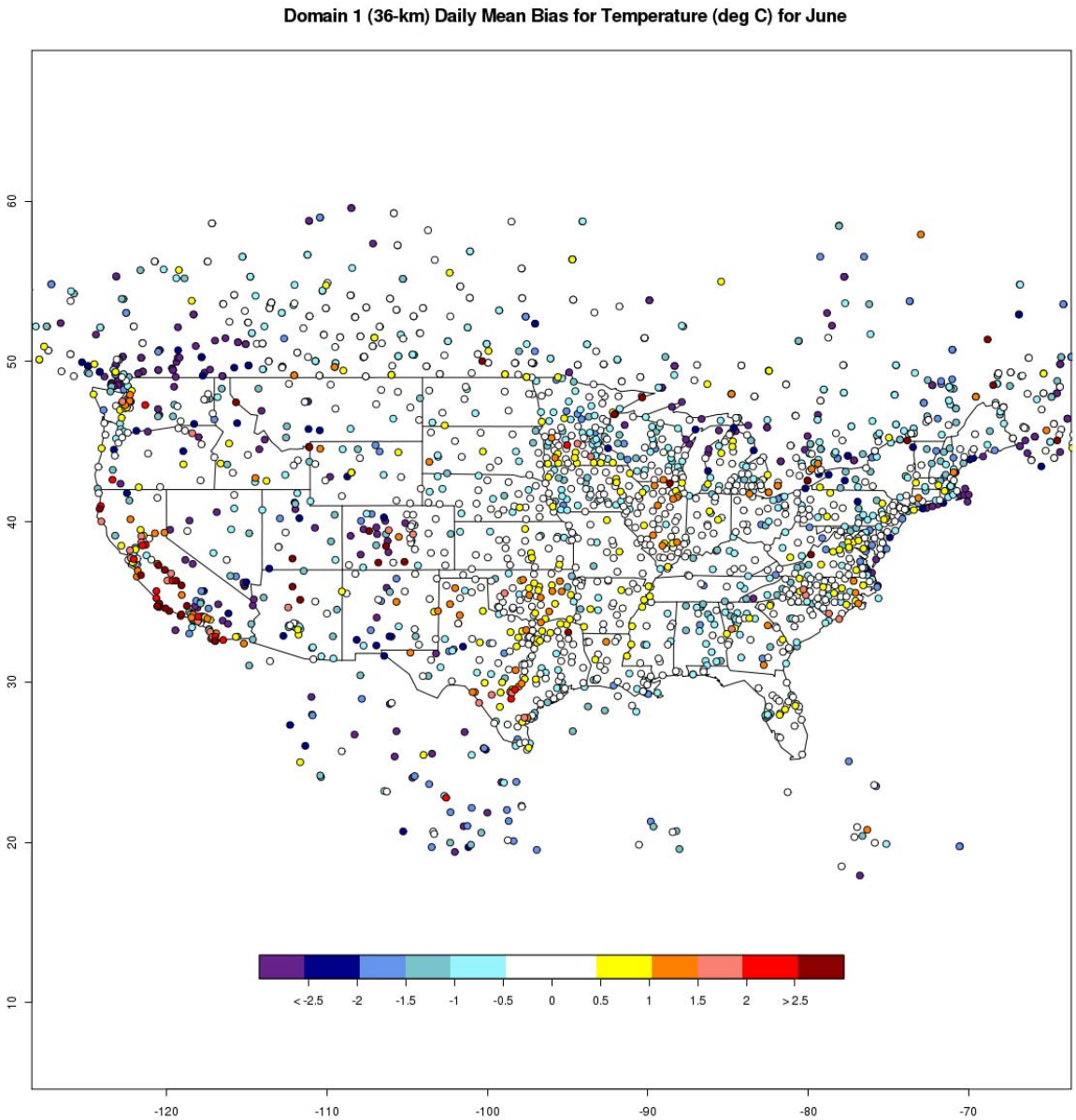

Figure 8-8. Spatial bubble plot of monthly temperature bias at individual observation locations for the course domain for June.

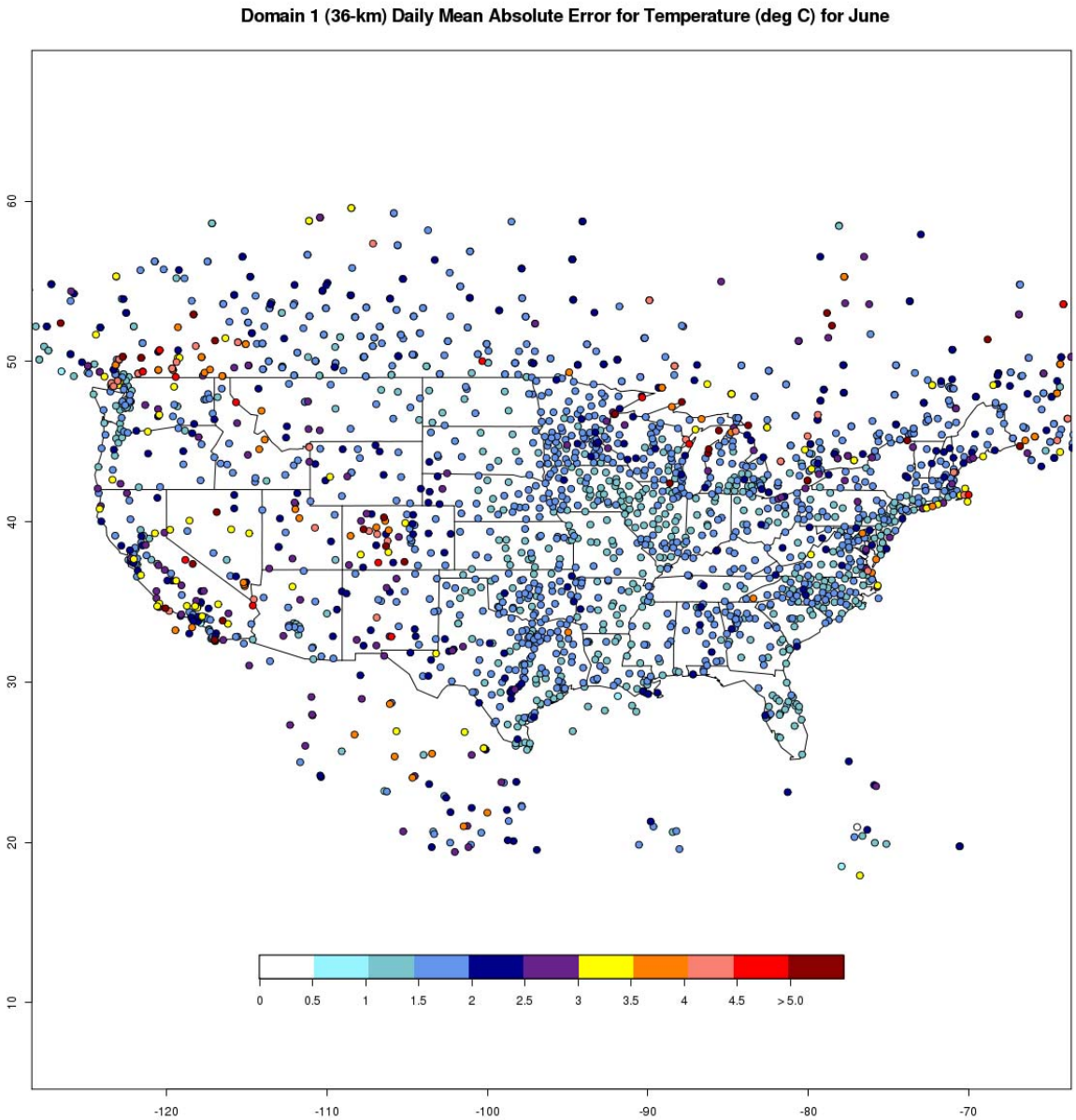

Figure 8-9. Spatial bubble plot of monthly temperature mean absolute error at individual observation locations for the course domain for June.

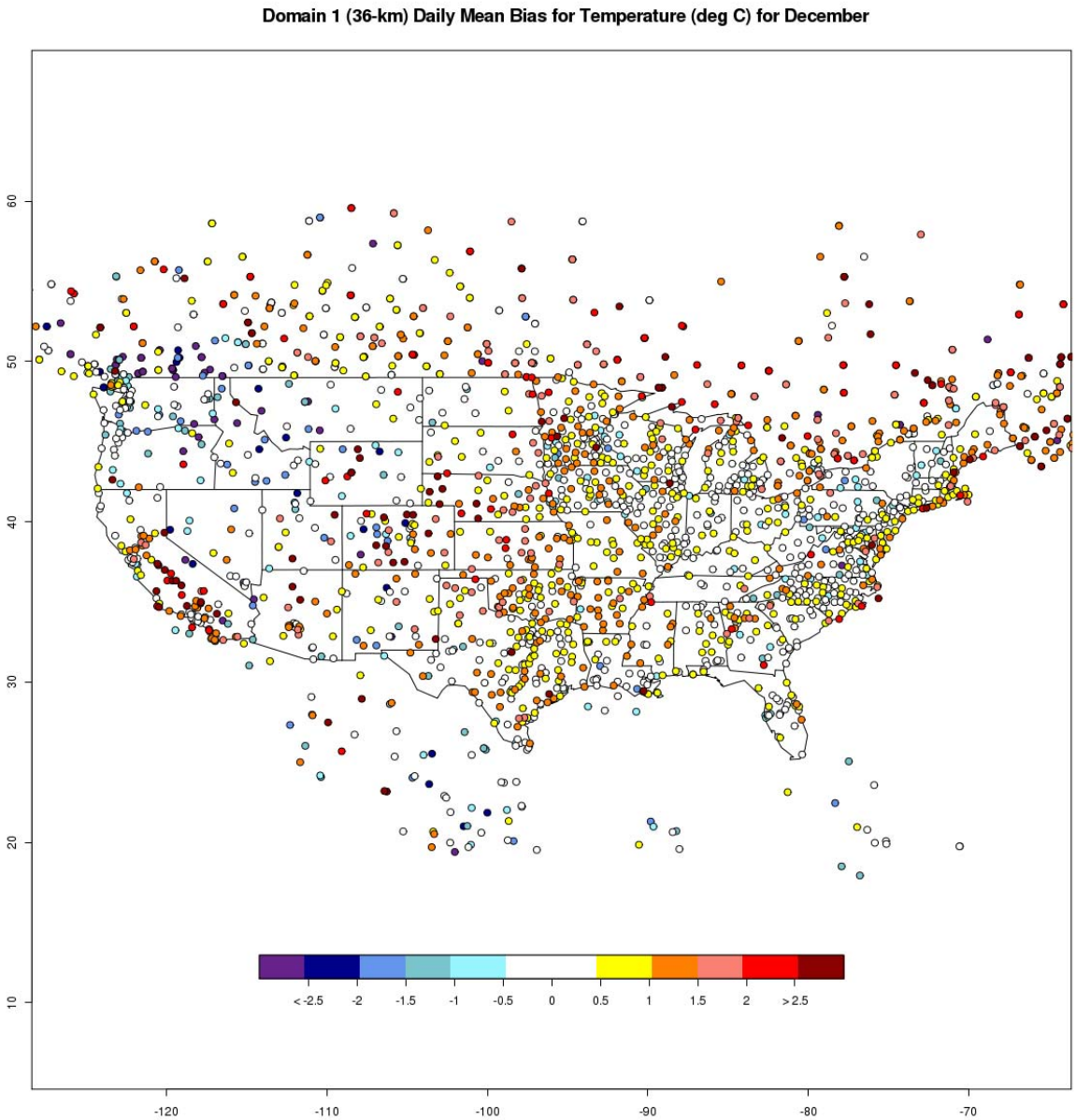

Figure 8-10. Spatial bubble plot of monthly temperature bias at individual observation locations for the course domain for December.

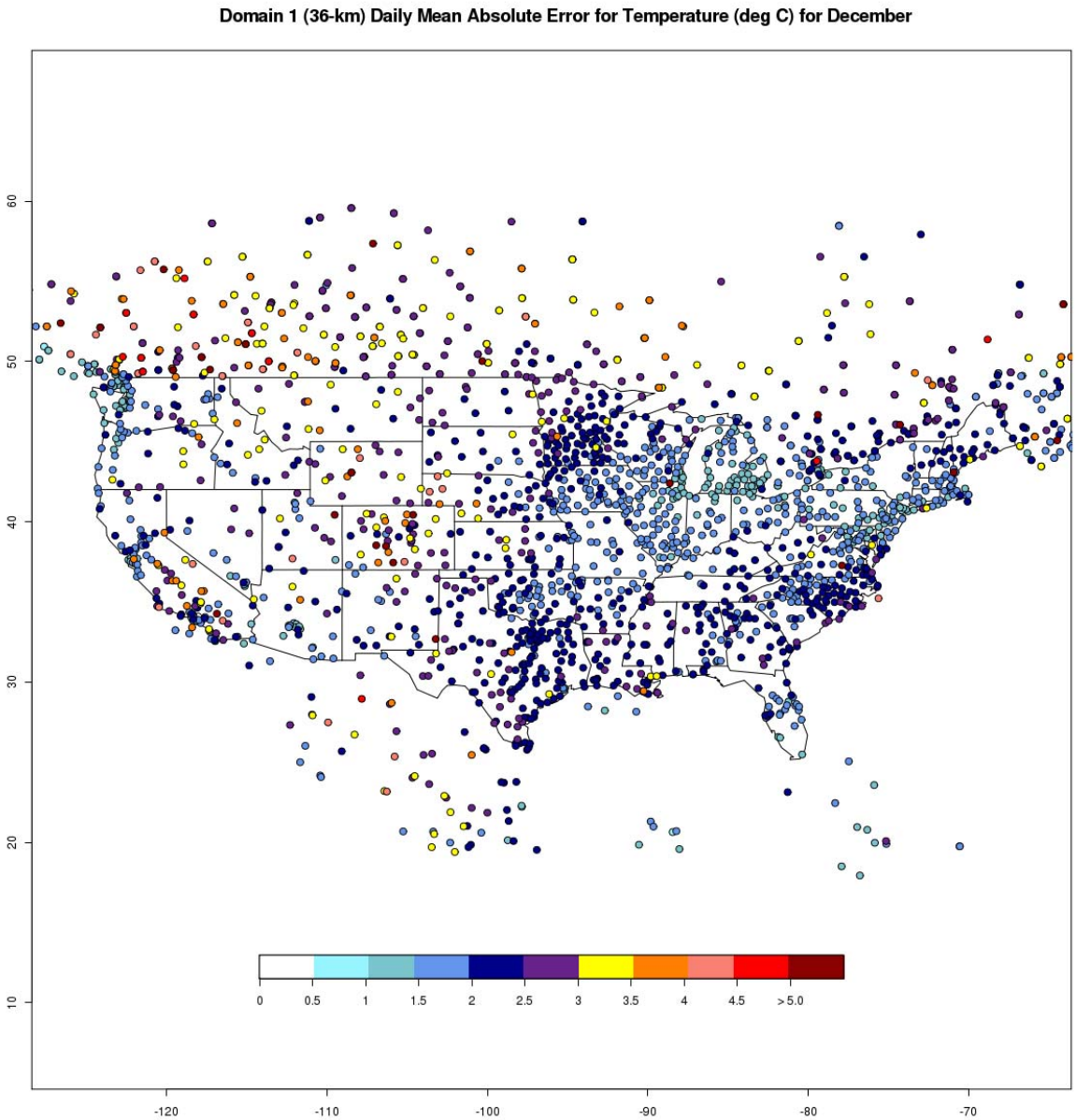

Figure 8-11. Spatial bubble plot of monthly temperature mean absolute error at individual observation locations for the course domain for December.

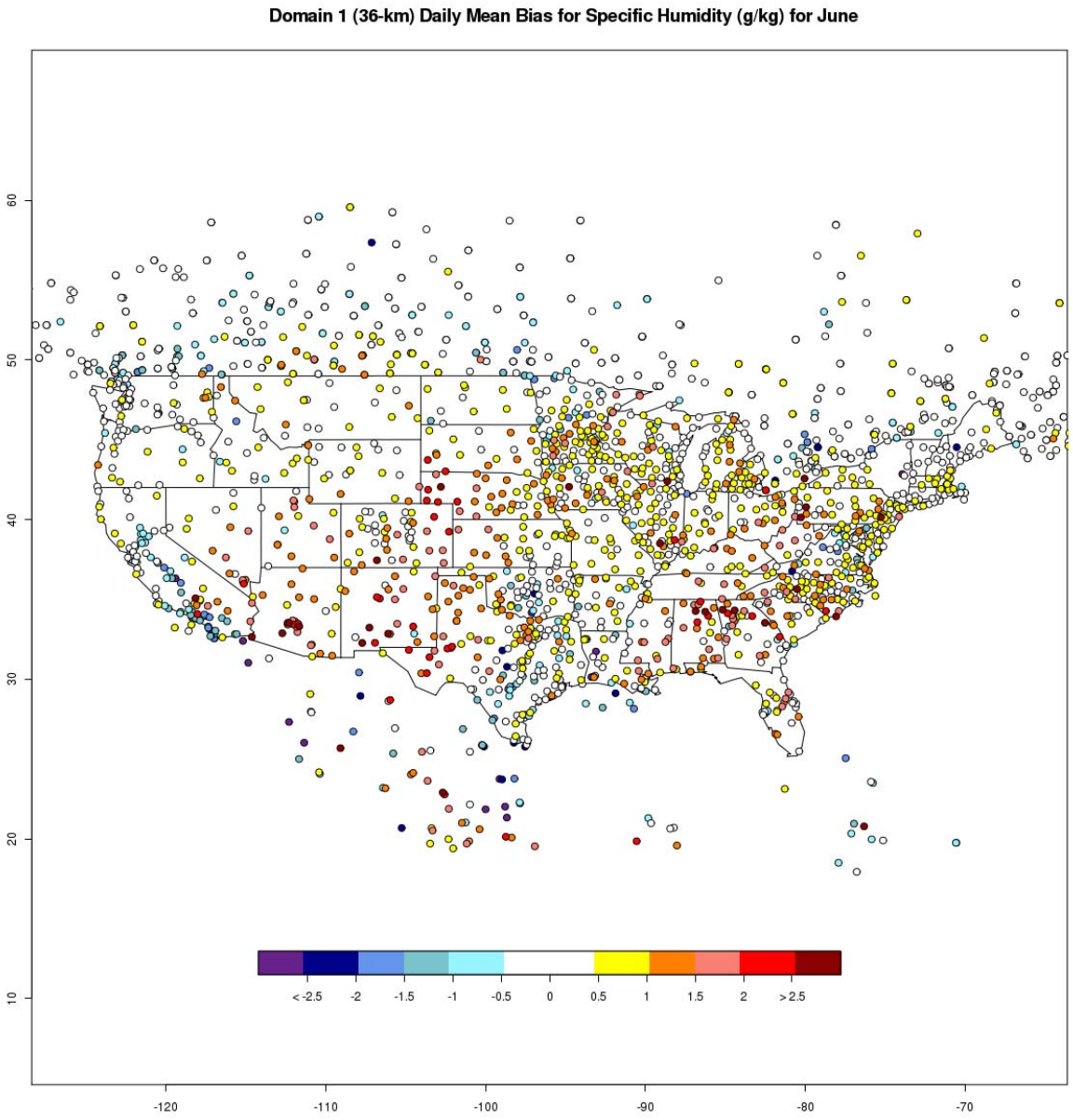

Figure 8-12. Spatial bubble plot of monthly specific humidity bias at individual observation locations for the course domain for June.

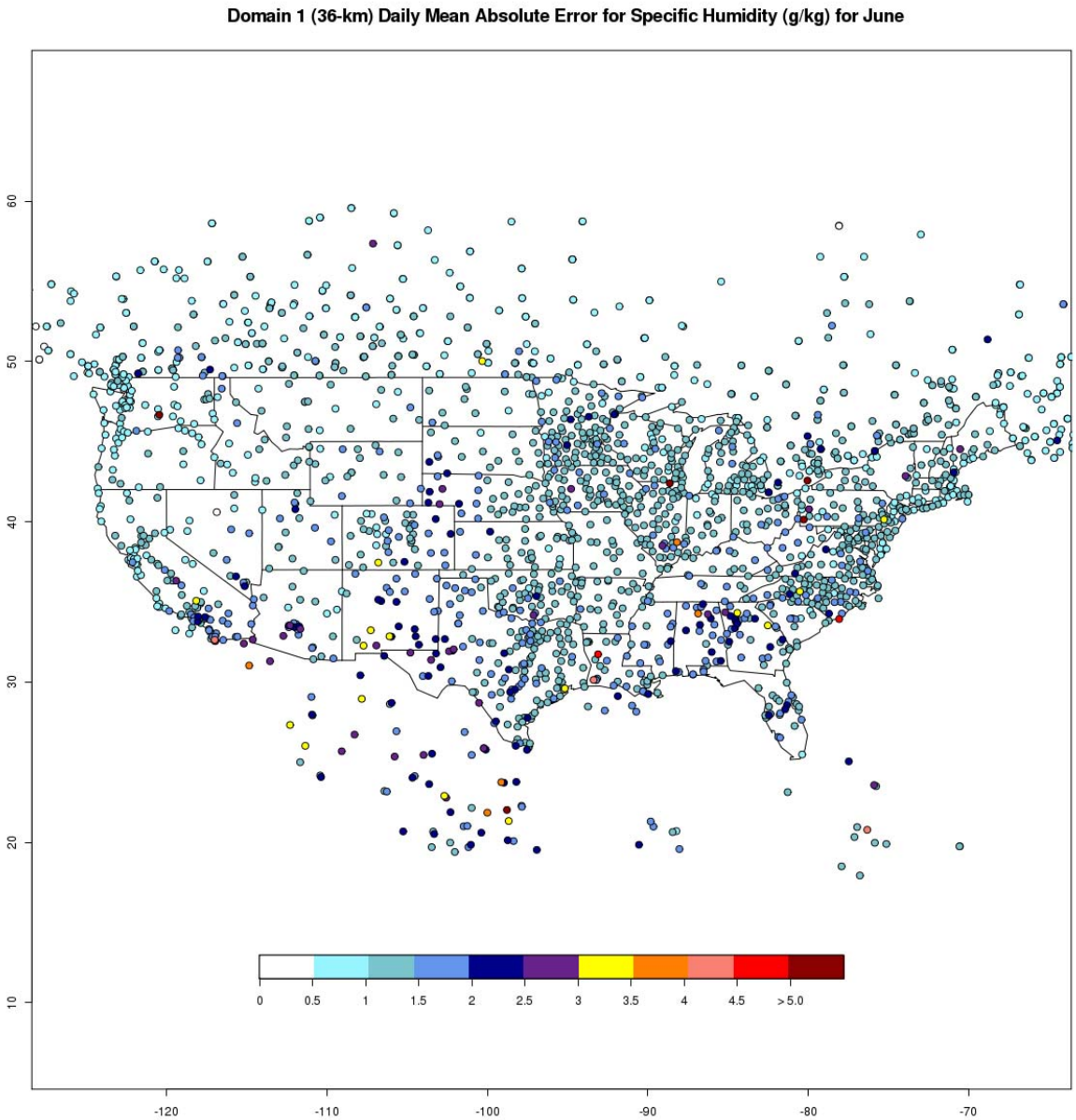

Figure 8-13. Spatial bubble plot of monthly specific humidity mean absolute error at individual observation locations for the course domain for June.

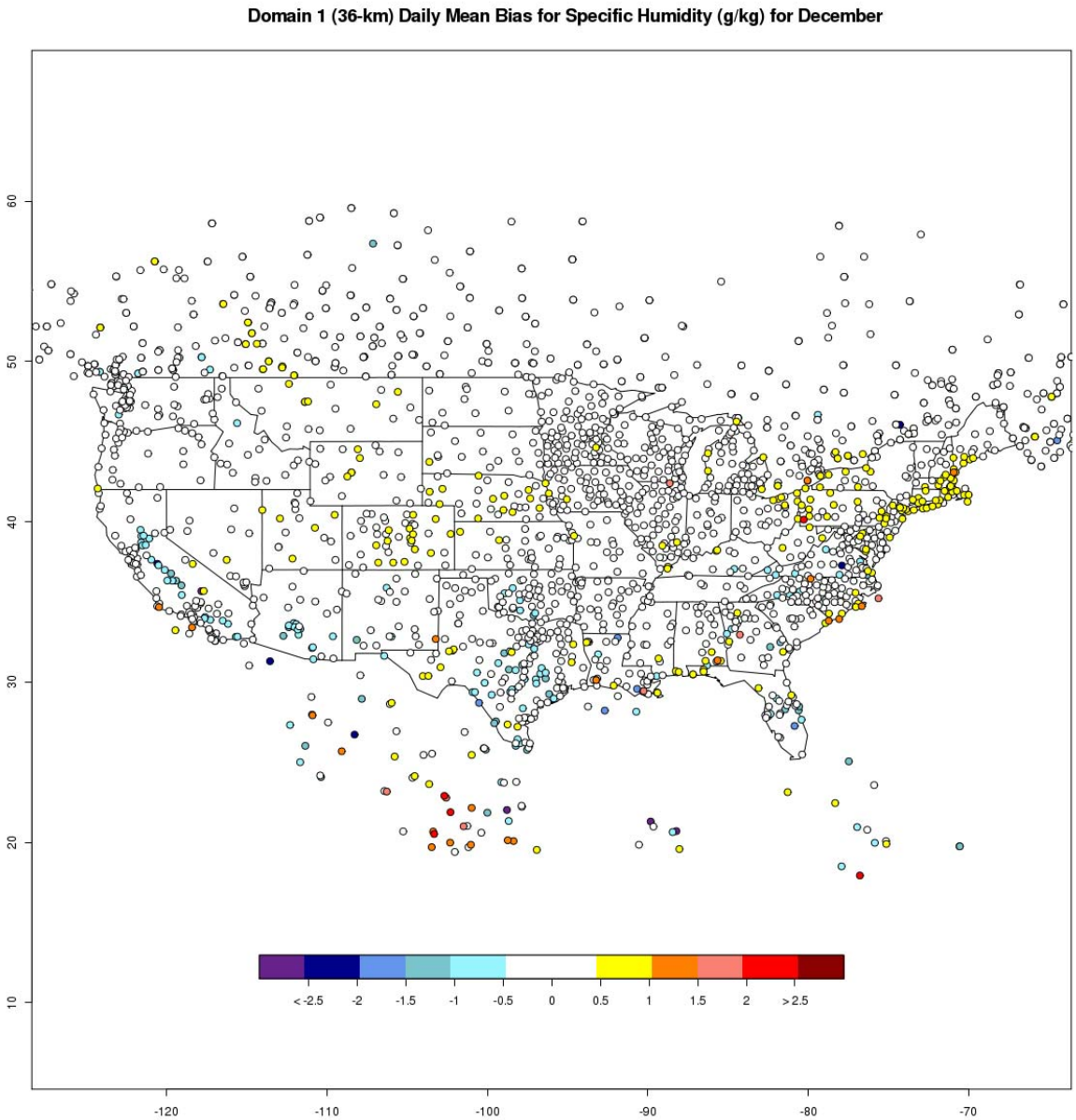

Figure 8-14. Spatial bubble plot of monthly specific humidity bias at individual observation locations for the course domain for December.

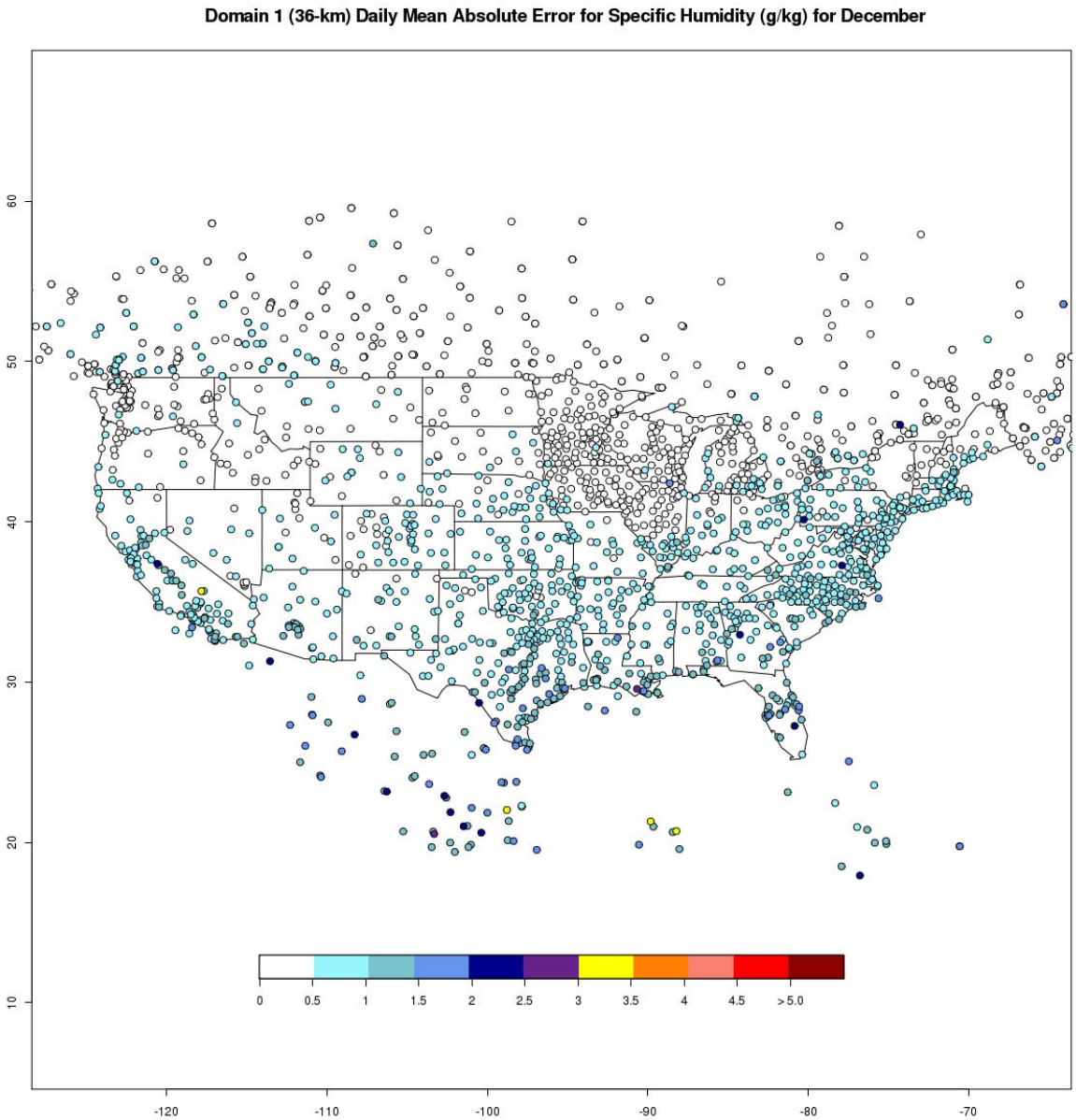

Figure 8-15. Spatial bubble plot of monthly specific humidity mean absolute error at individual observation locations for the course domain for December.

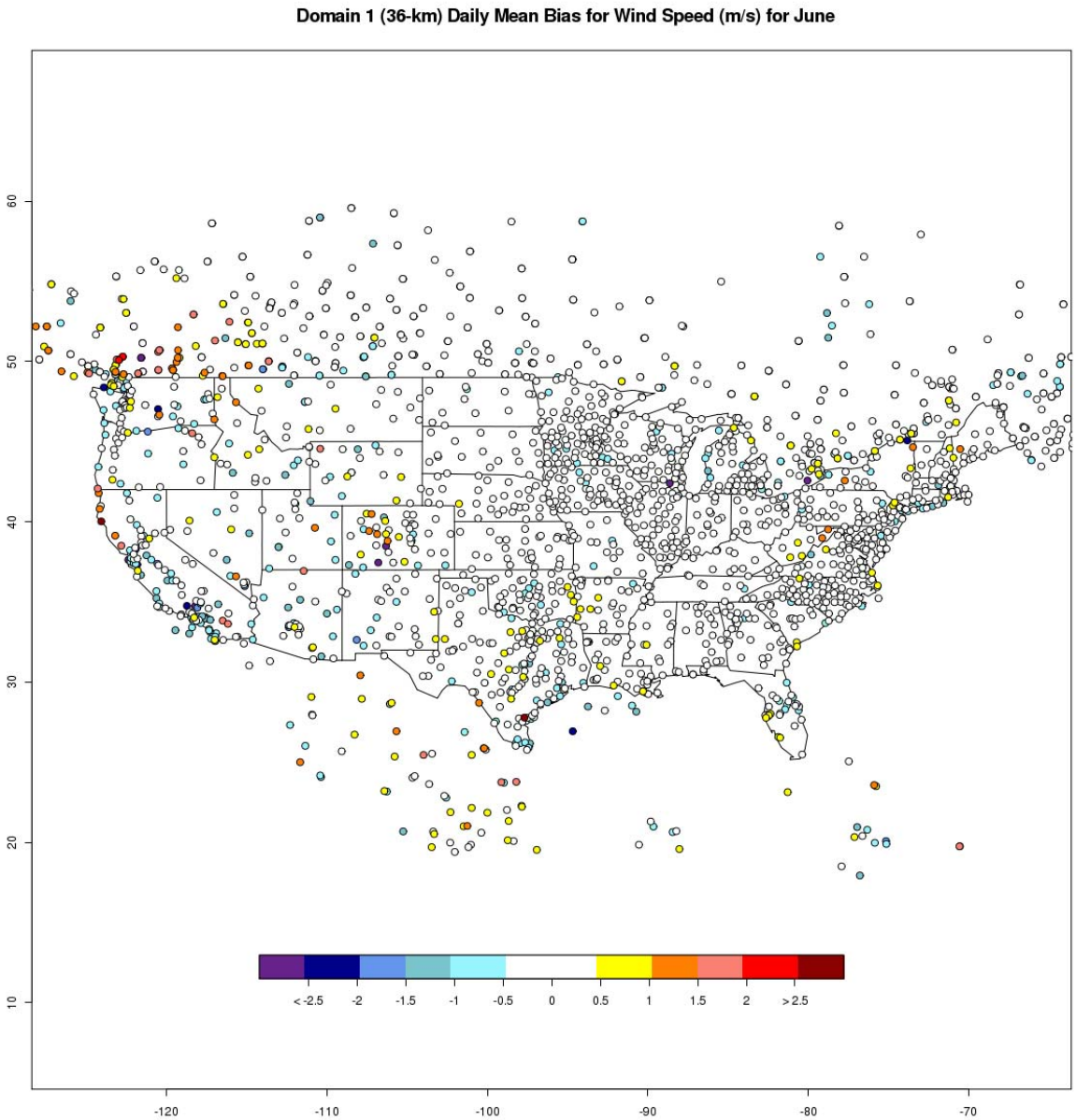

Figure 8-16. Spatial bubble plot of monthly wind speed bias at individual observation locations for the course domain for June.

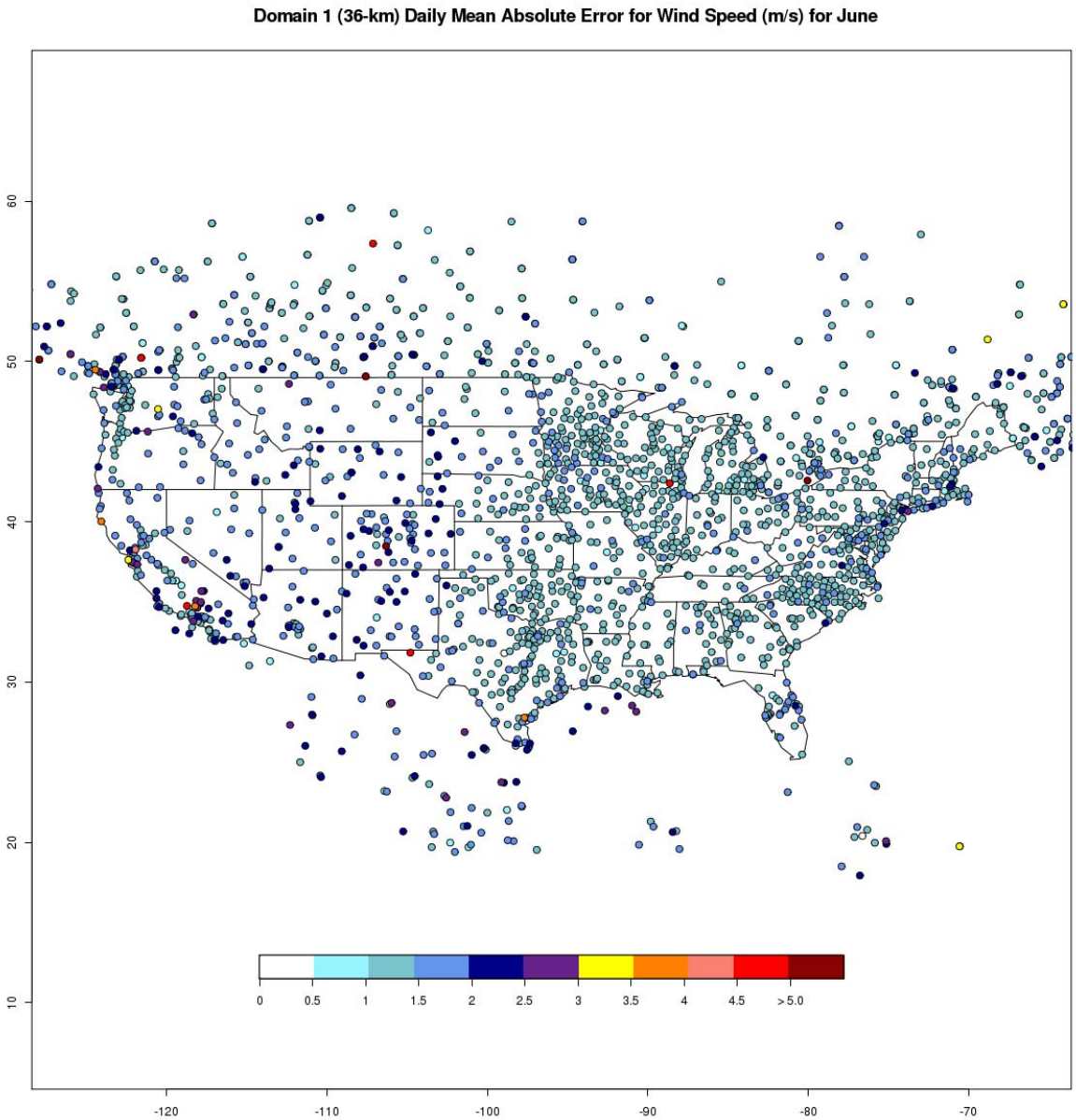

Figure 8-17. Spatial bubble plot of monthly wind speed mean absolute error at individual observation locations for the course domain for June.

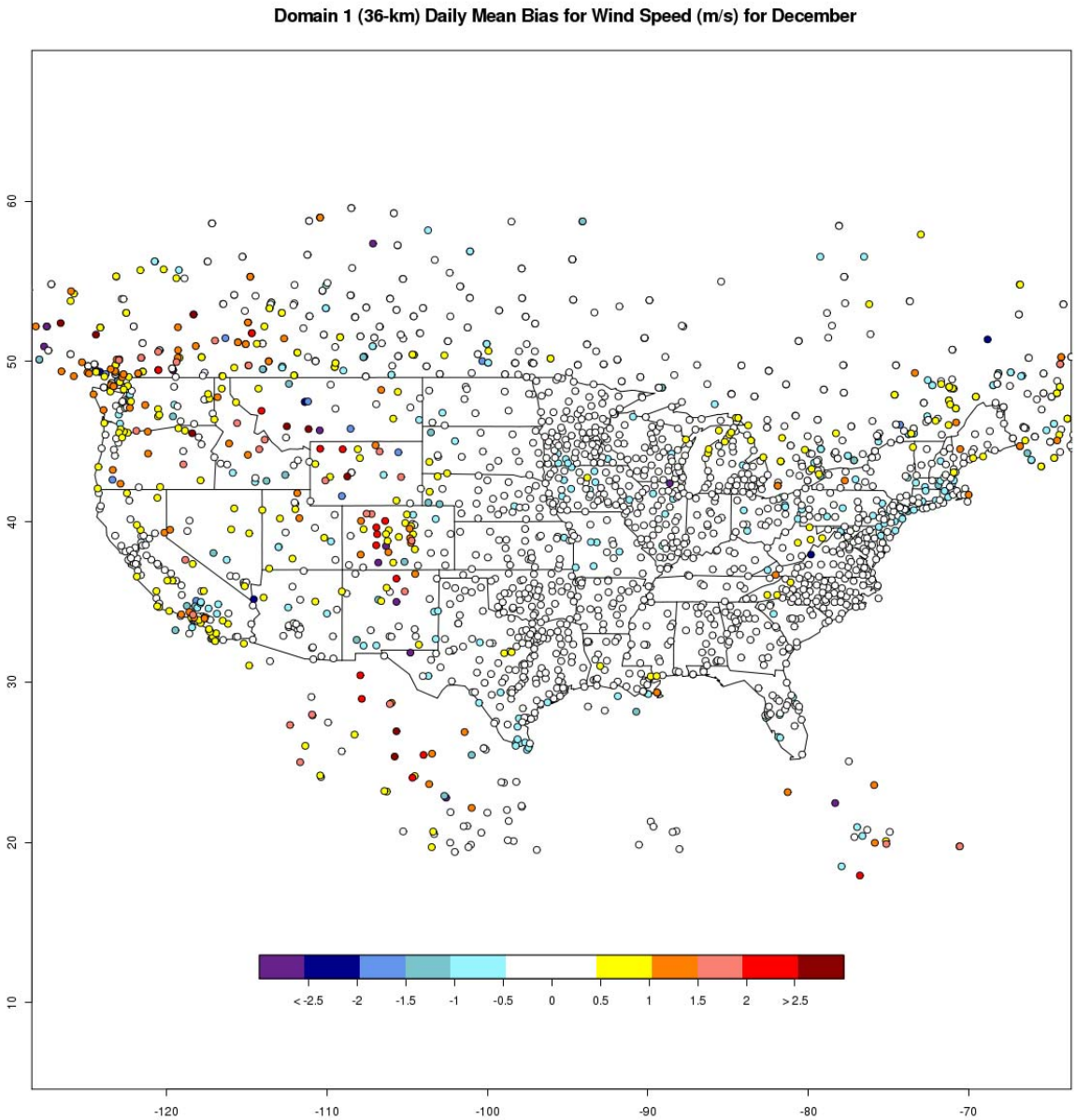

Figure 8-18. Spatial bubble plot of monthly wind speed bias at individual observation locations for the course domain for December.

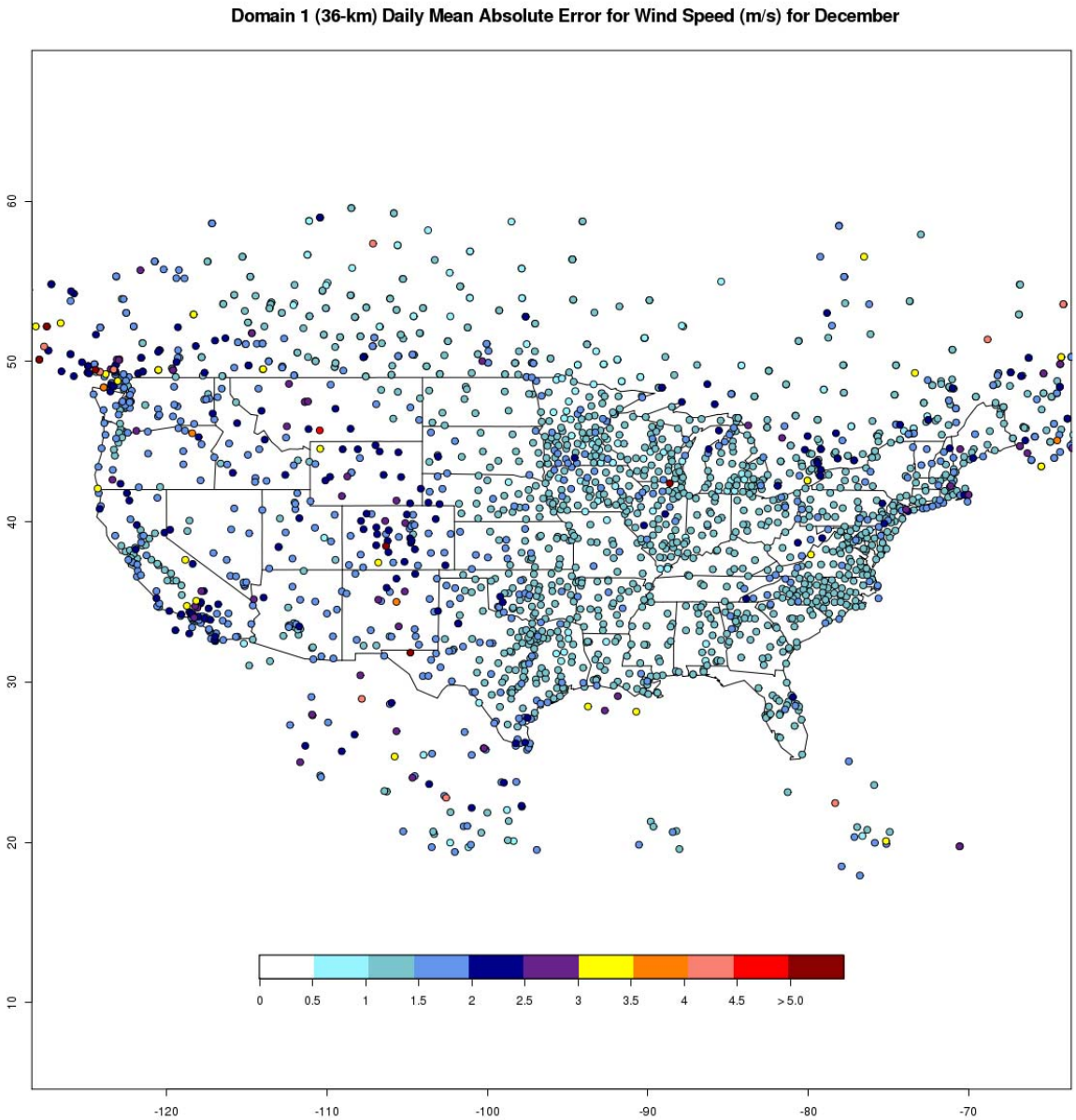

Figure 8-19. Spatial bubble plot of monthly wind speed mean absolute error at individual observation locations for the course domain for December.

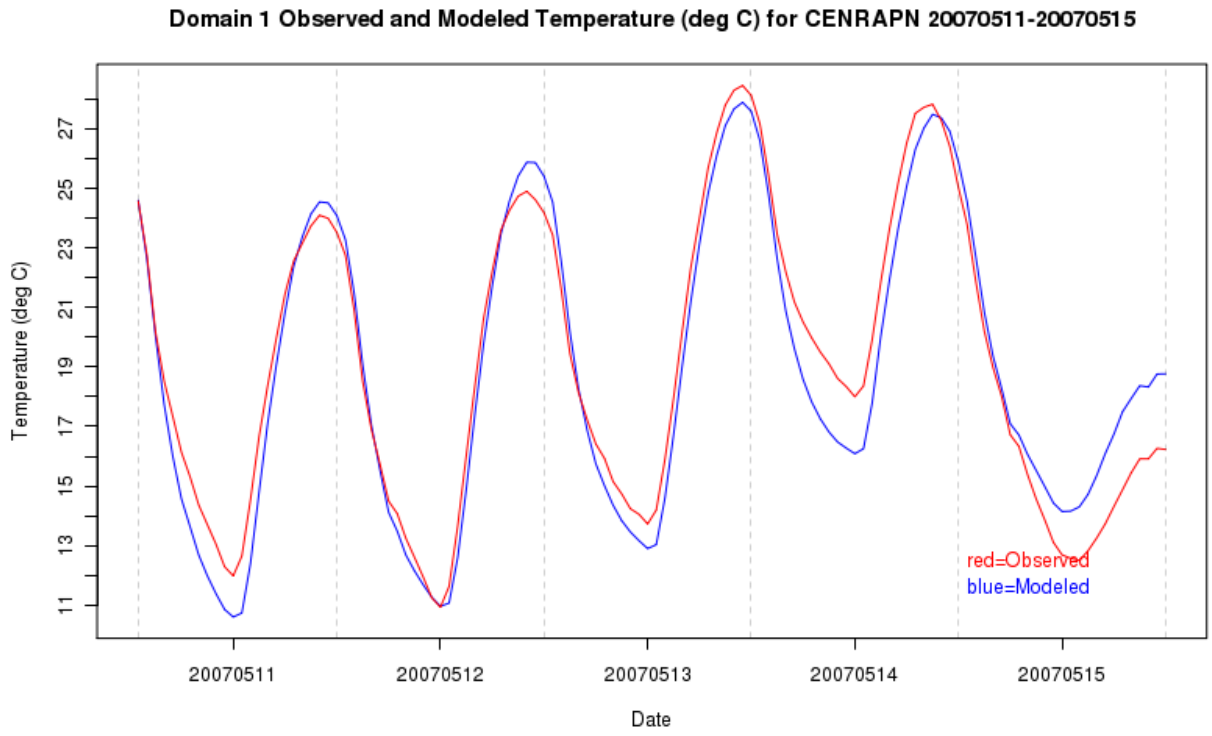

Figure 8-20. Timeseries of observed (red) and modeled (blue) temperature averaged across the CENRAPN region for the course domain from 2007/05/11 through 2007/05/15.

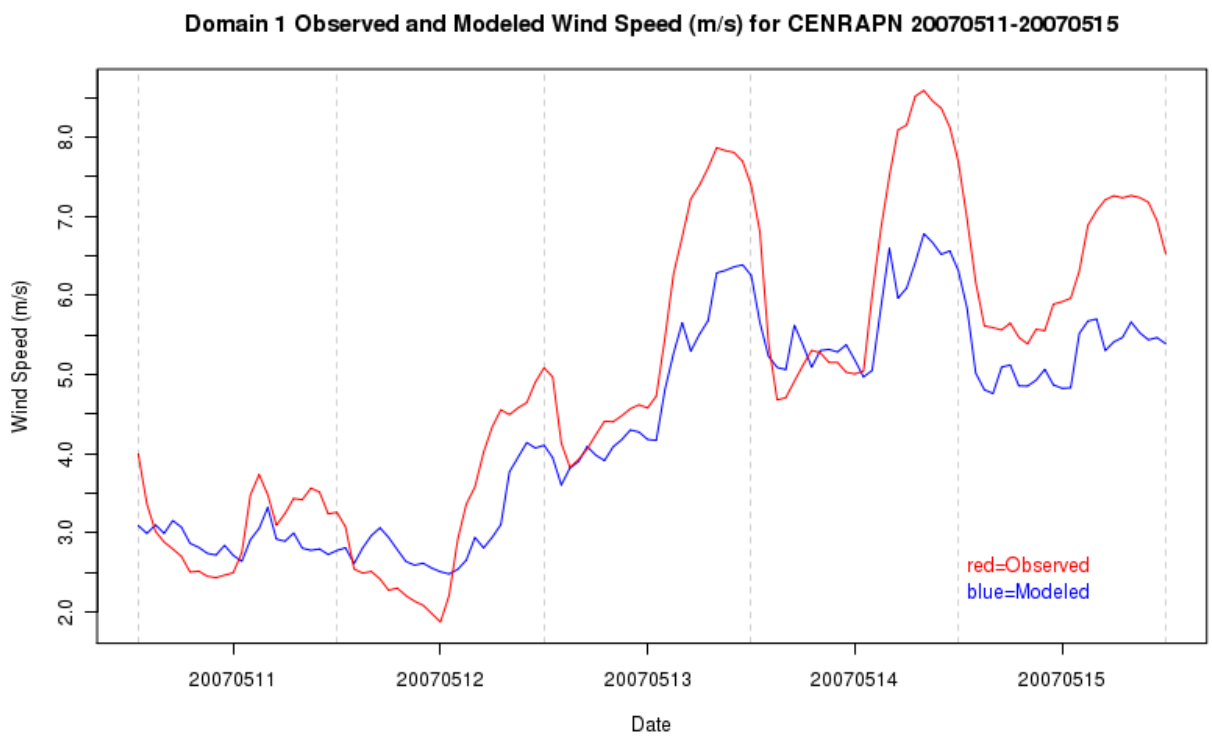

Figure 8-21. Timeseries of observed (red) and modeled (blue) wind speed averaged across the CENRAPN region for the course domain from 2007/05/11 through 2007/05/15.

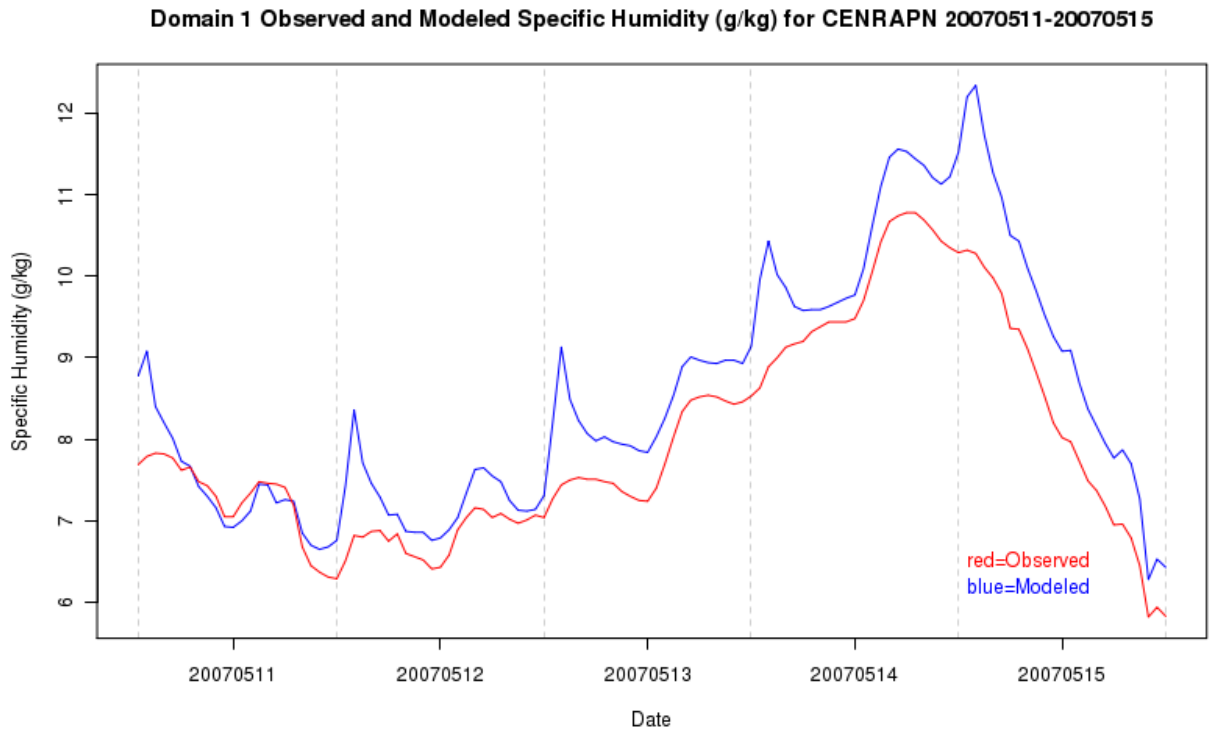

Figure 8-22. Timeseries of observed (red) and modeled (blue) specific humidity averaged across the CENRAPN region for the course domain from 2007/05/11 through 2007/05/15.

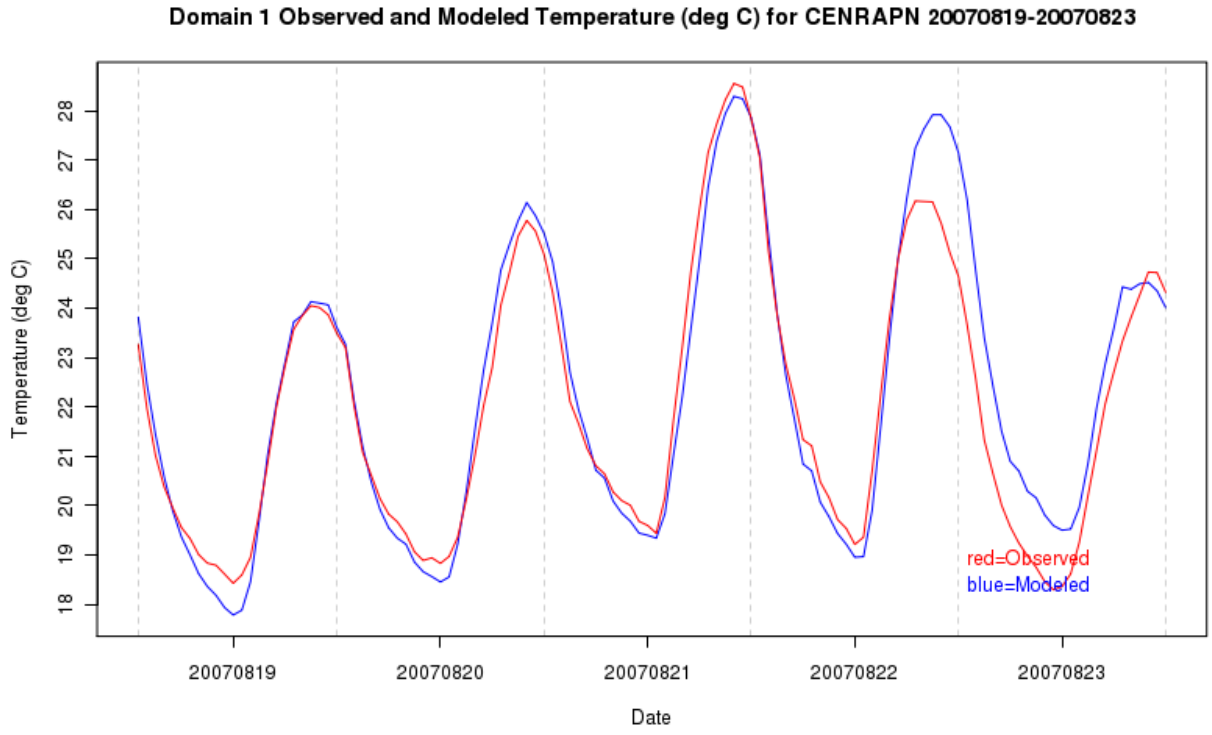

Figure 8-23. Timeseries of observed (red) and modeled (blue) temperature averaged across the CENRAPN region for the course domain from 2007/08/19 through 2007/08/23.

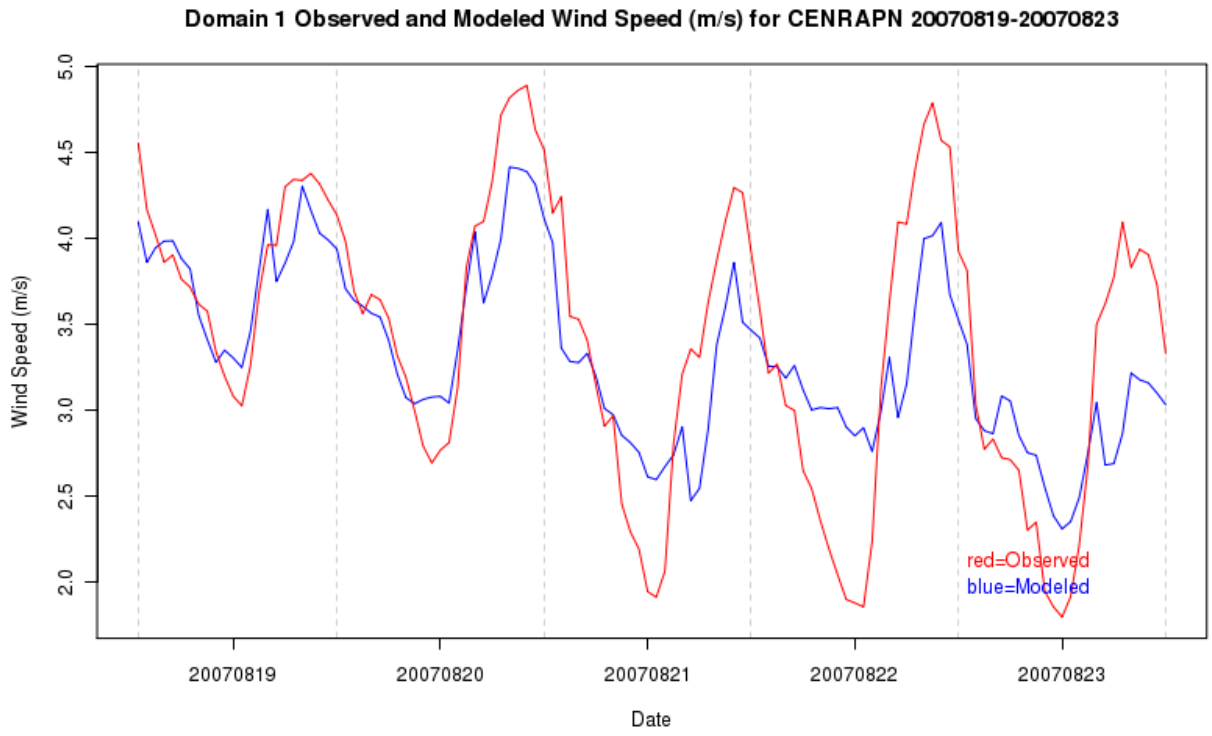

Figure 8-24. Timeseries of observed (red) and modeled (blue) wind speed averaged across the CENRAPN region for the course domain from 2007/08/19 through 2007/08/23.

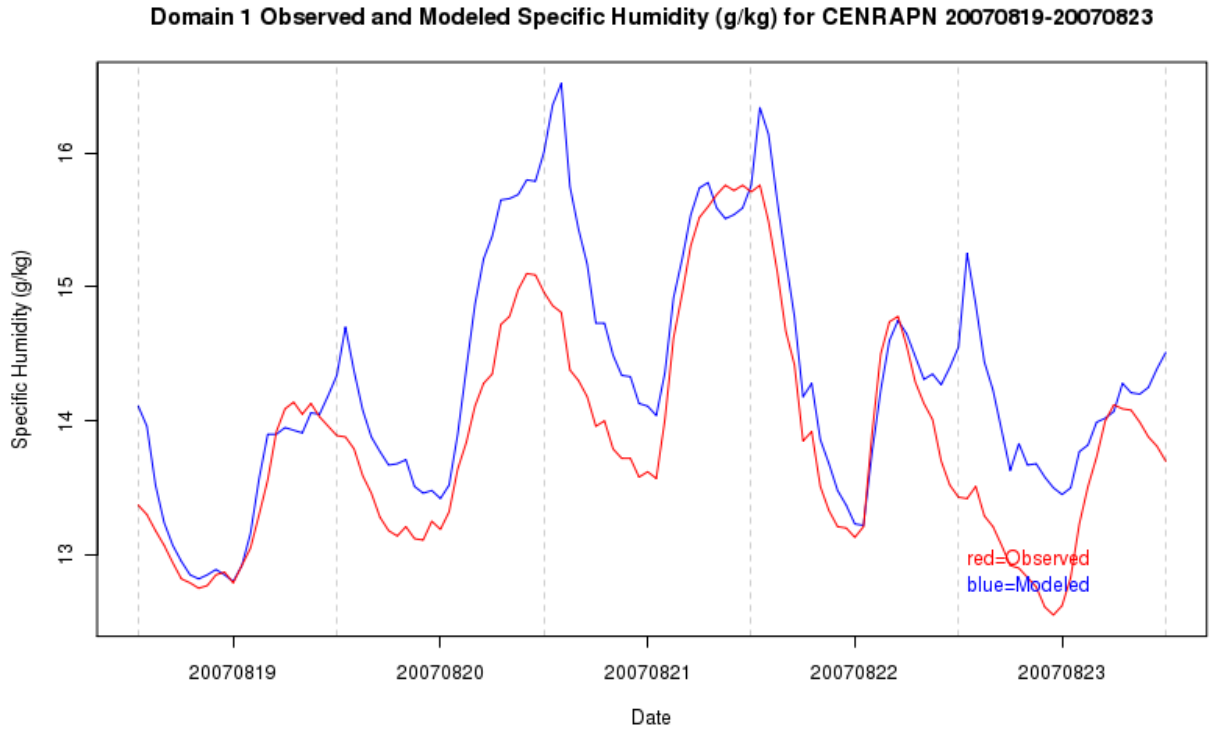

Figure 8-25. Timeseries of observed (red) and modeled (blue) specific humidity averaged across the CENRAPN region for the course domain from 2007/08/19 through 2007/08/23.

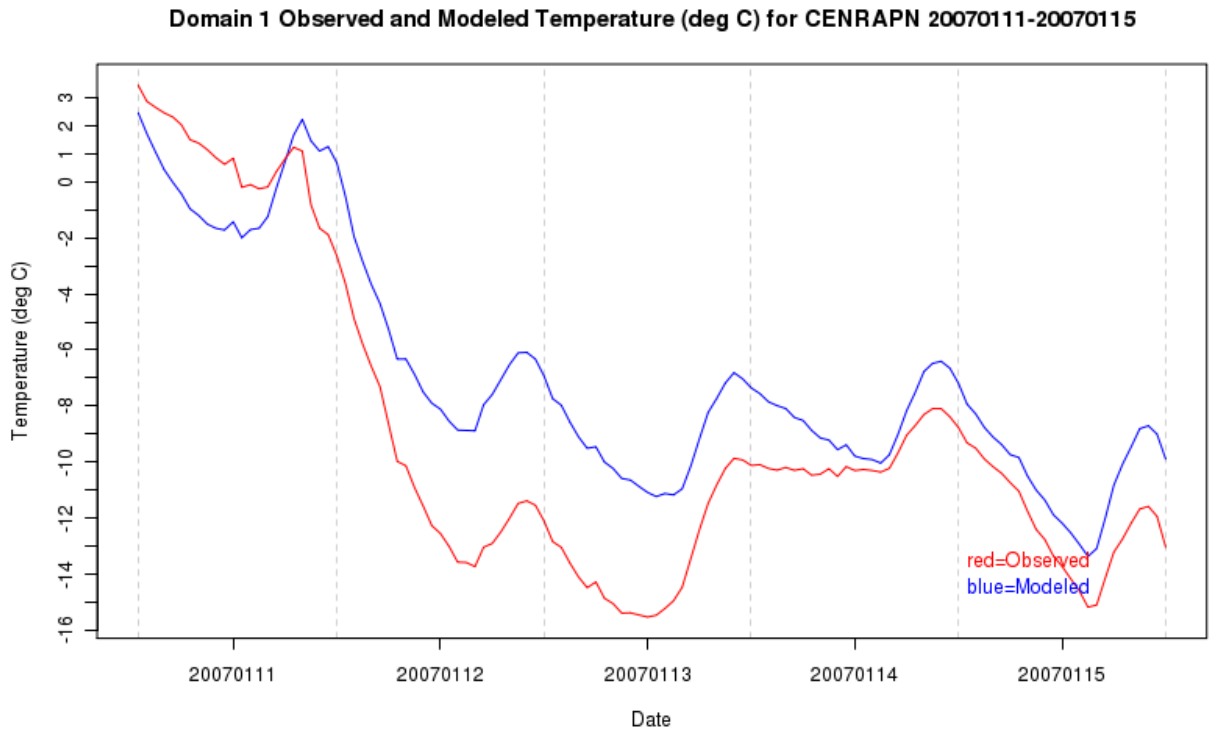

Figure 8-26. Timeseries of observed (red) and modeled (blue) temperature averaged across the CENRAPN region for the course domain from 2007/01/11 through 2007/01/15.

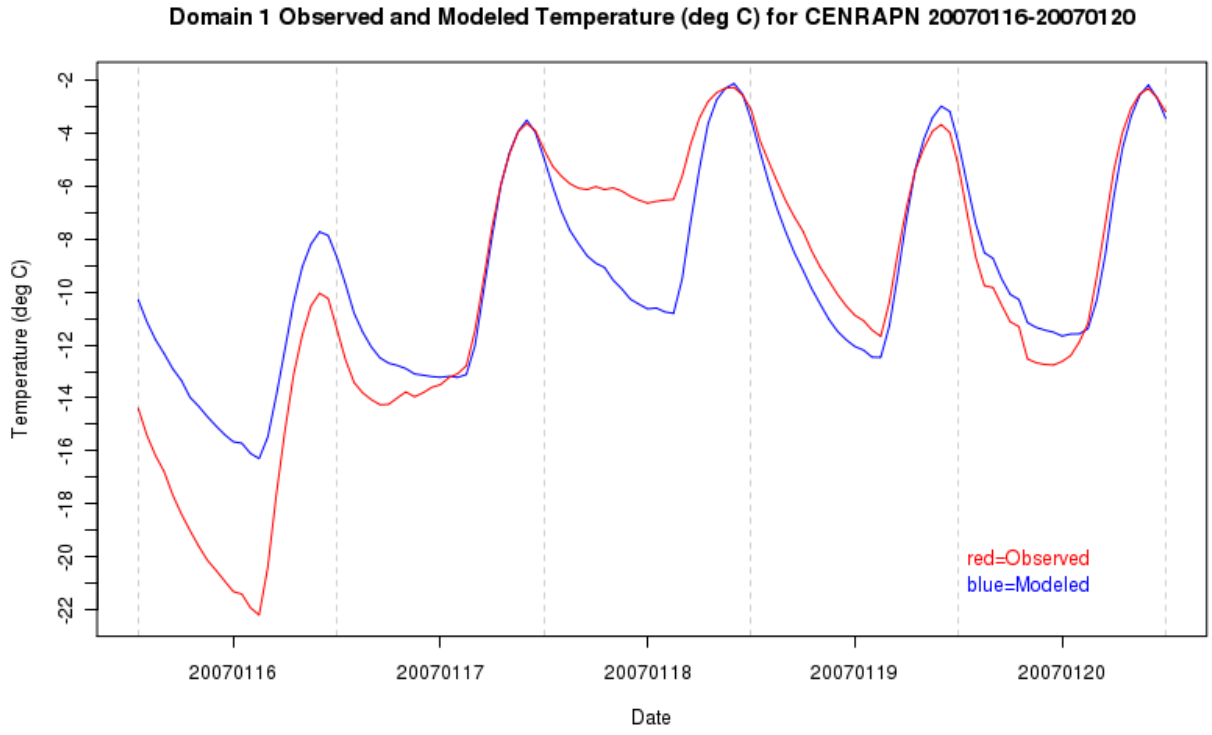

Figure 8-27. Timeseries of observed (red) and modeled (blue) temperature averaged across the CENRAPN region for the course domain from 2007/01/16 through 2007/01/20.

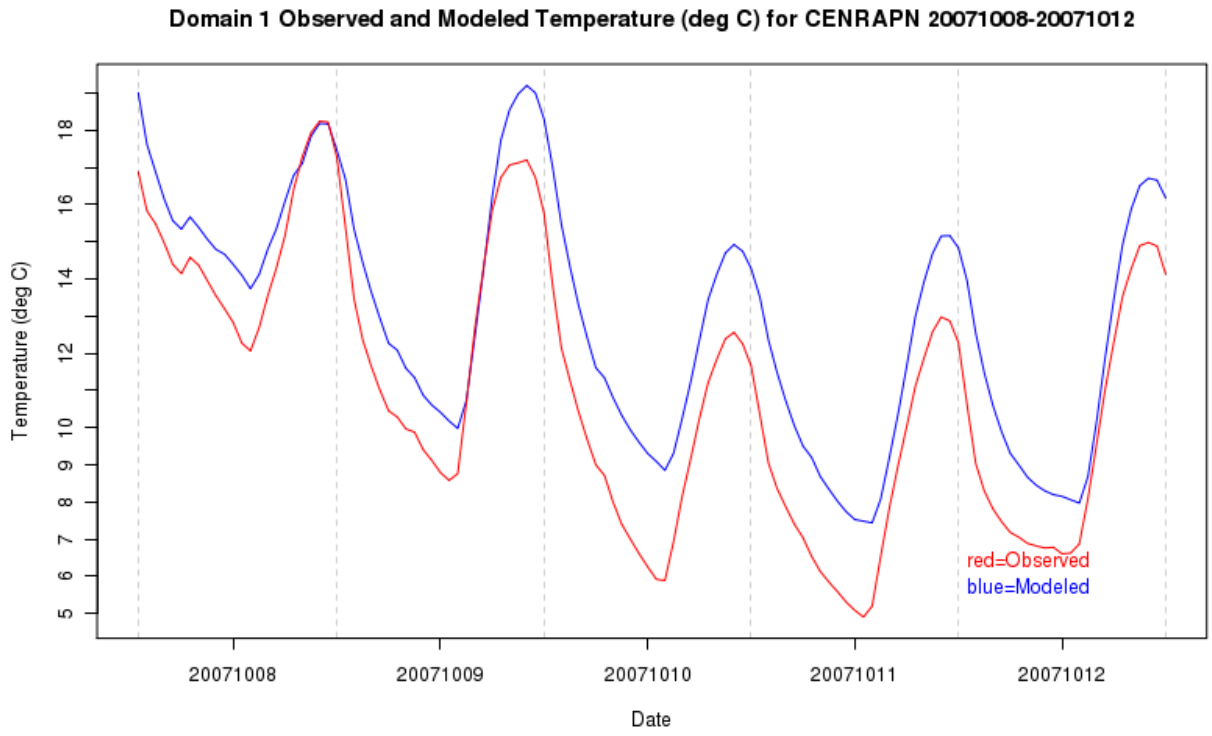

Figure 8-28. Timeseries of observed (red) and modeled (blue) temperature averaged across the CENRAPN region for the course domain from 2007/10/08 through 2007/10/12.

8.2.2 Nested Domain (12 km)

Figure 8-29 shows annual plots of the monthly performance statistics for all variables for the nested domain for the CENRAPN region. Temperature bias varies from -0.5 to 1.0 °C. A small under-prediction occurs in the spring and summer, while a significant over-prediction occurs in the fall and winter. Mean absolute error values range from 1.5 to 2.0 °C, with the best performance occurring in the summer. There is a slight over-prediction in specific humidity across the year. Bias values range from 0.0 to 0.5 g/kg. Mean absolute error ranges from 0.5 to 1.5 g/kg. The highest errors occur during the summer. Wind speed bias varies from -0.5 to 0.0 m/s. The slight under-prediction occurs during the spring and November. The remainder of the year is generally unbiased. Wind speed root mean square error is consistently near 2.0 m/s, but is highest in the spring.

Figure 8-30 shows similar monthly plots for the CENRAPS region in the nested domain. Temperature bias ranges from 0.0 to 1.0 °C. Temperature is over-predicted in the fall and winter. With the exception of April, the spring and summer are unbiased. Mean absolute error ranges from 1.5 to 2.5 °C, with the largest errors occurring in the winter. Specific humidity bias ranges from -0.5 to 0.25 g/kg. Bias values are nearly zero for all months, except for negative values near -0.5 g/kg for August and September. Mean absolute error ranges from 1.0 to 2.0 g/kg, with the highest error occurring in August. Wind speed is generally unbiased during the summer and fall, while a slight under-prediction exists in the winter and spring. Bias values range from -0.5 to 0.0 m/s. Root mean square error is consistently near 1.5 m/s across the entire year.

Figure 8-31 shows similar monthly plots for the MRPO region in the nested domain. Temperature bias varies from -0.75 to 0.5 °C. Temperature during the summer is nearly unbiased, while an over-prediction exists in the fall and winter, and under-prediction occurring in the spring. Mean absolute error ranges from 1.5 to 2.0 °C and is highest during the spring. A slight over-prediction of specific humidity occurs during most of the year. Bias values range from 0.0 to 0.5 g/kg. Mean absolute error ranges from 0.5 to 1.5 g/kg, with the largest errors occurring in the summer and fall. Wind speed bias values are near zero across the year, with a slight under-prediction during the winter and spring. Values range from -0.25 to 0.25 m/s. Root mean square error ranges from 1.75 to 2.0 m/s. The lowest errors occur during the summer.

Figure 8-32 shows an annual plot of daily temperature bias for the nested domain calculated for the CENRAPN region. Figure 8-33 shows a similar plot for daily temperature mean absolute error. Daily temperature performance is highly variable in all seasons except summer. There are several days of large negative and positive bias values. Less than half of the daily bias values in 2007 were within the benchmarks. The majority of daily mean absolute error values are below the respective benchmark. Nearly all values above the benchmark are within 1 °C of the 2 °C MAE goal (thus < 3 °C). Figure 8-34 shows an annual plot of daily wind speed bias for the nested domain for the CENRAPN region. Figure 8-35 shows a similar plot for wind speed mean absolute error. Over 90% of daily wind speed bias values are with the benchmarks. Of the days not within the benchmarks, most occur during the spring. For mean absolute error, all but two daily values are within the respective benchmark.

Figure 8-36 shows a bubble plot of temperature bias for June for the nested domain model output. Figure 8-37 shows a similar plot of temperature mean absolute error. During the summer temperature performance is best over the Midwest, but is good over most of the domain. Observation locations with poor performance exist along the Great Lakes and Atlantic coast. This suggests small scale land/sea breeze phenomena common near land/sea interfaces are not being properly resolved at the 12km grid scale. Figure 8-38 shows a bubble plot of temperature bias for December for the nested domain model output. Figure 8-39 shows a similar plot of temperature mean absolute error for December. During the winter temperature performance is best over the states of Michigan, Indiana, Ohio, Pennsylvania, New York, and New Jersey. Figure 8-40 shows a bubble plot of specific humidity bias for June for the nested domain. Figure 8-41 shows a similar plot of specific humidity mean absolute error. Humidity performance is best over the Midwest and Northeast, though performance is adequate over most of the domain.

Figure 8-42 shows a bubble plot of specific humidity bias for December for the nested domain. Figure 8-43 shows a similar plot of specific humidity mean absolute error for December. During the winter humidity performance appears best over the Midwest and Northern Plains, while being generally weaker over the southern half of the U.S, though actual humidity values are much lower over the northern half of the U.S., thus reducing the range of possible values. Figure 8-44 shows a bubble plot of wind speed bias for June for the nested domain model output. Figure 8-45 shows a similar plot for wind speed mean absolute error. In the summer wind speed performance is very good across the entire domain. No geographic region stands out. Figure 8-46 shows a bubble plot of wind speed bias for December for the nested domain. Figure 8-47

shows a similar plot for wind speed mean absolute error. Similar to temperature, wind speed performance is very good across the entire domain in these spatial analyses.

Figure 8-48 through Figure 8-53 show timeseries of observed and modeled temperature, wind speed, and humidity averaged across the CENRAPN region. The two sample time periods, May 11-15 and August 19-23, are the same as the timeseries for the course domain. The model results are very similar to those for the course domain. Modeled temperature reproduced the diurnal variations in temperature reasonably well. Daily minimums were frequently underpredicted slightly. Daily maximums were occasionally overpredicted and underpredicted. Modeled wind speed did not reproduce all the diurnal variation in the observations. Daily maximum wind speeds were frequently underpredicted. Daily minimum wind speeds were frequently overpredicted. Daily peaks in specific humidity are frequently overpredicted.

Figure 8-54 and Figure 8-55 show timeseries of observed and modeled temperature averaged across the CENRAPN region from January 11-20, when temperature performance was poor. From January 12-17 daily temperature bias ranged from 0.7 to 3.0 K. Similar to the results from the course domain, modeled temperature was consistently too high across this entire period. On January 18 and 19 when large negative bias was reported the timeseries shows a significant underprediction of nighttime minimum temperatures. Figure 8-56 shows a timeseries of observed and modeled temperature averaged across the CENRAPN region from October 8-12. During this time daily temperature bias values ranged from 0.8 to 2.6 K. Again, the timeseries shows that modeled temperature was consistently too high across the entire period.

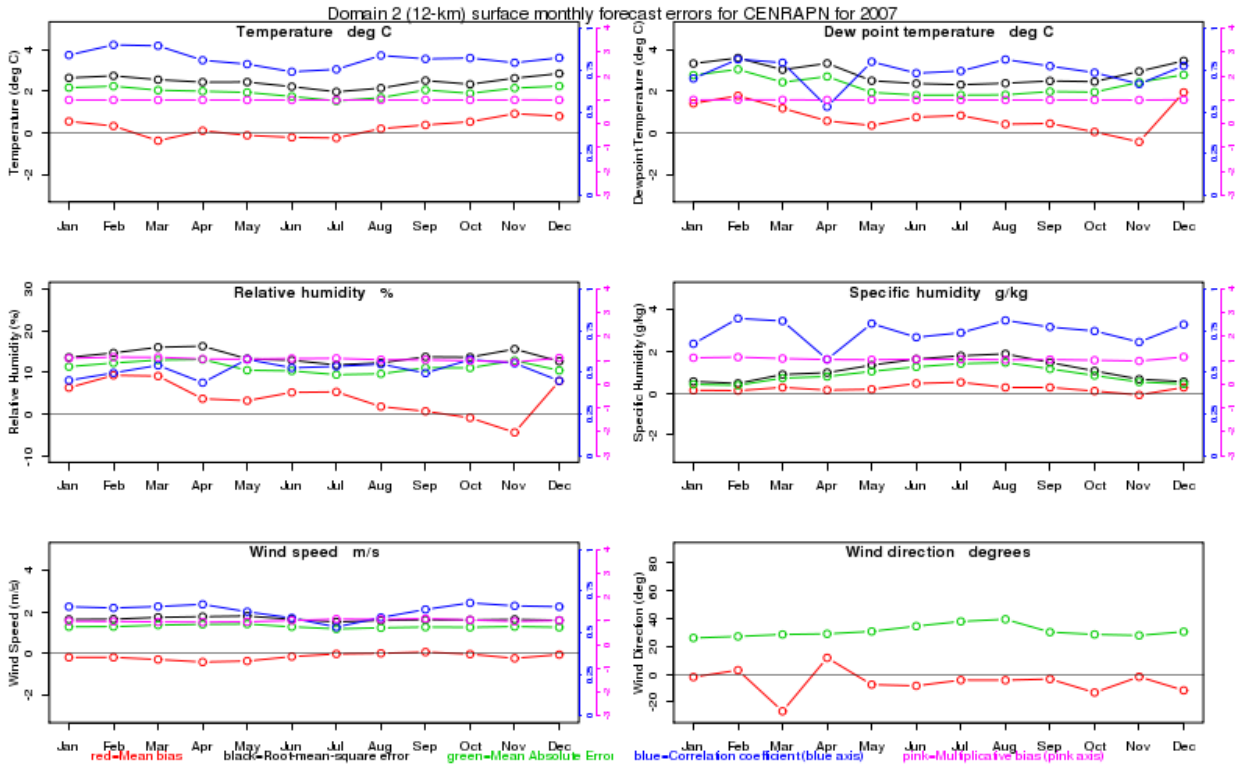

Figure 8-29. Monthly surface statistics for the nested domain for the CENRAPN region.

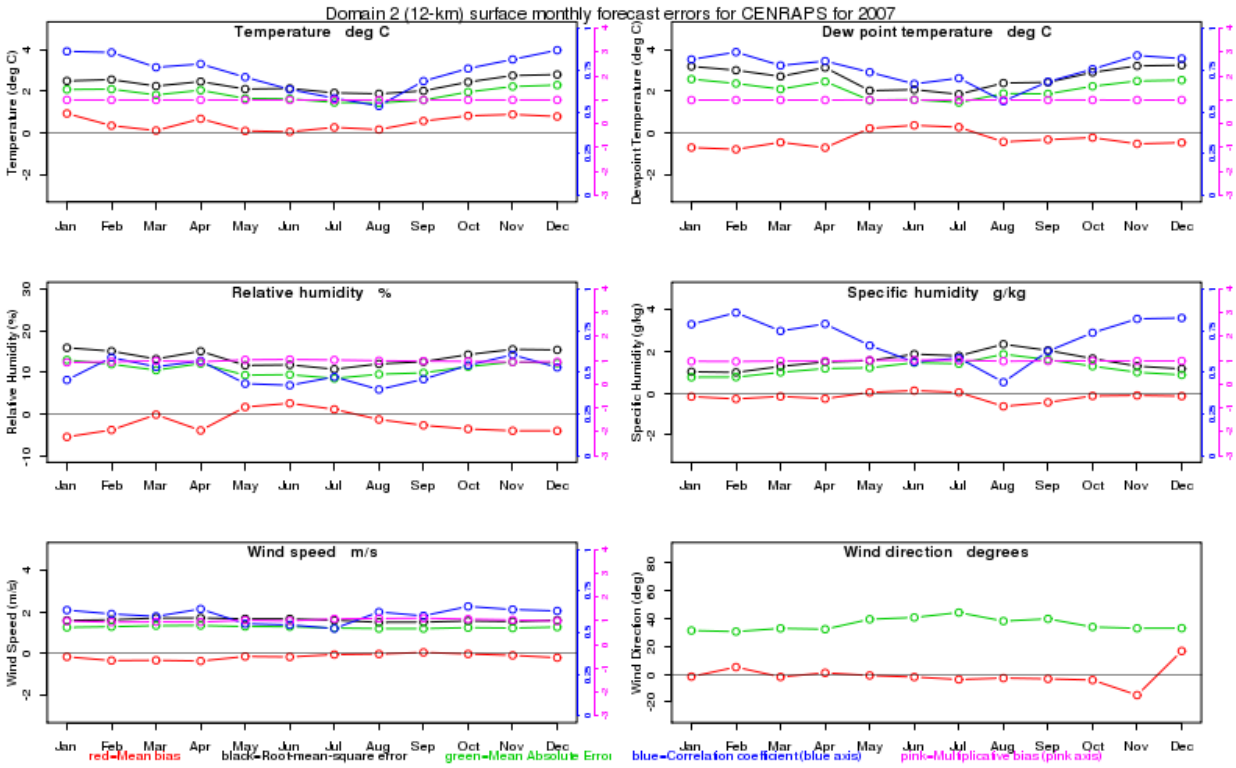

Figure 8-30. Monthly surface statistics for the nested domain for the CENRAPS region.

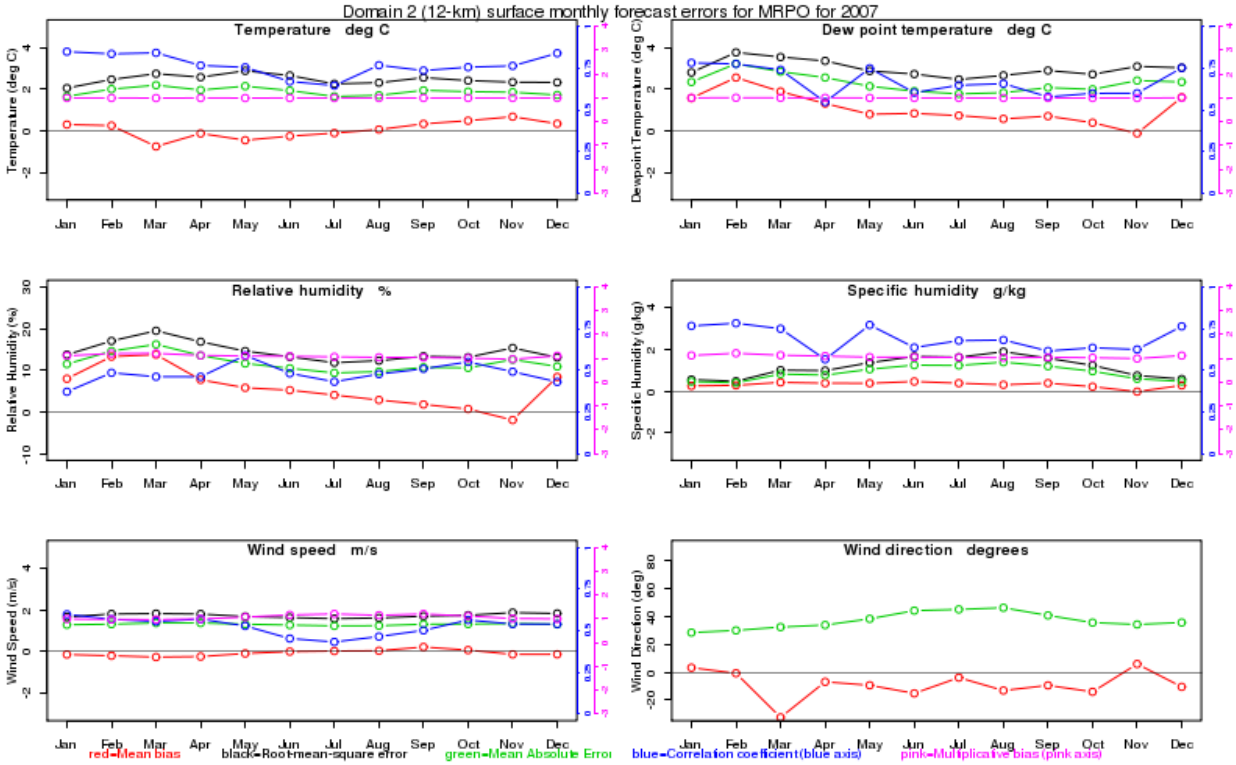

Figure 8-31. Monthly surface statistics for the nested domain for the MRPO region.

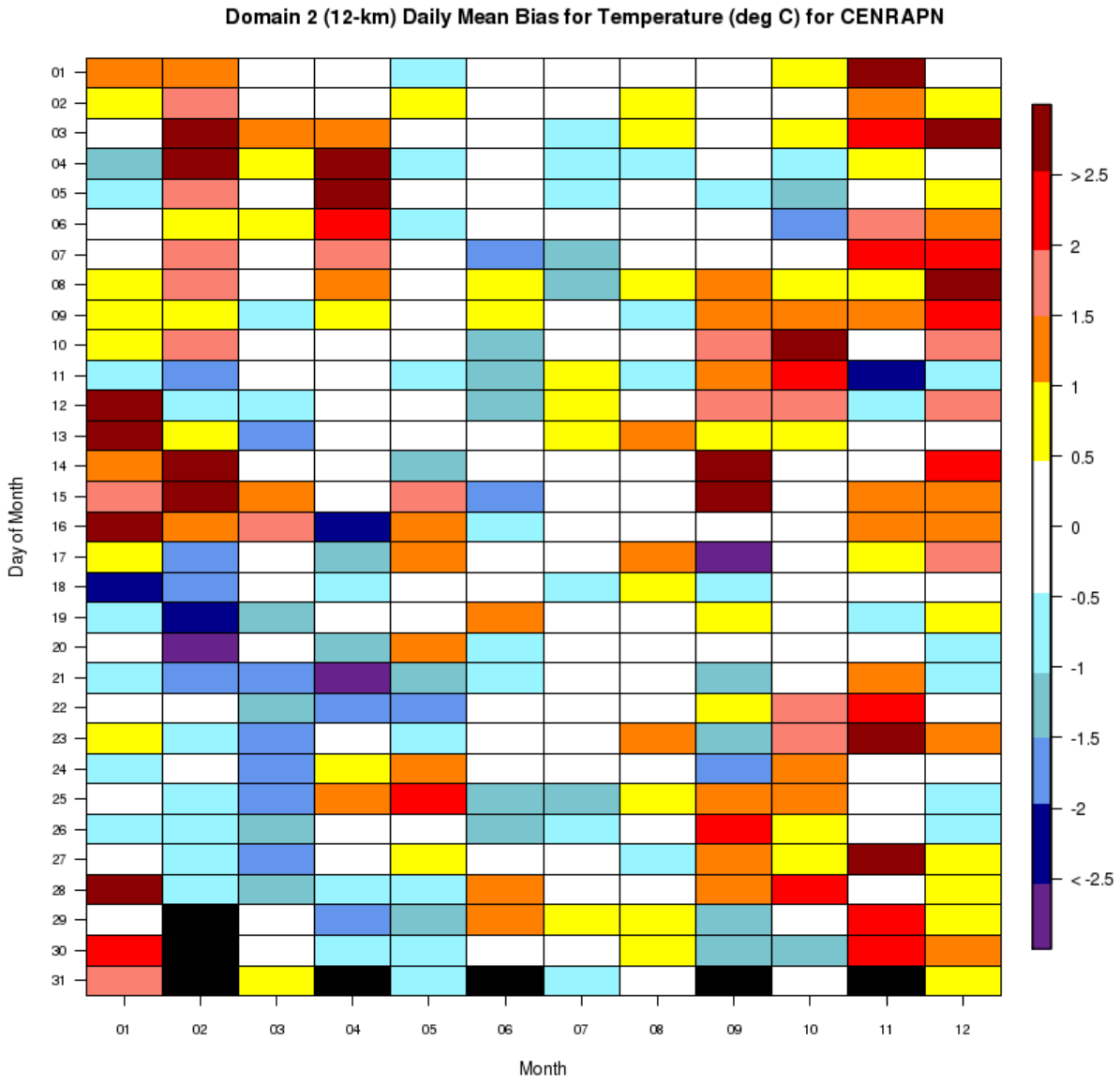

Figure 8-32. Bakergram showing daily temperature bias for the nested domain for the CENRAPN region.

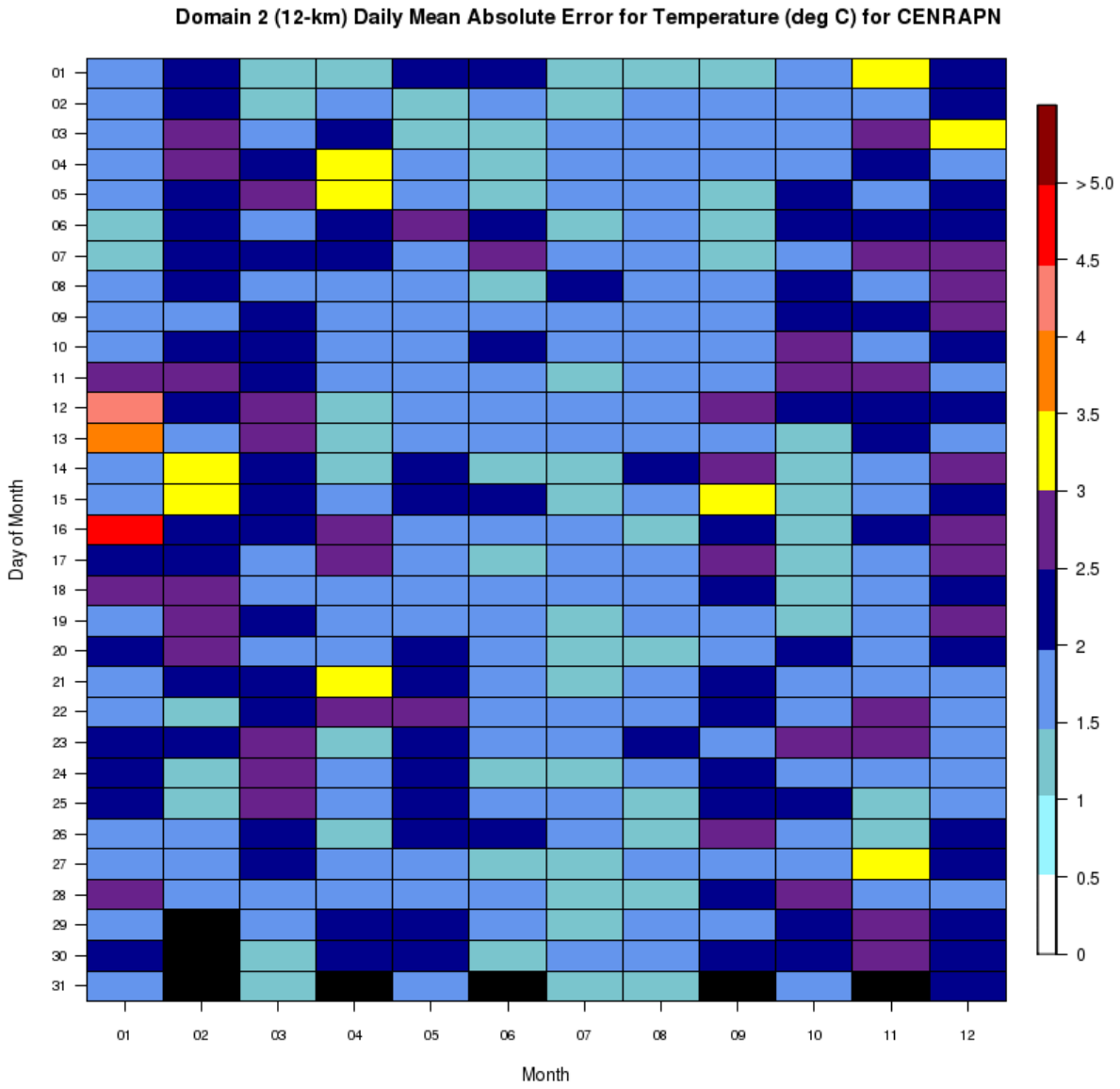

Figure 8-33. Bakergram showing daily temperature mean absolute error for the nested domain for the CENRAPN region.

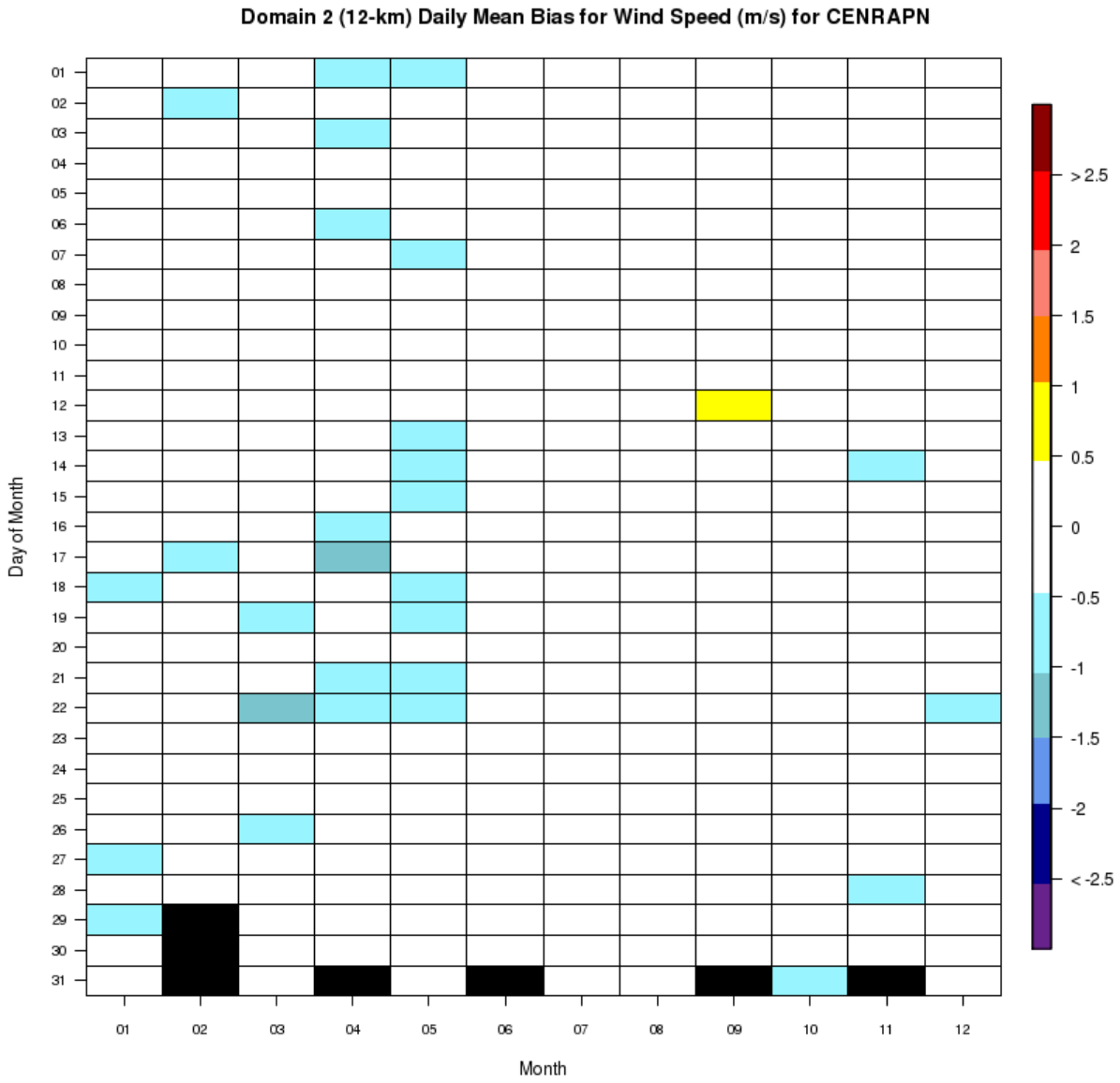

Figure 8-34. Bakergram showing daily wind speed bias for the nested domain for the CENRAPN region.

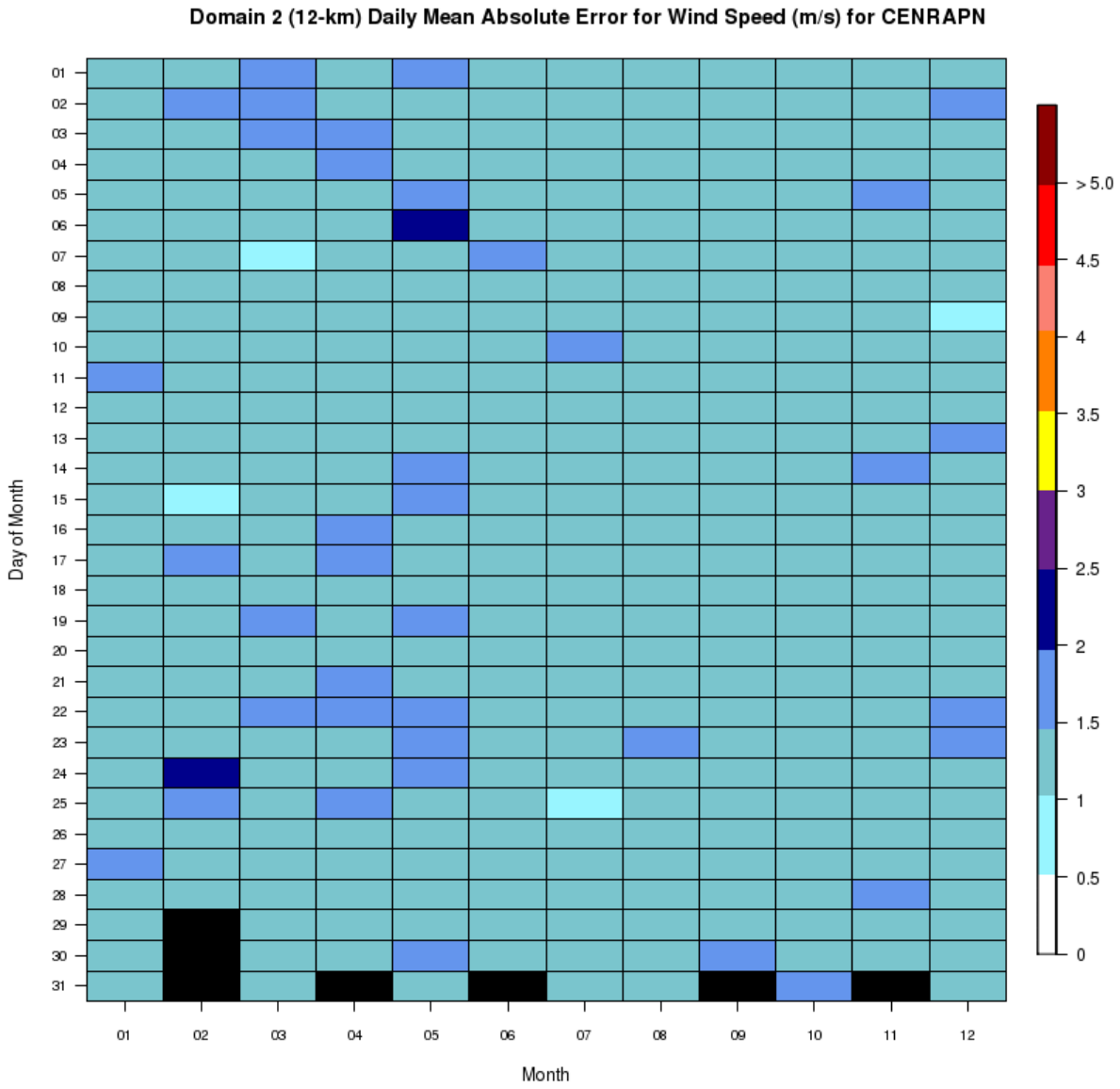

Figure 8-35. Bakergram showing daily wind speed mean absolute error for the nested domain for the CENRAPN region.

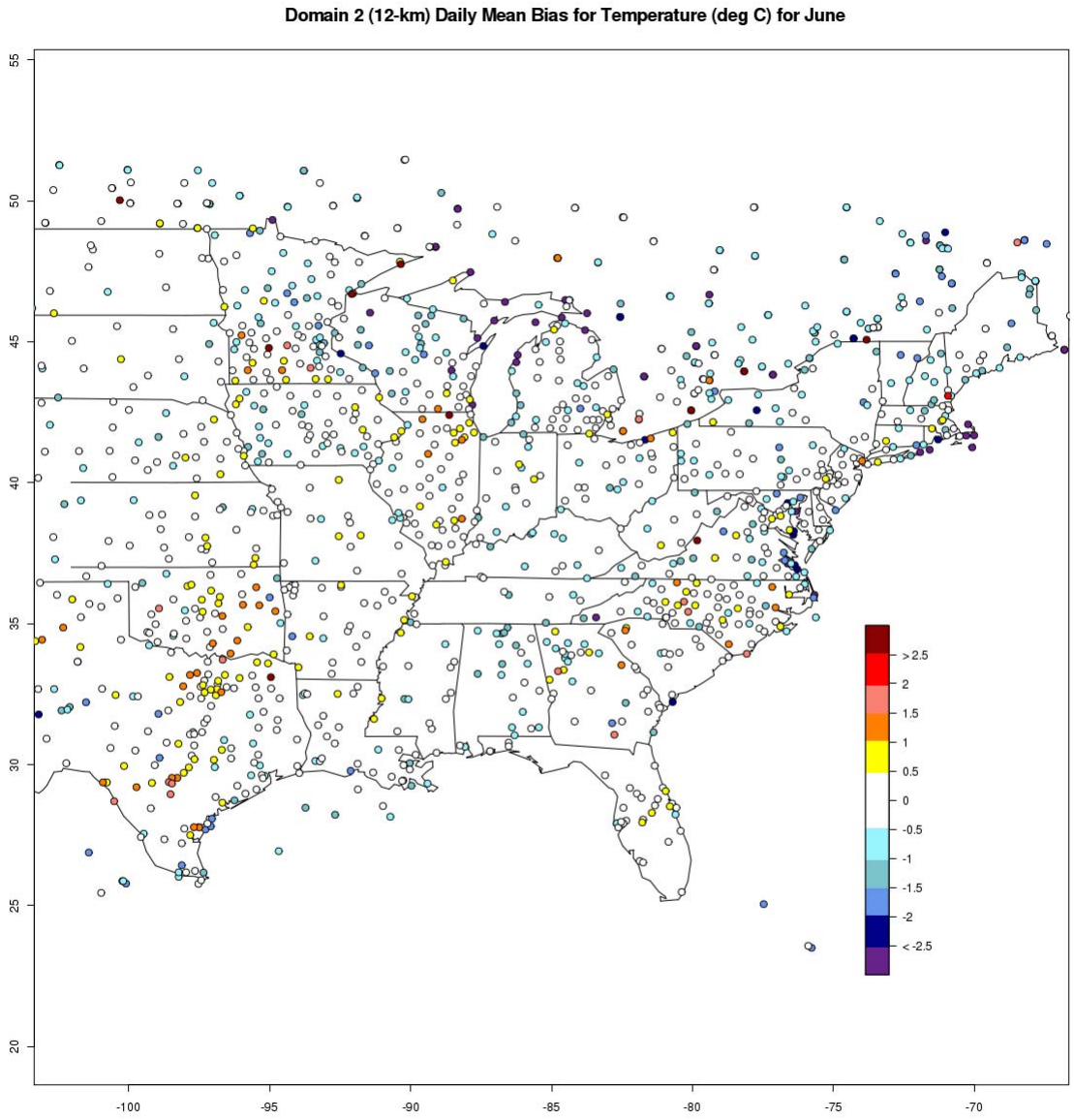

Figure 8-36. Spatial bubble plot of monthly temperature bias at individual observation locations for the nested domain for June.

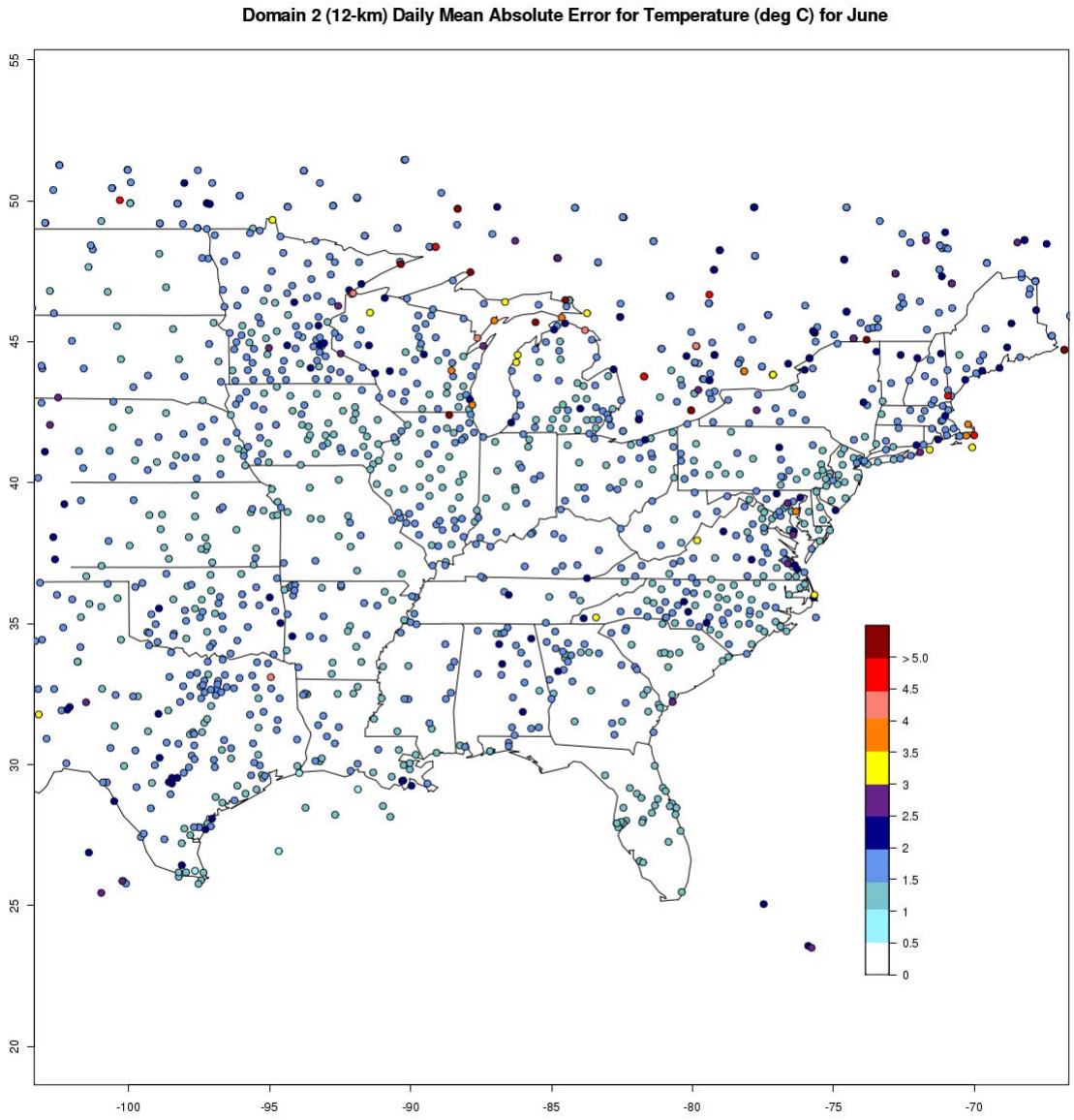

Figure 8-37. Spatial bubble plot of monthly temperature mean absolute error at individual observation locations for the nested domain for June.

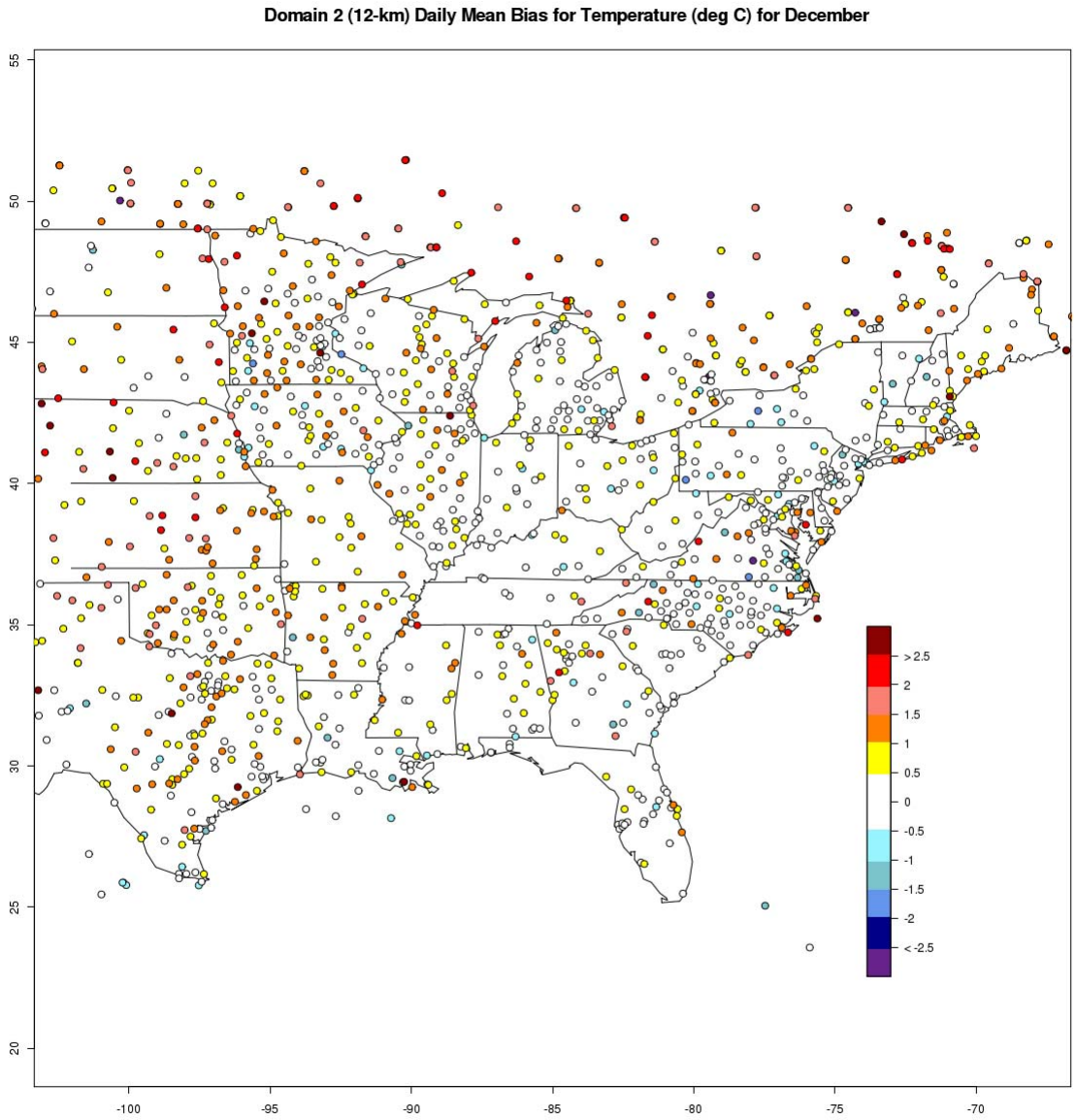

Figure 8-38. Spatial bubble plot of monthly temperature bias at individual observation locations for the nested domain for December.

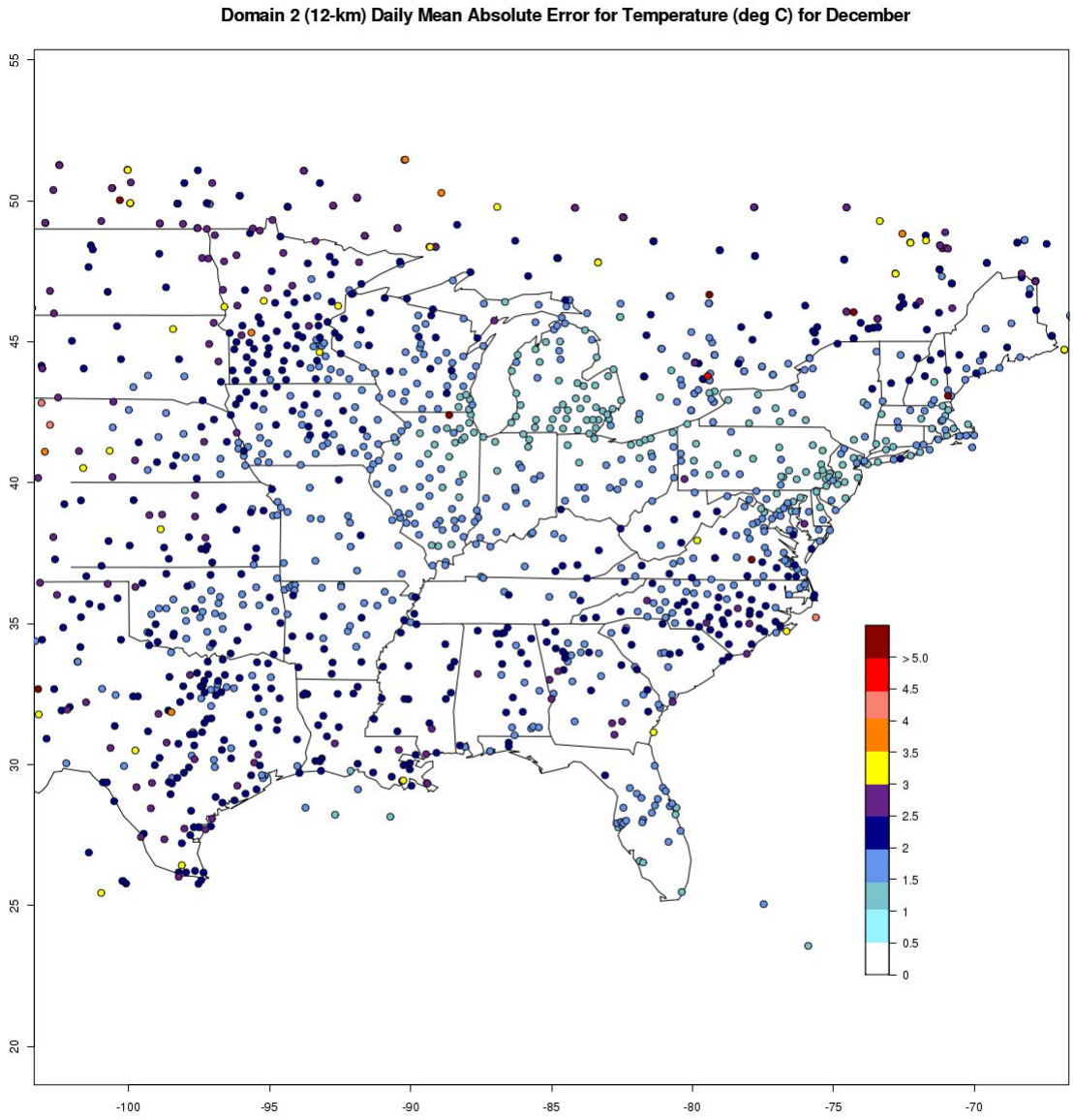

Figure 8-39. Spatial bubble plot of monthly temperature mean absolute error at individual observation locations for the nested domain for December.

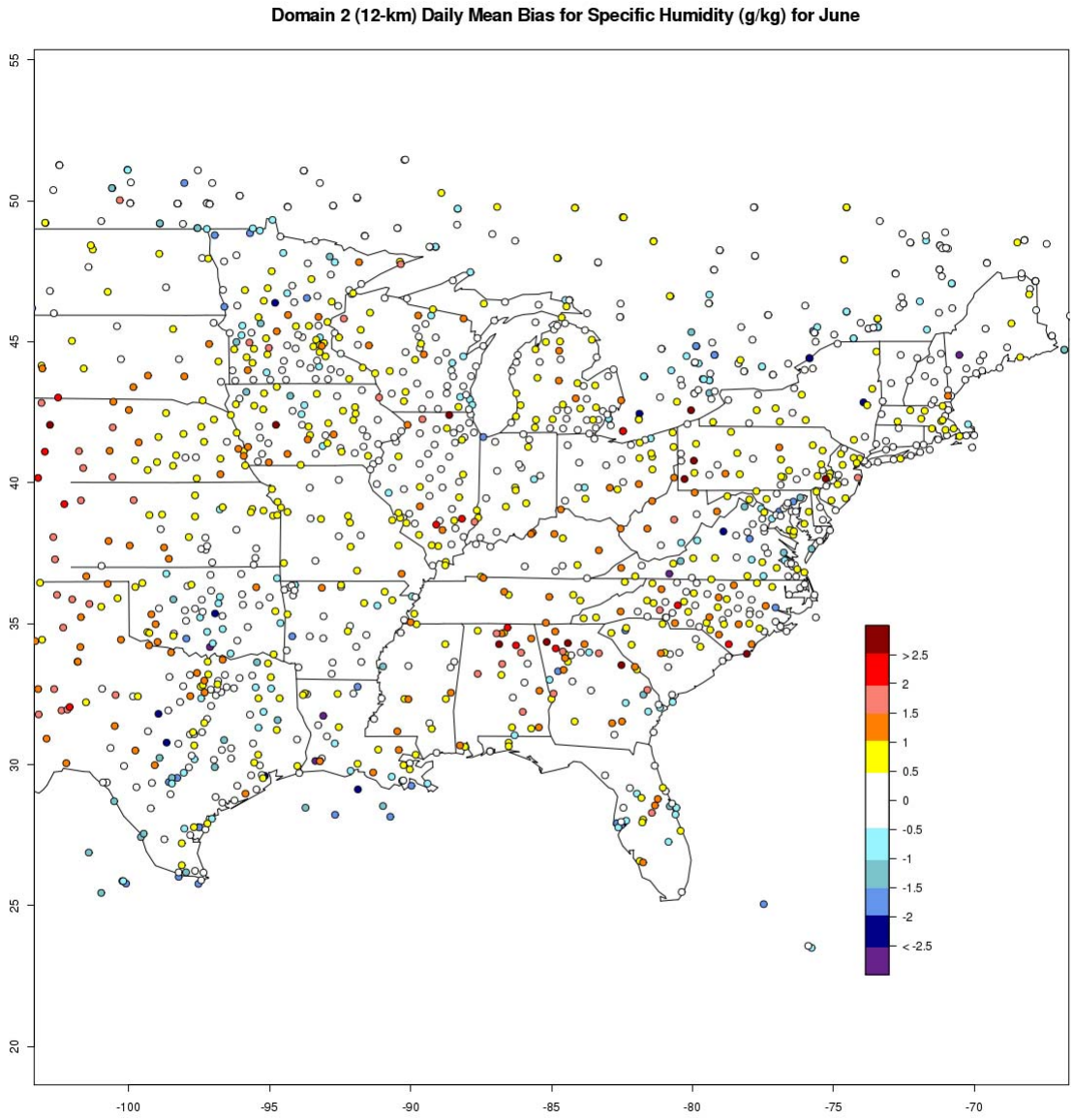

Figure 8-40. Spatial bubble plot of monthly specific humidity bias at individual observation locations for the nested domain for June.

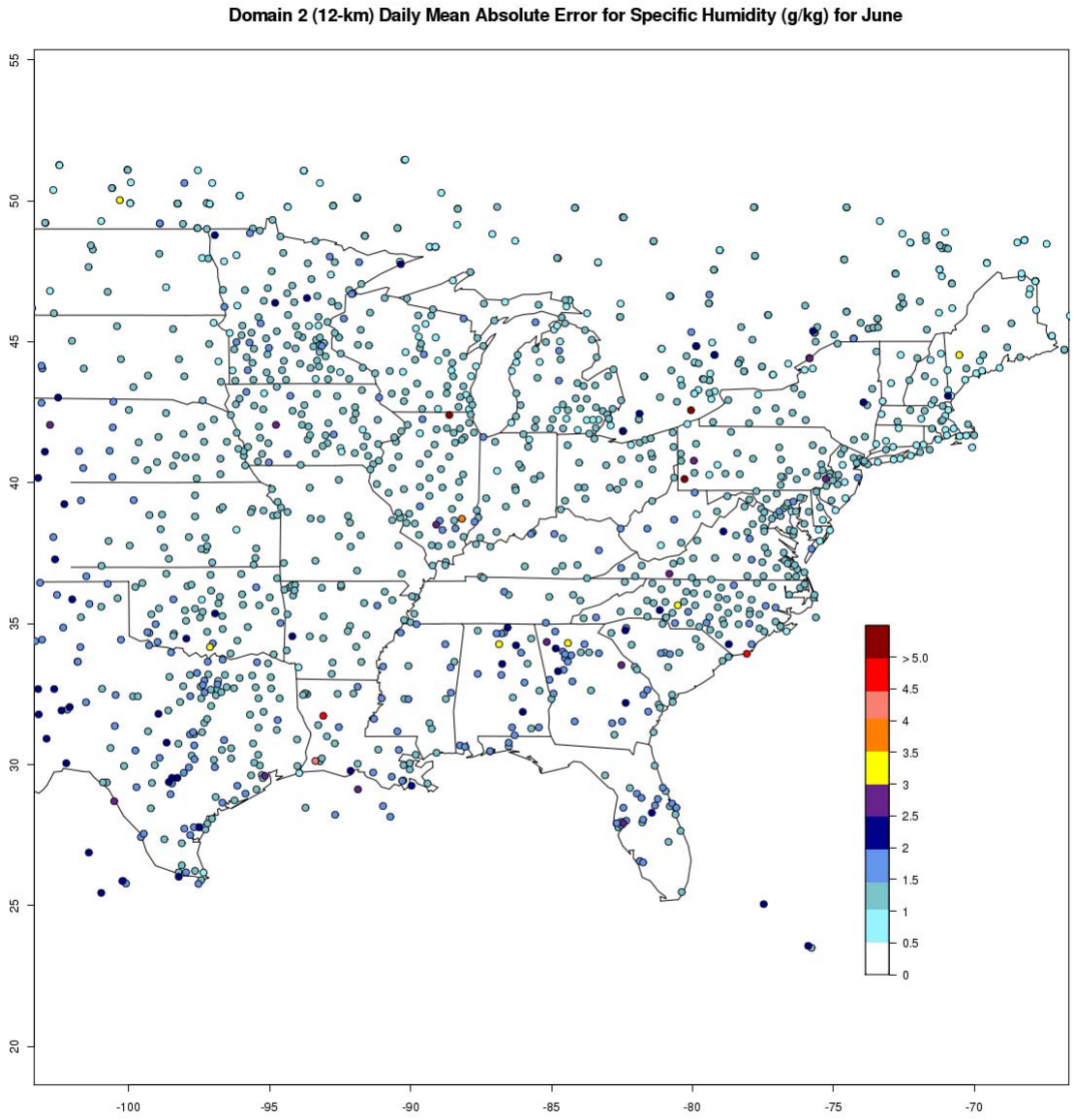

Figure 8-41. Spatial bubble plot of monthly specific humidity mean absolute error at individual observation locations for the nested domain for June.

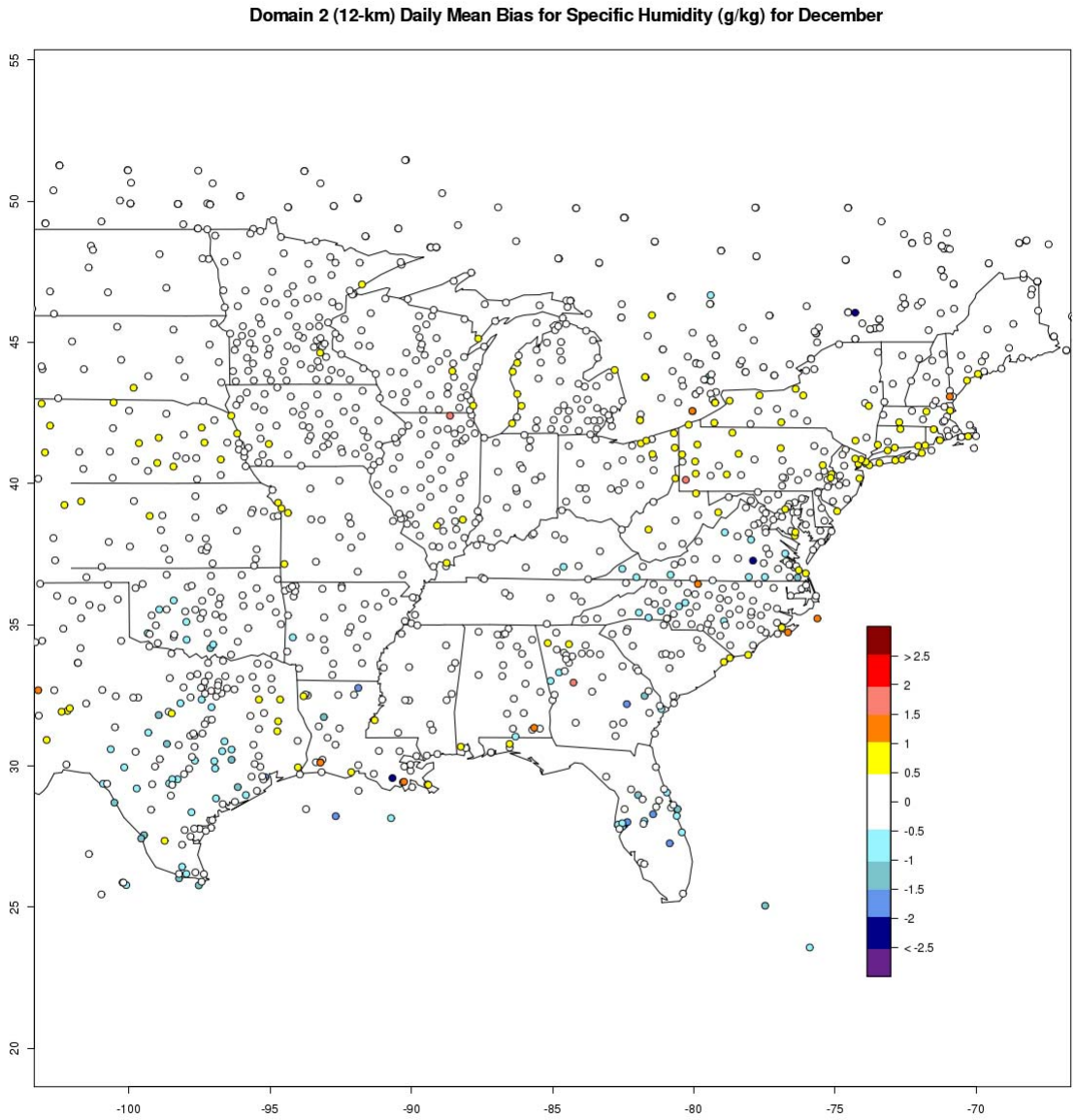

Figure 8-42. Spatial bubble plot of monthly specific humidity bias at individual observation locations for the nested domain for December.

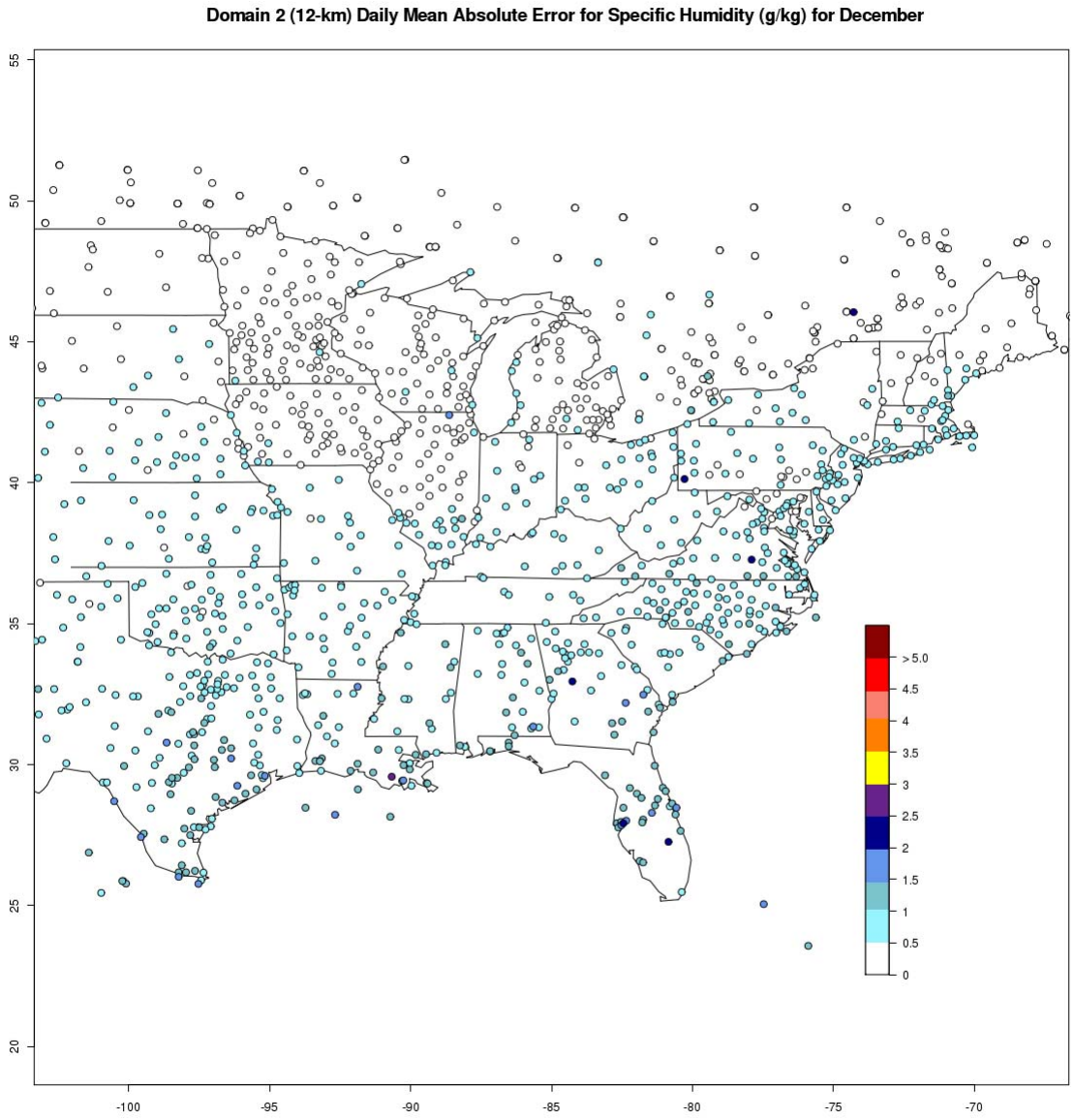

Figure 8-43. Spatial bubble plot of monthly specific humidity mean absolute error at individual observation locations for the nested domain for December.

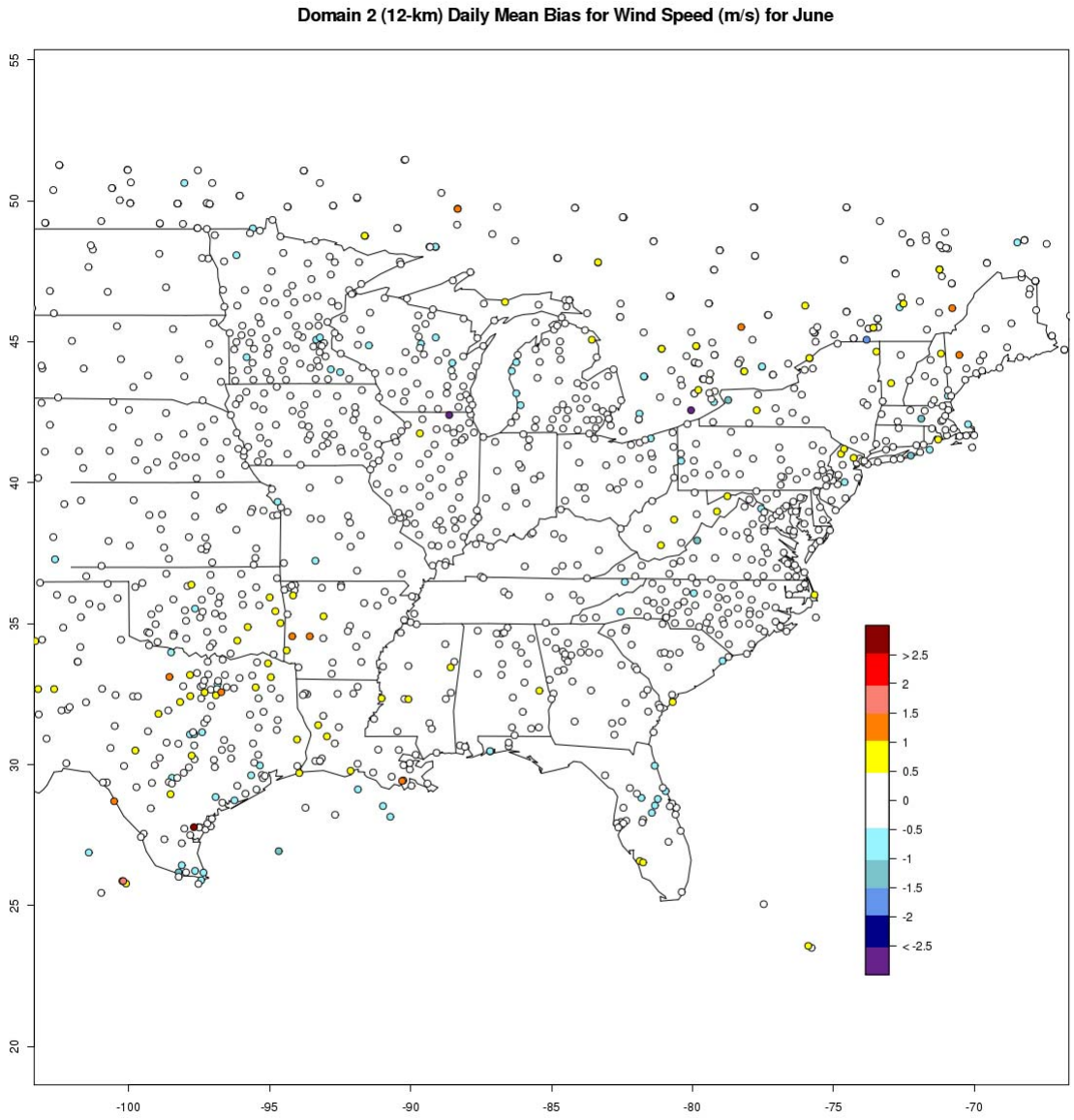

Figure 8-44. Spatial bubble plot of monthly wind speed bias at individual observation locations for the nested domain for June.

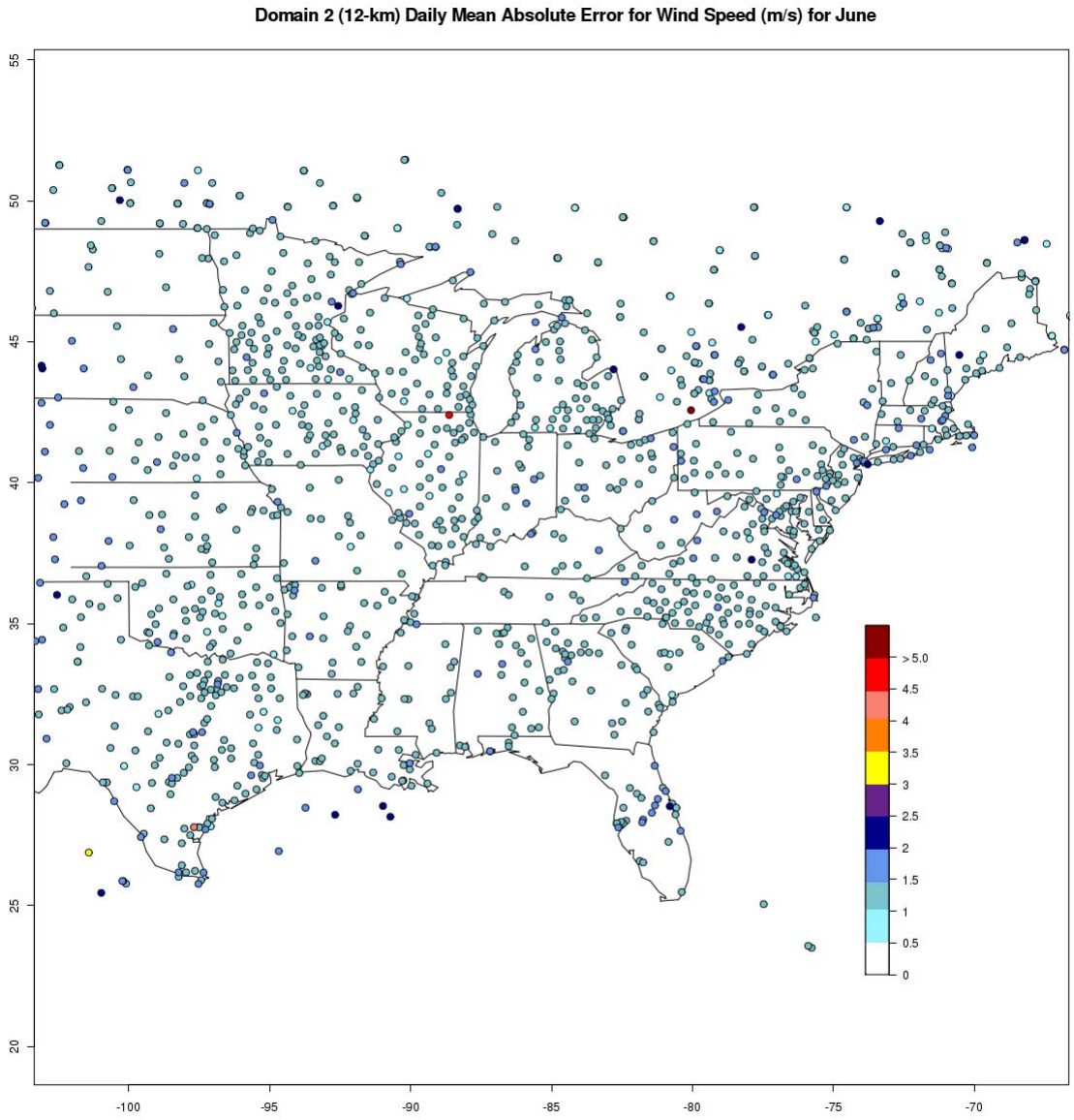

Figure 8-45. Spatial bubble plot of monthly wind speed mean absolute error at individual observation locations for the nested domain for June.

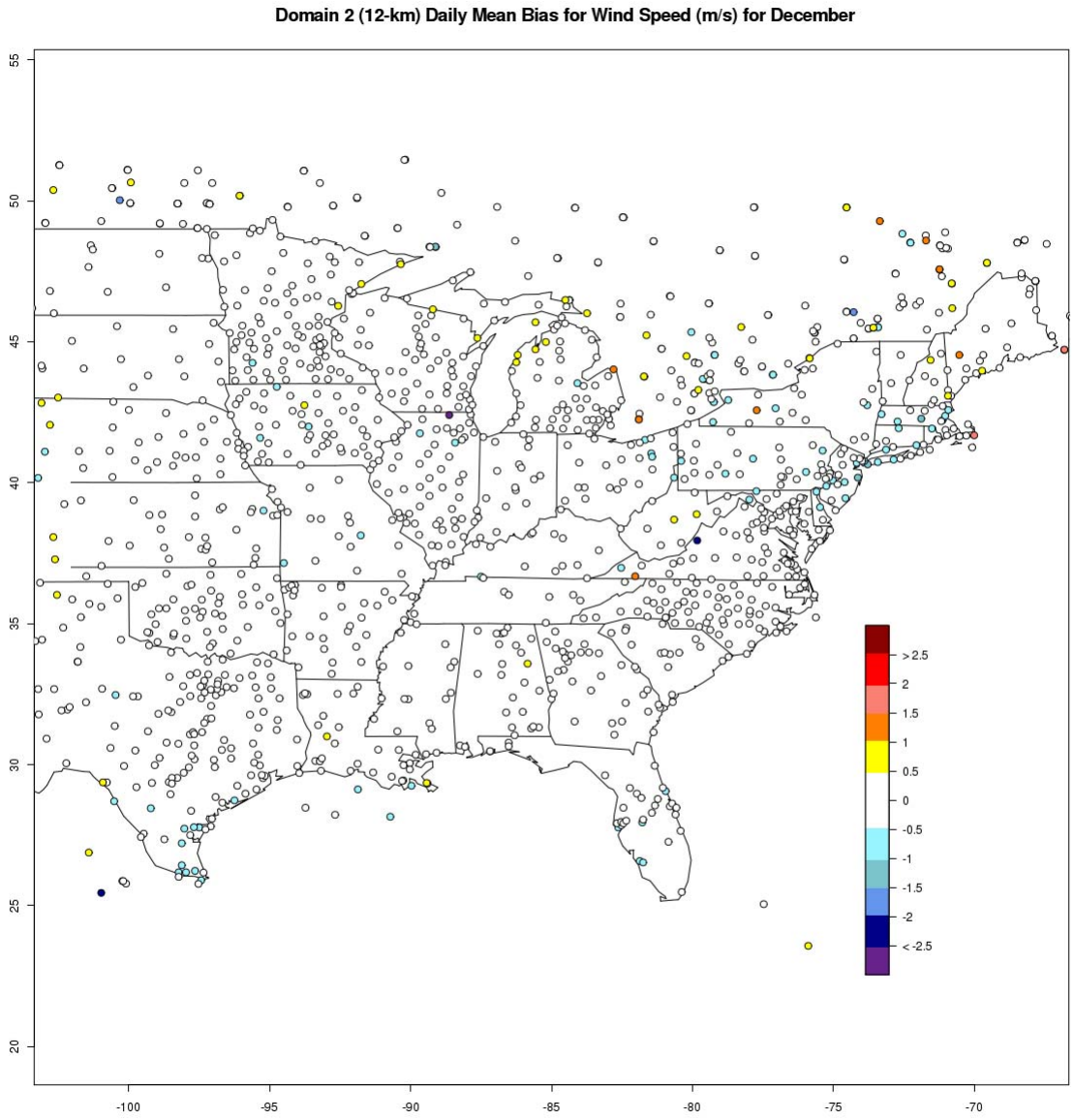

Figure 8-46. Spatial bubble plot of monthly wind speed bias at individual observation locations for the nested domain for December.

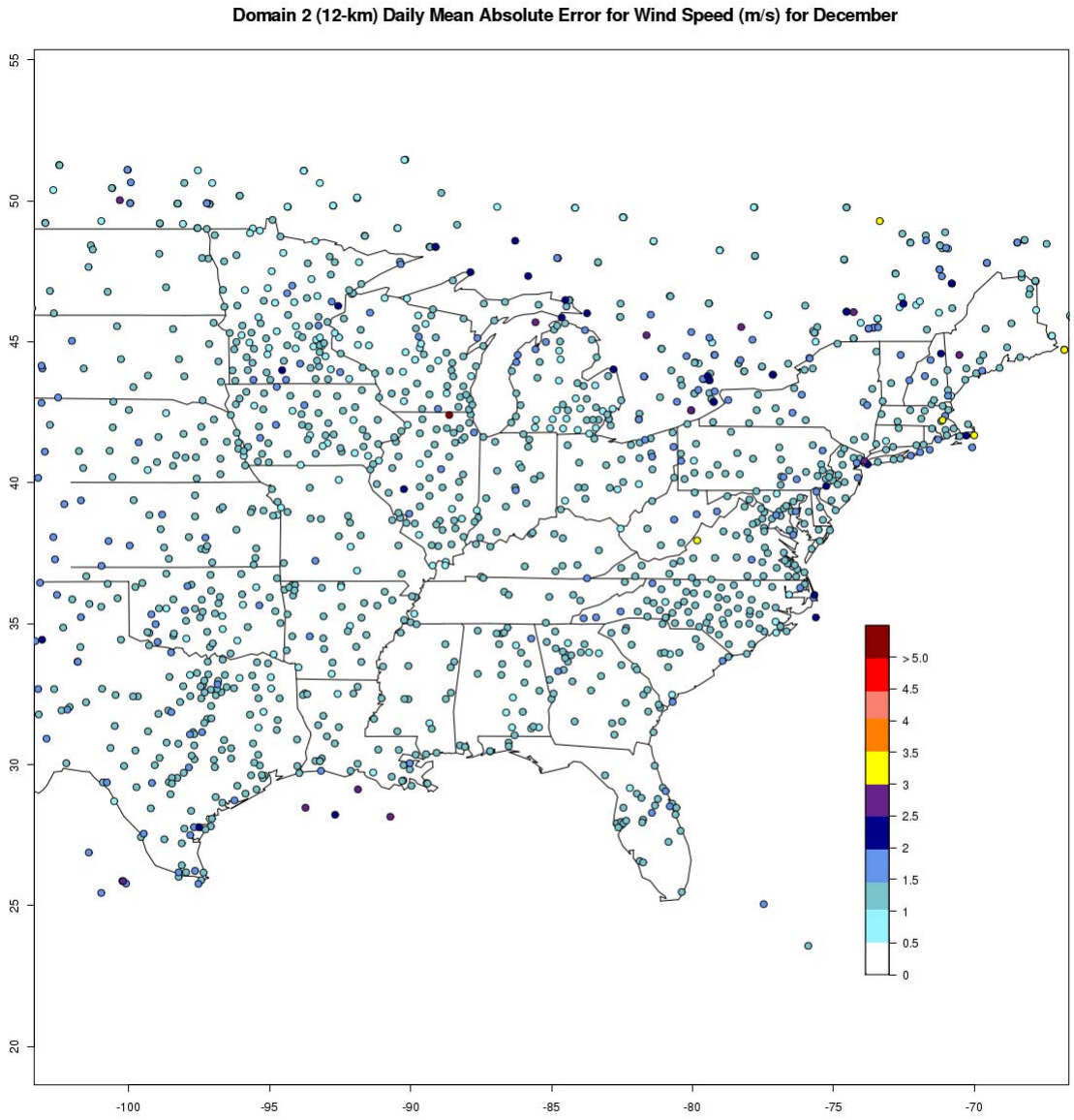

Figure 8-47. Spatial bubble plot of monthly wind speed mean absolute error at individual observation locations for the nested domain for December.

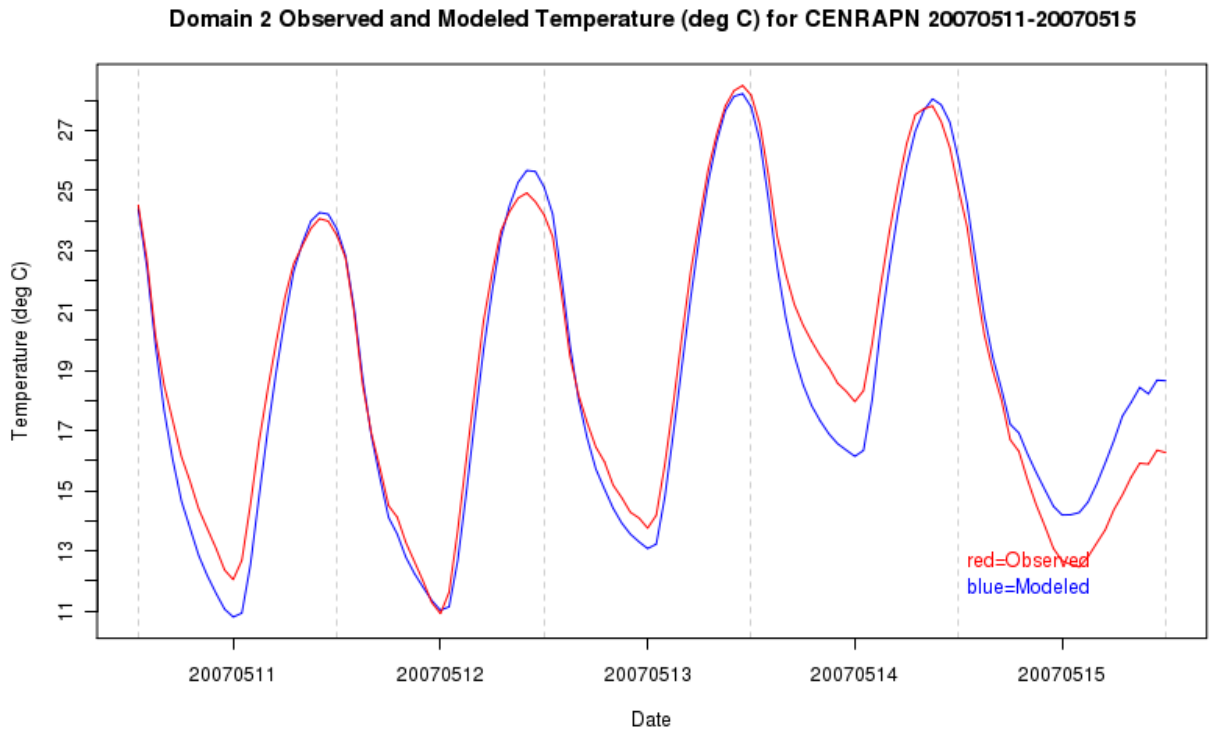

Figure 8-48. Timeseries of observed (red) and modeled (blue) temperature averaged across the CENRAPN region for the nested domain from 2007/05/11 through 2007/05/15.

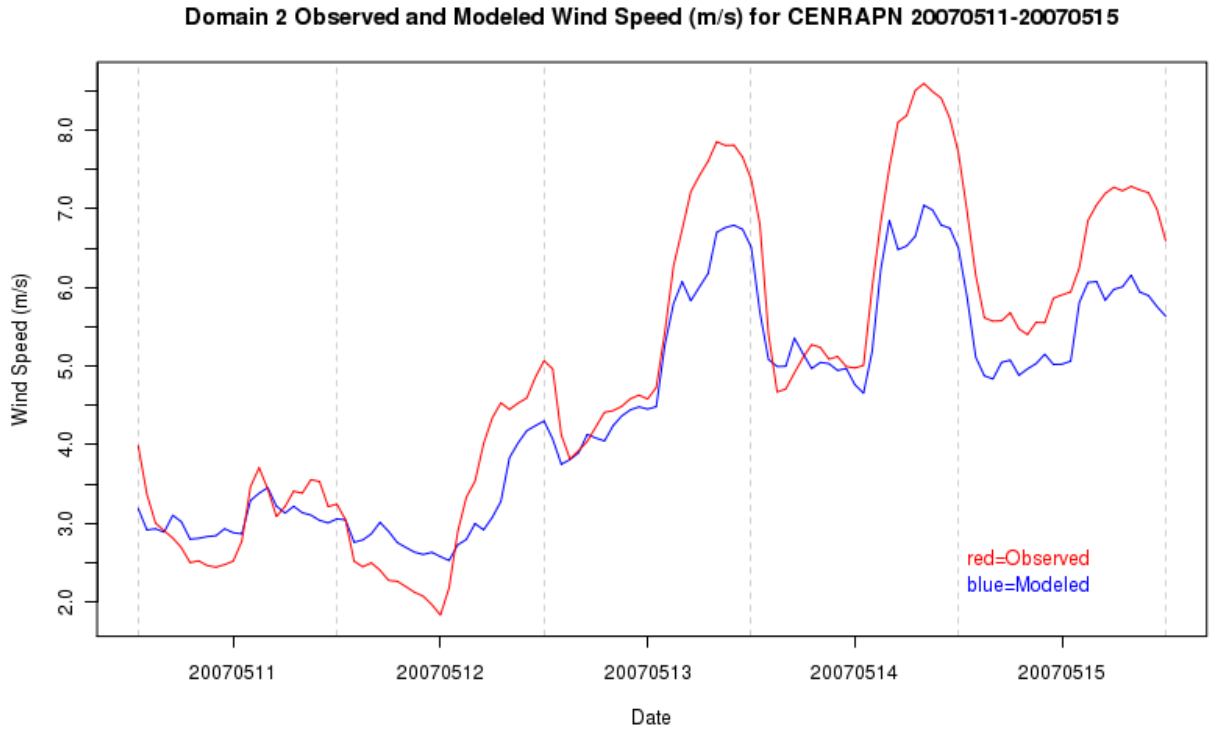

Figure 8-49. Timeseries of observed (red) and modeled (blue) wind speed averaged across the CENRAPN region for the nested domain from 2007/05/11 through 2007/05/15.

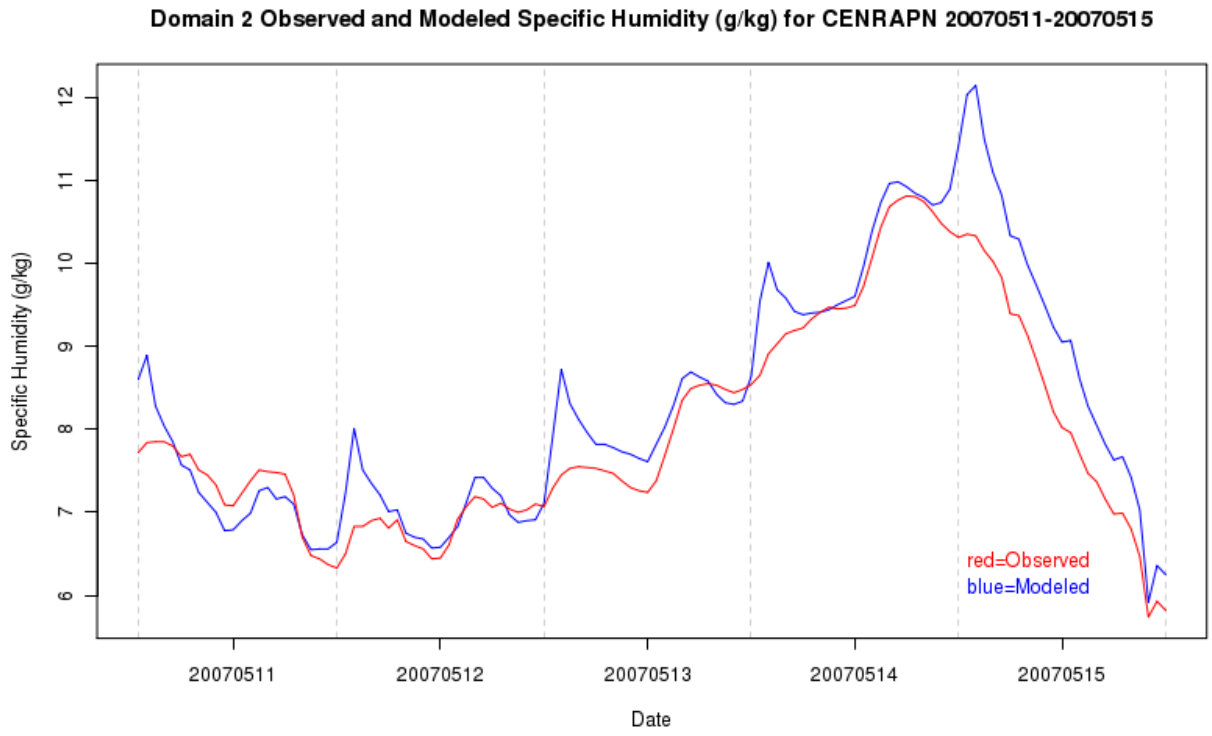

Figure 8-50. Timeseries of observed (red) and modeled (blue) specific humidity averaged across the CENRAPN region for the nested domain from 2007/05/11 through 2007/05/15.

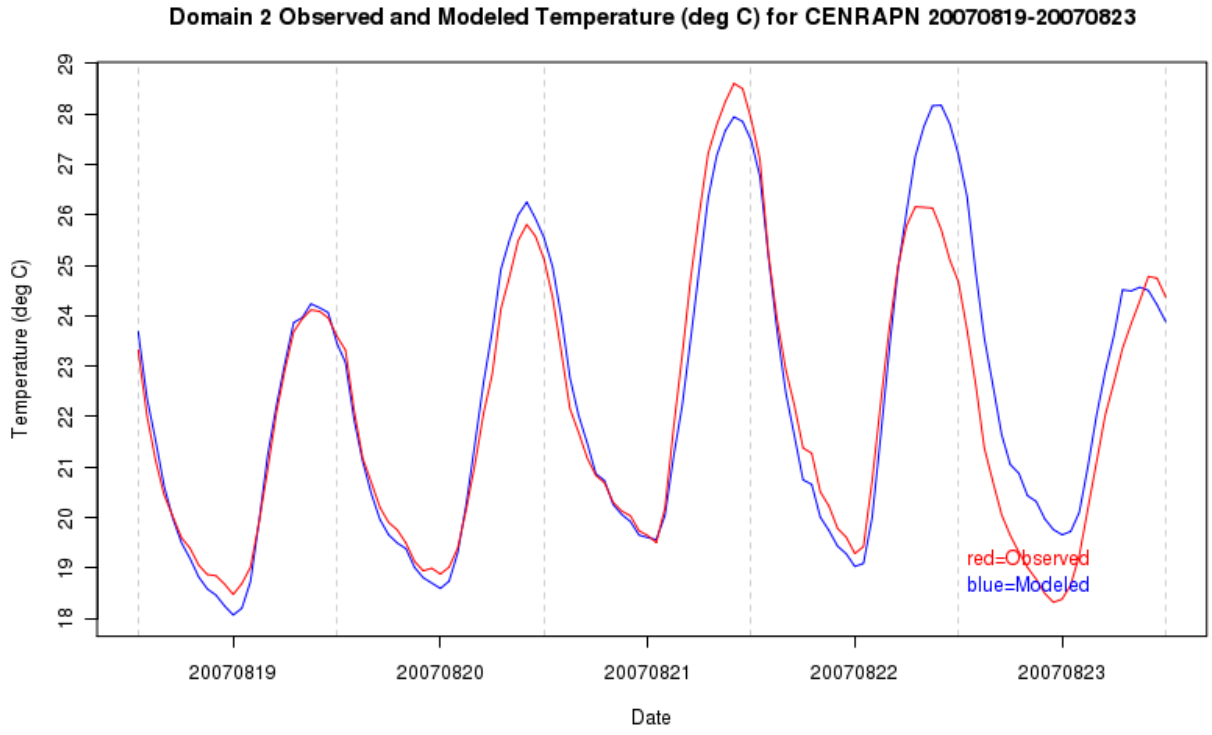

Figure 8-51. Timeseries of observed (red) and modeled (blue) temperature averaged across the CENRAPN region for the nested domain from 2007/08/19 through 2007/08/23.

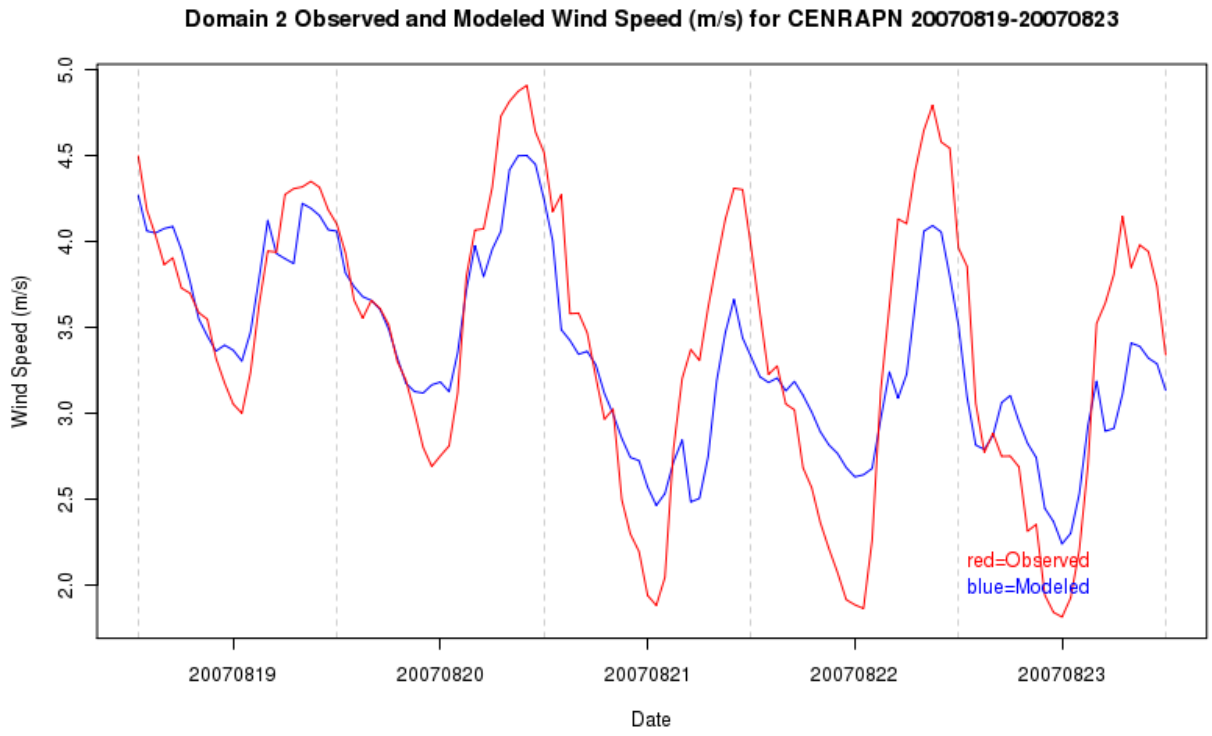

Figure 8-52. Timeseries of observed (red) and modeled (blue) wind speed averaged across the CENRAPN region for the nested domain from 2007/08/19 through 2007/08/23.

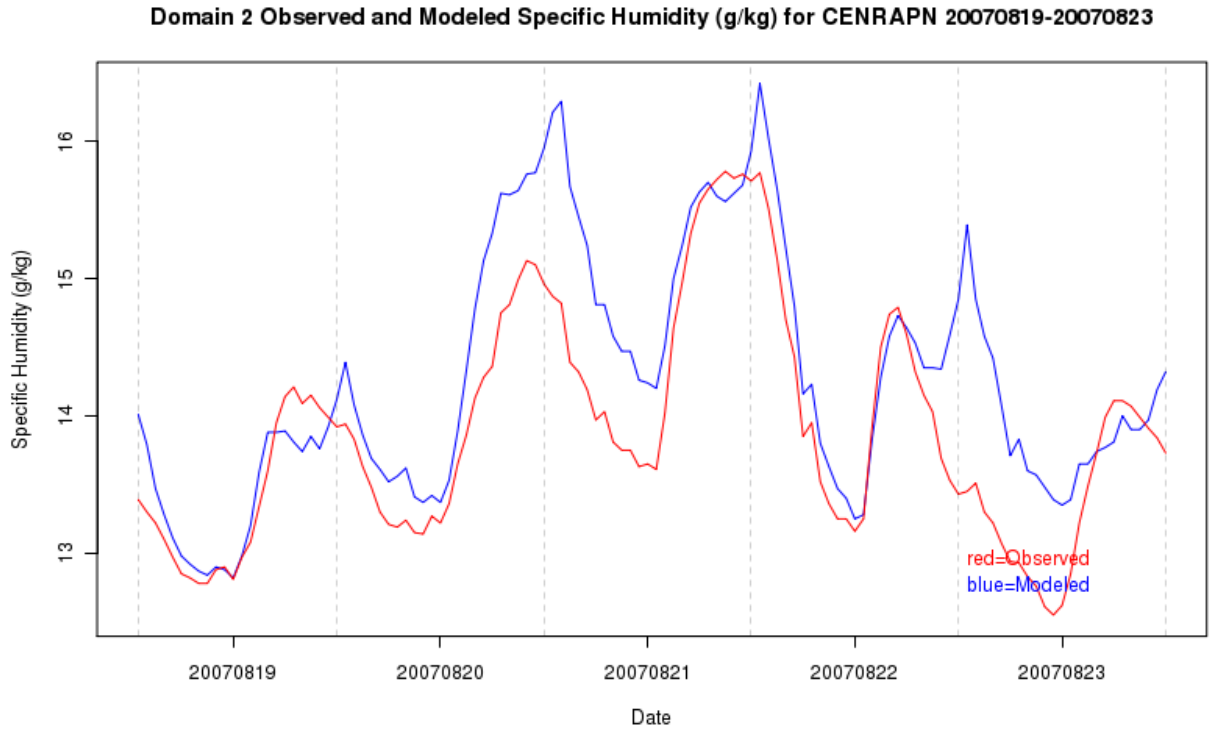

Figure 8-53. Timeseries of observed (red) and modeled (blue) specific humidity averaged across the CENRAPN region for the nested domain from 2007/08/19 through 2007/08/23.

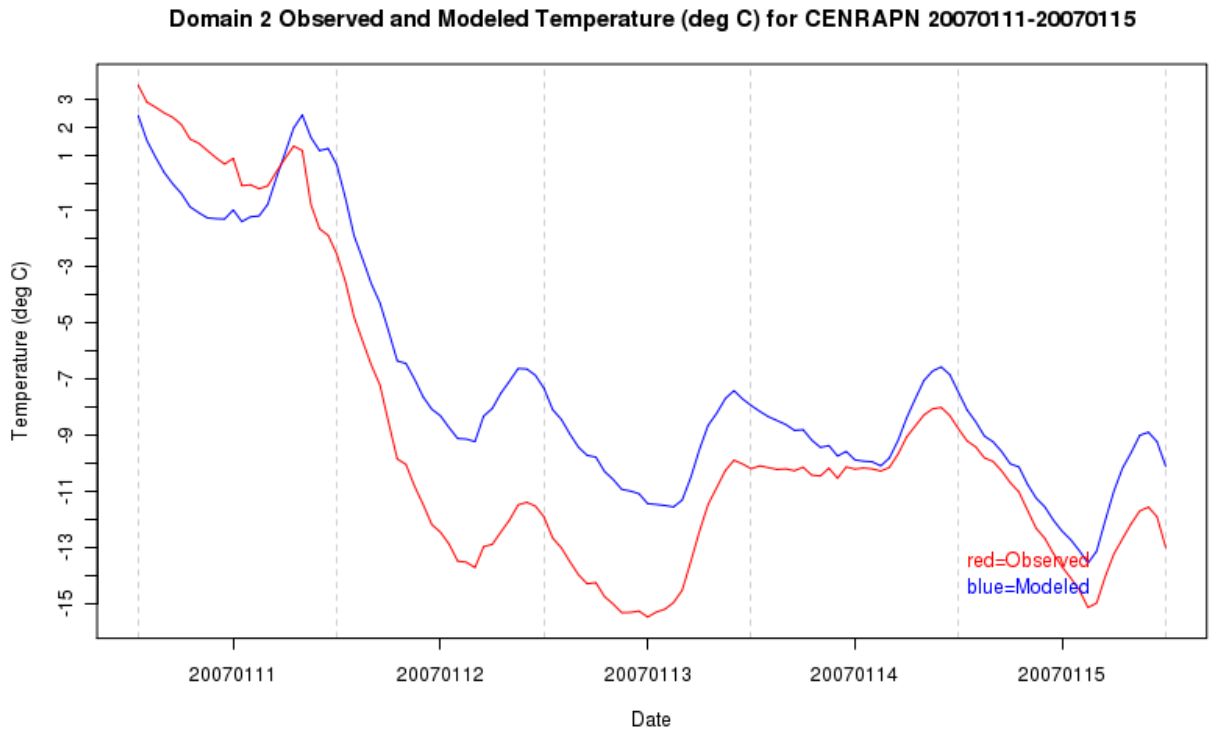

Figure 8-54. Timeseries of observed (red) and modeled (blue) temperature averaged across the CENRAPN region for the nested domain from 2007/01/11 through 2007/01/15.

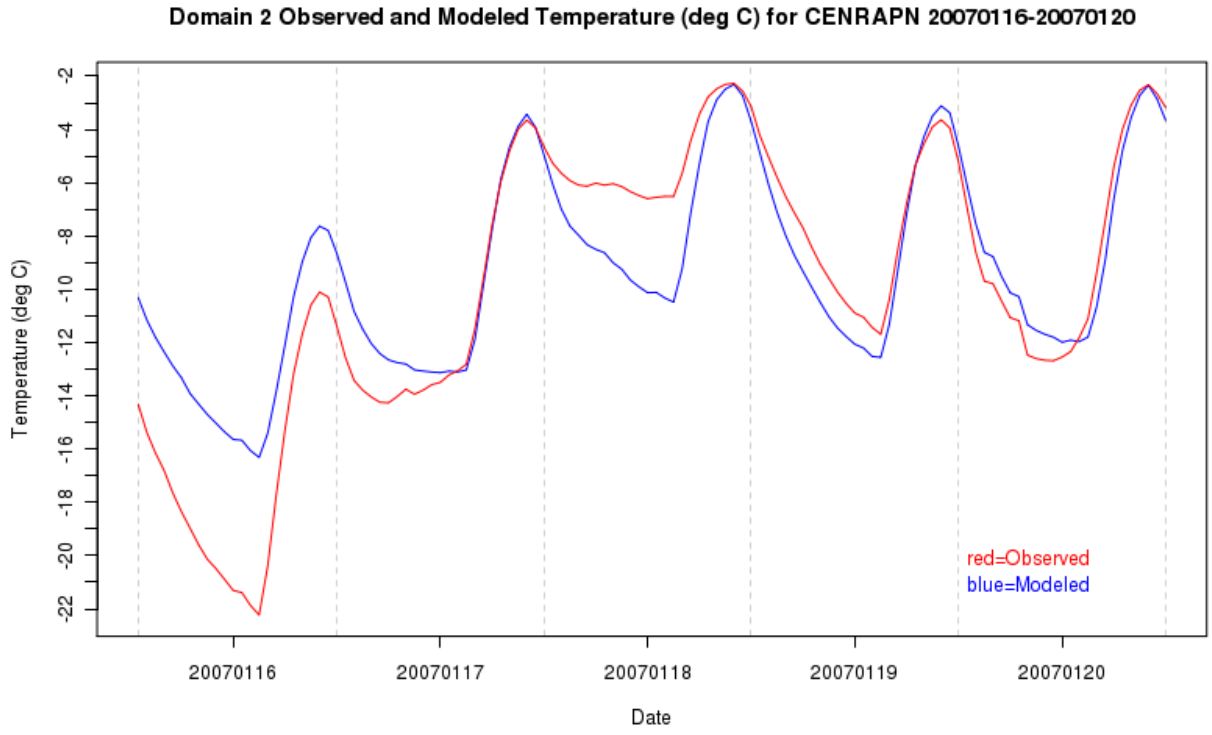

Figure 8-55. Timeseries of observed (red) and modeled (blue) temperature averaged across the CENRAPN region for the nested domain from 2007/01/16 through 2007/01/20.

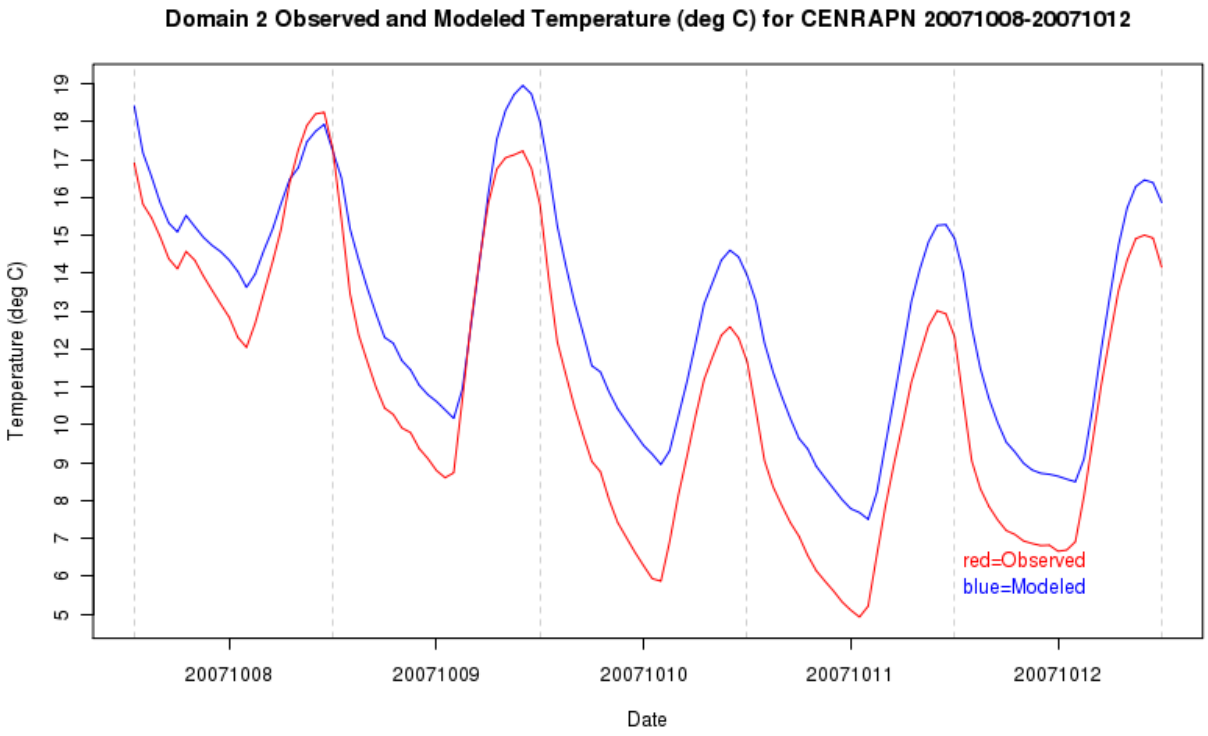

Figure 8-56. Timeseries of observed (red) and modeled (blue) temperature averaged across the CENRAPN region for the nested domain from 2007/10/08 through 2007/10/12.

9. CONCLUSIONS

An annual meteorological simulation for calendar year 2007 was generated by a collaborative group of state air quality agencies to drive future continental scale air quality modeling. The WRF model was selected as the state-of-the-science mesoscale meteorological model to be used. This effort was one of the first to utilize WRF, as previous modeling studies have used MM5. This warranted a sensitivity analysis of the physics parameterizations available for use with WRF. Though no configuration yielded superior results, a configuration was chosen that the group felt produced optimal performance. A contract was established between SESARM and AER to conduct a model performance of both the sensitivity analysis and the 2007 production simulation.

The statistical evaluation reveals a warm bias during the autumn and winter months for both the course and nested domains. A slight positive bias in humidity exists in the summer months over the CENRAPN and MRPO regions for both domains. A slight negative bias in wind speed exists during the winter and spring for both domains, though it is slightly more pronounced for the course domain.

Increasing the resolution of the WRF runs from 36 km to 12 km generally does not decrease errors in simulated fields over the Central and Eastern U.S, at least on a monthly basis. A slight improvement in wind speed error for the nested domain is seen when comparing to the course domain.

McNally and Stella (2009) present the performance results of several MM5 simulations conducted within the past decade. Monthly temperature errors for the 2007 WRF simulation are comparable to the MM5 runs over the CENRAP states. However, the MM5 runs exhibit a cold bias during the fall and winter, whereas the WRF results show a warm bias. Humidity performance is also comparable to the MM5 runs, with a very modest improvement in mean absolute error during the summer. Wind speed comparisons are not possible. The MM5 results are reported using index of agreement. This metric was not calculated as part of the AER performance evaluation.

The analyses available from AER and presented in this document do not necessarily constitute a thorough and complete performance evaluation. Evaluating the meteorological model's ability to accurately represent precipitation, clouds, and upper air fields are important in assessing the model output's applicability to air quality simulations. A precipitation evaluation was not conducted by AER, and upper air analyses were sparse. It is not uncommon for model evaluation studies to give the analysis of the surface fields priority. Since the evaluation of other important atmospheric quantities in the sensitivity analysis did not raise any suspicion no additional evaluation will be conducted on this annual WRF simulation. Future work may be performed if deemed necessary.

Based on the configuration and implementation of the WRF model, along with the results of the model performance evaluation, the annual simulation for 2007 is adequate for use for the regions of interest. Both the 36 and 12 km model fields are acceptable for use in photochemical

modeling. The WRF model is considered the state-of-the-science mesoscale meteorological model and has been recently updated to include the FDDA tools preferred in a retrospective analysis. The physics options selected were shown to provide an optimal configuration. Many of these options are implemented by other agencies involved in air quality modeling, including EPA. Daily error statistics for temperature, humidity, and wind speed are within their respective benchmarks for a significant portion of the year. No major deficiencies were discovered during the performance evaluation, although some large bias values (both positive and negative) for temperature were observed. Errors not within the benchmarks are generally not far removed.

10. REFERENCES

Appel, K. W., S. J. Roselle, R. C. Gilliam, and J. E. Pleim, 2009: Sensitivity of the Community Multiscale Air Quality (CMAQ) Model v 4.7 results for the Eastern United States to MM5 and WRF meteorological drivers. *Geosci. Model Dev. Discuss.*, **2**, 1081–1114.

Atmospheric and Environmental Research, Inc., 2011: WRF Meteorological Modeling Performance Evaluation and Documentation. Prepared for Southeastern States Air Resources Managers, Inc.

Baker, K., D. McNally, and W. Ji, 2007: An evaluation of an annual 2005 MM5 simulation to support photochemical and emissions modeling applications. http://www.ladco.org/reports/technical_support_document/references/mm5mpe2005.pdf

Black, T., 1994: The new NMC mesoscale Eta model: description and forecast examples. *Wea. Forecasting*, **9**, 265-278.

De Meij, A., A. Gizella, C. Cuvelier, P. Thunis, B. Bessagnet, J. F. Vinuesa, … H. M. Kelder, 2009: The impact of MM5 and WRF meteorology over complex terrain on CHIMERE model calculations. *Atmos. Chem. Phys.*, **9**, 6611–6632.

Dudhia, J., 1993: A non-hydrostatic version of the Penn State/NCAR mesoscale model: Validation tests and simulation of an Atlantic cyclone and cold front. *Mon. Wea. Rev.*, **121**, 1493-1513.

Emery, C., and E. Tai, 2001: Meteorological modeling and performance evaluation of the September 13-20, 1999 Ozone Episode. Prepared for the Texas Near Non-Attainment Areas through the Alamo Area Council of Governments, by ENVIRON International Corp, Novato, CA.

Gilliam, R., and J. Pleim, 2010: Performance assessment of new land surface and planetary boundary layer physics in the WRF-ARW. *J. Appl. Met. Climatol.*, **49**, 760-774.

Gilliam, R., J. Pleim, and T. Otte, 2009: Multiscale meteorological modeling for air quality applications, EPA Atmospheric and Modeling Analysis Division Peer Review Conference, January 27-29, Research Triangle Park, NC

Iacono, M., J. Delamares, E. Mlawer, M. Shepard, S. Clough, and W. Collins, 2008: Radiative forcing by long-lived gases: Calculations with AER radiative transfer models, *J. Geophys. Res.*, **113**, D13103, doi:10.1029/2008JD00994

Johnson, M., 2007: Meteorological model performance evaluation of an annual 2002 MM5 (version 3.6.3) simulation. http://www.iowadnr.gov/portals/idnr/uploads/air/insidednr/regmodel/2002mm5v363_evaluation_v204.pdf

Kain, J. S., and J. M. Fritsch, 1990: A one-dimensional entraining/detraining plume model and its application in convective parameterization. *J. Atmos. Sci.*, **47**, 2784-2802.

Kain, J. S., and J. M. Fritsch, 1993: Convective parameterization for mesoscale models: The Kain-Fritsch scheme, *The representation of cumulus convection in numerical models*, K. A. Emanuel and D.J. Raymond, Eds., Amer. Meteor. Soc., 246 pp.

Knievel, J., G. Bryan, and J. Hacker, 2007: Explicit numerical diffusion in the WRF model. *Mon. Wea. Rev.*, **135**, 3808-3824.

Lin, M., T. Holloway, T. Oki, D. G. Streets, and A. Richter, 2009: Multi-scale model analysis of boundary layer ozone over East Asia. *Atmos. Chem. Phys.*, **9**, 3277-3301.

Lin, Y., and K. E. Mitchell, 2005: The NCEP Stage II/IV hourly precipitation analyses: development and applications. Preprints, 19th Conf. on Hydrology, American Meteorological Society, San Diego, CA, 9-13 January 2005, Paper 1.2.

McNally, D., 2003: Annual application of MM5 for calendar year 2001. Prepared for Pat Dolwick, USEPA, March 31st 2003.

McNally, D., and G. Stella, 2009: Evaluation of 36/12 km MM5 for calendar year 2007 over the Continental and Midwest/Eastern United States. Prepared for Midwest Ozone Group.

Morrison, H., G. Thompson, and V. Tatarskii, 2009: Impact of cloud microphysics on the development of trailing stratiform precipitation in a simulated squall line: Comparison of one- and two-moment schemes. *Mon. Wea. Rev.*, **137**, 991-1007

National Oceanic and Atmospheric Administration, 1998: Automated Surface Observing System User's Guide. http://www.nws.noaa.gov/asos/pdfs/aum-toc.pdf

Olerud, D., and A. Sims, 2004: MM5 2002 modeling in support of VISTAS (Visibility Improvement – State and Tribal Association) (DRAFT). Prepared for Mr. Mike Abraczinskas, VISTAS Technical Analysis Workgroup.

Pinker, R. T., and I. Laszlo, 1992: Modeling surface solar irradiance for satellite applications on a global scale. *J. Appl. Meteor*., **31**, 194-211.

Pleim, J. E., 2006: A simple, efficient solution of flux-profile relationships in the atmospheric surface layer. *J. Appl. Meteor. And Clim.*, **45**, 341-347.

Pleim, J. E., 2007: A combined local and nonlocal closure model for the atmospheric boundary layer. Part I: Model description and testing. *J. Appl. Meteor. Clim.*, **46**, 1383–1395.

Pleim, J. E., and R. Gilliam, 2009: An indirect data assimilation scheme for deep soil temperature in the Pleim-Xiu land surface model. *J. Appl. Meteor. Clim.*, **48**, 1362-1376.

Shin, H. H., S.-Y. Hong, and J. Dudhia, 2009: Orographically-induced Gravity Wave Drag (GWDO) parameterization in the WRF model. http://www.mmm.ucar.edu/wrf/users/workshops/WS2009/abstracts/P2B-01.pdf

Skamarock, W., J. Klemp, J. Dudhia, D. Gill, D. Barker, M. Duda, X.-Y. Huang, W. Wang, and J. Powers, 2008: A description of the Advanced Research WRF version 3, NCAR Tech. Note, NCAR TN-475+STR, 113 pp.

Stoelinga, M. T., 2006: A users' guide to RIP version 4: A program for visualizing mesoscale model output. http://www.mmm.ucar.edu/mm5/documents/ripug_V4.html

Tesche, T. W., 1994: Evaluation Procedures for Regional Emissions, Meteorological, and Photochemical Models. Presented at the 86th Annual Meeting of the Air and Waste Management Association, 14-18 June, Denver, CO.

Vincent, L. A., W. Wijngaarden, and R. Hopkinson, 2007: Surface temperature and humidity trends in Canada for 1953-2005. *J. of Climate*, **20**, 5100-5113.

Witcraft, N., D. Baker, T. Downs, M. Ku, W. Hao, G. Sistla, … D.-L. Zhang, 2010: Protocol for WRF meteorological modeling in support of regional SIP air quality modeling in the SEMAP (Draft).

Xiu, A., and J. E. Pleim, 2001: Development of a land surface model. Part I: Application in a mesoscale meteorology model. *J. Appl. Meteor.*, **40**, 192-209.

APPENDIX A: ANALYSIS OF 2008 CLIMATOLOGY

A regional air quality modeling system is commonly employed to support state air pollution planning activities. This modeling system consists of a mesoscale meteorological model, such as MM5, RAMS, or WRF, a gridded emissions model (e. g. EMS, SMOKE, CONCEPT), and a photochemical transport model, such as CAMx or CMAQ. The modeling system requires hourly data, and is typically implemented over an entire year. When basecase and emissions control strategy simulations are conducted, the same meteorology is used as inputs to both runs. The year from which meteorology is modeled is often determined by the most recent completed year in the 3-year cycle of the National Emissions Inventory (NEI). Since 2008 is the most recent reporting year for the NEI and EPA provided only limited development of the 2005 NEI, 2008 is a logical candidate to be the focus of new annual meteorological simulations. In regulatory photochemical applications, optimum use of annual simulation of meteorology can occur only if that year is representative of conditions that have occurred in recent years. Averages of variables such as temperature and precipitation should at least be similar to climatological averages. For a given region's emissions scenario, meteorology is a dominant factor driving air pollution concentrations. A robust assessment of air quality programs is dependent upon a base year which does not deviate towards unusually clean conditions.

Meteorological Review

Every year the National Oceanic and Atmospheric Administration's (NOAA) National Climatic Data Center prepares an annual climate summary to quantify the overall meteorological statistics of the previous year. Averages of temperature and precipitation across each season, as well as the entire calendar year, and geographic regions, are calculated and compared to previous records dating back to 1895. This information provides useful insight into how the overall meteorology of the previous year compares to other recent years and also to climatological averages. This document is a summary of the 2008 annual climate report (http://www.ncdc.noaa.gov/oa/climate/research/2008/ann/us-summary.html). An emphasis is placed on the meteorological conditions which occur over the central U. S., since regional air quality over Iowa is greatly affected by the production and transport of air pollutants from this area. Figure A-1 shows the meteorological modeling domains used in previous annual meteorological simulations using the Penn State/NCAR Mesoscale Model (MM5) by Iowa DNR.

Compared to the climatology of the previous century, the mean temperature, as averaged across the contiguous U. S. in 2008, was surprisingly close to the 114 year average. The average of 53.0°F, shown in Figure A-2, while close to the long-term climatological mean, deviates sharply from conditions observed over more recent years. Compared to the last ten years, the 2008 temperature average was much lower than previously recorded values and thus not similar to years such as 1999, 2002, and 2005 which have been a focus of air quality modeling studies.

Determining the representativeness of an air quality planning base year from averages encompassing a yearly dataset covering the continental United States can be informative, but is certainly not without limitations. While conclusions can be drawn from averages which clearly depart from the mean, temporal-spatial variability combined with high and low values within a given year can lead to near-normal averages. The climate across the contiguous U. S. is not consistent and variability between climatic regions and seasons needs to be examined. While the

country as a whole was much cooler in 2008 than the previous year, this trait was not consistent across various regions of the U. S. The mountain west experienced an annual average temperature that was consistent with the previous nine years and higher than climatology, as shown in Figure A-3. The northeast was also warmer than normal in 2008. The much above normal pattern in this region was concentrated in New Jersey and Delaware (see Figure A-4), which experienced their 10th and 11th, warmest years on record, respectively. The region whose annual average temperatures heavily influenced the decline in annual mean temperature for the U. S. was the central and Midwestern U. S. Six states (Iowa, Nebraska, Illinois, Missouri, Wisconsin, and Arkansas) experienced annual average temperatures that ranked in the top 20 lowest temperatures on record (see Figure A-4). Iowa, which had the coolest year relative to its climatology of the 48 contiguous states, recorded an annual average temperature that ranked as the 11th lowest on record. Figure A-5 depicts the approximate -2 °F deviation from climatology observed in Iowa in 2008. A preliminary weather summary for Iowa in 2008 was prepared by the Iowa Department of Agriculture and Land Stewardship, and is available here: http://www.iowaagriculture.gov/climatology/weatherSummaries/2008/fas2008.pdf.

The pattern across the contiguous U.S. of the average temperatures for the summer months relative to climatology was similar to the entire year; however these values were consistently slightly higher. Figure A-6, in combination with Figure A-4, shows that regions warmer than normal over the entire year were also warmer than normal during the summer, with the departures being even further removed (warmer) from normal. In the meantime, regions much colder than normal for the entire year had mean temperatures over the summer still below climatology, however the departures were closer to the climatological average.

Precipitation across the contiguous U. S. was highly variable. The western-most states remained very dry, while periods of record rainfall were experienced across the central and Midwestern parts of the U. S. Figure A-7 shows the nationally averaged precipitation for 2008 was within the variability of precipitation amounts from previous years. Thirteen states (Kansas, Iowa, Missouri, Michigan, Illinois, Indiana, New York, New Hampshire, Vermont, Massachusetts, Connecticut, Rhode Island, and Maine), shown in Figure A-8, from the central plains to the northeast, had annual precipitation amounts with a rank in the top 10 of the climatological record. Missouri and New Hampshire experienced their wettest year on record. The largest extremes in precipitation occurred during the spring months, shown in Figure A-9. The southwest was very parched, with California recording its driest spring on record. Meanwhile, the Midwest was very wet during the spring. The departures from normal for the summer months, shown in Figure A-10, were similar in direction and location to spring, however, generally not as extreme. A notable exception was the extreme northeast, where a very wet summer occurred.

A focused look at the east-north-central climate region shows the annual average temperature in 2008, shown in Figure A-11, to be significantly lower than both the 2007 value and the climatological average. Precipitation in this region, along with the northeast, was well above normal in 2008. Many regions experienced excessive rainfall and record flooding, mainly occurring in the late spring and early summer. In one of the most extreme cases, Missouri experienced 10 to 15 inches more precipitation in 2008 than in recent years. Based on temperature and precipitation, the meteorology of 2008 for the eastern part of the contiguous

U.S. was not representative of the conditions that occurred in either previously modeled years or climatology.

Air Quality Review

Atmospheric concentrations of air pollutants are dependent upon not just the emissions of the pollutants and their precursors, but also meteorology and the oxidative capacity of the atmosphere. Assuming emissions did not change drastically in 2008 compared to recent years[1], evidence of the impacts of the 2008 meteorology can be seen through changes in ozone concentrations over the central and eastern U. S. Ozone is produced during the warmer half of the year through the chemical reactions of volatile organic compounds and oxides of nitrogen in the atmosphere in the presence of heat and sunlight. Ozone formation rates are proportional to temperature and downwelling solar radiation. The lower temperatures and the cloudy skies associated with the excessive precipitation acted to suppress ozone concentrations across the spring and summer months over the central and northeastern U. S. in 2008. Table A-1 displays the ten highest 4th high daily maximum 8 hour average ozone concentrations in 2005 for monitors located in EPA Regions 1, 2, and 5. Their respective 2008 values are also displayed and show significant decreases from 2005 to 2008. The reductions in ozone concentrations are most pronounced in the states of Wisconsin, Michigan, and Ohio. Figure A-12 shows a map of 8 hour ozone design values for 2005-2007 across Iowa, while Figure A-13 shows a similar map for 2006-2008. Design values for the Iowa monitors decreased by an average of 3.5 ppb.

The relationship between meteorological variables and fine particulate pollution is more complex. Particulate pollution is comprised of several different compounds, including ammonium sulfate, ammonium nitrate, organic and inorganic carbon species, and crustal material (dust). Ammonium sulfate and ammonium nitrate are important components of regional scale air pollution in the Midwest. Both are secondarily formed in the atmosphere from emissions of precursor gases, but are influenced much differently by meteorology. Ammonium nitrate formation occurs in areas of high relative humidity and low temperatures and in the presence of fog. Ammonium sulfate formation, however, favors warmer, humid air. Table A-2 displays the 98th percentile PM2.5 concentrations for 2005 and 2008 at 10 Midwest and Northeast monitors. These monitors show significant decreases in the peak PM2.5 concentrations from 2005 to 2008. Figure A-14 shows a map of 24-hour PM2.5 design values for 2005-2007 across Iowa, while Figure A-15 shows a similar map for 2006-2008. Design values for the Iowa monitors decreased by an average of 3 $\mu g/m^3$ when 2008 data replaced 2005 in the design value calculations.

In summary, calendar year 2008 is not representative of recent meteorological conditions, or of conditions conducive to air quality planning activities for areas in the Midwest. This conclusion could easily be extended to include much of the Northeastern United States. The extreme floods occurring in the Midwest coupled with much cooler temperatures created situations which suppressed the formation of secondarily formed pollutants. While 2008 aligns with the triennial NEI development cycle, in the Midwest this year is not well suited for regulatory regional modeling applications.

[1] Evaluating the accuracy of this statement is beyond the scope of this document. It is known that industrial operations experienced disruptions associated with flooding in certain parts of the U.S. Additionally, the economic downturn resulted in various emissions reductions.

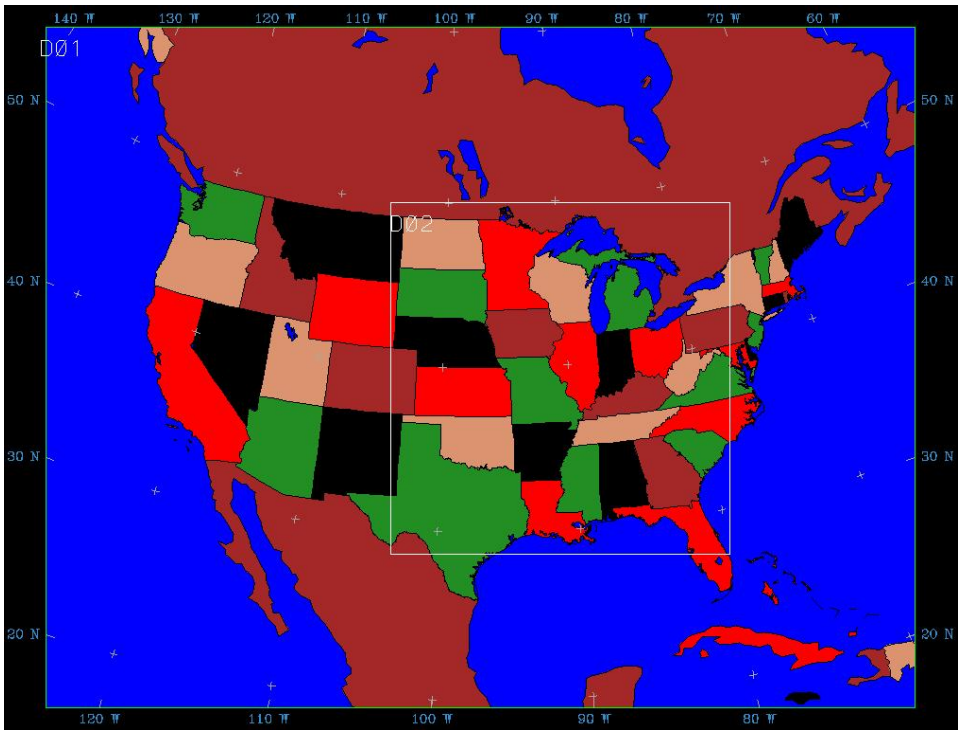

Figure A-1. The 36 km course (D01) and 12 km nested (D02) IDNR meteorological modeling domains from previous applications of MM5.

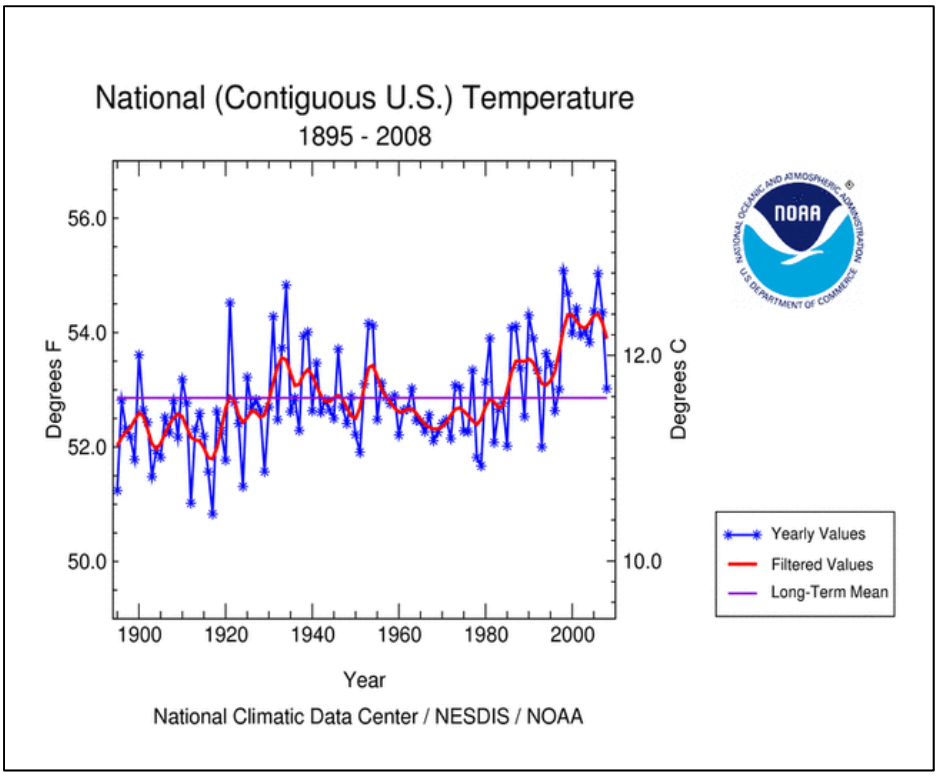

Figure A-2. Annual average temperature across the contiguous U. S. since 1895. From the National Climatic Data Center.

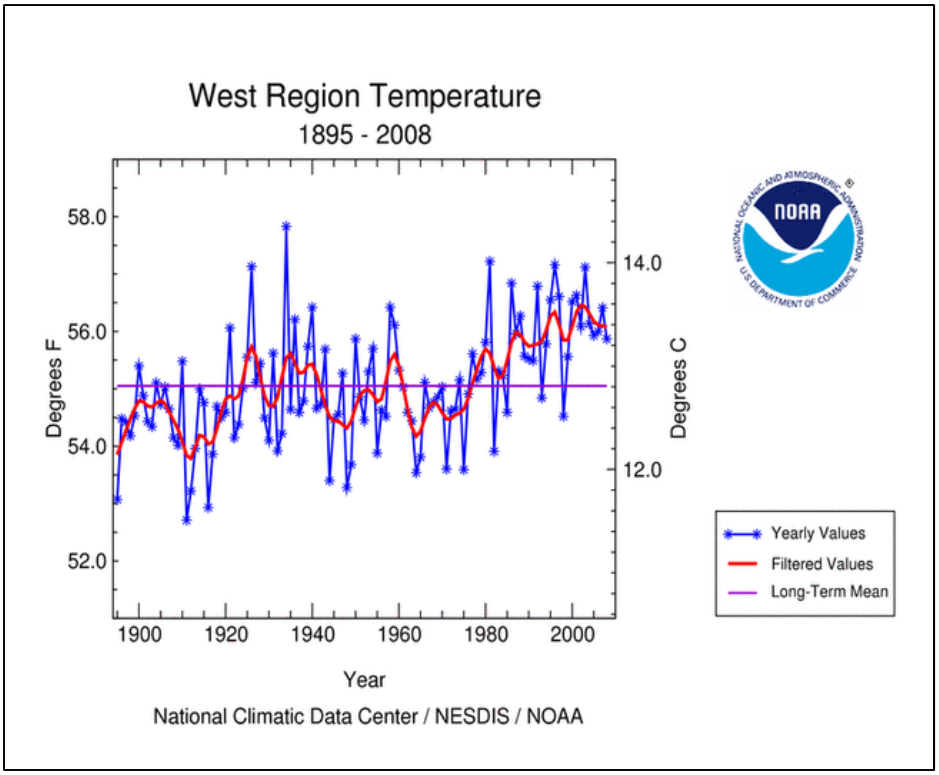

Figure A-3. Annual average temperature across the western U. S. since 1895. From the National Climatic Data Center.

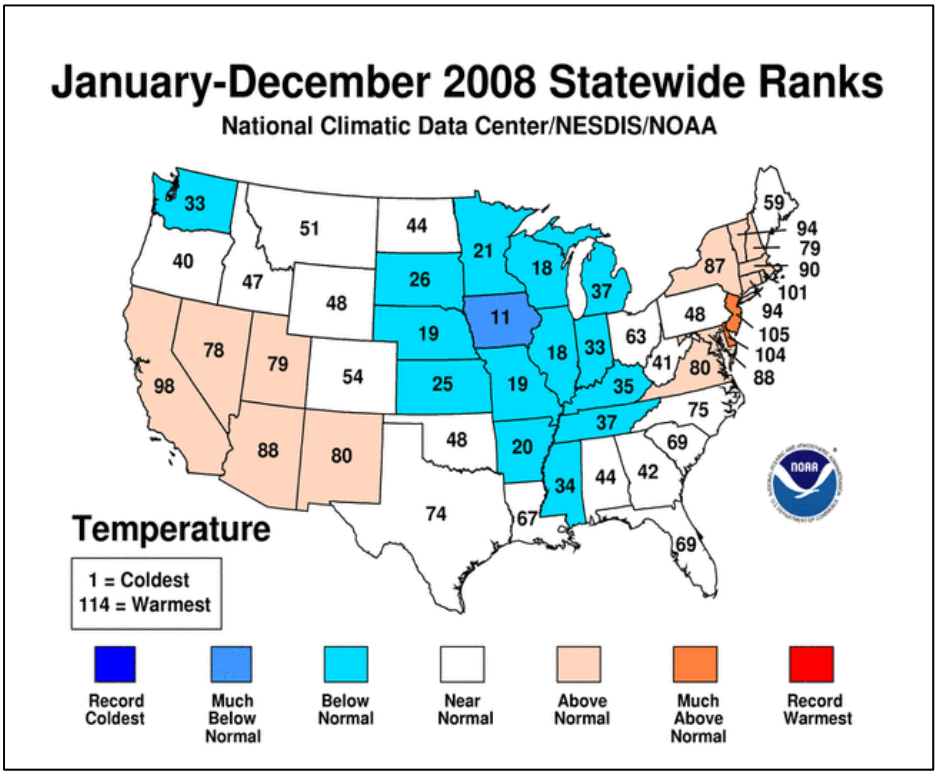

Figure A-4. Annual average temperature statewide ranks in 2008. From the National Climatic Data Center.

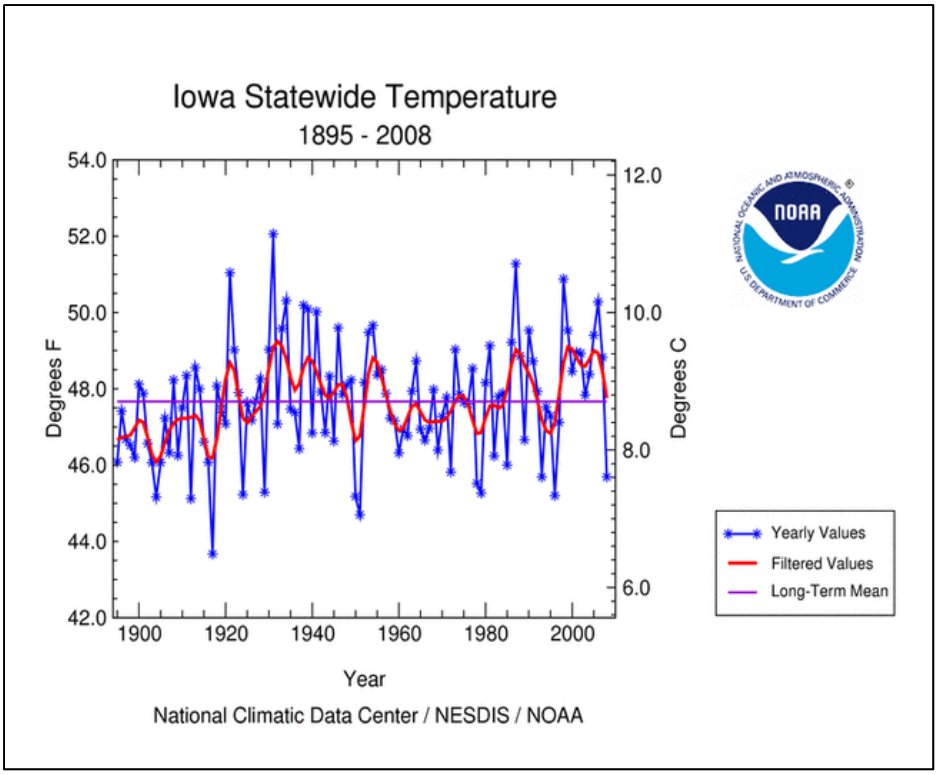

Figure A-5. Annual average temperature across Iowa since 1895. From the National Climatic Data Center.

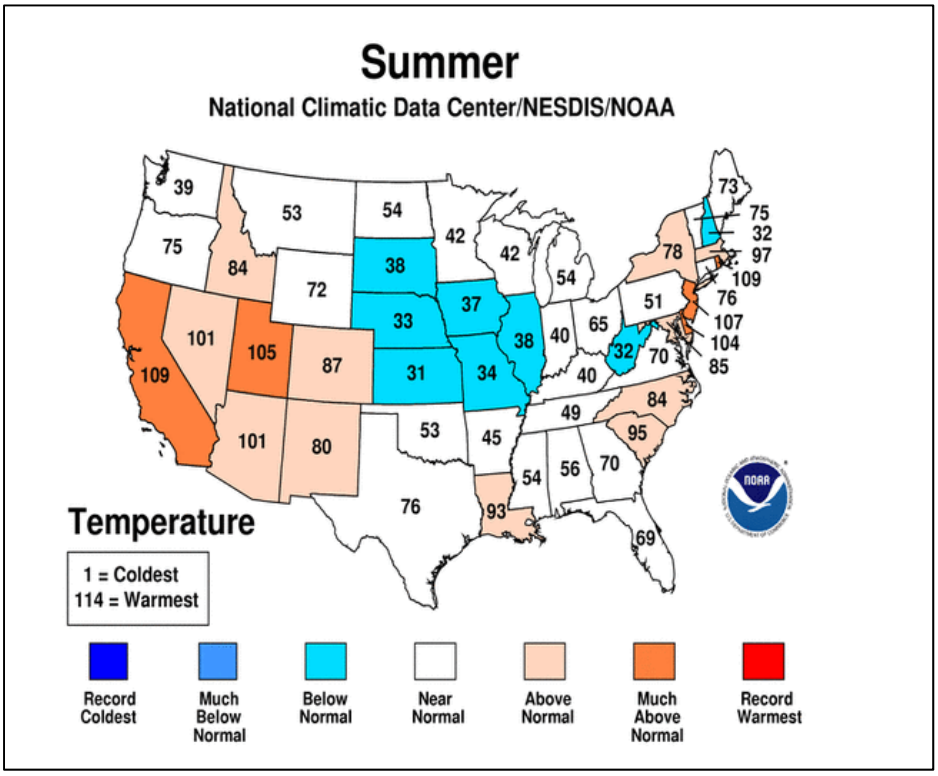

Figure A-6. Average temperature statewide ranks for the summer months in 2008. From the National Climatic Data Center.

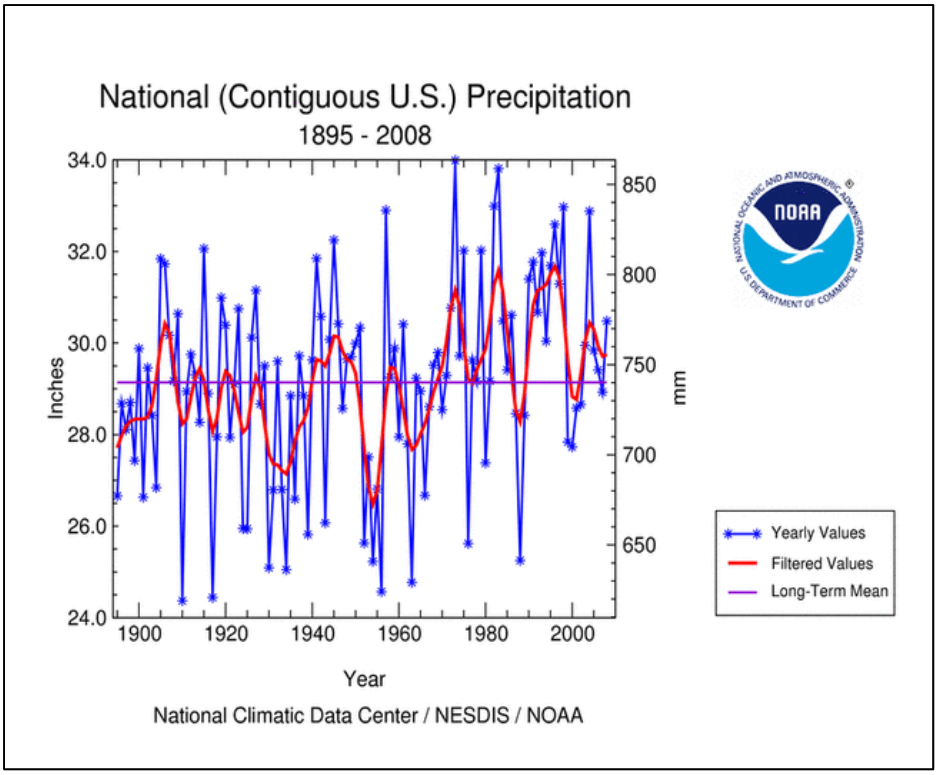

Figure A-7. Average precipitation across the contiguous U. S. since 1895. From the National Climatic Data Center.

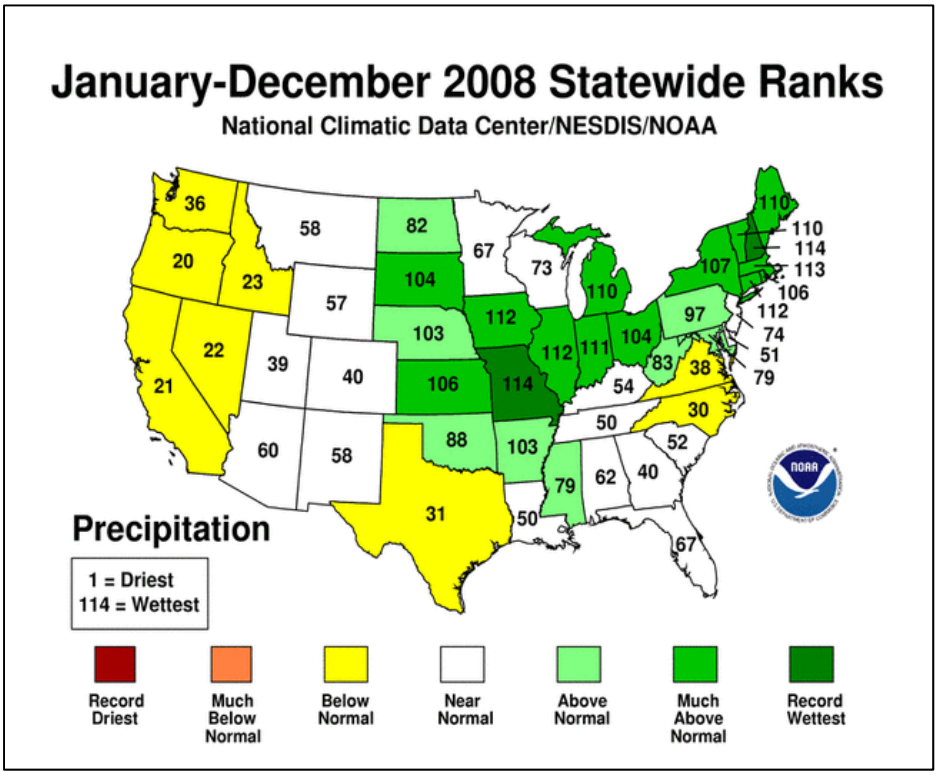

Figure A-8. Annual accumulated precipitation statewide ranks in 2008. From the National Climatic Data Center.

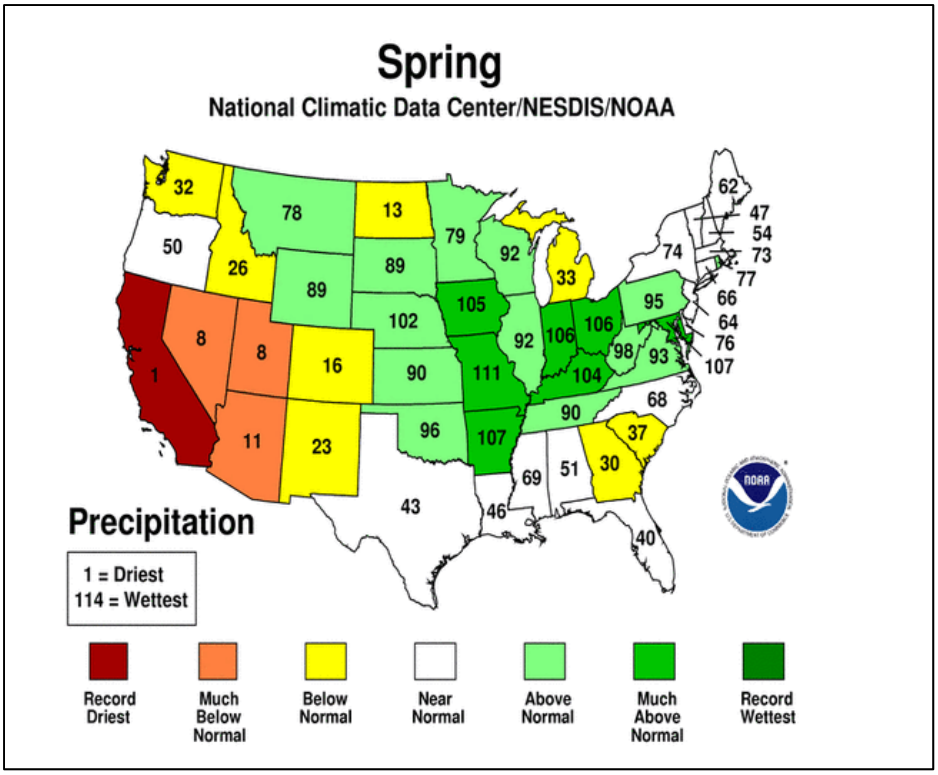

Figure A-9. Accumulated precipitation statewide ranks for the spring months in 2008. From the National Climatic Data Center.

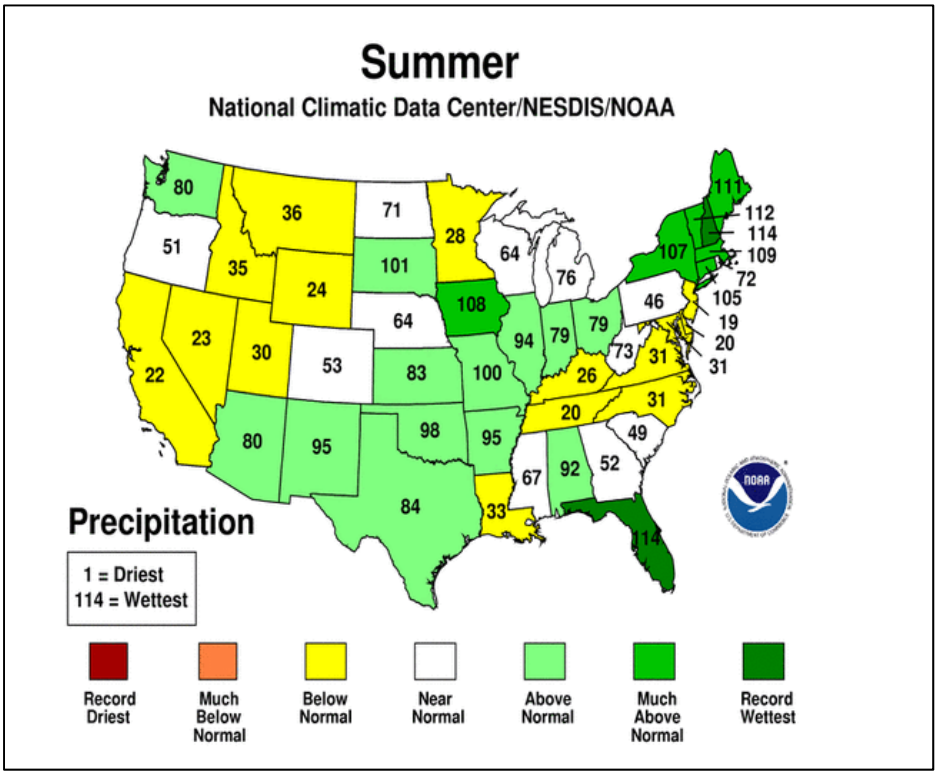

Figure A-10. Accumulated precipitation statewide ranks for the summer months in 2008. From the National Climatic Data Center.

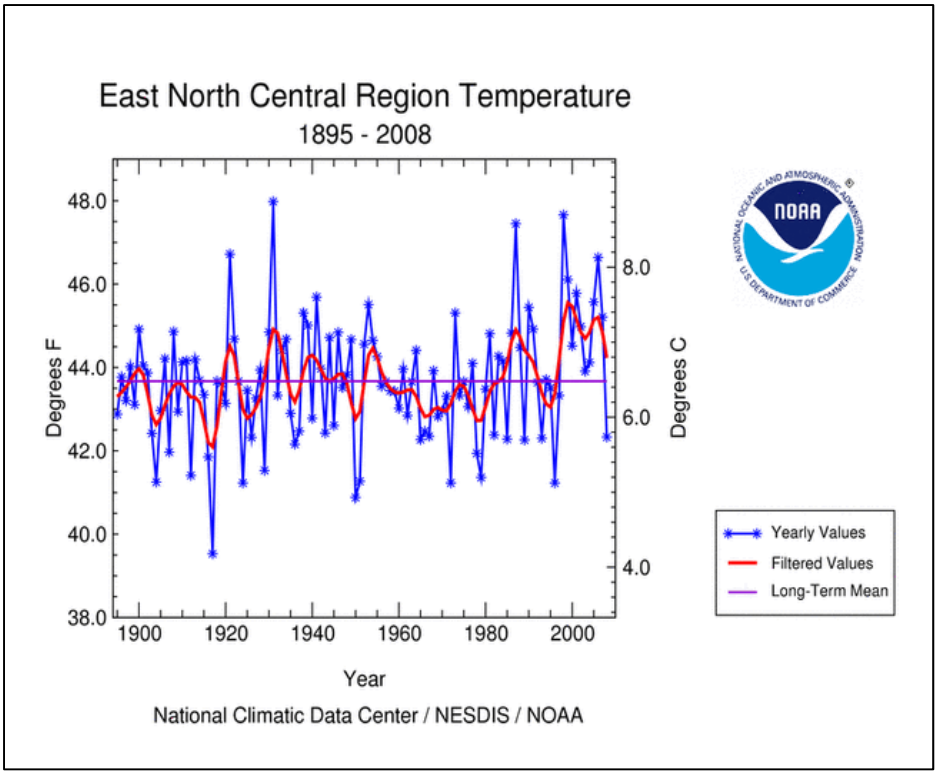

Figure A-11. Annual average temperature across east north central region of the U. S. since 1895. From the National Climatic Data Center.

Table A-1. Comparison of 4th highest daily maximum 8 hour average ozone concentrations in 2005 and 2008 at 10 Midwest and Northeast monitors.

Station ID	Location	2005 O_3 4th high (ppm)	2008 O_3 4th high (ppm)
090011123	Danbury, CT	0.104	0.086
550290004	Newport State Park, WI	0.101	0.069
340290006	Jackson Township, NJ	0.101	0.085
361030002	East Farmingdale, NY	0.098	0.083
390850003	Eastlake, OH	0.097	0.078
551170006	Kohler-Andrae State Park, WI	0.097	0.075
090131001	Shenipsit State Forest, CT	0.097	0.084
360790005	Putnam County, NY	0.096	0.079
090070007	Middletown, CT	0.096	0.082
550710007	Two Rivers, WI	0.095	0.064

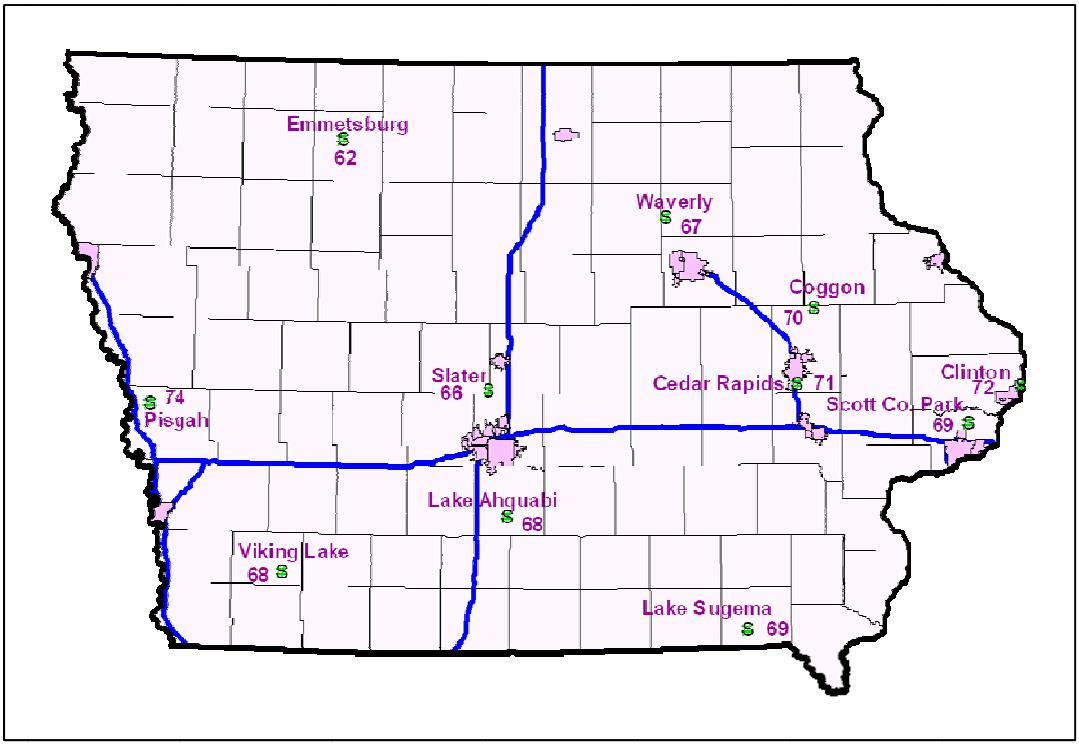

Figure A-12. Ozone 2005-2007 design values in ppb for Iowa monitors.

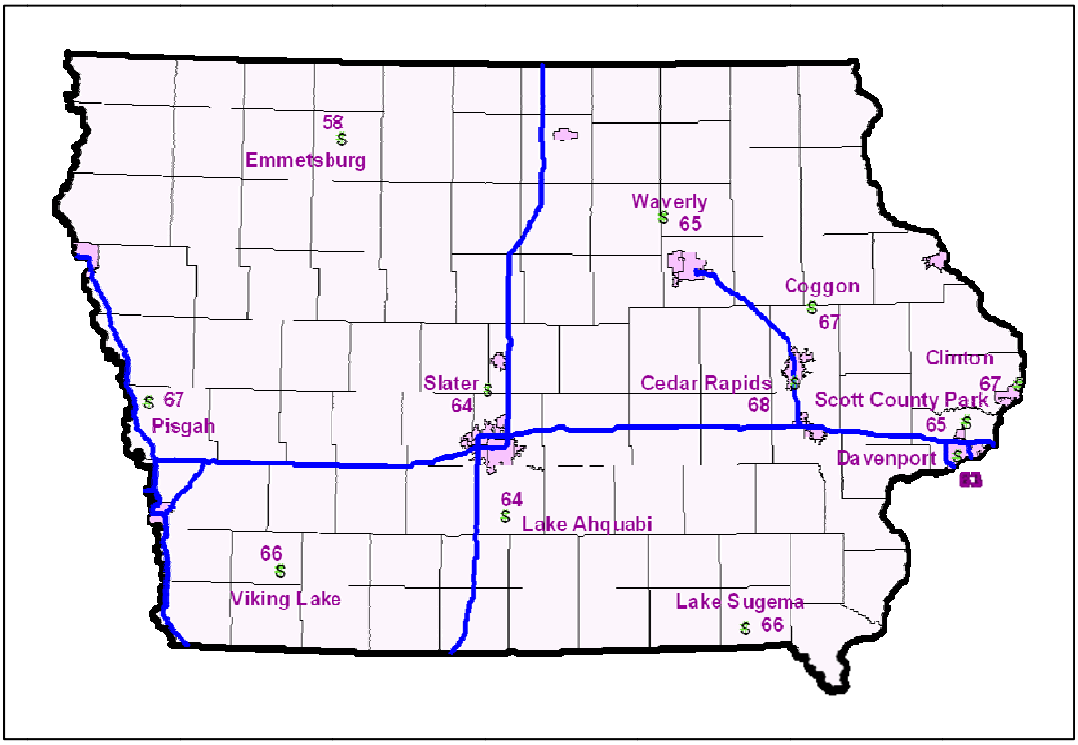

Figure A-13. Ozone 2006-2008 design values in ppb for Iowa monitors.

Table A-2. Comparison of 98th percentile 24-hour average $PM_{2.5}$ concentrations in 2005 and 2008 at 10 Midwest and Northeast monitors.

Station ID	Location	2005 98th Percentile 24-hour Average $PM_{2.5}$ Concentration ($\mu g/m^3$)	2008 98th Percentile 24-hour Average $PM_{2.5}$ Concentration ($\mu g/m^3$)
261630019	Detroit, MI	52.3	32.4
170311016	Mccook, IL	51.5	33.9
390350060	Cleveland, OH	49.5	40.3
180970081	Indianapolis, IN	45.7	31.2
170310076	Chicago, IL	45.1	29.7
260810020	Grand Rapids, MI	44.7	26.5
340390004	Elizabeth, NJ	43.8	34.6
090091123	New Haven, CT	40.8	36.8
171630010	East St. Louis, IL	39.6	32.3
360610128	New York, NY	38.2	25.7

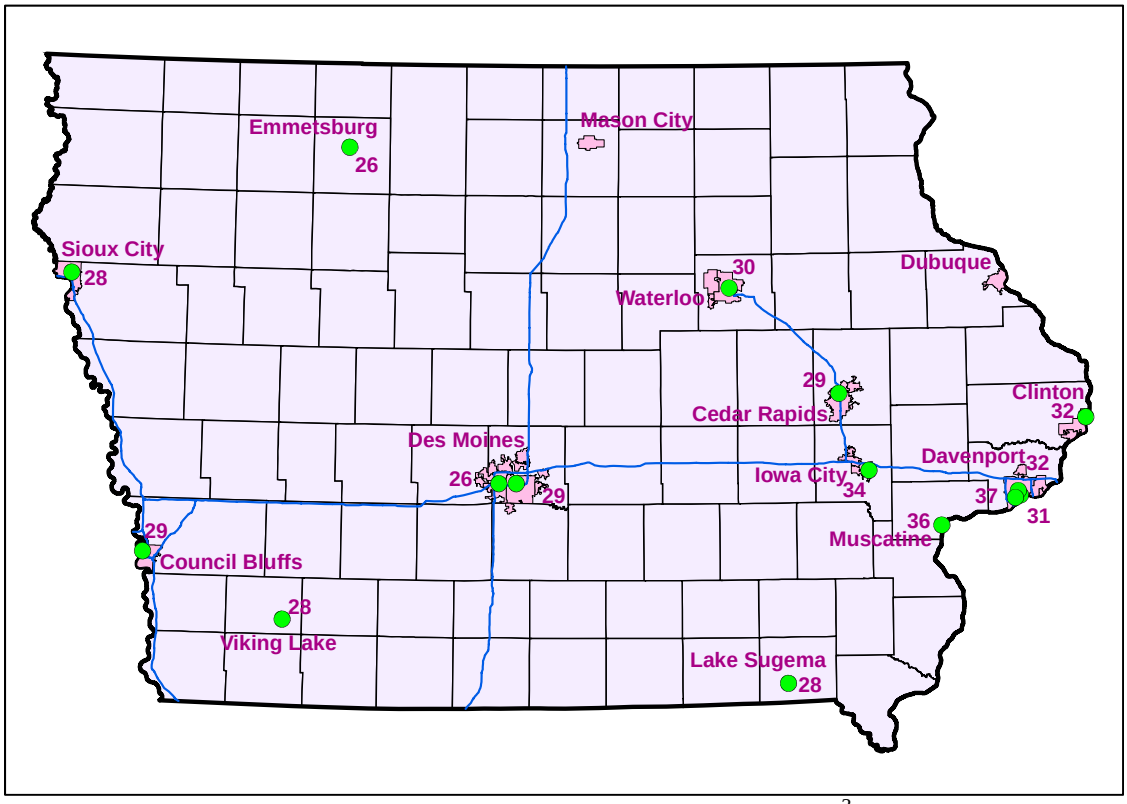

Figure A-14. 24 hour PM2.5 2005-2007 design values in $\mu g/m^3$ for Iowa monitors.

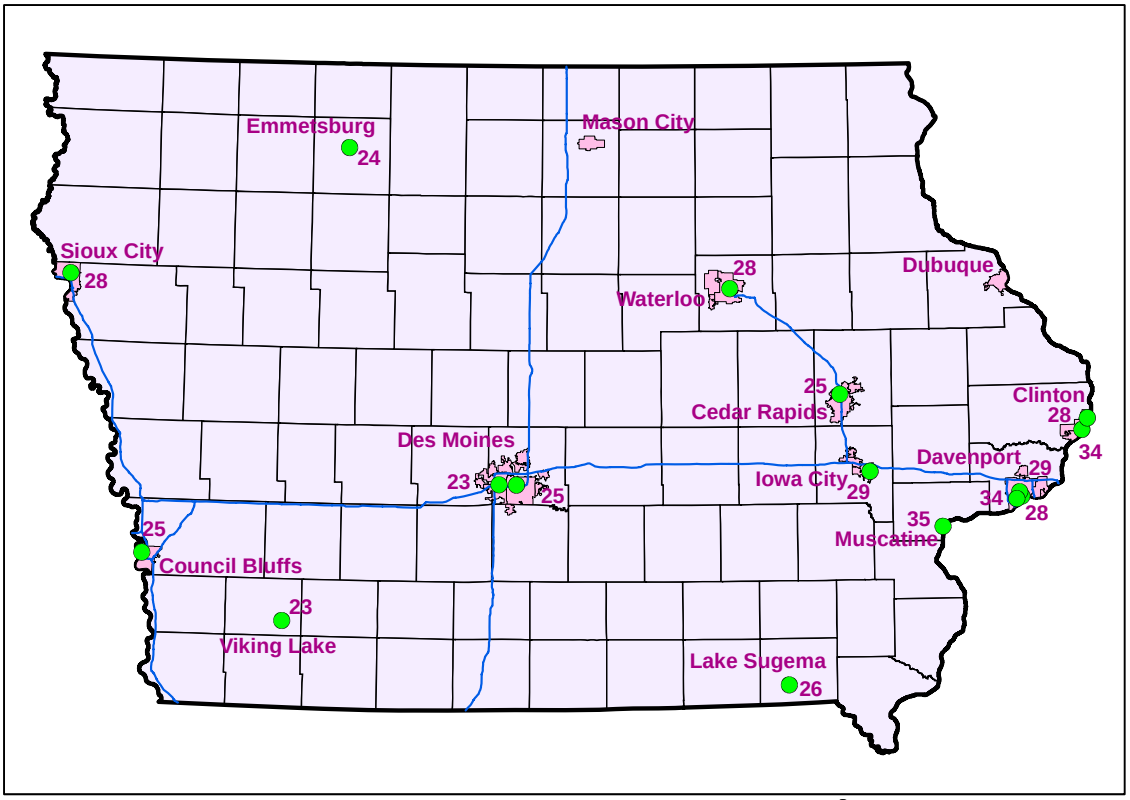

FigureA-15. 24 hour PM2.5 2006-2008 design values in µg/m^3 for Iowa monitors.

APPENDIX B: WRF NAMELISTS

WPS Namelist

```
&share
 wrf_core = 'ARW',
 max_dom = 2,
 start_date = '2006-12-16_12:00:00','2006-12-16_12:00:00',
 end_date   = '2006-12-31_21:00:00','2006-12-31_21:00:00',
 interval_seconds = 10800,
 io_form_geogrid = 2,
 opt_output_from_geogrid_path = '/l1/dbrown/WRF/WPS',
 debug_level = 200
/

&geogrid
 parent_id         =   1,   1,
 parent_grid_ratio =   1,   3,
 i_parent_start    =   1,  66,
 j_parent_start    =   1,  18,
 e_we              =  165, 250,
 e_sn              =  129, 250,
 geog_data_res     = '10m','5m',
 dx = 36000,
 dy = 36000,
 map_proj = 'lambert',
 ref_lat   =  40.0,
 ref_lon   = -97.0,
 truelat1  =  33.0,
 truelat2  =  45.0,
 stand_lon = -97.0,
 geog_data_path = '/r0/WRF/geog'
/

&ungrib
 out_format = 'WPS',
 prefix = '/r0/2007wrfv311/ungrib/ETA',
/

&metgrid
 fg_name = '/r0/2007wrfv311/ungrib/ETA',
 io_form_metgrid = 2,
 opt_metgrid_tbl_path = '/l1/dbrown/WRF/WPS/metgrid',
/
```

OBSGRID Namelist

```
&record1
 start_year                  =  2006
 start_month                 =    12
 start_day                   =    16
 start_hour                  =    12
 end_year                    =  2006
 end_month                   =    12
 end_day                     =    22
```

```
 end_hour                     =    00
 interval                     = 10800/

&record2
 grid_id                      = 2
 obs_filename                 = "/r0/madis/little_r_obs/obs/OBS"
 trim_domain                  = .FALSE.
 trim_value                   = 5
 remove_unverified_data       = .TRUE.
 remove_data_above_qc_flag    = 32768
/

&record3
 max_number_of_obs            = 120000
 fatal_if_exceed_max_obs      = .TRUE./

&record4
 qc_test_error_max            = .TRUE.
 qc_test_buddy                = .TRUE.
 qc_test_vert_consistency     = .TRUE.
 qc_test_convective_adj       = .TRUE.
 max_error_t                  = 5
 max_error_uv                 = 5
 max_error_z                  = 8
 max_error_rh                 = 20
 max_error_p                  = 600
 max_buddy_t                  = 8
 max_buddy_uv                 = 8
 max_buddy_z                  = 8
 max_buddy_rh                 = 40
 max_buddy_p                  = 800
 buddy_weight                 = 1.0
 max_p_extend_t               = 1300
 max_p_extend_w               = 1300/

&record5
 print_obs_files              = .TRUE.
 print_found_obs              = .FALSE.
 print_header                 = .FALSE.
 print_analysis               = .FALSE.
 print_qc_vert                = .FALSE.
 print_qc_dry                 = .FALSE.
 print_error_max              = .FALSE.
 print_buddy                  = .FALSE.
 print_oa                     = .TRUE./

&record7
 use_first_guess              = .TRUE.
 f4d                          = .TRUE.
 intf4d                       =  10800
 lagtem                       = .FALSE. /

&record8
 smooth_type                  =  1
 smooth_sfc_wind              =  0
 smooth_sfc_temp              =  0
 smooth_sfc_rh                =  0
```

```
 smooth_sfc_slp              =  0
 smooth_upper_wind           =  0
 smooth_upper_temp           =  0
 smooth_upper_rh             =  0/

&record9
 oa_type                     = 'Cressman'
 mqd_minimum_num_obs         = 30
 mqd_maximum_num_obs         = 1000
 radius_influence            = 25,24,23,22,
 oa_min_switch               = .TRUE.
 oa_max_switch               = .TRUE./


&plot_sounding
 file_type                   = 'raw'
 read_metoa                  = .TRUE.
 grid_id                     = 1
/
 file_type                   = 'qc'
 file_type                   = 'results'
 file_type                   = 'discard'

&plot_level
 file_type                   = '3D'
 grid_id                     = 1
/
```

WRF Namelist

```
 &time_control
 run_days                            = 0,
 run_hours                           = 132,
 run_minutes                         = 0,
 run_seconds                         = 0,
 start_year                          = 2007, 2007,
 start_month                         = 08,   08,
 start_day                           = 03,   03,
 start_hour                          = 12,   12,
 start_minute                        = 00,   00,
 start_second                        = 00,   00,
 end_year                            = 2007, 2007,
 end_month                           = 08,   08,
 end_day                             = 09,   09,
 end_hour                            = 00,   00,
 end_minute                          = 00,   00,
 end_second                          = 00,   00,
 interval_seconds                    = 10800
 input_from_file                     = .true.,.true.,
 history_interval                    = 60,  60,
 frames_per_outfile                  = 1,   1,
 restart                             = .false.,
 restart_interval                    = 5000,
 auxinput1_inname                    = "metoa_em.d<domain>.<date>"
 io_form_history                     = 2
 io_form_restart                     = 2
```

```
io_form_input                       = 2
io_form_boundary                    = 2
debug_level                         = 0
/

&domains
time_step                           = 120,
time_step_fract_num                 = 0,
time_step_fract_den                 = 1,
max_dom                             = 2,
s_we                                = 1,     1,
e_we                                = 165,   250,
s_sn                                = 1,     1,
e_sn                                = 129,   250,
s_vert                              = 1,     1,
e_vert                              = 35,    35,
p_top_requested                     = 5000,
num_metgrid_levels                  = 27,
num_metgrid_soil_levels             = 4,
eta_levels                          = 1.0000, 0.9974, 0.9940, 0.9900,
                                      0.9854, 0.9796, 0.9723, 0.9635,
                                      0.9528, 0.9401, 0.9252, 0.9079,
                                      0.8882, 0.8659, 0.8410, 0.8133,
                                      0.7828, 0.7494, 0.7133, 0.6742,
                                      0.6323, 0.5878, 0.5406, 0.4915,
                                      0.4409, 0.3895, 0.3379, 0.2871,
                                      0.2378, 0.1907, 0.1465, 0.1056,
                                      0.0682, 0.0332, 0.0000
dx                                  = 36000, 12000,  3333.33,
dy                                  = 36000, 12000,  3333.33,
grid_id                             = 1,     2,
parent_id                           = 0,     1,
i_parent_start                      = 1,     66,
j_parent_start                      = 1,     18,
parent_grid_ratio                   = 1,     3,
parent_time_step_ratio              = 1,     3,
feedback                            = 0,
smooth_option                       = 0
/

&physics
mp_physics                          = 10,    10,
ra_lw_physics                       = 4,     4,
ra_sw_physics                       = 4,     4,
radt                                = 30,    15,
sf_sfclay_physics                   = 7,     7,
sf_surface_physics                  = 7,     7,
bl_pbl_physics                      = 7,     7,
bldt                                = 0,     0,
cu_physics                          = 1,     1,
cudt                                = 5,     5,
isfflx                              = 1,
ifsnow                              = 1,
icloud                              = 1,
surface_input_source                = 1,
num_soil_layers                     = 2,
pxlsm_smois_init                    = 0, 0
```

```
sf_urban_physics                    = 0,
maxiens                             = 1,
maxens                              = 3,
maxens2                             = 3,
maxens3                             = 16,
ensdim                              = 144,
slope_rad                           = 1,
topo_shading                        = 1,
shadlen                             = 25000.,
/

&fdda
grid_fdda                           = 1,  1
gfdda_inname                        = "wrffdda_d<domain>",
GFDDA_END_H                         = 1310, 1310,
gfdda_interval_m                    = 180, 180,
fgdt                                = 0,
if_no_pbl_nudging_uv                = 0,
if_no_pbl_nudging_t                 = 1, 1,
if_no_pbl_nudging_q                 = 1, 1,
if_zfac_uv                          = 0,
k_zfac_uv                           = 0,
if_zfac_t                           = 0,
k_zfac_t                            = 0,
if_zfac_q                           = 0,
k_zfac_q                            = 0,
guv                                 = 5.0E-4,3.0E-4,
gt                                  = 5.0E-4,3.0E-4,
gq                                  = 1.E-5,1.E-5,
if_ramping                          = 0,
dtramp_min                          = 60.0,
io_form_gfdda                       = 2,
grid_sfdda                          = 1, 1
sgfdda_inname                       = "wrfsfdda_d<domain>",
sgfdda_interval_m                   = 180, 180,
sgfdda_interval_s                   = 10800, 10800,
sgfdda_end_h                        = 1310, 1310,
io_form_sgfdda                      = 2,
guv_sfc                             = 5.0E-4,3.0E-4,
gt_sfc                              = 0, 0,
gq_sfc                              = 0, 0,
rinblw                              = 250
/

&dynamics
w_damping                           = 1,
diff_opt                            = 1,
km_opt                              = 4,
diff_6th_opt                        = 2,      2,
diff_6th_factor                     = 0.12,   0.12,
base_temp                           = 290.
damp_opt                            = 3,
zdamp                               = 5000.,  5000.,
dampcoef                            = 0.2,   0.2,
khdif                               = 0,      0,
kvdif                               = 0,      0,
non_hydrostatic                     = .true., .true.,
```

```
 moist_adv_opt                       = 2,      2,
 scalar_adv_opt                      = 2,      2,
 /

 &bdy_control
 spec_bdy_width                      = 5,
 spec_zone                           = 1,
 relax_zone                          = 4,
 specified                           = .true., .false.,
 nested                              = .false., .true.,
 /

 &grib2
 /

 &namelist_quilt
 nio_tasks_per_group = 0,
 nio_groups = 1,
/
```

APPENDIX C: OTC WRF CONFIGURATION

Option	OTC	SESARM/IA
Planetary Boundary Layer	Blackadar	ACM2
Land Surface Model	Pleim-Xiu	Pleim-Xiu
Microphysics	WSM6	Morrison
Longwave Radiation	RRTM	RRTMG
Shortwave Radiation	Dudhia	RRTMG
Cumulus	Kain-Fritsch	Kain-Fritsch
Timestep	90 seconds	120 seconds